Single particle imaging in the cell nucleus : a quantitative approach

Vincent Récamier

Université Paris Descartes

Ecole doctorale ED n°474 Interdisciplinaire Européenne

"Frontières du Vivant"

Institut de Biologie de l'Ecole Normale Supérieure (IBENS) /

Equipe Imagerie de la machinerie transcriptionnelle

Single particle imaging in the cell nucleus: a quantitative approach

Par Vincent Récamier

Thèse de doctorat de Biologie Cellulaire

Dirigée par Xavier Darzacq

Présentée et soutenue publiquement le 20 Novembre 2013

Devant un jury composé de :

Larson, Daniel, Investigator, **Rapporteur**

Mathieu Coppey Chargé de recherche **Rapporteur**

Lindner, Ariel, Chargé de recherche

Leake, Mark, Professor

Zimmer, Christophe, Chargé de recherche

Darzacq, Xavier, Chargé de recherche

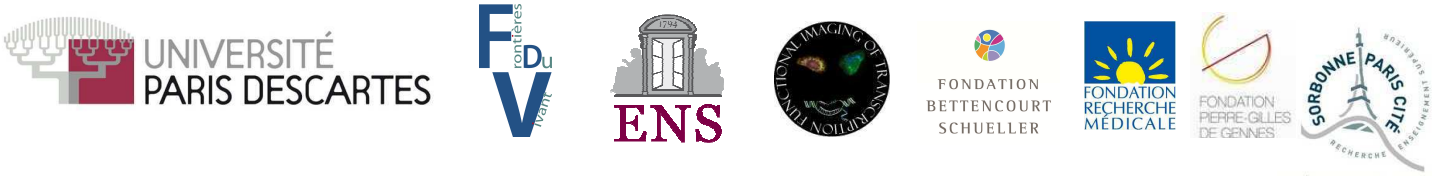
UNIVERSITÉ
PARIS DESCARTES
Frontières
Du
Vivant
ENS
FONDATION
BETTENCOURT
SCHUELLER
FONDATION
RECHERCHE
MÉDICALE
FONDATION
PIERRE-GILLES
DE GENNES
SORBONNE PARIS CITÉ

Résumé:

Le noyau cellulaire est le siège de réactions chimiques dont le but est l'expression de gènes, la duplication du génome et du maintien et l'intégrité de l'information génétique. Ces réactions sont régulées au cours du cycle cellulaire ou en réponse à un stress. Parmi elles, la transcription permet qu'une séquence d'ADN soit reproduite sous forme d'ARN messager. La transcription est un exemple frappant de processus fondamental pour la cellule impliquant parfois un nombre très faible de molécules. En effet, il n'y a souvent dans un même génome que quelques copies d'un même gène. Le but de cette thèse est d'imager les processus nucléaires dans des cellules humaines à l'échelle de la molécule unique et d'en extraire les grandeurs caractéristiques.

Depuis les années 90, des inventeurs de génie ont développé des méthodes simples à partir de microscopes inversés ordinaires pour observer des molécules individuelles jusque dans le noyau des cellules. Nous avons utilisé ces méthodes pour suivre des facteurs de transcription qui régulent la transcription d'un gène. Nos mesures montrent que, bien que hiératique, l'exploration du noyau par les facteurs de transcriptions est régulée par leurs propriétés chimiques. L'agencement des composants du noyau guide les facteurs de transcription dans la recherche d'un gène. Comme exemple de cet agencement, nous nous sommes ensuite intéressés à l'organisation de l'ADN dans le noyau pour montrer qu'elle présentait les caractéristiques d'une structure auto-organisée, une structure fractale. Cette structure change en réponse aux aléas de la vie de la cellule. Dans une dernière étude, nous avons suivi un locus dans le noyau d'une levure. La structure du noyau, qui est révélée par notre méthode, contraint la diffusion du locus à un régime de *reptation*.

Tous ces résultats montrent combien la structure du noyau et les réactions chimiques qui y ont lieu sont interdépendantes. Cette thèse a également permis le développement de méthodes de quantification précises des réactions cellulaires à l'échelle de la molécule unique

Mots clés: Transcription, recherche de cible, organisation du noyau, microscopie super résolutive.

Abstract: The cell nucleus is a chemical reactor. Nuclear components interact with each other to express genes, duplicate the chromosomes for cell division, and protect DNA from alteration. These reactions are regulated along the cell cycle and in response to stress. One of the fundamental nuclear processes, transcription, enables the production of a messenger RNA from a template DNA sequence. While mandatory for the cell, transcription nevertheless may involve a very small number of molecules. Indeed, a single gene would have only few copies in the genome. During my PhD, I studied nuclear processes in human cells nuclei at the single molecule level with novel imaging techniques. I developed new statistical tools to quantify nuclear components movement that revealed a dynamic nuclear architecture.

Since the 90s, simple methods have been developed for the observation of single molecules in the cell. These experiments can be conducted in an ordinary inverted microscope. We used these methods to monitor nuclear molecules called transcription factors (TF) that regulate transcription. From TF dynamics, we concluded that nuclear exploration by transcription factors is regulated by their chemical interactions with partners. The organization of the components of the nucleus guide transcription factors in their search of a gene. As an example of this organization, we then studied chromatin, the de-condensed form of nuclear DNA, proving that this folding displays the characteristics of a self-organized fractal structure. This structure changes in response to cellular fate and stress. In yeast, we showed that the interminglement of chromatin constrained DNA locus movement in a *reptation* regime.

All these results show the interdependence of the structure of the nucleus and of its chemical reactions. With combination of realistic modeling and high resolution microscopy, we have enlightened the specificity of the nucleus as a chemical reactor. This thesis has also enabled the development of accurate methods for the statistical analysis of single molecule data.

Keywords : Nucleus organization, Transcription, Target search, Super resolution microscopy.

I would like to thank the members of my thesis committee, the professors Daniel Larson, Mathieu Coppey, Christophe Zimmer, Ariel Lindner and Mark Leak for giving me a significant part of their time and providing me with valuable advises.

This thesis would not have been completed without several financial supports. I'm grateful to the Fondation pour la Recherche Médicale, the PG de Gennes foundation, the Bettencourt Schueller foundation and their contributors, especially the anonymous ones. Giving money for science is a proof of faith in the future. The world is so cruelly lacking of optimism and there are indeed so many incredible discoveries in science to come.

There are many people I would like to thank for those three years in Xavier Darzacq's lab, in the Institut de Biologie de l'Ecole Normale Supérieur, and in the FdV program. I hope they will not mind if I do not mention them all, because I'm afraid that I would miss somebody. I would not have imagined research to be so much fun.

Still, I would like to mention here two persons who dared to introduce a mathematician in a biology lab, no matter what would be broken.

Xavier Darzacq, my thesis supervisor, who is a great scientist, man and friend.

Francois Taddei, head of the FdV Phd program whose insight on the future of science and on education is exceptional.

The ultimate goal of those scientific years was to try to connect two brains: mine, and the (big) one of **Ignacio Izeddin** who was involved in all the projects presented here. If any praise shall be given for this work, he deserves a significant part.

Above all, I would like to thank my wife Gabrielle.

She married a financial engineer who chose to become a high school teacher who chose to become a PhD student. Nevertheless, during all those years, she never stopped supporting me.

I challenge every man on earth of finding a better proof of love.

“Qu’un mathématicien puisse imposer un modèle (…) sans acquérir une longue et nécessaire expérience pratique, cela me terrifie”

“There’s nothing as frightening as a mathematician imposing a model without having acquired a long and mandatory practical knowledge”

Pierre Gilles de Gennes “Les objets fragiles” Plon

“Assez de théorie, de l’action!”

“Enough with theory, action!”

Pierre Gilles de Gennes motto, written on his desk at the Ecole Supérieure de Physique de Chimie de Paris (ESPCI)

In 1982 Pierre Gilles de Gennes published two articles on polymer physics. This ensemble was about kinetics of reaction in polymer melts. It introduced the notion of “compact diffusion” and developing the notion of “reptation”. To a large extent, this thesis relies on those two concepts. Reading De Gennes non-scientific writing, I also discovered a man whose practical vision of life, research and teaching changed my own perception. This thesis is humbly dedicated to the memory of Pierre Gilles de Gennes who has become a personal hero.

1 FOREWORD 11

2 INTRODUCTION 15

2.1 MODELING SINGLE PARTICLE NUCLEAR MOTION 15

2.1.1 NUCLEAR PARTICLE DIFFUSION 16
2.1.2 REACTION KINETICS AND DIFFUSION 27
2.1.3 CONCLUSION ON MODELING 35

2.2 NUCLEAR SINGLE PARTICLE MICROSCOPY 37

2.2.1 SUPER RESOLUTION 37
2.2.2 SPT PALM 47
2.2.3 FLIP (FLUORESCENT LOSS IN PHOTO-BLEACHING) 50
2.2.4 CONCLUSION ON MICROSCOPY 53

2.3 STATISTICAL ANALYSIS OF LIVE CELL SINGLE PARTICLE TRAJECTORIES 55

2.3.1 MEAN SQUARE DISPLACEMENT AND FREE DIFFUSION 56
2.3.2 CONSTRAINED DIFFUSION IN A CELL 61
2.3.3 FITTING MSD CURVES TO A POWER LAW 66
2.3.4 ALTERNATIVE STATISTICS TO MSD 69
2.3.5 ANALYSIS OF AN HETEROGENEOUS SET OF TRAJECTORIES 82
2.3.6 CONCLUSION ON STATISTICS 89

3 RESULTS 91

3.1 I-SPT PALM 91

3.1.1 SUMMARY 91
3.1.2 ABSTRACT 93
3.1.3 INTRODUCTION 94
3.1.4 RESULTS 97
3.1.5 DISCUSSION 111
3.1.6 EXPERIMENTAL PROCEDURES 116

3.2 P-TEFB DYNAMICS 119

3.2.1 SUMMARY 119
3.2.2 ABSTRACT 120
3.2.3 INTRODUCTION 120
3.2.4 RESULTS 122
3.2.5 DISCUSSION 131

3.2.6 MATERIAL AND METHODS 132
3.3 SINGLE CELL CORRELATION FRACTAL DIMENSION OF CHROMATIN 137
3.3.1 SUMMARY 137
3.3.2 ABSTRACT: 138
3.3.3 INTRODUCTION 138
3.3.4 RESULTS 141
3.3.5 DISCUSSION 151
3.3.6 MATERIAL AND METHODS 155
3.4 YEAST LOCUS MOBILITY 158
3.4.1 INTRODUCTION 158
3.4.2 RESULTS 160
3.4.3 DISCUSSION 164
4 CONCLUSION 171
5 BIBLIOGRAPHY 173
6 SUPPLEMENTARY INFORMATION 197
6.1 I-SPT-PALM 197
6.1.1 SUPPLEMENTARY FIGURES 197
6.1.2 SUPPLEMENTARY TEXTS 205
6.2 P-TEFB DYNAMICS 216
6.2.1 SUPPLEMENTARY TEXTS 216
6.3 SINGLE CELL CORRELATION FRACTAL DIMENSION OF CHROMATIN 221
6.3.1 SUPPLEMENTARY FIGURES 221
6.3.2 SUPPLEMENTARY TEXTS 228
6.1 YEAST LOCUS MOBILITY 233
6.1.1 SUPPLEMENTARY FIGURES 233

1 Foreword

The nucleus of a cell as a chemical reactor

The cell nucleus hosts the genetic information encoded in the DNA. In a human cell, the nucleus is composed of 5% nuclear acids and 40% proteins that will serve three broad tasks: express the genes, duplicate the chromosomes for cell division, and protect DNA from alteration. The cell fate is determined by the interaction between nuclear constituents, and the development of biochemistry has enlightened the high number of possible partners inside the nucleus and the various types of nuclear interactions:

- *Protein-DNA interactions* have been widely studied as a consequence to the development of Chromatin Immuno Precipitation (ChIP) techniques. All regions of the nucleic DNA do not have the same affinity to proteins and the binding of proteins in the vicinity of a gene would trigger or inhibit gene expression.
- *The study protein-protein interactions* is referred as "proteomics". A nuclear protein can exist simultaneously in different conformations and can be integrated in complexes of various sizes and functions.
- *DNA-DNA interactions***.** Recently, high throughput sequencing methods have been developed to find physical interactions between DNA regions mediated by proteins. The spatial organization of the genome could play a crucial role in nuclear reactions.

The above list is not exhaustive and should also include, for example, RNA. Interactions between nuclear components are regulated. Cells constitute dynamic systems that keep changing along their living cycle and as a response to their environment. The understanding of the time interplay of nuclear reaction is crucial for deciphering the runing of the cell and to cure its possible dysfunctions.

Biochemistry assays measure the level of nuclear interactions for a pool of cells at a given time of the cell cycle. Huge databases of those interactions have been created to be worldwide accessible and bioinformatics efforts are concentrated into extracting the architecture of cell reactions network. The main unit of this architecture is the *pathway:* a succession of chemical

interactions whose final purpose is the regulation of a cellular function One example of such a function is *transcription*.

Transcription

Transcription is the nucleic chemical reaction that consists in the production of a messenger RNA (mRNA) from a template gene. The mRNA will later be translated into a protein in the cytoplasm. In the chemical pathway of transcription, a transcription factor (TF) is a general term for a molecule that regulates mRNA production. A TF can be either *specific* to a particular gene or mandatory for the expression of every gene, the latter being called *general*. An example of a general TF is the RNA-Polymerase II, a complex composed of 12 subunits that will incorporate nucleotides in the nascent mRNA. The frontier between generic and specific TF is very narrow, some TF being required for the transcription of most (but not all) of the genes.

In 1962, Jacob and Monod showed the time regulation mechanism of a single gene in bacteria by a combination of activation and repression of specific TFs at a DNA locus. This fundamental advance explained the way transcription could be time regulated but left an open issue: How will a TF find its specific DNA target inside the nucleus? Recent advances in cell microscopy have allowed to peek inside the nucleus and to follow single molecules in search of their substrate.

Single molecule imaging

Since the discovery of the Green Fluorescent Protein (GFP) in the 1960's, functional fluorescent imaging has become a routine technique of cell biology. By tagging nuclear factors with fluorescent molecules, we are now able to locate proteins into the cell and to follow them through time. During the last decades, intense efforts have been developed to increase the resolution of fluorescent microscopes. *Superresolution* or single particle imaging now enables to directly see where single molecules are and to record their trajectories into the nucleus.

Compared to biochemistry, the time ranges of fluorescent microscopy are orders of magnitude lower. The typical time range of biochemistry assays is one hour. We can now quantify with superresolution nuclear interactions that last milli-seconds and measure the cell-to-cell variability. Since the field is emerging, there is still a need to develop robust quantification from the data produced by single particle imaging. The introduction of this thesis reports some of the recent advances in nuclear single molecule quantification. I will first introduce how we can

model the motion of a single particle inside a cell. Then, I will present superresolution from a quantitative point of view and finally the statistics that we can compute on single particle data.

Results

In the result session I will introduce four studies that explicitly quantify nuclear interactions at the single molecule level in the nucleus of human cells, using superresolution microscopy.

- *The protein-DNA interaction* from the DNA binding molecule H2B and the specific TF c-Myc.
- *protein-protein interaction* via a general transcription factor, the positive transcription elongation factor b (P-TEFb) that binds to RNA-polymerase II to trigger transcription.
- *DNA-DNA interaction***.** We imaged in 3D a the single molecule level the organization of chromatin, the de-condensed nuclear form of DNA (Session3). We also measured the movement in yeast of a DNA locus.

Those results clearly show the influence off nuclear structure on the nuclear chemical reactions kinetics such as transcription and DNA repair.

2 Introduction

2.1 Modeling single particle nuclear motion

In the nucleus of cells, molecules diffuse in search of partners and their intra nuclear movement has been studied for four decades with bulk imaging techniques (Axelrod et al., 1976). Under the assumption that the measured fluorescence is proportional to nuclear concentration, ensemble measurement of moving molecules such as FRAP (Fluorescent Recovery After Photo-Bleaching) are described by macroscopic reaction-diffusion equations. The experimentalist fixes the underlying model of diffusion, and then confronts the model to the bulk data. Since possible models are numerous, it is difficult to rule them all out and get to the exact description of the movement (Mueller et al., 2010).

Imaging molecules with single particle tracking (SPT) imaging techniques enables direct measurement of chemical interactions. Therefore SPT data can theoretically be explained with weaker assumption. For that reason, cellular live single particle assays have been a significant breakthrough in the measurement of reaction kinetics, but has until recently been restricted to membrane dynamics (Alcor et al., 2009). In the nucleus, the particles whose movement has been recorded are:

- **Macromolecular complexes and organelles** such as Cajal bodies (Platani et al., 2002). Because of their size, macromolecules diffuse slowly which enable a long lasting imaging.
- **Inert reactants.** Quantum dots have been introduced by micro injection inside the nucleus and followed through time (Bancaud et al., 2009). Since quantum dots are not supposed to react chemically, it is not the nuclear functions but rather the nuclear architecture that is revealed with those assays.
- **Loci.** DNA is a long macromolecule whose segments can be labeled by coating fluorescent protein. For instance, by inserting repeats of tetracyclin or Lactose operators (TetO and LacO) at a specified locus and expressing fluorescent TET or Lac repressor

(TETr and Lacr)(Miné-Hattab and Rothstein, 2012)(Weber et al., 2010a). Another option is to express fluorescent sequence site specific partners (Bronstein et al., 2009). When DNA is damaged, one pathway for repairing is to use the homologue as a template(Alberts, 2008). How loci find their homologous sequence is not fully understood, but is investigated with single particle tracking.

- **Nuclear factors** such as the transcription factor Oct4 (Plachta et al., 2011), Stat1 (Speil et al., 2011a) or p53 (Mazza et al., 2012a)**.** Because nuclear factors will bind to specific DNA sequences such as gene promoters, transcription dynamics are driven by the search of DNA sequences at the single molecule level(Normanno et al., 2012).

In this modeling section, I will explicit the models of nuclear particle movement that have been developed. Those can be discriminated in two categories: *free diffusion* and *anomalous diffusion.* In a second part, I will focus specifically on the research of a specific sequence of nuclear DNA by nuclear factors or damaged loci. Target search mechanisms have been studied for a century in the broad context of random walk and among the concepts introduced by one has had a tremendous impact on theoretical biology of the nucleus, *the first passage time.*

2.1.1 Nuclear Particle diffusion

2.1.1.1 General Formalisms

2.1.1.1.1 Requirements for an accurate modeling of nuclear particle motion

Before going further on the precise mathematics, there are four features of the nucleus that should be integrated into intra nuclear single particle dynamics models. Although those features seem obvious, their exact formulation is not and to a large extent, the eukaryotic nucleus is still *terra incognita.*

- **The nucleus is a closed environment.** In eukaryotes, the nucleus has finite boundaries, and particle motion occurs in a finite volume. However, we know that the membrane is porous and protein-nuclear membrane interaction is still thoroughly studied (Lowe et al., 2010). Theoreticians of nuclear movement have modeled the membrane by simply discarding it (von Hippel and Berg, 1989), or by *instant transport* of the nuclear molecule to a random position when it hits the membrane (Coppey et al., 2004).

- **The nucleus is not empty.** The nucleus hosts nucleic acids and proteins, but is it a crowded or sparse space? As a preliminary response, the DNA packing ratio in a eukaryotic nucleus, that is the volume of DNA divided by the volume of the cell, is estimated to be only 2×10^{-3} (Phillips, 2013). However DNA is not the only molecule inside the nucleus and this number is only a lower bound for crowding. To model the motion of nuclear elements, rather that the space available for diffusion, it's more the spatial distribution of chemical partners that is important. Indeed nuclear proteins dynamics are drastically changed by the protein's ability to interact with its environment (Phair and Misteli, 2000)
- **DNA is folded inside the nucleus.** Chromosomes are meter long molecules that folds into a micrometric envelope. How DNA organization interferes with nuclear wanderers is not fully understood. Actually, early modeling of DNA interacting protein motion have simply discard packing (Coppey et al., 2004). Recently, however, it has been proposed that DNA nuclear folding can be a key feature for nuclear chemical reaction such as gene regulation(Lomholt et al., 2009). Modeling how DNA is packed inside the nucleus, has been subjected to intense research recently with multiple techniques (Mateos-Langerak et al., 2009).
- **Nuclear particle motion is not deterministic.** The first observations that were made on transcription factor single molecules dynamics showed the stochastic nature of their motion, even in bacteria (English et al., 2011). Any model of nuclear particle dynamics should incorporate randomness. However, gene transcription is a regulated mechanism (Alberts, 2008). So, specifically addressing transcription factor motion, at which level can this regulation occurs, if any?

2.1.1.1.2 Equations of particle diffusion

Now that we have in mind the basic feature of nuclear particle diffusion, we need a mathematical formalism to express them. The evolution of the time dependent position $r(t)$ can be modeled by three **diffusion equations** that are presented below from the most deterministic to the most probabilistic:

The Langevin Equation (Berg, 1993) :

$$m\ddot{r}(t)+\gamma\dot{r}(t)+\nabla K(r(t))=\zeta(t) \qquad (1)$$

Here m is the mass, γ is the viscosity of the medium, K is a term that accounts for the contribution of local forces derived from a potential and $\zeta(t)$ is the noise that accounts for the thermal agitation of molecules. The Langevin equation is issued from Newtonian mechanics and is deterministic. The particle motion is completely described by its position and velocity. For statistical inference, that is the estimation of statistical parameters from a set of trajectories the Focker-Planck equation offers a more suitable framework.

The Focker-Planck equation (Berg, 1993) expresses the probability $p(r,t)$ to find the particle at position r and time t. $p(r,t)$ is sometimes referred as the propagator of the motion.

$$\frac{\partial p}{\partial t}=D(t)\left(\Delta p+\nabla K\right) \qquad (2)$$

Here $D(t)$ is the diffusion term that accounts for the thermal agitation of the molecules and K is a potential term. This approach has been very powerful for complex statistical inference. It has also been widely used when authors wanted to confront the data to non-mechanistic models such as random walks on complex media. For all those models, the propagator $p(r,t)$ can be mathematically obtained regardless the physical origins of diffusion (Bénichou et al., 2010)

The Stochastic diffusion equation formalism enables more flexibility than the Focker-Planck equation (Gardiner, 1985).

$$dR_t=\mu(R_i,Y_i,t)dt+D(R_t,Y_i,t)dW_t \qquad (3)$$

Here, R_t accounts for the stochastic process of the position, μ for the deterministic trend, and W_t a stochastic noise process. With the stochastic equation, the diffusion term $D(R_t,Y_i,t)$ can be probabilistic. Y_i is an explanatory random variable that will account for instance for different conformations of the protein . Such formalism can be used in most state change measurements such as binding (Das et al., 2009). Recently, and mainly due to their importance in finance, statistical tools for stochastic calculus have been extensively developed but with little application to the interpretation of single particle data

2.1.1.2 Free diffusion

With those mathematical formalisms, we can now model nuclear exploration. Unconstrained diffusion is sometimes labeled as “free diffusion” as opposed to anomalous diffusion, and the simplest model of free diffusion is Brownian motion.

2.1.1.2.1 Brownian motion

In 1827 when looking at small grain of pollens in water, Robert Brown found a hieratic movement. Later, Langevin and Einstein found independently the physical origin of the phenomenon with the conservation of energy and successive bouncing of the particles to its neighbors. The equations of Brownian motion were later experimentally proved by Perrin. The absence of acceleration and external forces reduces diffusion equations to their simplest form: (Hida, 1980).

$$dX_t = \sqrt{2D}dW_t \qquad (4)$$

$$\frac{\partial p}{\partial t} = D\Delta p \qquad (5)$$

$$\dot{r}(t) = \sqrt{2D}\zeta(t) \qquad (6)$$

The only parameter left to characterize the movement is the diffusion coefficient, whose definition is given by the Stoke Einstein equation (7):

$$D = \frac{k_B T}{6\pi\gamma r} \qquad (7)$$

Where r is the Stoke radius of the molecule and γ is the viscosity of the medium. Brownian behavior has been confirmed for a wide range of phenomenon but is not true at all length and time scales. Looking at glass beads, Lie et al. recently showed experimentally that free unconstrained motion was indeed ballistic at short time scales and Brownian at higher time scales (Pusey, 2011)(Li et al., 2010). Mathematically, Brownian motion is the continuous limit of a discrete free random walk. For that reason, the Donsker theorem imposes:

- The shape of the propagator (8) to be simple Gaussian in every direction:

$$p(r,t) = \frac{1}{\sqrt{2\pi \times 2Dt}} e^{\frac{-r^2}{2\times 2Dt}} \qquad (8)$$

- The projection of the motion on orthogonal axis to be statistically independent.

2.1.1.2.2 Diffusion and binding

Now that we have a model of free diffusion, the simplest way to incorporate interactions of the nuclear particles is via binding. A single molecule binding-diffusion model would incorporate an hidden variable Y_t that switches between two states: *bound* (0) and *diffusive* (1) with corresponding diffusion coefficients $D(Y_t = 0) = 0$ and $D(Y_t = 1) = D > 0$. The transition between those states occurs according to rates k_{on} and k_{off}.

$$Y_t = 0(bound) \underset{k_{on}}{\overset{k_{off}}{\rightleftarrows}} Y_t = 1(diffusive) \qquad (9)$$

With transition probabilities $\Pr(Y_{t+h} = 0 | Y_t = 1) = k_{on} h$ and $\Pr(Y_{t+h} = 1 | Y_t = 0) = k_{off} h$ during observation time h.

For DNA binding proteins, numerous methods have been proposed to measure k_{off}. Those methods include single particle tracking (Gebhardt et al., 2013) but also FRAP, FCS, Competition CHIP. Addressing the same factor, different techniques will rather coherently exhibit the same binding kinetics(Mazza et al., 2012a). The model presented here is over-simplification of the real intra-nuclear binding. In most observed cases, a single coefficient k_{off} is not enough to describe the movement (Gebhardt et al., 2013).

To my knowledge, as opposed to k_{off}, no assay so far has been able to reliably measure k_{on} for nuclear factors. One possible reason could be that that the particle cannot bind anywhere and only *to binding sites* k_{on}. In such a scenario the formulation $\Pr(Y_{t+h} = 1 | Y_t = 0) = k_{off} h$ is not valid and depends on the spatial distribution of those binding sites (Mueller et al., 2010). What have been measured, nevertheless is the effective k_{on}^*, that is the product of k_{on} with ratio of bounds compared to unbound proteins at the equilibrium (Sprague et al., 2004).

2.1.1.3 Anomalous diffusion

2.1.1.3.1 Definition

For Brownian motion, equation (6) integrated and averaged gives the following time to distance dependence (10), referred as the theoretical *mean square displacement* MSD.

$$\left\langle \left| r(t) - r(0) \right|^2 \right\rangle = 2dDt \qquad (10)$$

Where $\langle . \rangle$ denotes the mathematical expectancy and d is the dimension of the space (1, 2 or 3). As a result, if the squared displacement scales linearly with time, the diffusion is said to be *normal.*. As opposed to normal diffusion, the motion is *anomalous* if the MSD have the following scaling(11)

$$\left\langle \left| r(t) - r(0) \right|^2 \right\rangle \propto t^{\alpha}, \alpha < 1 \qquad (11)$$

I refer to Höfling and Franosh for a complete review of anomalous diffusion inside the cell (Höfling and Franosch, 2013). Only four type of models have been proposed to explain anomalous diffusion (Metzler R. and Klafter J., 2000):

- The continuous time random walk (CTRW) is a binding-diffusion model with binding times so large that k_{off} does not exist. CTRW is related to the more general notion of *ergodicity*, that I will develop the statistical analysis of SPT section.
- Fraction Langevin Motion (FLM) and Fractionnal Brownian Motion (FBM) are modified version of the Langevin and Focker-Planck equations with *fractional derivatives*
- Regimes of diffusion of monomers on a polymeric chain
- Random walk on complex media

2.1.1.3.2 Equations of diffusion with fractional derivatives.

2.1.1.3.2.1 Fractional Langevin motion (FLM)

Brownian motion is Markovian, meaning that only the last position of the particle is needed to estimate the conditional future. The fractional Langevin equation is a modified version of the Langevin Equation that integrates a form of memory to make it non-markovian (Kobelev and Romanov, 2000)

It can be expressed as follow (Weihua Deng, 2009):

$$m\frac{d^2r(t)}{dt^2} = -\bar{\gamma}\int_0^t (t-\tau)^{2H-2}\frac{dr}{d\tau}d\tau + \eta\xi(t) \qquad (12)$$

with $\eta = \sqrt{\frac{k_B T\bar{\gamma}}{2D_H H(2H-1)}}$, D_H is a scale factor for the diffusion coefficient , $\bar{\gamma}$ is a generalized friction constant and H is the anomalous term, also called the *Hurst coefficient*. The friction term of the equation is not proportional to the speed, as it is for the ordinary Langevin equation, but to an integrated past displacement. The scaling of the square displacement is:

$$\left\langle \left| r(t)^2 - r(0)^2 \right| \right\rangle \propto t^{2-2H} \qquad (13)$$

The Fractional Langevin equation accounts for displacement of units of a flexible molecule (Min et al., 2005) but it most relevant application is particle motion in non-Newtonian or visco elastic fluids. Weber et al proposed a combined visco elastic medium–polymer model for the anomalous square displacement scaling of a locus in bacteria (Weber et al., 2010a). In real non Newtonian fluids, however, fractional Langevin dynamics seem to be only a limit case (Ott and Bonitz, 2009)

2.1.1.3.2.2 Fractional Brownian motion (FBM)

Another possibility to introduce anomalous motion is via fractional derivatives of the Focker Planck equation (Metzler R. and Klafter J., 2000). Solutions of the equation are integrated *Fractional Brownian motions* (FBM) .

$$\frac{\partial}{\partial t}p(r,t) = K_\alpha D_t^{1-\alpha}\frac{\partial}{\partial r^2}p(r,t) \qquad (14)$$

With $D_t^{1-\alpha}$ being the Riemann-Liouville operator and K_α being a scaling factor:

$$D_t^{1-\alpha}\frac{\partial}{\partial r^2}p(r,t) = \frac{\partial}{\partial t}\int_0^t d\tau\frac{p(r,\tau)}{(t-\tau)^{1-\alpha}} \qquad (15)$$

The solution of the equation will have the following anomalous scaling $\left\langle r^2 \right\rangle \propto t^\alpha$.

To the extent of my knowledge, there is no one to one correspondence between the solutions of fractional Brownian and fractional Langevin equations, but the mechanism of non markovianity

is similar. FBM is more convenient for sequential simulation even if it implies computing a correlation matrix of increasing size (Dieker, 2004)

FBM and FLM have been suggested as an explanation of the observed anomalous exponent α in nuclear factor kinetics (Weigel et al., 2011). In the specific case of loci movement, polymer physics have also grounded the existence of anomalous exponents $\alpha \neq 1$.

2.1.1.3.3 Polymer regimes

Looking at the movement of DNA loci. authors sreported several anomalous exponents in yeast and bacteria (Weber et al., 2010a) and in human cells(Bronstein et al., 2009). DNA is a long polymeric chain, whose monomeric unit can either be considered one nucleosome (MacKintosh, 2012) or one base (Schiessel et al., 2001). Polymer physics has hypothesized the anomalous motion of a monomeric unit according to the "regime" of diffusion, that is the time scale at which the motion is observed. Polymeric models are therefore good candidates to explain the anomalous motion of loci that was observed *in-vivo*.

2.1.1.3.3.1 The Rouse model ($\alpha = \frac{1}{2}$) and the Zimm model ($\alpha = \frac{2}{3}$)

The Rouse and Zimm models are models of diffusion of a monomer of a free polymer chain in a diluted regime. The difference between the Zimm and the Rouse is the added electro-static repulsion between monomers in the Zimm model. It has been shown in vitro that in diluted regimes, naked single stranded DNA would undergo Zimm mode of motion while double stranded DNA would undergo a Rouse mode of motion (Shusterman et al., 2004). The first and second order of the 3D MSD are for the Rouse and Zimm model (Rouse, 1953)(Zimm, 1956):

$$\text{Rouse: } \left\langle \left| r(t) - r(0) \right|^2 \right\rangle \propto 6D_g t + \left(\frac{48 k_B T}{\pi \gamma} \right)^{\frac{1}{2}} t^{\frac{1}{2}} \qquad (16)$$

$$\text{Zimm: } \left\langle \left| r(t) - r(0) \right|^2 \right\rangle \propto 6D_g t + 2\left(\frac{k_B T}{\eta} \right) t^{\frac{2}{3}} \qquad (17)$$

With η being the viscosity of the medium and γ being the friction coefficient. The term $6D_g t$ reflects the simple diffusion of the center of mass of the total polymer chain. The resulting

motion of those two models is anomalous in the *second order term*. For the motion to be anomalous at every scale, the global motion of the chain needs to be zero. This is for instance the case for polymer brushes (Zhao and Brittain, 2000), polymers that are anchored. For polymer brushes the first order term of the MSD vanishes, leaving only the anomalous terms.

2.1.1.3.3.2 The reptation model $\alpha = \frac{1}{4}$ *and* $\alpha = \frac{1}{2}$

In 1971 de Gennes introduced the reptation model of polymer diffusion in the presence of fixed obstacles (de Gennes, 1971). In 1982, he extended reptation to polymer melts in semi diluted regimes (de Gennes, 1982a). Reptation explains the anomalous motion of a polymer chain of N monomers, in an entangled regime where the chain creates "blobs" or entanglement segregated by "kinks", with an averaged of monomers N_e per entanglement. Reptation appears in entangled polymer solutions provided that the time is comparable to the Rouse time T_R. T_R is the time where the rouse chain reaches equilibrium at the kinks. De Genes gives $T_R \cong W^{-1}N^2$ where W is the microscopic frequency of the monomer Rouse movement.

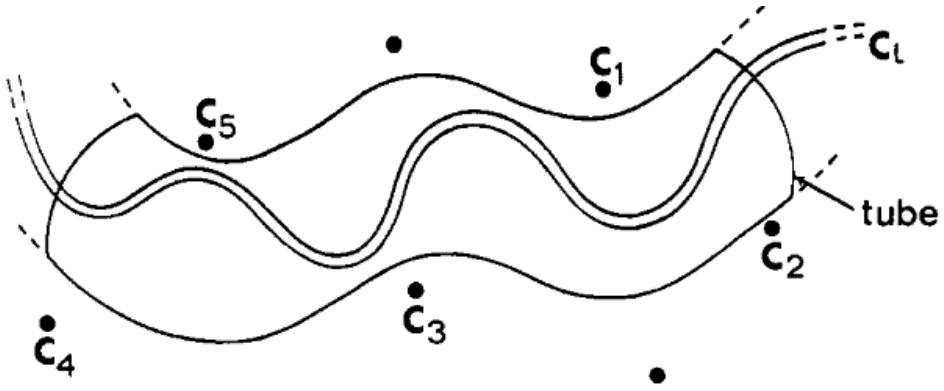

Figure 1: Original drawing of PG De Gennes for the introduction of the reptation model in the case of fixed obstacles. The chain is trapped in a tube defined by adjacent constraints $C_1 \ldots C_5$

In a reptation mode of motion, the polymer is segregated by "kinks" in topological segregated "blobs". The disposition of those blobs is governed by diffusion so that an alternative way to represent the reptation constraint is a tube whose conformation is that of a random walk (Figure 1). Such description is similar to that of the equilibrium globule which has been suggested as a

possible explanation for chromosome organization in the nucleus of eukaryotes (Grosberg et al., 1993). Along this tube, the motion of a monomer is given by successive diffusions:

- For $t > T_R$ the chain has reached equilibrium at the kinks. Motion of a monomer of the chain would be random walk from entanglement to entanglement so that $\langle x^2 \rangle \cong (\delta^2 D^T t)^{1/2}$ where $\delta \propto N_e^{-1/2} a$ is the *diameter of the tube* and D^T is the linear diffusion coefficient along this tube. In the end, we get an anomalous $\alpha = \frac{1}{2}$
- For $t < T_R$ the equilibrium has not been reached at the kinks. At the kink the motion is governed by diffusion so that: $\langle x^2 \rangle \cong (\delta^4 a^4 W t)^{1/4}$, with W being the mode of the Rouse chain. We get $\alpha = \frac{1}{4}$.

The reptation model also includes the Rouse behavior at very short time lower than T_δ where the monomer does not see the effect of entanglement. In the end, three anomalous regimes are expected from reptation (Figure 2) .

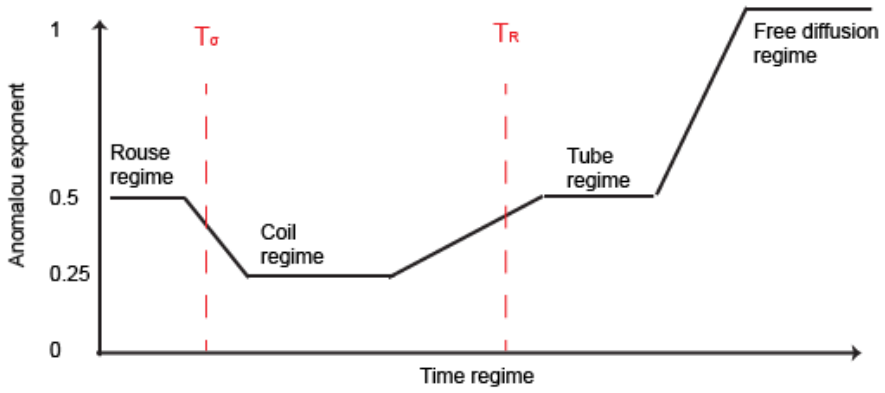

Figure 2: Anomalous scaling coefficient of the MSD for reptation model as a function of the time regime

The validity of the DNA reptation mode has not been demonstrated experimentally so far in the nucleus. In vitro studies showed reptation during the relaxation of constrained phage DNA (Perkins et al., 1994). In silico experiments trying to reproduce the nucleus showed that

monomer motion was mostly Rouse-like even under high confinement (Weber et al., 2010a). Theorists showed however that the DNA wrapping along the histone octamer could induce a reptation-like mode of motion of the base (Schiessel et al., 2001).

2.1.1.3.4 Diffusion on disorded media

Another possible model of anomalous diffusion inside the cell is the random walk on a fractal network (Ben-Avraham, 2004). Fractals are self-similar mathematical objects built upon the repetition of simple rules and characterized by a non-integer number: *the fractal dimension* df (Falconer, 2003). The fractal nature of the nucleus and especially of chromatin has been studied for a decade and I refer to (Bancaud et al., 2012) for a complete review on the subject. On the Results part of this thesis I will present a new technique based on super-resolution to compute the fractal dimension of chromatin.

Random walk on fractals is sub-diffussive due to the spatial correlation of displacements. The anomalous scaling factor is (18):

$$\left\langle \left| r(t) - r(0) \right|^2 \right\rangle \propto t^{\alpha} = t^{\frac{2}{dw}} \qquad (18)$$

where dw is the *dimension of the walk* that is specific to the fractal. The number of known determiistic fractals is finite and each of them has different dimensions dw and df (Ben-Avraham, 2004). If every single fractal constitutes a system on its own, we can question the relevance of a general fractal model for nuclear sub-diffusion. With probability, we can create an infinite number copies of fractals, different but sharing the same fractal characteristics. Random walks on those random fractals seem to share some additional common features:

- For a sub-class of random fractals, *percolation clusters,* Alexander and colleagues conjecture that spectral dimension $d_s = \frac{2d_f}{d_w}$ is a constant (Alexander et al., 1982):

$$d_s \approx \frac{4}{3} \qquad (19)$$

The name of this conjecture is the Alexander Orbach conjecture (AO). According to Ben Avraham (Ben-Avraham, 2004) the conjecture has not been resolved so far.

- If the fractal is "homogenous enough", Ben Avraham suggested the propagator on a random fractal to have the following general form, for the regime $r >> t^{1/dw}$.

$$P(r,t) = \frac{r^{df-d}}{t^{ds/2}} \Phi\left(\frac{r}{t^{1/dw}}\right) \qquad (20)$$

Where d is the embedding dimension and Φ being exponential . Bancaud et al. used this form to compute the fractal dimension of the nucleus from the motion of an inert tracer(Bancaud et al., 2009).

Because of those common features, random walk on random fractals have been considered as a "universal model" of sub-diffusion in a crowded environment (Dix and Verkman, 2008). However, Appelhans and colleagues failed to reproduce the anomalous motion observed in vivo, on an in vitro model of random fractals made with polymers (Appelhans et al., 2012). Because it is unsure how much of the reality of crowding the fractal model can reproduce, Saxton argued that the fractal interpretation of anomalous motion should be confronted to an accurate in-vitro model of crowding, that has not been developed yet (Saxton, 2012a).

2.1.2 Reaction kinetics and diffusion

In the previous part, I have described models of movement of single particles inside the nucleus. Now, we will describe how this motion can influence nuclear reaction dynamics and especially transcription. I will now describe the simplest model of single molecule.

2.1.2.1 General Formalisms

In the simplest model single molecule transcription, a population of N single type transcription factors TF diffuses in the nucleus in search of promoter B on DNA modeled as a fixed target. Anytime a transcription factor passes through the target B, a mRNA is produced. (Figure 3).

$$TF + B \rightarrow mRNA \qquad (21)$$

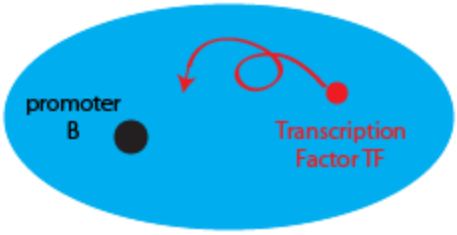

Figure 3: Simplest schematic description of transcription. A transcription factor TF diffuses inside the nucleus in search of a promoter B. Anytime the TF reaches B, a mRNA is produced.

In such a scenario, the reaction rate, the number of mRNA produced, is the number of TFs that pass through the DNA site, which can be computed in either one of the two following ways:

- To compute the flux of TFs through the target B in a "continuous regime"
- To compute, for each molecule, the time needed to pass through the target and to sum over all the particles.

The **first passage time** (FPT) is the time needed for a random walker to find a target. Since the pioneer work of Polya (Pólya, 1921), FPT has been intensively studied by theoretical physicists and mathematicians (Burschka, 1997). It has been for instance shown that optimal strategies of target search exist and that animals use those strategies (Humphries et al., 2010).

2.1.2.2 Free diffusion

On this section we assume that transcription factors diffuse freely with the same fixed diffusion coefficient D.

2.1.2.2.1 Continuous regime

Let's assume that the target B is a sphere of radius r_B. Assuming a fixed concentration $[TF]$ of transcription factors and integrating the flux of TF through the sphere via Fick's law, we obtain the rate of transcription k_T

$$k_T = 4\pi D r_B [TF] \qquad (22)$$

This result, however is an over-simplification since (i) the target gene may not be spherical (ii) binding could be enhanced or repressed by electrostatic interaction (iii) only a small fraction of the target surface may interacting with the TF . In order to account for a more complex target, Von Hippel and Berg(von Hippel and Berg, 1989) proposed the following rescaled equation:

$$k_T = 4\pi kafD[TF] \qquad (23)$$

With k being the surface ratio, a being the interaction distance and f being an parameter accounting for electrostatic interaction.

2.1.2.2.2 First passage time in confined geometry

On the continuous regime model, as we have seen, the main problem is to define an effective cross section of the interaction between the TF and its target. This first passage time formalism, on the opposite, is robust to any particular geometry of the target.

In 1980, Szabo (Szabo et al., 1980) showed that the averaged mean first passage time (MFPT) could reproduced the reaction rate of the continuous regime. In a sphere of radius R for a target of size a, the mean first passage of a particle is given as a function of the distance to the target r by eq(24) (Schmit et al., 2009):

$$\tau_{3d}(r) = \frac{1}{D}\left(-\frac{r^2}{6} - \frac{R^3}{3r} + \frac{a^2}{6} + \frac{R^3}{3a}\right) \qquad (24)$$

Integrated on the whole volume, one gets the inverse mean reaction rate:

$$\overline{\overline{\tau_{3d}}} = \frac{1}{D(R^3 - a^2)}\left(\frac{R^6}{3a} - \frac{3R^5}{5} + \frac{R^3a^2}{3} - \frac{a^5}{15}\right) \qquad (25)$$

and we can reproduce the continuous limit regime:

$$\lim_{R\to\infty} [TF]\frac{4}{3}\pi R^3 \frac{1}{\overline{\overline{\tau_{3D}}}} = 4\pi Da[TF] = k_T \qquad (26)$$

The flexibility of the formalism is wide and can be applied to many kinds of geometry, concentrations, and type of diffusion. For instance, an optimal concentration of transcription factors was estimated in silico, in the context of crowding, to reach the highest reaction rate (Schmit et al., 2009). Different target geometries have also been investigated with MFPT such as the *narrow escape approximation* (Holcman et al., 2011). It can be convenient for MFPT estimation to discretize the space and to model it as a lattice, the motion being reduced to a discrete random walk (Bénichou et al., 2010). However, lattice models of reaction rate significantly differ from continuous models if the number of particles is small (Yuste and Lindenberg, 2001).

2.1.2.2.3 Facilitated Diffusion

In 1968, Riggs and collegues reported that E Coli Lac repressor binding to DNA in vitro was 1000 fold faster than upper limit of the free diffusion model (Riggs et al., 1968). This observation led to assumption that DNA target search process was enhanced compared to a random process. In 1989 Von Hippel and Berg proposed the facilitated diffusion model(von Hippel and Berg, 1989). The facilitated diffusion model will combine 3-dimentionnal diffusion and 1D sliding on the DNA chain (Figure 4).

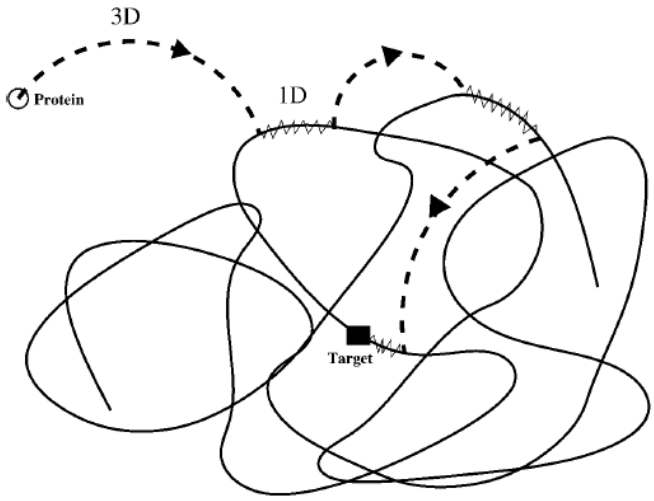

Figure 4 ***Schematic description of facilated diffusion.*** *The transcription factor alternates between 1D diffusion and 3D diffusion phases in search of its DNA target sequence (reproduced from(Coppey et al., 2004))*

I refer to the exhaustive review on facilitated diffusion written by Davide Normanno (Normanno et al., 2012). Recently, Elf et al. proved in vivo facilitated diffusion for the Lac repressor in bacteria (Hammar et al., 2012). Even if observed for the Lac repressor, facilitated diffusion does not seem to the default search mode of transcription factors. Wang et al. showed that promoter search of RNA polymerase was mainly dominated by 3D diffusion in Escherichia Coli (Wang et al., 2012). The nature of the observed 1D sliding was highly discussed by the committee. Some argued for example that the salt concentration of the pioneer experiments does not seem to correspond to in-vivo conditions increasing the affinity of the TF to DNA in-vitro (Normanno et al., 2012). Szelkun and Halford showed with plasmids incorporating restriction enzymes that 1D sliding is indeed constant attaching and detaching from the DNA fiber in a so called “hopping and junping” model(Halford and Szczelkun, 2002)(Graham et al., 2011).

From a modeling point of view, facilitated diffusion is described by 4 parameters that are (i) the diffusion coefficient along the DNA fiber in 1D, D_{1d} (ii) the diffusion coefficient in 3D D_{3d} ,(iii) the association rate k_{on}, and dissociation rate k_{off} of the DNA segment:

$$D_{1d} \underset{k_{on}}{\overset{k_{off}}{\rightleftarrows}} D_{3d} \qquad (27)$$

A simplification can be to discard 3D diffusion and to model it with random instant rebinding anywhere on the DNA strand. Let's consider a DNA target situated between fragments of respective sizes M and L, the total DNA strand length being M+N. We have the following mean first time that fairly reproduce the Facilitated diffusion rate that was observed in vitro (Coppey et al., 2004):

$$\bar{\tau} = \left(k_{on} + k_{off}\right) \times \left\{ \frac{\sqrt{\frac{1}{Dk_{off}}}(L+M)}{\tanh\left(\sqrt{\frac{1}{Dk_{off}}}L\right) + \tanh\left(\sqrt{\frac{1}{Dk_{off}}}M\right)} - 1 \right\} \qquad (28)$$

The facilitated diffusion model has been expanded to take into account the particular geometry of DNA folding for instance DNA coiling (Lomholt et al., 2009) and fractal DNA geometries (Bénichou et al., 2011). 1D diffusion has also been modified to integrate a search state and a recognition state (Bauer and Metzler, 2012).

DNA folding has a tremendous impact on the facilitated diffusion model. We have seen that with an extended DNA chain, the first passage time was reduced by facilitated diffusion, but this may be wrong if DNA is tightly packed. In a nucleus homogeneously filled in 3D by chromatin, **facilitated diffusion lead to a lower reaction rate** k_T because 1D diffusion is highly redundant and 3D diffusion is not (Mirny, 2008) (Kolesov et al., 2007)**.** Foffano et al. showed a similar result in-sillico in spherical geometry with 10 copies of transcription factor (Foffano et al., 2012). Interestingly, Foffano and colleagues showed that there was an impact of facilitated diffusion of the search rate for cylindrical geometry of the nucleus, which is, in my opinion, due the proximity of the cylindrical exploration with 2D exploration. Therefore, even if the number of copies of TF inside the nucleus is small, facilitated diffusion is not necessary expected to diminish the search time. If the number of copies of TF inside the nucleus is significant (Wang

and colleagues suggested >500 pM in bacteria), then, facilitated diffusion, by slowing done diffusion, is expected to have a negative impact on the reaction rate.

2.1.2.3 Anomalous diffusion

TF diffusion characteristics such as the diffusion coefficient, have an influence on the transcription reaction kinetics. Incorporating anomalous exponent in the first passage time scheme, two universal classes of models appear: *compact diffusion* and *non-compact diffusion.*

2.1.2.3.1 Compact-non compact diffusion

In 1982, Pierre Gilles de Gennes (de Gennes, 1982b) assessed the kinetics of a reaction where reactantq vanishes to create a product (29):

$$A + A \rightarrow product \qquad (29)$$

In this fundamental paper PG de Genes characterized two universal regimes according to the dimension of the walk dw and dimension of the space df that we have expressed in the specific case of diffusion on a fractal (eq (18)). However df, dw and the compact - non compact formalism are not subrogated to this model and the formalism applies in all cases of diffusion, either anomalous or free. The idea of de Genes is to explain the kinetics of the reaction as a function of the scanning efficiency of the walker. If we call “site” a fundamental unit of space, we can measure this efficiency by looking at the average number of distinct sites $S(t)$ visited during a given period of time t. De Gennes showed that

$$S(t) \propto t^{-\frac{df}{dw}} \qquad (30)$$

The motion was qualified as **compact** if $dw > df$ and **non-compact** if $df > dw$. For non-compact search the integral of S converges asymptotically leading to a single reaction rate similar to the continuous regime of free diffusion that we have already seen before:

$$k_T \propto \int_0^{\infty} Dbt^{-\frac{df}{dw}} dt \propto Db \qquad (31)$$

where b is the target and D is a scaling factor[1] . For compact mode of motion, the rate is time dependent.

On the compact interpretation of diffusion, I would like to make the following remarks:

- Compact diffusion is *recurrent.* For recurrent search, the probability of going back to a an initial position after a certain number of steps does not vanish (Montroll and Weiss, 1965), Recurrent searches was first introduced in the twenties by Polya in the case of 1D free diffusion[2] (Pólya, 1921) (Hardy, 1959).
- In de Gennes' work the space dimension is not considered fractional and $df = 1, 2, 3$. In a fundamental article of 1986, Kopelman extended De Gennes results to fractals (Kopelman, 1986).
- For De Gennes and Kopelman, for compact diffusion there is not one single rate of reaction (29) because the reaction creates a non-homogeneous concentration in the reactor. In fact the average concentration as a function of the distance is a *probability*, the probability that the two reactants found each other. Kopelman showed theoretically and proved experimentally on foam that there was not a single reaction rate for fractal reactions.
- We have already seen the Alexander Orbach conjecture, that was introduced the same year of de Gennes' article postulating that the spectral dimension ds is stable for percolation cluster $ds \approx \frac{4}{3}$(19). Would that mean that for all random walk on random fractals, the motion is compact? Meakin and Stanley investigated a more universal class of random fractal than percolation clusters and showed that indeed for that class of fractals $ds \neq 4/3$ (Meakin and Stanley, 1983).

[1] In the case of free diffusion, D would be the diffusion coefficient.

[2] 1D diffusion is compact since df=1 and dw=2 for 1D Brownian motion

2.1.2.3.2 Anomalous diffusion and first passage kinetics

The chemical transcriptional reaction $TF + B \rightarrow mRNA$ differs from the classical reaction $A + A \rightarrow product$. For reaction $TF + B \rightarrow mRNA$ there is no consumption of the reactant at the site B. For that reason concentration does not vary at least at the macroscopic scale. There is only one single reaction rate no matter the mode of motion of the TF, compact or not, and mass action applies. However there are still some big differences between compact and non-compact dynamics of the transcription factor:

We have seen that the inverse of the reaction rate k_T is the mean first passage time $\bar{\tau}$. Indeed for compact fractional diffusion in 2D $\left\langle |r(t) - r(0)|^2 \right\rangle \propto t^{\alpha}$ ($\alpha < 2$), Gitterman et al. computed the global mean first passage time (32) in 2000 for an arbitrary target in a confined geometry of size L, that was independent of the size of the target (Gitterman, 2000) .

$$\bar{\tau} = \frac{4}{\alpha\pi}\left(\frac{L}{\pi\sqrt{D_\alpha}}\right)^{2/\alpha} \sum_{m=1}^{\infty} \frac{(-1)^m}{(2m+1)^{1+2/\alpha}} \qquad (32)$$

The most striking feature of this reaction rate is that it is independent from the size of the target gene B. If the gene target is very small, the mean first passage time is significantly diminished in a compact mode of motion, a result that has been introduced by Guigass and Weiss as the "discovery of slowness"(Guigas and Weiss, 2008). But the most significant breakthrough for the application of the compact not compact mode of motion to transcription was the computation of the mean first passage time *as a function of the distance to the site.* Condamin and colleagues saw De Gennes 's concentration at a given distance r as a "rescaled" mean first passage time $\bar{\tau}(r)$, (Condamin et al., 2007). They computed the mean first passage time as (33).

$$\bar{\tau}(r) \propto \begin{cases} N\left(A - Br^{dw-df}\right) & for \quad dw < df \\ N\left(A + B\ln(r)\right) & for \quad dw = df \\ N\left(A + Br^{dw-df}\right) & for \quad dw > df \end{cases} \qquad (33)$$

With A and B being structural constants and N being the lattice volume. Condamin et al. latter introduced the probability to share the same transcription machinery for two distant sites of the closed volume as an additional observable (Condamin et al., 2008). In an additional paper Benichou and al. computed the exact shape of the first passage time distribution, and not only the

mean in terms of the radial distance to the site and time rescaled by the GMFPT (Bénichou et al., 2010).

Because of the radial dependence of the mean first passage time for compact diffusion, two genes that are close to each other have a higher probability to share the same transcription machinery than two genes that are distant. Indeed, genes that are co–regulated are often found close to each other inside the nucleus and it is still unknown whether this co-localization is induced by transcription or by other nuclear components to enhance transcription(Kolesov et al., 2007). Because of the recurrence of compact exploration, Meyer and colleagues showed that it could induce a bursting mode of expression of genes regulated by a small number of copies of nuclear TF (Meyer et al., 2012).

2.1.3 Conclusion on modeling

In this section, we have investigated several modes of motion of nuclear elements, from free to anomalous diffusion. We have also shown that the type of particle diffusion can have a high impact on the nuclear reactions rates. Pioneer studies showed that nonspecific interactions can also play role in this regulation (Dundr and Misteli, 2001). On the results part, we will investigate the motion of nuclear reactants in relation with their chemical properties and discuss the implication of the motion in the specific case of transcription.

Now that we have a model of nuclear particle motion, I will introduce the imaging assays that enable the recording of nuclear single particle motion.

2.2 Nuclear single particle microscopy

Since the 1960's, and the discovery of GFP (Shimomura et al., 1962), functional microscopy has become a routine technique to understand cellular structures and dynamics. Recently a method is called sptPALM (Single particle tracking Photo Activated Light Microscopy) (Manley et al., 2010) has been developed to reach single molecule accuracy in the following functional proteins in cells with an ordinary inverted light microscope.

In a first part, I will introduce the mathematics of PALM imaging that is PALM on fixed dead cells. Then I will introduce the specific properties of nuclear sptPALM, where super-resolution is performed on the nucleus of living cells and when we can record the mobility of its components. In a third part, I will try to make the link between SptPALM and another imaging techniques, FLIP (Fluorescent Loss In Photo-Bleaching.

2.2.1 Super resolution

Super resolution was introduced to break the fundamental diffraction limit of Light microscopy. Upon response to a point source, because of diffraction through the optical path, the microscope will produce a blurry image, the point spread function (PSF). This makes two imaged molecules closer than 100nm impossible to be separated with ordinary inverted microscope. Super–resolution uses time to overcome this limitation.

2.2.1.1 PALM and STORM principle

In 2006 two methods were conjointly developed for super resolution with a conventional inverted microscope. PALM (Betzig et al., 2006) and STORM (stochastic optical reconstruction microscopy))(Rust et al., 2006). These approaches rely on the stochastic activation of fluorescence to intermittently photo switch individual photoactivatable molecules to a bright state, which are then imaged and photobleached. Thus, very closely spaced molecules that reside in the same diffraction-limited volume (and would otherwise be spatially indistinguishable), are temporally separated. Merging all of the single-molecule positions obtained by repeated cycles

of photoactivation followed by imaging and bleaching produces the final superresolution reconstructedimage (Figure 5).

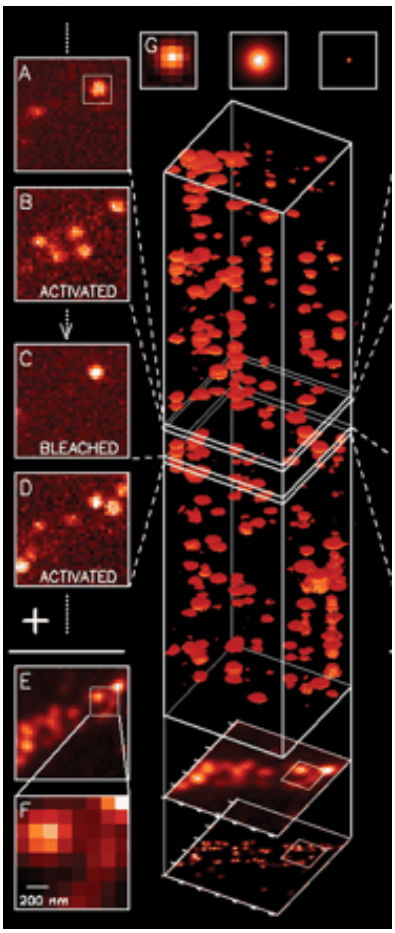

Figure 5 The principle behind PALM. A sparse subset of Photo activated probes is illuminated (**A** and **B**) and then partialy bleached after a pulse of illumination (C).The process is repeated (**C** and **D**) until the population of inactivated, unbleached molecules is depleted. Suming the molecular images across all frames results in a diffraction-limited image (**E** and **F). reproduced from** (Betzig et al., 2006)

PALM and STORM are based on the same principles, but were originally published using different photoswitchable probes. PALM was developed using photoactivatable or photoconvertible fluorescent proteins as the switchable probes, whereas STORM was originally published using the synthetic carbocyanine dyes, Cy3 and Cy5. In contrast to the situation with classical fluorescence microscopy, superresolution microscopy allows biological structures to be defined with nanometric accuracy, so that their distributions and dynamics can be analyzed.

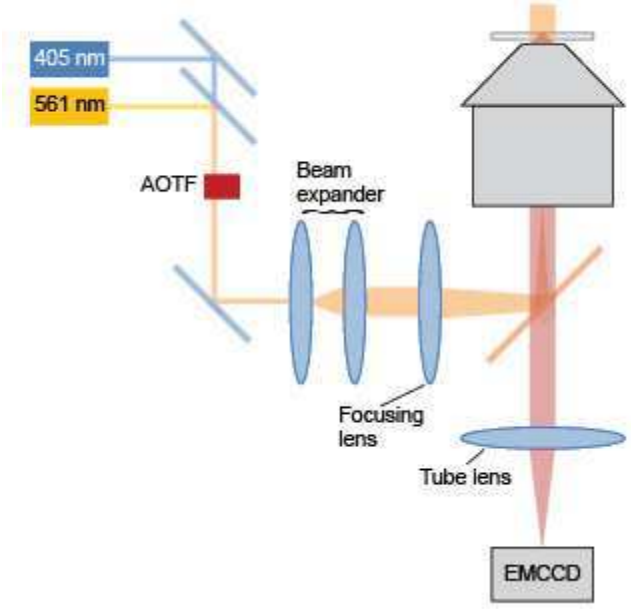

Figure 6: schematics of the PALM experimental set-up. The activation (405 nm) LASER and the excitation (561 nm) LASER are aligned on a single beam using a dichroic beamsplitter. Their intensity and on/off switching ratio is independently controlled with an acousto-optic tunable filter (AOTF). The combined LASER beam is expanded through a beam expander and focused on the rear plane of the objective in an inverted microscope, with the help of a long-pass dichroic. The emission from the sample is imaged through the tube lens with an EMCCD

Figure 6 is a representation of a typical PALM set-up. Photoactivation and readout LASERs (405 and 561 nanometers, respectively) are positioned so that they can be shuttered or used simultaneously when necessary. A cooled electron-multiplying charge-coupled device (EMCCD) camera system is attached to the microscope. The specimen is mounted in a specialized holder and bolted to the precision x-y stage for gathering transient images of single molecules. A high numerical aperture objective is positioned beneath the specimen. Central to the instrumentation is a high-speed computer system that acquires and processes images recorded by the camera.

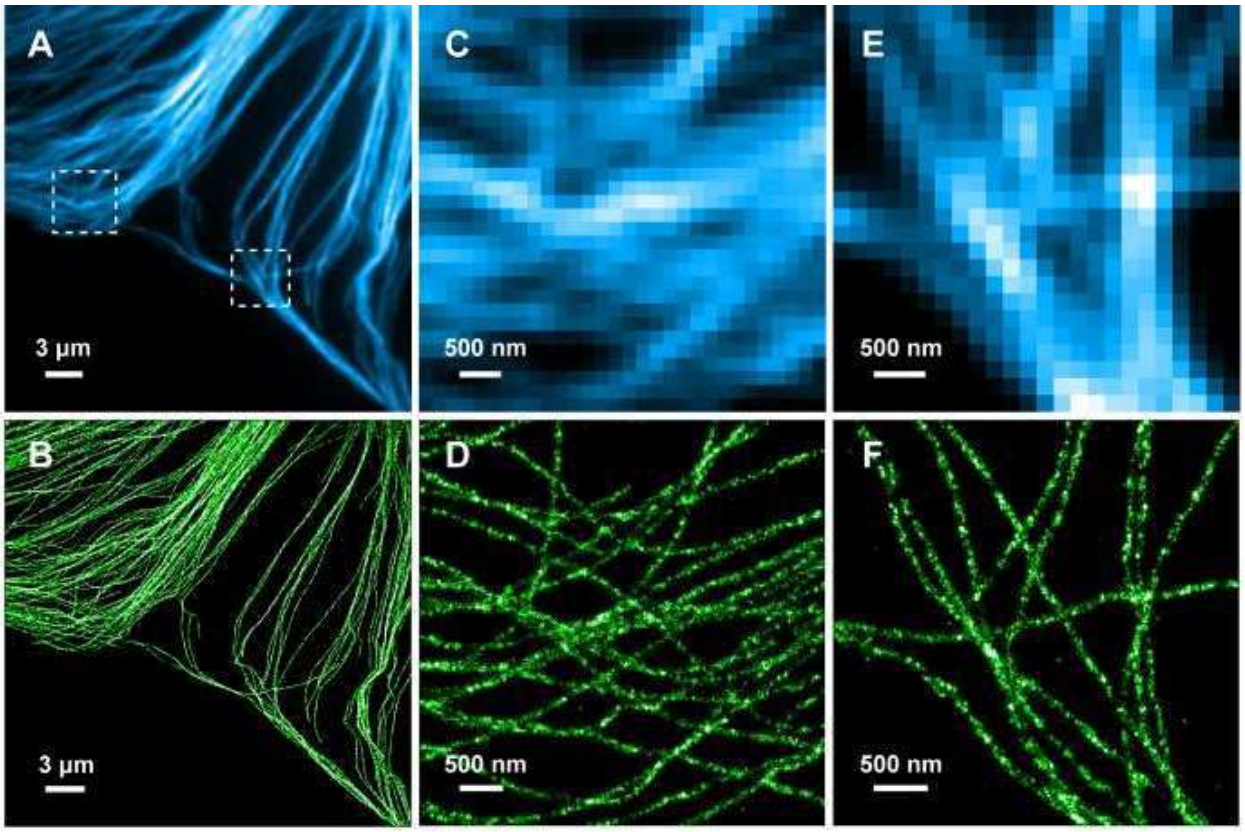

Figure 7: Comparison off images of cell micro-tubules. *(a), (c), (e), conventional microscopy. (b), (d), (f), super resolution microscopy (STORM) reproduced from (Bates et al., 2007)*

Super resolution images differ fundamentally from conventional microscopy images, as they are computer-reconstructed images (Figure 7). On the following section, I will try to mathematically express those differences.

2.2.1.2 Differences between Super resolution microscopy and conventional fluorescent microscopy

2.2.1.2.1 Conventional microscopy

For **conventional wide field fluorescent microscopy,** there are four different steps in the construction of the final image I: **blurring**, **discretizing**, **integrating** and **amplifying.** The exact mathematical formulation of those four steps can be heavy (Grünwald et al., 2008) . Here, for clarity, I will adopt the formalism of Thompson (Thompson) that is maybe less precise, but to my opinion easier to follow. I will also refer to the density after successive transformations as "data".

I will confront conventional fluorescent microscopy to a 3D time –independent density of fluorescent emitter s.

- The density s is convoluted with the point response of the microscope, *the point spread function* h that accounts for the diffraction pattern through the optical path: The data is *blurred:* $h \otimes s$
- Each point is submitted to photonic noise (stage $\overline{Q}$) that can be modeled as a Poisson time and spatial process of intensity $h \otimes s$ (Murphy and Davidson, 2012) . After this treatment, our data is a collection of dimensionless photons with time and spatial origin. The data is *discretized* : $\overline{Q}(h \otimes s)$
- Then data is pixelised (stage $\overline{M}$). Pixelisation can be modeled as the integration of the discrete data over a partition of hyper-volumes, the *pixels*. Pixels have the following time and spatial dimension: square in the xy directions, a probability profile in the z direction called *the focal depth of the system* and the exposure time camera $t_{\exp}$ in the time dimension. The data is summed or *integrated:* $\overline{M}\overline{Q}(h \otimes s)$
- The signal is converted to electric charge according to known quantic efficiency. At this stage there is also one perturbation *called electronic noise* due to the non-linear conversion that is often modeled as a Gaussian white noise on the pixels. Finally, each pixel *amplified* by the electo-multiplier device (EM) .

$$I = EM(\overline{M}\overline{Q}(h \otimes s)) \qquad (34)$$

I used this formulation for validation of image tprocessing in the results part of this thesis. I fixed a density of emitter, a Dirac in the case of a single molecule, and I applied the previous steps to construct an artificial fluorescent image.

2.2.1.2.2 Ideal Super resolution microscopy PALM

PALM experiments rely on the sequential photo activation of molecules imaged during several frames. For that reason, the raw output of a PALM experiment is a collection of images $\{I_t\}$ with a sparse subset of the emitter ensemble s spatially resolved. Here I will assume an ideal PALM

experiment, where only one molecule emits light in one acquired frame. Thus, the signal per frame I_t is

$$I_t = EM(\overline{M}\overline{Q}(h \otimes 1_{\{x_i,y_i,z_i\}})) \qquad (35)$$

where $1_{\{x_i,y_i,z_i\}}$ is the spatial Dirac function at position of the single molecule $\{x_i, y_i, z_i\}$. The purpose of PALM is now to invert the function $EM(\overline{M}\overline{Q}(h \otimes .))$ to find the exact position $\{x_i, y_i, z_i\}$ of the molecule. For 2D representation, afterwards, only the spatial projection $\{x_i, y_i\}$ is computed and displayed. Ideal super resolution imaging is therefore equivalent to **Monte Carlo sampling** of the density of emitters s. Since the function $EM(\overline{M}\overline{Q}(h \otimes .))$ is not deterministic, the position is not known exactly but *inferred* from the frame I. Here is the fundamental difference between conventional fluorescent and super resolution imaging: after image processing, PALM final output is not an image but a set of coordinates, for instance in 2D $\{\{x_i, y_i\}\}$.

If one wants to display the coordinates $\{\{x_i, y_i\}\}$ on an image I', one needs to add bulk to the points. Since the position of individual emitters is only known up to a given uncertainty, the *effective point spread function* h^i_{eff}, one solution is to use this uncertainty for display. In that case the final image I' is obtained by the sum over all individual detections $\{x_i, y_i\}$

$$I' = \sum_{\{x_i,y_i\}} h^i_{eff} \otimes 1_{\{x_i,y_i\}} \qquad (36)$$

This effective point spread function h^i_{eff} differs from the real point spread function h because:

- It accounts for the optics but also for the computational efficiency to recover the exact position of the emitter $\{x_i, y_i\}$
- It is theoretically only limited by the quantity of information available for the inference of the position and therefore only by the number of photons that can be collected by the camera

Giving to each detection on a reconstructed image a weight proportional to the uncertainty of the detection also means that ideal PALM detection with 0 uncertainty cannot be displayed at all. There is therefore a trade-off for ideal representation. As a function of the number of detected molecules, Fizgeralald and colleagues computed a density filter $\hat{g}$ for optimal representation of the density s (Fitzgerald et al., 2012)

$$I' = \sum_{\{x_i,y_i\}} \hat{g} \otimes 1_{\{x_i,y_i\}} \qquad (37)$$

In 3D, Beheiry and Dahan computed several texture method for optimal rendering (Beheiry and Dahan, 2013).

2.2.1.2.3 Real Super resolution microscopy PALM

2.2.1.2.3.1 Fluorophore persistence

We have seen that ideal super resolution imaging is equivalent to the Monte Carlo sampling of the density of emitters s. However, for real super resolution, the sampling is not independently distributed. Activation puts fluorophores into a non-stable "triplet state", an activated emitter will emit light for several frames until it *bleaches* with stochastic *blinking*.

The persistence of the fluorophore for several frames is a drawback for analyzing super-resolved image on fixed cells since it is not straightforward to count molecules that can appear repeatedly. But this persistence is an advantage for live cell imaging because it allows the imaging of individual molecules until they bleach and therefore the recording of their motion (Manley et al., 2010)

2.2.1.2.3.2 Point spread function and detection

One of the critical point of super resolution imaging is the detection of the exact position of the fluorophore $\{x_i, y_i\}$. Detection is equivalent to the inversion the point response of the microscope and camera, represented by the function $EM(\overline{MQ}(h \otimes .))$. For accurate detection of the single molecule position, one needs to know the shape of the function or at least geometrical properties on which we can base the inference.

The point spread function h for an ideal microscope, for and a molecule exactly in focus is (Murphy and Davidson, 2012)

$$h(r) = \left(\frac{2J_1(ra)}{r} \right)^2 \text{ with } a = \frac{2\pi NA}{\lambda} \qquad (38)$$

NA being the numerical aperture, λ being the wavelength and J_1 being the first Bessel function. Unfortunately, there is no analytic formula for J_1 which is a severe drawback for inference. Several algorithms have been developed to compute a realistic PSF and to integrate it over the pixels of a camera (Nasse and Woehl, 2010). More recently, authors also argued that we cannot base the inference on a *point* spread function since fluorophores are not points but indeed dipoles (Mortensen et al., 2010). For simplification however, simplified Gaussian versions of the PSF is predominantly used.

The PSF can be modeled by a succession of rings of increasing radius and of decreasing height, the Airy disks. The radius of the first peak is given by:

$$r = 1.22\lambda / 2NA \qquad (39)$$

One simplification is to consider only the first peak and to model it with a Gaussian with full width half maximum equal to $d = \lambda / 2NA$. Zhang and colleagues showed that this approximation is not accurate for wide field microscopy but good for LASER scaning microscope (Zhang et al., 2007). I refer to (Ober) for a comparison between Airy and Gaussian function for maximum efficiency of the maximum likelihood estimator.

For computational speed, alternative methods to maximum likelihood inference have been proposed to find the position, the most popular way being 2d Gaussian least square fit after a preliminary filtering (Mashanov and Molloy, 2007). But since PALM images are noisy, sometimes the simplest method is the best. For example, Thompson and colleagues showed that 2D Gaussian fit did not improve much a simple center of mass computation for noisy data (Thompson et al., 2002). Recently, Parthasarathy proposed a novel method based only on the symmetric properties of the PSF, *the radial symmetry center* (Parthasarathy, 2012).

2.2.1.2.3.3 Cramer Rao Lower bound and pointing accuracy

Now that the single molecule is detected, we can question the efficiency of the detection and the pointing accuracy. For an ideal microscope with infinitely small pixels, photonic noise can be considered as N observations drawn from a distribution of probability distribution function (PDF) h' 3. In such a scenario, for Gaussian PSF h the natural average of those observations reaches maximum likelihood to estimate the center of h which would be the 2D position of the imaged molecule. The standard deviation of the mean $\sigma(x)$, that gives the uncertainty of this estimated position x is given by the Cramer Rao lower bound.

$$\sigma^2(x) = \frac{\varepsilon^2}{N} = \frac{d^2}{8N\ln(2)} \qquad (40)$$

with d being the full width half maximum and ε the standard deviation of the Gaussian PSF. Thompson et al proposed the following correction to integrate pixel size and (Thompson et al., 2002)

$$\sigma = \sqrt{\frac{\varepsilon^2}{N} + \frac{a^2}{12N} + \frac{8\pi\varepsilon^4 b^2}{a^2 N^2}} \qquad (41)$$

With a being the pixel size and b the standard deviation of the background noise.

The formula has become the standard method to compute theoretical pointing accuracy, or signal to noise ratio. A more experimental approach, which is also very popular, consists on the sequential detection of stable fluorocrhom such as a quantum dot. The ratio between the number of photons collected during the experiment and real tagged fluorophore giving a *rescaled pointing accuracy* (Betzig et al., 2006).

---

[3] Readers may be a confused here as result of the notation of the *Probability density function* (PDF) noted h' and of the Point spread function (PSF), noted h. I leave it this way since the PDF we refer to, here, is a modeling of the physical PSF.

2.2.1.2.3.4 Two or more particle per frames

In real PALM imaging there is not only one particle per frame, but many. Several methods have been developed to simultaneously find several single particle positions in an image whose signal overlap. Serge et colleagues did iterative fitting: once a single particle is detected, its signal is removed from the frame and all the particles are detected after several *deflection loops* (Sergé et al., 2008).

Another solution is to preliminary *deconvolve* the signal with econvolution nonlinear filtering (Weisstein)(Henriques et al., 2010). Wavelet analysis was introduced to discard small objects that would not qualify as single particles (Genovesio et al., 2006)(Olivo-Marin, 2002). The most promising technique is, to my opinion, compressed sensing in which the single particle position is given according to a *sparse matrix* whose distance to the real data is iteratively minimized (Zhu et al., 2012)

2.2.1.3 Developments

The methodology of PALM has been significantly enhanced during the past years in two directions, the reduction of out of focus noise and the 3D determination of the particle position.

- For the reduction of out of focus noise, different methods have been proposed, the most commonly used being TIRF (total internal reflection Fluorescent microscopy) (Information et al., 1981) that uses for excitation an evanescent wave. The signal to noise ratio is dramatically increased but the observation is limited to a 200 nm depth above the coverslip. Hi-LO (highly inclined and laminated optical sheet) (Tokunaga et al., 2008) is a modification of the technique that enables deeper sample illumination.
- Numerous efforts have been undertaken to extend PALM imagig to 3D by shaping the PSF so that the position can be determined from a 2D fit of *h* (Izeddin et al., 2012) (Thompson et al., 2010) or by illuminating simultaneously several focal planes (Hajjoul et al., 2009) (Abrahamsson et al., 2013)

2.2.1.4 Statistical analysis of PALM outputs

Ideal PALM outputs are dimensionless observations of a spatial distribution, namely a *point pattern*. Real PALM data is polluted by blinking and fluorophore persistence. To use spatial statistics on real PALM outputs, one needs to discard blinking that would alter the exact counting

of molecules. A method called pair correlation PALM (PC PALM) has been developed to remove double counts from the final output in 2D (Sengupta and Lippincott-Schwartz, 2012). Spatial statistics have long been developed for geology and ecology but is still not so widely applied on PALM (Owen et al., 2012)(Owen et al., 2010). I refer to the result part 3.3.3 for application of spatial statistics to real PALM data.

2.2.2 Spt PALM

In 1996 Schmidt et al showed that it was possible to track moving lipids in solution with 5ms exposure time (Schmidt et al., 1996) and since that pioneer experiment, single molecule tracking has become a powerful tool to understand the mechanisms of bio-chemistry in vitro and in vivo.

SptPALM has been a natural development of PALM to do the imaging **on live cell** and to record displacement of the tagged protein (see Manley and colleagues for review (Manley et al., 2010)).

2.2.2.1 Tracking moving single particle

2.2.2.1.1 Detection

A plethora of computer algorithms have been developed to monitor single molecule in vivo (see Levi and Gratton for a complete description (Levi and Gratton, 2007)). Motion significantly affects pointing accuracy actually, even if the sample is fixed and the only motion is set up artifact (Pertsinidis et al., 2010). Moving particles signal differs from immobile, as their signal is indeed a **motion blur,** the convolution between the movement and the PSF. To get an accurate moving particle position there is a trade-off between a high exposure time that will increase the number of collected photons and a low exposure time that will decrease the motion blur.

Exposure time is also bounded by the energy transfer of the full chip EMCCD camera, To decrease exposure time to the microsecond range, stroboscopic illumination has been proposed, for instance, with a non-mechanistic illumination shutter like an AOTF (acousto-optic ttunable filter)(English et al., 2011).

2.2.2.1.2 Tracking

The next move of is to track the molecule for several frames (Saxton, 2008a). In that case, there are two broad categories of tracking methods if the expected trajectory is long (a least 100 frames) or short (a few frames).

- **For short trajectories** and identical particles there is not much information that can be used to link detections to another. Simple routines such as connecting particles to the closest neighbor on the consecutive frame and fixing a maximum radius are sometimes the best (Ghosh and Webb, 1994)(Mashanov and Molloy, 2007). Tracking algorithms can also use other features than coordinates to connect detections between consecutive frames such as brightness (Smith et al., 2011). Connecting **simultaneously** one frame detections to their corresponding detections on the consecutive frame can reduce miss-assignement for dense samples. This can be done by finding the displacement that maximize the correlations between consecutive frame (Gelles et al., 1988) (Shafique and Shah, 2005) or by minimizing a global "cost" that depends on spatial distance between consecutive detections (Jaqaman et al., 2008).
- **For long trajectories**, it is possible to compute from the past the a-priori position of the particle on the next frame (Ng et al., 2005)(Simo Srkk, 2004). For instance, the time dependent diffusion coefficient of a particle inferred from the past can help associating particle according to their speed (Sergé et al., 2008). Most methods use Kalman filtering and its related likelihood (Genovesio et al., 2006)(Wu et al., 2010), but the distinction between past and future is indeed purely theoretical for trajectory reconstruction, as tracking is most often processed *after* the images are recorded. One efficient method, is to treat the time acquisitions as a whole and to use particle matching and graph theory to converge to the trajectories (Sbalzarini and Koumoutsakos, 2005).

2.2.2.2 From single particle to global statistics

From single particle assays, we get trajectories of individual molecules. The crucial point of tracking algorithm is to minimize *tracking errors*, the possible miss assignments of particles on consecutive frames. Tracking errors significantly alter the validity of the conclusions that can be drawn from SPT assays. There are two kinds of tracking errors: type 1 (false positive) and type 2 (false negative) (Figure 8).

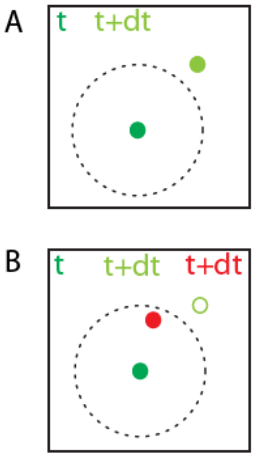

Figure 8: Type 1 and type 2 tracking error .

Moving particles are sequentially detected at frame recorded at time t and sequential frame at t+dt .

Panel A type 2 tracking error (false negative): the moving particle moves further than the limit of an over-restrictive tracking algorithm pictured by the dot circle. The trajectory is stopped.

Panel B type 1 tracking error (false positive): The particle either moves far away or bleach or de-focalized. Another particle comes within the limit of the tracking algorithm and is wrongly assigned to the detection at time dt.

Any tracking method is a tradeoff between type 1 and type 2 errors. A restrictive algorithm that stops tracking whenever there is an ambiguity will decrease type 1 and increase type 2 error. If the motion is uniform (all the particle behaves the same) such as Brownian motion, then type 2 error is expected to cause a reduction of the number of observed displacements and in the end a loss is a consistency of the statistic (Ng et al., 2005). By limiting the observed translocations, it is also possible that the recorded motion appears to be slower than in reality (Wieser and Schütz, 2008). Type 1 errors on the other hand will lead to observed displacements that have nothing to do with the movement and therefore will strongly alter the validity of the conclusion that are drawn from the motion.

So far, to my opinion, tracking algorithms have been predominantly developed to minimize type 2 error rather than type 1 error, which makes them unsuitable for intra nuclear sptPALM. Nuclear sptPALM have often reported motions that were heterogeneous, with populations of particles moving at different speed (Holtzer et al., 2007), (Grünwald et al., 2008), (Speil et al., 2011b). Intra-nuclear SPT has, to my knowledge, mostly been performed using the projection of the motion in 2D. Due to more rapid de-focalization of the fast moving particles, any statistic on sptPALM data is biased (Figure 9) and any tracking algorithm that would be over-restrictive increases the bias. For that reason, we have developed our own tracking method for which type 1 error is reduced while type 2 error is high but carefully measured.

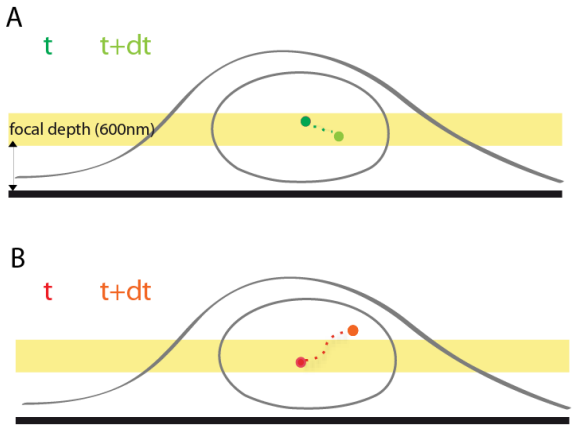

Figure 9: Selection bias for intra nuclear SptPALM. Panel A: a slow moving protein that stays in focus (the focal depth of the camera) for several frames. Panel B: a fast moving protein that de-focus between two frames

Trying to quantify the different populations from spt PALM, there will be a biased towards the slow moving populations since they are image longer.

2.2.3 FLIP (Fluorescent Loss in Photo-Bleaching)

2.2.3.1 Bulk imaging techniques

SPT PALM is of course not the only technique for the following of nuclear factors, Numerous imaging assays have been developed to measure the mobility of nuclear factor tagged with a fluorochrome. Below is a non-exhaustive list:

- **FRAP**,(Fluorescent Recovery After Photo Bleaching) . In a FRAP experiment, a nuclear area is bleached and the recovery of the fluorescence is monitored. By linking the fluorescence with the molecule concentration, we can extract the kinetics of the tagged molecule (Köster et al., 2005).
- **FCS** (Fluorescent Correlation Spectroscopy). In a FCS experiment, we monitor the variation of fluorescence inside a small region and we link those variation with the entrance or escape of a tagged protein(Thompson, 2002).
- **FLIP** (Fluorescence Loss in Photo Bleaching). In a FLIP experiment a region of a cell is cantinuouslly bleached and we monitor the loss of photo bleaching at a distant point from bleaching area (Köster et al., 2005).

FRAP, FCS and FLIP are bulk imaging techniques. It is the global motion of the pool of fluorescent molecules that is observed. The measured fluorescence is assumed to be proportional to the nuclear concentration, eventually corrected from photo bleaching. FRAP, FCS and FLIP

are indirect measure of the movement. The kinetics that can be extracted from those techniques depend on the model that is fitted to the data, and the number of possible models has increased huge as the techniques become popular(Mueller et al., 2010).

	FCS	FRAP	FLIP
Time range	Nano second-millisecond	Milli second-second	second-minute
Spatial range	0-100nm	1-10 µm	The entire cell
probe concentration	nM	µM	µM

FLIP has not been extensively used compared to FRAP. Here, I will explicit the link between Spt-PALM and FLIP in broad context of mean first passage time.

2.2.3.2 Protocol

Fluorescent Loss in Photobleaching (FLIP) relies on the bleaching of a precise area by LASER and the analysis of the resulting profile. In a FRAP experiment, the system is left to evolve after a short but intense LASER bleach. In the FLIP experiment, the intensity measurement is done at a given distance from the bleaching area, and the bleaching is continuous or at least periodic The first FLIP experiments where done on Golgi proteins (Cole et al., 1996) to assess the link between distant cicternae of the Golgi. The global and constant bleaching of distant cicternae accelerates the bleaching of distant one and we can, with FLIP, measure the exchange rate between hose compartments. FLIP can so be used to qualitatively assess shuttling rates, for instance between the cytoplasm and the nucleus (Köster et al., 2005)

The typical duration of a FLIP experiment is 100s, and to estimate quantitative parameters, the measured intensity I in a given area needs to be corrected from the background level B and bleaching due to imaging measured on a distant cell of the imaging area KI and then rescaled by the signal at time t=0.

$$\tilde{I}_{(t)} = \frac{\left[I_{(t)} - B_{(t)}\right] / \left[KI_{(t)} - B_{(t)}\right]}{\left[I_{(0)} - B_{(0)}\right] / \left[KI_{(0)} - B_{(0)}\right]} \qquad (42)$$

The resulting intensity $\widetilde{I}_{(t)}$, let aside additional noise, ranges from 0 to 1 and can be fitted to a single exponential decay function $f(t) = 1 - e^{-t/\tau}$. This strategy has for instance been used to estimate dissociation constants in eukaryote cells of Fibrillarin and SF2/ASF out of their respective nuclear compartments, the nucleoli and the nuclear splicing nuclear factors (Phair and Misteli, 2000) and later expanded to other ribosomal proteins (Chen and Huang, 2001). A decay of florescence that is not explained by a single exponential has been seen as the signature of the aggregate movement of different populations. For instance the polymerase population inside a cell can be divided between a free, a bound and an engaged population (Kimura et al., 2002)(Hieda et al., 2005). Recently it has been proposed that the decay rate of the FLIP experiment could represent not only the dissociation rate, but also the restriction of the movement imposed by the geometry before going to bleaching area. For instance Dieteren et al have extended the measurement of effective diffusion coefficient by FRAP to predict the FLIP rate as a function of the number of barriers in the mitochondrial matrix (Dieteren et al., 2011).

2.2.3.3 Link with sptPALM

Models to be confronted to the FLIP analysis are still lacking, and so far only a few parameters have been extracted from the FLIP experiment. With the notable exception of ((Köster et al., 2005)), FLIP has mostly been used not to assess spatial exploration of cellular factor but rather a dissociation constant k_{off}. The link with mobility have been introduced through a combination of FLIP and FRAP "Continuous Fluorescent Photobleaching (CFP)" (Wachsmuth et al., 2003), but only looking at *the integrated value* of the fluorescence $I(t)$ and not the fluorescence as a function of the distance to the bleaching point $I(t,r)$. This quantity that we call *RFLIP* (Figure 10) for *Radial* FLIP is directly related to sptPALM.

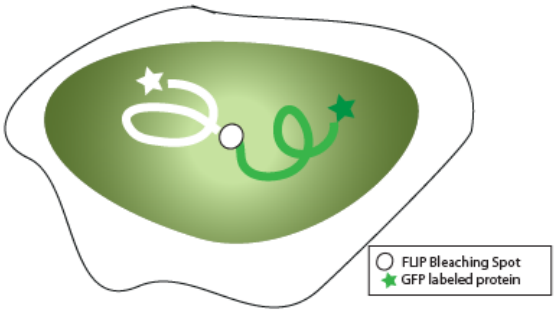

Figure 10: Schematic principle of an ideal RFLIP experiment. *A bleaching laser is focused on a small and limited region of the nucleus, the bleaching spot. Anytime a fluorescent particle passes through the bleaching spot, it is bleached. The remaining fluorescence as a function of the distance to the bleaching spot is therefore proportional to the fraction of particle that has not pass through the bleaching point. .*

We have seen in the previous section that the motion of nuclear factors can be modeled either by the local exploration or the mean first passage time. If SPT-PALM is directly related to local movement, an ideal RFLIP is the direct measure of the distribution of **the first passage time** through the LASER bleaching spot.

Let's assume that the nucleus is isotropic around the bleaching spot, so that that $I(r,t)$ is the same at every point of annular region of radius r and that there is no side effect of the shape of the nucleus. In such a case, $I(r,t)$ corresponds to the fraction of unbleached proteins at radius r at a time t Here we assume the reversibility of the exploration process so that any protein trajectory inside the nucleus has the same probability to occur whatever the direction. *If we mentally reverse time* the fraction $I(r,t)$ of light that remains at a particular place corresponds to the fraction of particles that was there at time t and that have not passed through the bleaching point. It is therefore a *survival probabilit*y that depends only on the position inside the nucleus. $I(r,t)$. For ideal RFLIP, $I(r,t)$ is an exact quantification of the *rescaled mean first passage* that I've presented at equation (33). The implication of this relation will be discussed in part 3.2.4.2

2.2.4 Conclusion on microscopy

Single molecule microscopy is a rather young discipline that was built upon the genius idea of using time to overcome the limitations of conventional fluorescent microscopy. Because of its versatility and relative low cost, PALM microscopy has been awarded method of the year by nature magazine (Betzig et al., 2006). So far, PALM microscopy has mainly been restricted to membrane or thin samples. PALM and its living cell corresponding sptPALM however, are

limited for precise quantification due to various selection biases like bleaching, blinking and movement out of focus. Another drawback of PALM is that the data is only accessible after heavy image analysis. But, still, PALM enables functional imaging of the organelles with resolution one order of magnitude lower than obtained with conventional microscopy.

When applied to live cell imaging, PALM set-ups enables the tracking of molecules at high resolution. SptPALM is a nice tool to understand the heterogeneity of the movement within a micro-metric range, but, at a larger scale, nuclear exploration is better assessed with ensemble measurement such as FLIPs. Finally, it is by confronting the same problem to different microscopic assays that we can reliably understand the movement of nuclear factors(Mazza et al., 2012a).

2.3 Statistical analysis of live cell single particle trajectories

Single molecule tracking (SMT) or single particle tracking (SPT) has shed light on the specific exploration of cellular organelles by its active constituents. So far, live cell SPT has been mostly restricted to membrane (Alcor et al., 2009) but numerous efforts have developed to extend the analysis deeper inside the cell, to the cytoplasm or to the nucleoplasm. In this section, I will not only discuss nuclear SPT studies, because there's only a few, but I will review the statistics that can be used to interpret SPT data in all the compartments of the cell. Biological questions that justify the use of SPT fall in the following global categories:

- **Bio-measuring:**. Using single molecule tracking, we can directly measure at the single molecule level chemical reaction kinetics. Those type of measurement can be for instance actin filament groth rates (Das et al., 2009) or nuclear pore transport rates (Lowe et al., 2010).
- **Interaction:s** Chemical partners inside the cell interact in various ways. They can bind to each other or can be spatially restricted to specific organelles. SPT can help understand what kinds of phenomenon bring the partners together ,such as a force derived from a potential (Masson et al., 2009)
- **Rheology:** By introducing tracers inside the cell and studying their movement, scientists can measure the physical properties of the cell components (Etoc et al., 2013) and resolve their architecture (Bancaud et al., 2009).
- **Target search:** We have seen in the first session that chemical reactions such as transcription are significantly enhanced in a cell. How a reactant will find its substrate inside the cell is not fully understood and single particle tracking can help understand how a transcription factor will find its way to a specific gene (Plachta et al., 2011) or how a virus will scan a cellular membrane ((Rothenberg et al., 2011)).

Lexicon of single molecule tracking: The final outputs of SMT assays are lists of time-indexed points or positions, in 2D: $\left(x_i(t), y_i(t)\right)$ and in 3D : $\left(x_i(t), y_i(t), z_i(t)\right)$ that I will refer as $\vec{r}_i(t)$ or

trajectories that represent the successive position of a tracer i. The recording of the position is sequentially done each Δt interval of time, called *inter-frame*, for a maximum of N points and total duration of $(N-1)\Delta t$. In fact, for most experiments, the recording of the position is not instantaneous and the photonic captor is usually open during an *acquisition time* t_E. More over the exact position is not known exactly $\vec{r}_i(t)$ but within a probabilistic distribution of given variance σ_0 called *pointing accuracy* or *localization error*. In the previous section, we introduced tracking errors. Here we discard those errors and assume that trajectories faithfully reflect the behaviort of one single molecule moving in its environment

2.3.1 Mean square displacement and free diffusion

We have seen in the first section that the simplest model of random exploration is the *Brownian motion* or *free diffusion model* characterized by a single parameter, the diffusion coefficient *D*. For Brownian motion, the second moment of the propagator integrated and summed other d independent dimensions gives the dependence between the square linear distance and time of equation (10) reproduced here:

$$\left\langle \left| \vec{r}(t) - \vec{r}(0) \right|^2 \right\rangle = 2dDt \qquad (43)$$

The statistical estimation of this equation has given rise to the ordinary MSD analysis (see (Wieser and Schütz, 2008) for a complete review)..

2.3.1.1 Definition and computation of the MSD

Let's suppose that we observe by SPT a Brownian motion, and that we need to measure the diffusion coefficient D of a single trajectory. We have the sequential N detections (x_n, y_n) in 2D recorded every time interval Δt without localization error. The computation of the mean square displacement MSD for the time interval $n\Delta t$, is obtained as follow.

$$MSD(n\Delta t) = \frac{1}{N'} \sum_{i-j=n} (x_i - x_j)^2 + (y_i - y_j)^2 \qquad (44)$$

The averaging is done between the N' pairs of detection that are $n\Delta t$ distant.

Before even trying to estimate the diffusion coefficient, we can question the robustness of this statistic and compute its variance. Even with this simple definition, the computation of the MSD is not straightforward. Brownian motion has independent increments, which means that distant displacements or *segment* are independent from one another. However displacements that time-overlappes are correlated. Two types of averaging $MSD(n\Delta t)$ can be applied: over the N_1 independent segments or on the whole set. Qian et al. showed that averaging over independent segments do not improve much the variance of $MSD(n\Delta t)$, σ_n (Qian et al., 1991)). In the first case the variance is, with central limit theorem:

$$\sigma_n = (4Dt)\ N_1^{1/2} \qquad (45)$$

When averaging $MSD(n\Delta t)$ over all the segments and not only the independent ones, the scaling remains the same

$$\sigma_n = (4Dt)\ F(n,N)^{1/2} \qquad (46)$$

With a form of $F(n,N)$ that changes as a function of $N_A = N - n + 1$.

For $n < N_A$ $F(n,N) = \left(n^2 N_A + 2N_A + n - n^3\right)/\left(6nN_A^2\right)$, and for $n > N_A$ $F(n,N) = 1 + \left(N_A^3 - 4nN_A^2 + 4n - N_A\right)/\left(6n^2 N_A\right)$

The variance increases with time lag n (Figure 11). To fairly compute MSD, Saxton suggested to use only lag times smaller than ¼ of the trajectory (Saxton, 1997). Despite further developments that refined this value, ¼ remains a benchmark in the scientific community. For ¼, we are in the $K >> n$ regime, and we have the following simplification

$$F(n,N) = \left((2n^2 + 1)\right)/(3nK) = \left((2n^2 + 1)\right)/(3n(N - n + 1)) \qquad (47)$$

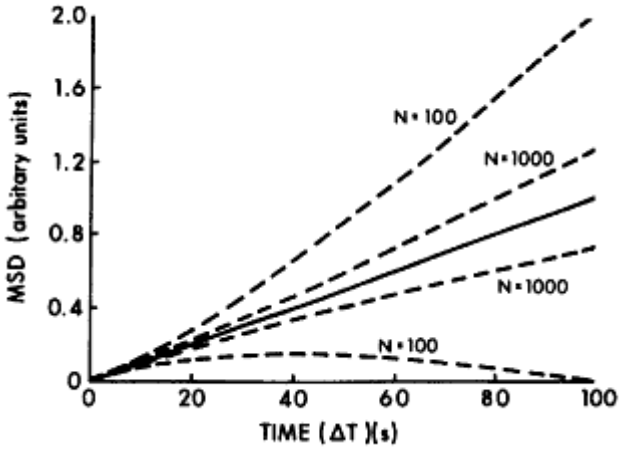

Figure 11: Single trajectory MSD with relative statistical error σ_n . The envelope is $\pm\sqrt{\sigma_n}$. The plot is done as function of N the length of the trajectory (from (Qian et al., 1991)

2.3.1.2 Experimental limitations: pointing accuracy, lag times...

The previous results shows that MSD is only precise up to a given lag time, and this limit depends on the trajectory length. Therefore, why not restrict the analysis to the first MSD curve points, or, more drastically to the first one? Unfortunately, initial points are also biased by lociztion error σ_0 and exposure time t_E (Wieser and Schütz, 2008). For large time lags, the influences σ_0 and t_E vanishes, but for short time lags, it can be critical. Michalet (Michalet, 2010) recently explored in details the implication σ_0 and t_E on the mean square displacement of a single trajectory. t_E *shrinks* the time interval between two independents detections and σ_0 lift the MSD(t) curves up. More precisely, in 2D we have the following expectancy of the MSD curve:

$$MSD(t) = \left(4\sigma^2 - \frac{4}{3}Dt_E\right) + 4Dt \qquad (48)$$

In most SPT reports, the localization error σ^2 I s obtained by imaging an immobile protein. Authors cross-linked the cell, for instance with para-formaldeide (PFA) and detect the same protein and find the standard deviation of successive detections (Manley et al., 2008) . Such protocol however, neglects the influence of motion blur on pointing accuracy. Here σ^2 is the error that integrates the ability to detect accurately an immobile protein, that is distributed with

standard deviation σ_0 and the uncertainty of accurately detect the center of mass of a moving protein that is with s_0 being the standard deviation of the point spread function of the set up.

$$\sigma = \frac{S}{\sqrt{N}} = \sigma_0 \sqrt{1 + \frac{Dt_E}{s_0^2}} \qquad (49)$$

Now, estimating the variance σ_n of the nth Δt interval, Michalet and colleagues obtained:

$$\sigma_n = 4D\Delta t F(n,N,x)^{-1/2} \text{ with } x = \frac{\sigma^2}{D\Delta t} \text{ and } K = N - n$$

$$F(n,N,x) = \frac{1}{6K}(6n^2K - 4nK^2 + 4n + K^3 - K) + \frac{1}{K}(2nx + x^2) \text{ for } n > K$$

$$F(n,N,x) = \frac{2}{6K^2}(4n^2K + 2K - n^3 + n) + \frac{1}{K}\left\{2nx + \left[1 + \frac{1}{2}\left(1 - \frac{n}{K}\right)\right]x^2\right\} \text{ for } n < K$$

The influence of the exposure time t_E is tremendous and most experimentalists have tried to experimentally reduce it. Since the acquisition time of most detector such as EMCCD or C-MOS cameras are usually limited to a 5-10 ms lower bound, the most popular way to reduce t_E is stroboscopic illumination. The shutter that drives sample illumination is only open during a short fraction of time. Some shutters also allow the modulation of the amplitude during t_E. To accurately find the position of the center of mass of the movement during t_E, it can be worthy to collect more photons in the center of the trajectory. In a more recent article authors refined the influence of exposure to MSD variance, changing the value $x = \frac{\sigma^2}{D\Delta t}$ to $x = \frac{\sigma^2}{D\Delta t} - 2R$ (Michalet and Berglund, 2012) with $R = \frac{1}{\Delta t}\int_0^{\Delta t} S(t)[1 - S(t)]dt$ and S being the illumination percentage occurring during frame interval. In the end, R ranges between 0 to ¼.

2.3.1.3 Fitting the diffusion coefficient

Now, finding the diffusion coefficient, we need to fit the MSD curve to a line, with equation: $y = at + b$, a with eing an estimate of $2dD$. Linear fit is often performed with *ordinary least square regression.* However we have seen on the previous paragraph for single trajectory MSD,

the variance of $MSD(n\Delta t)$ increases as a function of the time lag which makes ordinary least square regression non suitable. For Brownian motion, the variance is fortunately known. One solution is therefore to compute the MSD least square regression up to the ¼ limit with weights that should be inversely proportional to the variance (Saxton, 1997).

With localization error, the ¼ limit is not an optimum. Michalet showed the existence of an of optimal number of points $p_{\min}$ for the computation of the least square regression of the MSD curve (Michalet, 2010). However, for a weighted least square regression, authors did not find an analytic expression for $p_{\min}$ but an heuristic that is independent of N but only relies on the illumination ratio $x = \frac{\sigma^2}{D\Delta t}$.

$$p_{\min} = E(2 + 2.7x^{0.5}) \qquad (50)$$

where E is the integer part. Michalet and Berglund latter refined to $p_{\min} = E(2 + 2.7x^{0.5})$ to $p_{\min} = E(2 + 2.3x^{0.52})$ and detailed an algorithm to sequentially find D and $p_{\min}$ (Michalet and Berglund, 2012). At optimal time $p_{\min}$ the question between a weighted and an unweighted least square regression is not relevant. The variance σ_D of the least square estimate of the diffusion coefficient $\hat{D}$ was found to be the same for weighted and un-weighted regression and to be

$$\frac{\sigma_D}{D} \propto \sqrt{\frac{3}{N-2}} \qquad (51)$$

Without localization error and against the ¼ consensus, (Michalet, 2010) found that the best protocol was to use only the first 2 points of the MSD curve.

2.3.1.4 Discussion on the ordinary MSD analysis

The lack of consensus in the scientific community for the computation of the simplest statistic of SPT, the MSD curve is an example of the technical difficulties of SPT that remain largely unaddressed. Here, I will briefly cite two MSD related problems that have risen in my PhD and for which I have not found the answer yet:

- What is the influence of the electronic and out of focus noise on the detection accuracy of moving proteins? Electronic cameras and out of focus photons emitters give an

additional variance σ^2. The effect of noise on immobile particle is known (Betzig et al., 2006) but as the particle moves the signal is spread and a significant part fall into the noise standard deviation. To compute the influence of noise as a function of the diffusion coefficient will be of great interest. My intuition is that that a longer exposure time will be eager to capture stochastic restricted motion. This is the reason why in our lab, for intra cellular single molecule tracking, we have favored a protocol opposed to stroboscopic illumination where we illuminate the sample for almost the whole inter-frame interval.

- What is the influence of the cellular motion during acquisition of the trajectory? When assessing the question of a cellular component movement the cell most experimentalist discard cellular motion and deformations. In our lab studying the motion of a yeast locus, we have used a membrane bound organelle, the spindle pole body (SPB) as fixed cellular reference. However this only corrects translational displacement and not rotations or deformations and the reference is also under the influence of localization accuracy problems. To circumvolve the problem some authors have studied the relative motion of a pair single particle. For instance two loci on different alleles (Miné-Hattab and Rothstein, 2012) or two beads of latex under the same magnetic field (Sainis et al., 2007). For Brownian motion, the computation of this relative MSD only doubles the variance but what for more complicated motion?

Because free diffusion is related to stochastic thermal agitation, scientists are more interested in deviation from Brownian motion. The linearity MSD curve is a well-established test for normal diffusion. If the MSD curve significantly deviates from a line, the motion is not free.

2.3.2 Constrained diffusion in a cell

The “shape” of the MSD curves is the most used empirical criterion to address a particle motion inside the cell. A linear MSD would mean a stochastic organization of obstacles. A MSD curve that over perform would qualify the movement as “facilated diffusion”. Facilated diffusion means that particles have an additional energy source to reach a distance larger than expected upon thermal agitation and therefore imposes the existence of a molecular motor. Facilated

diffusion has been shown for instance looking a virus HiV1 sliding on a microtubule (Arhel et al., 2006).

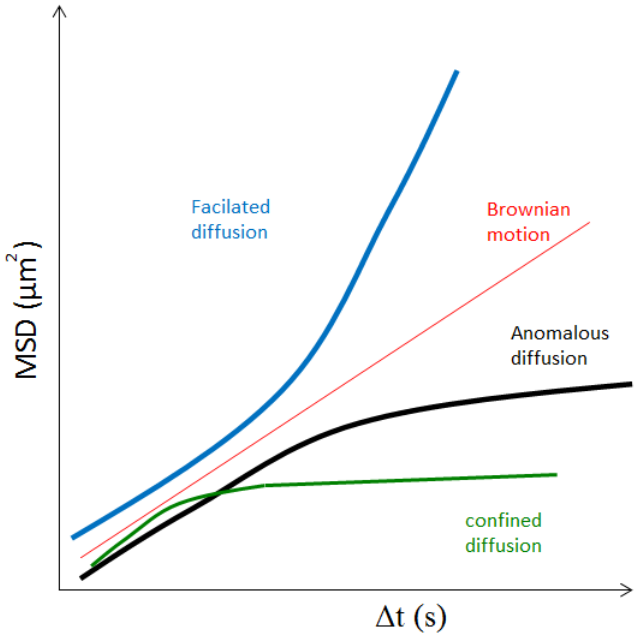

***Figure 12: Qualitative interpretation of the MSD curve.**. Adapted from (Sainis et al., 2007)*
*A MSD curve that is below a line would be the signature of a motion that is restricted compared to Brownian motion and is called "sub-diffusion" (**Figure 12**). Literature has described two kinds of restriction. One that is due to physical barriers that particle shall cross to proceed further. The motion is in that case labeled as "confined" if the crossing is impossible and "corralled" if it is possible. The last type of motion that can be shown with MSD is "anomalous diffusion".*

2.3.2.1 Confinement

In 1993 Kusumi and colleagues investigate gold particles in plasma membranes confined into a limited area ((Kusumi et al., 1993). They proposed that the confinement they observed was due to membrane associated cyto-skeleton network. This conclusion was drawn from the bending shape of the MSD curves. To understand how confinement would bend the MSD, Kusumi and colleagues computed the expected mean square displacement in the simple case of a square where x and y dimensions can be treated separately. Even in this simplified framework, the result is quite complicated and successive reflections have to be sequentially added:

$$MSD_{square}(t) = \frac{L^2}{3} - \frac{32L^2}{\pi^4} \sum_{k=1(odd)}^{\infty} \frac{1}{k^4} \exp\left(-\left(\frac{k\pi}{L} \right)^2 D_{micro} t_{lag} \right) \qquad (52)$$

Where L is the square radius and D_{micro} is the diffusion coefficient in the absence of confinement. Only 15 years later was resolved the shape of the MSD in the much more realistic case of circular or spherical confinement (Bickel). The exact formula, that will not be reproduced here, uses zeros of Bessel functions.

Those complicated expected form of MSD curves makes them useless for fitting. In the case of a circular confinement, Kusumi and colleagues used a much simpler form that integrates only one reflection and therefor only one exponential:

$$MSD_{circle}(t) = R^2 \left(1 - \exp\left(-\frac{4 D_{micro} t_{lag}}{R^2} \right) \right) \qquad (53)$$

The validity of this simplification was later discussed by Saxton (Saxton, 1995) but remains a widely used protocol in the field (Marshall et al., 1997) (Miné-Hattab and Rothstein, 2012) (Jin et al., 2008) (English et al., 2011). I refer to Wieser and colleagues for very complete review on the influence of illumination time and pointing accuracy on confined MSD in different geometries (Wieser and Schütz, 2008).

The MSD analysis of smoothens the data and the shape and nature of the confinement are often hidden in the averaging. It is tempting to remove the time averaging from MSD and to consider only an initial time. This method is sometimes referred as square displacement, "range", or ensemble averaged MSD.

2.3.2.2 Confinement in a complex environment

As we have seen, even the simplest geometry such as squares and disk and without any localization accuracy introduced bias, can have a strong influence on the MSD curve. The exact architecture of the cell can be way more complicated than a square or a disk (Dietrich et al., 2002).

Exploration changes as a function of the geometry and bouncing against the wall can also change the speed and so the apparent diffusion coefficient. For instance, Chatterjee et al. have theoretically shown the increase of the "apparent diffusion coefficient" in the presence of

particular network or geometry (Chatterjee, 2011) and Domanov and Holcman showed the influence of the lateral confinement on the diffusion coefficient (Domanov et al., 2011)(Holcman et al., 2011). Experimental evidences also exist of the influence of the confining geometry on the instantaneous diffusion coefficient. Defining "apparent diffusion coefficient" as the linear regression of the first 3 points of a trajectory MSD and looking at the motion of inner protein L25 inside E coli English et al. showed the motion was much rapid in the middle of the cell even for molecules that couldn't feel the confinement (English et al., 2011).

To decipher the motion of SM trajectories experimentalists needsto clearly understand the constrained at stakes. For instance, the projected motion of Kaede membrane protein in E-coli can artificially appear as non-Brownian and heterogeneous due to the geometry of the nuclear envelope (Bakshi et al., 2011). When Bakshi and colleagues considered the cellular membrane as cylindrical and decomposed the motion on the two axis of the cylinder as 1D sliding and 2D wandering along a circle, the motion was indeed nothing else than a Brownian on a particular environment. So, when the environment appears to display particular symmetry such as the different axes of the bacteria, one solution to plot MSD along the different axis.

Now, what if the geometry does not have any particular symmetry? This question arises for most of the biological constrains. A solution is to divide the trajectory into subsets where the geometry can be linearized. For instance Long and Vu used "splines" to extract the exact diffusion coefficient in the case of diffusion a curvi-linear path (Long and Vu, 2010). They divided the trajectory in several compartments of same number of detected single molecule. For each trajectory on this this path Long and Wu computed the curvilinear coordinate along the spline (SCSA spline curve spatial analysis) and the diffusion along the curvilinear axis and orthogonally from the axis (SCDA: spline curve diffusion analysis)

2.3.2.3 Corral motion

Barriers in biology such as membranes are never fully hermetic and molecules can pass through them. Confinement is therefore mostly transient, as it has been shown for instance following gold covered with anti-biotin antigens (Dietrich et al., 2002). Motion in a transient confinement is referred as "corral". In 1995, Saxton first computed the escape time from a porous corral with Bessel functions (Saxton, 1995)

$$t_{ESC} / \tau = \frac{4 + ha}{2\pi ha} \qquad (54)$$

where τ is the time to explore a corral, a its typical size and h the permeability of the membrane. The existence of a corral motion can have drastic implication for reaction kinetics since the probability to inter-act with neighbors is greatly enhanced by corrals. (Saxton, 2008b).

Corralled motion have been long described in biological dynamics. For instance, the diffusion of phospholipid DOPE in membrane of eukaryote cells showed successive compartments (Murase et al., 2004). The shape of the MSD in the case of corral motion is only empirically known but, as far as I know, there is no analytic formula for it.

How to distinguish a "porous" confinement from a hard-wall one? One argument is obvious: in a porous confinement, the particle can cross the barrier. However, this particularity is obviously smoothed by MSD averaging. As an alternative to MSD, Jin and colleagues defined the range as

$$Range(n\Delta t, t_0) = \left[\left(x(t_0 + n\Delta t) - x(t_0)\right)\right]^2 + \left[\left(y(t_0 + n\Delta t) - y(t_0)\right)\right]^2 \qquad (55)$$

With initial time t_0. The range can provide an empirical measure of the dwell time in the confinement. Dietreren and colleagues fitted the range to a super-diffusive form (of the MSD Dieteren et al., 2011).

$$a_1 t^2 + a_2\left[1 - \exp(a_3 t)\right] \qquad (56)$$

According to Dieteren et all., when a particle cross a potential barrier to go from one compartment to another, the diffusion is facilitated and the fit gives $\frac{1}{a_3}$ to the residence time.

An alternative to the range was also proposed by Tejedor and colleagues in the so called Mean Maximal Exclusion MME (Tejedor et al., 2010). The computation of MME relies on the probability $\Pr(r_{\max} = r_o, t)$ which is the probability to have reached at least once the distance r_o as a function of the time. In the case of confined diffusion, which is not discussed by Tejedor and colleagues, the distribution of $\Pr(r_{\max} = r_o, t)$ is similar to the range. For instance, a sharp break of $\Pr(r_{\max} = r_o, t)$ is expected to appear much sooner that the confinements plateau of the MSD.

2.3.3 Fitting MSD curves to a power law

2.3.3.1 Anomalous scaling coefficient

When the MSD of a trajectory is well approximated by a power law $MSD(t) \propto t^{\alpha}$, the motion is labeled as anomalous. I refer to the first section of the introduction for the theoretical models that can lead to an anomalous scaling of the diffusion coefficient 2.1.1.3.

Anomalous motion implies the estimation of the anomalous coefficient α. Because α can be directly linked to a structure that constrains the motion, anomalous diffusion has been very popular in the field of single molecule studies. For instance, Saxton re-interpreted the case of single molecules undergoing corral diffusion with an anomalous scaling (Saxton, 2007) The idea beneath it is that if geometry of the space is made of corrals of various sizes, then it is much of a fractal structure. Dramatic implication of anomalous diffusion for inner cells chemical reaction kinetics has made anomalous diffusion even more popular in the SMT field (Saxton, 2008b) (Bénichou et al., 2010)

The determination of the MSD anomalous coefficient and the validity of the power law shape of the MSD is most usually done in a log-log scale:

$$\log(MSD(t)) \propto \alpha \log(t) \qquad (57)$$

Saxton (Saxton, 2007) suggested to plot the logarithmic version of the MSD divided by the time: $\log(MSD(t)/t) \propto (\alpha - 1)\log(t)$ for the convenience that deviation from the horizontal is more easily spotted by the experimentalist and that it is a way to weight the least square fit for a MSD whose variance increase linearly with the time. As the popularity of the anomalous diffusion models was increasing, so did the number of studies that criticized it.

2.3.3.2 Critics of the anomalous diffusion scaling

We have seen in the first section that diffusion is a highly stochastic process and that the variance of MSD increases linearly with time (Qian et al., 1991). Therefore an anomalous MSD curve with α close to 1 will fall into the confidence envelope of $MSD(n\Delta t) \pm \sigma_n$ (Figure 11). So assuming a Brownian motion the probability to accurately fit an anomalous diffusion to the MSD curve can be significant. The opposite is also true. For instance, there is probability that an anomalous motion will never be detected from the MSD curve. Indeed the MSD is only one

aspect of the motion, the order 2 moment, that does not faithfully describe the movement the way higher moment would (Ferrari et al., 2001).

What is most limiting to finding of anomalous diffusion is localization error. At short time range, the localization error σ is not smoothed in log-log scale so that the MSD curve look anomalous but is not (Martin et al., 2002). If the ratio $\alpha = \frac{2\sigma^2}{4D}$ is high so that a free diffusion coefficient D is small compared to the localization accuracy then the log log scale can show artificial anomalous scaling. Specifically if Δt is the maximum time interval of the MSD, the apparent anomalous scaling coefficient given by the log log fit would be: $\alpha_{app} = \frac{1}{1+\frac{2\sigma^2}{4D\Delta t}}$.

Transitions between different regimes or segregated compartments can also explain anomalous scaling (Murase et al., 2004). Monte Carlo simulations on corrals show that corral motion can be fit with anomalous models even on the simplest corral geometry (Ritchie et al., 2005). In a striking study, Lill and colleagues showed by Monte Carlo that the distribution sizes of bacteria, and the pooling of all the MSD curves can explain the anomalous MSD that was measured imaging the motion of the green fluorescent protein (GFP) that has no known chemical partner inside the bacteria E coli (Lill et al., 2012).

The limited number of models that can mathematically explain anomalous scaling is also a strong argument against their efficient description of real motion. To rule out possible critics, one solution is to compare the motion observed to an in-vitro physical model. Comparing the motion of Qdot labeled aquaporin -1 in a membrane and in solution Dix and Verkman found similar anomalous scaling. They concluded that this scaling was rather induced by lipid protein or protein-protein interactions rather that by the fixed obstacles or high order super-molecular interaction that the fractal model predicts (Dix and Verkman, 2008). Most of the time however, it is impossible to reproduce in–vitro the condition observed in-vivo. For instance, The membrane is not flat as we can see by hopping prob-ion conductance topography (Adler et al., 2010). A Projected Brownian motion on this 3D folded membrane can appear to be anomalous, with slowing and acceleration but it will be only an artifact due to 2D projection.

2.3.3.3 Ergodicity and CTRW

As we have just seen, averaging heterogeneous motions can lead to an artificial anomalous α. Mathematicians have introduced another model of sub-diffusion where the averaging does not even converge. This model of anomalous diffusion is the continuous time random walk (CTRW). A CTRW is a Brownian motion with long residence time. More precisely, if the distribution of residence time is so wide that it cannot be averaged then the ensemble averaged MSD or range shows anomalous scaling. A typical long tailed distribution that fits this characteristic is a power law:

$$\psi(\tau) = \frac{K}{|\Gamma(-\alpha)|}\tau^{-1-\alpha} \qquad (58)$$

were K is a scaling factor. With such a distribution of waiting time, we get an anomalous ensemble MSD (Burov et al., 2011)

In order to show CTRW in a cell, experimentalists need to have enough traces to have the time average converged. With CTRW, ordinary MSD between different cells can be seemingly different although they are observation of the same process. One other aspect should be kept in mind addressing CTRW: it has no effect on the shape of the trajectory and only set an anomalous "clock" for the recording of the position. On the ordinary MSD curve, CTRW has no effect, at least if the motion is not confined (Lubelski et al., 2008).

Difference between the time and ensemble average of the MSD is called *ergodicity*. With an ordinary Brownian motion, all traces are samples of a same motion. Therefore, it is equivalent to compute the averaged MSD of traces or the MSD of one artificial trace made of all the traces joined one after the other. This is not the case for non ergodic process such as CTRW. In a cell, non ergodic processes were for instance shown for lipid granules in living yeast cell that exhibited long pauses (Jeon et al., 2011). It was also invocated as a possible explanation for the anomalous motion of telomeres in U2OS (Bronstein et al., 2009)

Consideration between time averaging and ensemble averaging can lead to an increasing complexity of the model. For instance, analyzing the motion of lipid granules in living yeast cell Jeonand colleagues showed CTRW at short times and FBM at longer time scales (Jeon et al., 2011). Studying ergodicity breaking, that is the variation of the diffusion coefficient among the

population, and looking at GFP-Kv2.1 channels labels with Qdots in the plasma membrane Weigel et al. showed that the motion was indeed a CTRW on a fractal ((Weigel et al., 2011). CTRW is a convenient model to integrate particle variability in the MSD analysis. A type of diffusion that would integrate that particles are stochastically different and do not see the same surrounding environment will exhibit ergodicity breaking that has nothing to do with CTRW.

To rule out CTRW from alternative models of sub-diffusion, one needs to compare MSD to an alternative statistic that is more dependent on the spatial organization of the trajectory than the MSD. For instance, theoretically, Dybiec and Gudowaska-Novak showed by Monte Carlo calculation that higher moments than MSD (which is the second moment) were more useful in the case of anomalous diffusion to discriminate the underlying model (Dybiec and Gudowska-Nowak, 2009). Confronting CTRW to FLM to explain anomalous motion of bacterial chromosome loci in bacteria, Weber et al chose FLM from the angle distribution (see paragraph 2.3.4.2). To decipher a movement of protein from single molecule data, one needs to have various statistics extracted from the traces so that in the end, a bunch of evidences will get to the real model.

2.3.4 Alternative statistics to MSD

We have seen that the MSD curve is useful statistic to assess the model of the observed motion. The first step is to confront the MSD curve to the null hypothesis of free diffusion. Once free diffusion is ruled out we have seen that even on the simple case of a square confinement, the analytic form of the MSD was so complicated that it was not suitable for inference. Alternative statistics are therefore required to fully understand the motion. They can be classified in 3 groups:

- The propagator $p(\vec{r},t)$ that expresses the probability to find the particle at position $\vec{r}$ and time t.
- The correlation between successive step translocations
- Point pattern statistics on the set of detections $\{(x_i,y_i)\}$ analyzed without time reference

2.3.4.1 Propagator:

The MSD is the second radial moment of the propagator $p(\vec{r},t)$ and its computation is only part of the information we can extract from single molecule trajectories. As an alternative to MSD, why not consider the whole $p(\vec{r},t)$? The only but important condition is to have enough data to populate and histogram of displacement with a given binning. For a Brownian motion in 1D the motion is isotropic so that the probability $p(\vec{r},t)$ only depends on the radial distance r, the central limit theorem imposes to have the following form:

$$p(r,t) = \frac{1}{\sqrt{2\pi \times 4Dt}} e^{\frac{-r^2}{2\times 4Dt}} \qquad (59)$$

If the model is not specified, a qualitative analysis of $p(r,t)$ can be important to choose the right one. The symmetry of the propagator is a characteristic of Brownian motion and therefore, a non-symmetric propagator is a strong argument against it. For instance, analyzing the distance between r between two beads of latex and defining Δr is the difference of distances between initial and final state Sainis et al showed a growing anisotropy of the propagator towards positive Δr and therefor proved repulsion of the beads (Sainis et al., 2007). Another example is the dwell time of matrix melanoprotease (MMPS) in collagen fibril. Along the axis of the fibril, $p(r,t)$ displays two peaks that appears with increasing time length meaning a kind of pausing (Sarkar et al., 2012). Sarkar et al concluded that the diffusion coefficient was different according to the time scale. In the end, $p(r,t)$ can help discriminate between confine, active transport and free diffusion (Jin et al., 2007) and (**Figure 13**).

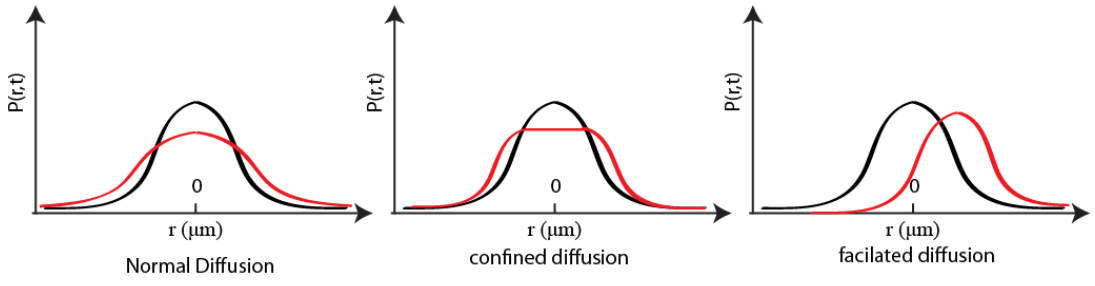

Figure 13: Qualitative evolution of the 1D propagator $p(\vec{r},t)$ ***for different models.*** *The particle position is at initial position (0,0) and the two colors refer to different times* $t_{black} < t_{red}$ *. Adapted from (Sainis et al., 2007)*

The computation of the propagator as an histogram, however, is highly dependent to binning. The cumulative step translocation histogram does not have this drawback. In 2D, it is even more interesting the cumulative square step translocation histogram. In the case of free diffusion the exact cumulative distribution function has a convenient simple form.

$$P(r^2,t) = 1 - \exp\left(-\frac{r^2}{4D(\Delta t)}\right) \qquad (60)$$

Vrljic et al. used this statistic compute D estimated at differ time lag for MHC membrane proteins (Vrljic et al., 2002).

2.3.4.2 Correlation and angles

Free diffusion is Markovian, meaning that a step translocation is not correlated with the following one. So are other motions such as the continuous time random walk (CTRW). The MSD is blind to Markovian hypothesis since all step square translocations are incorporated in the statistic regardless their relative position on the trace. Testing the correlation between successive translocation can rule out free diffusion. The correlation factor $C^{(\delta)}(\tau)$ is defined as function of the dead time τ and of the lag time δ as follow (Weber et al., 2010). (**Figure 14**).

$$C^{(\delta)}(\tau,\delta) = \left\langle \vec{r}(\tau+\delta) - \vec{r}(\tau).\vec{r}(\delta) - \vec{r}(0).\right\rangle \qquad (61)$$

Where $\langle . \rangle$ is time and ensemble averaging and $\vec{r}(0)$ is the initial position. The correlation factor is dependent to the size of the step translocations. To confront different time lags δ, and more precisely for $\delta = n\Delta t$, we shall define a unit-less parameter, the coefficient of variation by dividing $C_v^{(\delta)}(\tau)$ with the mean square displacement $\sigma^2 = \left\langle \left|\Delta r(\delta)\right|^2 \right\rangle$

$$C_v^{(\delta)}(\tau,\delta) = \frac{1}{\sigma^2}\left\langle \vec{r}(\tau+\delta) - \vec{r}(\tau).\vec{r}(\delta) - \vec{r}(0).\right\rangle \qquad (62)$$

Angles are a related statistic that is defined on successive displacements. Each pair of successive step translocations gives one angle value and the distribution of the angles are an indication of the geometry of the movement.

$$\theta_i(\tau,\delta) = \cos^{-1}\left(\frac{\left(\vec{r}_i(\tau+\delta)-\vec{r}_i(\tau).\vec{r}_i(\delta)-\vec{r}_i(0)\right)}{\left|\vec{r}_i(\tau+\delta)-\vec{r}_i(\tau)\right|\left|\vec{r}_i(\delta)-\vec{r}_i(0)\right|}\right) \qquad (63)$$

As it is expressed above, the angle values range in the interval $[0;\pi]$ or $[0;180°]$. In 2D, however the orientation of the vector product between $\vec{r}_i(\tau+\delta)-\vec{r}_i(\tau)$ and $\left|\vec{r}_i(\delta)-\vec{r}_i(0)\right|$ can extend the analysis to the interval $[0;2\pi[$ or $[0;360°[$.

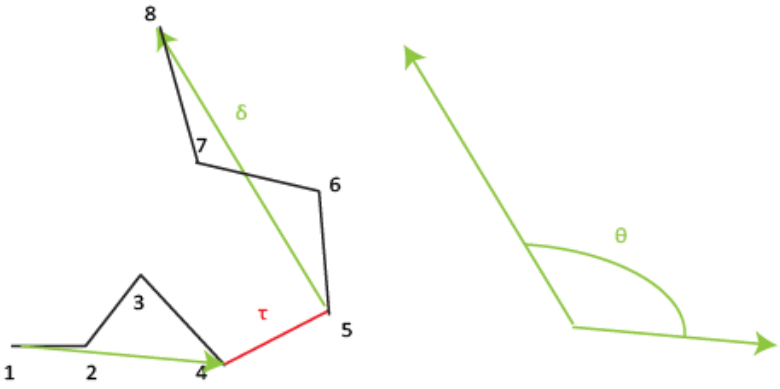

Figure 14: The correlation coefficient $C^{(\delta)}(\tau,\delta)$ ***and the angle*** $\theta_i(\tau,\delta)$ ***as a function of the time lag*** σ ***and dead time*** τ **.** *The numbers describe the time in arbitrary unit and here* $\tau = 1$ *and* $\delta = 3$. $C^{(\delta)}(\tau,\delta)$ *is the scalar product between the green vectors and* $\theta_i(\tau,\delta)$ *is their respective angles.*

The most straightforward use of angles and correlation statistics is to assess directed motion. For instance Bouzigues and Dahan computed $C^{(1)}(\tau = 1)$ on a sliding window to assess events of directed motion of GABA receptors in membranes (Bouzigues and Dahan, 2007). The distribution of angles has been similarly used to find directive motions of proteins inside cells in relation the cytoskeleton. To estimate micro-tubule plus end growth in drosophila oocytes, it was mandatory to find the ones that were effectively growing, and this was done with the angle

statistic (Hamilton et al., 2010). The case of viral infection of bacteria E-Coli was also studied with the angle statistic measured between the longitudinal and perpendicular axis of the cell (Rothenberg et al., 2011). Authors found a predominant 30° associated with a rotational behavior around the cell. They found that this value was optimal for an efficient scanning of the membrane by the virus in search for an entrance.

Angles and correlations are associated with the notion of persistence. A persistent random walk such as directed motion would display successive step translocations on the same direction and axis than the previous displacement. The resulting angle distribution would be enriched around the O° value and the coefficient of variation would be positive. Anti-persistent walk, on the contrary, would display a distribution of angles that are enriched around the 180° value. Raupach et al. have defined the "anti-persistence degree " as the integration of the angle histogram in the $[90°;180°[$ interval to compute the turning angles of beads in the cytoskeletal (Raupach et al., 2007). Confronting CTRW to FLM to explain anomalous motion of bacterial chromosome loci in bacteria, Weber et al chose FLM because anti –persistence revealed by $C^{(\delta)}(\tau)$ decreased as a function of δ which was signature of FLM (Weber et al., 2010b).

The study of Weber et al. however raised numerous questions and critics because of the bias induced by localization accuracy on the statistic $C^{(\delta)}(\tau)$ (Burov et al., 2011). Kikura and colleagues use the angles of quantum dot labeled Simian virion 40 sliding and tumbling in lipid bilayers of the membrane (Kukura et al., 2009), but did not publish exact quantification and instead rather qualitative assessments since the angle were biased by a low pointing accuracy. The argument has already been raised when looking at immobilized beads in a gel that nevertheless displays anisotropy (Niehaus et al., 2008).

Weber et al. replied to the critics with a complete and detailed study on the influence of confinement and localization accuracy on $C^{(\delta)}(\tau)$ (Weber et al., 2012a).

- *Localization accuracy* induces anti-persistence via a seemingly confined motion. For $\tau = 0$, even if the motion is purely Brownian with diffusion coefficient D there is a residual coefficient of variation that is directly related to offset of the MSD : $C_v^{(\delta)}(\tau = 0) = \frac{1}{\delta^2}\left[\frac{1}{3}Dt_E - \left\langle \vec{\varepsilon}^{\,2} \right\rangle\right]$. To investigate the influence of this correlation on the

statistic, one solution is to look at the evolution of the correlation with time. For Brownian motion with a low pointing accuracy, $C^{(\delta)}(\tau)$ displays negative correlation at very short time τ scale for Brownian motion that vanishes at long τ.

- *Confinement* induces also anti-persistence by a "bouncing on the walls" effect. To discard confinement, one solution is to study the influence of δ on the statistic. For small δ, we get decreasing anti-correlation until the particle *forget* its previous position in the confinement domain. For large δ, that correspond to a full exploration of the volume $C^{(\delta)}(\tau)$ displays no correlation except for $\tau = \delta$ where constant anti correlation is displayed without evolution with time lag that is the signature of confinement,

$$\frac{C_v^{(\delta)}(\tau = \delta)}{C_v^{(\delta)}(\tau = 0)} = -\frac{1}{2} \qquad (64)$$

The limitation of pointing accuracy can be turned an advantage in the case of movement of big particles. For instance Gu et al. computed the correlation of motion blurs with a Pearson coefficient to find out that the motion of Nano cargos in axons was indeed a rotational movement (Gu et al., 2012).

2.3.4.3 Point pattern related techniques

Motion blurs MB are created by the photons that hit the captor during exposure time. Without electronic noise induced by the camera and with infinitely small pixels, photons hits on the captor during exposure time would create a point pattern with no known time reference. Similarly, if we remove the clock that labels the points of trajectory, we would also get a point pattern. I will now describe methods that deliberately forget the time for SMT trajectory analysis, only considering the spatial distribution of their constitutive points.

2.3.4.3.1 Motion blurs

Motion blurs are the convolution between the axial projected point spread function PSF_{xy}, the pathway $R_{xy,t}$ that would follow the particle and the shot A_t noise defined by the arrival of photons.

$$MB = R_{xy,t} \otimes PSF_{xy} \otimes A_t \qquad (65)$$

Recovering $R_{xy,t}$ from the motion blur is an *inverse problem* involving de-convolution. To solve it, one needs to also remember that A_t and $R_{xy,t}$ are stochastic. Lots of de-convolution method exist (Sibarita, 2005) that will not be developed here. I will just briefly introduce two results that have been obtained in the specific case of single molecule tracking to infer parameters from motion blurs.

In the case of an infinitely accurate captor, a deterministic linear or circular displacement and Gaussian PSF, Wong et al computed the Cramer Rao lower bound limit of inference of the parameters of the movement (Wong et al., 2011). This means that up to a certain extent, we can recover the speed and initial position of a photon-emitting particle directly from the motion blur. For more complex mode of motion such as Brownian motion, the solution is not easily found. We have seen that the localization accuracy of a moving particle was function of the number of photons P

$$\sigma = \frac{S}{\sqrt{P}} = \sigma_0 \sqrt{1 + \frac{Dt_E}{s_0^2}} \qquad (66)$$

This variance is indeed the expected variance motions blur for a Gaussian PSF. On real motion blurs, Zareh and colleagues have developed a method to directly compute the diffusion coefficient from an heuristic version of this formula with real PSF (Zareh et al., 2012). They define the Pathway distribution function (PWD) as the convolution between the axial projected real PSF and the real pathway. PWD is thus the rmotion blur without photon or electronic noise and pixel size limitations. Since moving particles can move out of focus Zareh and colleagues is to considered only uni-modals motion blurs, fit them to a one-peak Gaussian and kept for analysis only those with a good fit quality. Once this done, the standard deviation along the xy focal plane is fit to the formula:

$$s_{x,y} = \sqrt{\sigma_0^2 + Axy.2D_{3D}t} \qquad (67)$$

Here σ_0^2 is found by imaging immobile particle and Axy is an heuristic found with simulations. Zareh et al applied this method for the determination of the diffusion coefficient of e-GFP molecules in membrane finding a narrow distribution of diffusion coefficients.

Motion blur inference is highly model dependent. Since time of arrival of the photons is lost in motion blurs, we cannot have the relation between position and time in the particle movement.

2.3.4.3.2 Kurtosis and Skewness

Considering the point pattern $\{\vec{r}_i = (x_i, y_i)\}$ made by a trajectory, the skewness S and the kurtosis K are defined by the ratios, in one dimension:

$$K = \frac{\left\langle \left| \vec{r}_i - \langle \vec{r}_i \rangle \right|^4 \right\rangle}{\left\langle \left| \vec{r}_i - \langle \vec{r}_i \rangle \right|^2 \right\rangle^2} \text{ and } S = \frac{\left\langle \left| \vec{r}_i - \langle \vec{r}_i \rangle \right| . \vec{i}^3 \right\rangle}{\left\langle \left| \vec{r}_i - \langle \vec{r}_i \rangle \right|^2 \right\rangle^{\frac{3}{2}}} \qquad (68)$$

where $\langle . \rangle$ is spatial averaging. S is an indicator of the distribution asymmetry, is defined in a particular $\vec{i}$ direction and is equal to 0 for symmetric distributions. K can be computed in 2D and 3D and is related to the "peakedness" of the distribution. It is equal to 3 in the case of a normal distribution. Authors often compute the normalize kurtosis $K' = \frac{K}{3} - 1$. When K' is positive the distribution would be more peaked than a normal distribution. Kurtosis can help rule out Brownian motion as a model of the movement. For instance, for a strictly confined motion or more exactly for a corral motion with fixed barriers, the rescaled kurtosis is negative. Since skewness is direction dependent, in 2D, Coscoy and colleagues added another parameter to decipher anisotropy called *anisotropy coefficient* ρ (Coscoy et al., 2007). ρ is the ratio of explicated variance between the linear regression and regression along the orthogonal axis. We have $\rho = 1$ for a purely isotropic distribution and $\rho < 1$ for anisotropic. Even for Bownian motion, $\rho = 1$ only stochastically occurs Coscoy et al chose to plot the cumulative distribution of ρ and found than ρ was more robust than S to assess anisotropy. Using ρ and K Coscoy and colleagues assessed the motion of GFP tagged microvilli of Epithelial cells and indeed found that the motion was not Brownian. Coscoy et al also performed a time window analysis to detect local confinement.

One can compute the kurtosis as a function of time to spot changes in the geometry of the movement:

$$K_\alpha(t) = \frac{\left\langle \left| \Delta\vec{r}_i(t) - \left\langle \Delta\vec{r}_i(t) \right\rangle \right|^4 \right\rangle}{3\left\langle \left| \Delta\vec{r}_i(t) - \left\langle \Delta\vec{r}_i(t) \right\rangle \right|^2 \right\rangle^2} - 1 \qquad (69)$$

Lushnikov et al. applied time kurtosis for the for corral diffusion in the specific case of a cage – type Gaussian potential: $U_i(l) = H\exp(-d_{i,l}^2/\sigma^2)$ (Lushnikov et al., 2012) were $d_{i,l}$ is the distance to a the frontier. If the corrals are isotropicaly distributed, $K_\alpha(t)$ will exhibit two peaks that correspond to the time needed to explore two adjacent corrals. Time position of the second kurtosis peak is given as a function of the lattice mesh size L and the effective diffusion coefficient D

$$\tau_{peak,2} = \frac{P^{-1}L}{5D}\ln\left(\frac{6}{5}\right) + O\left(\frac{L^2}{D}\right) \text{ where } P = H^{1/2}\pi^{-1/2}\sigma^{-1}e^{-H} \text{ P} \qquad (70)$$

Tejedor et al. used a related definition of the kurtosis $\left\langle r_{\max}^4(t)\right\rangle / \left\langle r_{\max}^2(t)\right\rangle$ to classify the mechanism that would lead to an anomalous behavior (Tejedor et al., 2010). With this statistic, Tejedor et al interpreted time dependent kurtosis of Lipid granules in yeast cell as "transient FBM" but acknowledged that it could be a simple effect of the heterogeneity of the lipidic particle that are trapped in corrals of various sizes. Kurtosis is the 4th moment of the distribution, compared to the MSD that is the second moment. We can go further and compute a whole anomalous moment scaling spectrum $\left\langle x^n(\tau)\right\rangle \propto t^\gamma$ (Ewers et al., 2005). Distribution of the spectrum is characteristic of the different anomalous diffusion models (Ferrari et al., 2001)

2.3.4.3.3 Radial density distribution

As we have seen, point pattern statistics are useful to find confinement, real or transient, out of single molecule trajectories. A particle is confined when a force is opposed to its natural spreading behavior. Damien Hall list all the potentials derived from for molecular interaction that can influence single particle trajectory (Damien Hall, 2010) . They range from macromolecular crowding, free overlap, hard particle (wall), square well, saw tooth (inter-action that is seen up to a given range) , soft sphere and Lenard-Jones (attractive at long scale and repulsive at small scale)

Crane et al visualized Q dots labeled aquaporin 4 dynamics in cell plasma membrane (Crane et al., 2008). Aquaporin 4 forms immobile ensemble known as orthogonal arrays of particle (OAP). Crane et al. investigated the potential of the force that keeps aquaporin 4 with *Radial density distribution,n* a method that was introduced by Jin and colleagues (Jin et al., 2007). They finally measured a spring like potential inside OAP.

Radial density distribution analysis work as follow on a set of detections of a trajectory (**Figure 15**):

- Computation of the center of mass of the set of detections
- Computation for all the points of the distance to the center of mass r
- Setting of a small radial interval Δr
- Computation of the number of points $N(r)$ that fall in an annular region of width Δr at distance r of the center of mass
- Computation of the radial density distribution.

$$d(r) = N(r)/\pi\left[(r+\Delta r/2)^2 - (r-\Delta r/2)^2\right] \qquad (71)$$

The density is analytically related to the potential with the formula $d(r) = d(0)\exp(-V(r)/k_B T)$. This method is therefore scale independent. Whatever the diffusion coefficient or confinement size, it can assess the potential, at least qualitatively.

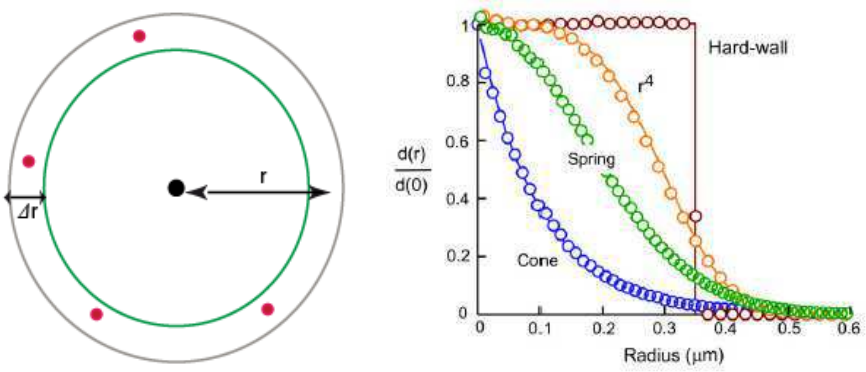

Figure 15: Computation of the radial density distribution $d(r)$. *Left panel : the single particle detections* (x_i, y_i) *are counted as a function of the estimated center of the potential. The shape of the radial density distribution is directly related to the*

nature of the potential (left panel from (Jin et al., 2007))

However, to efficiently use the method, one needs to have a set of long lasting trajectories. Crane et al used only trajectories longer than >200 frames used to find the ratio free/immobile and trajectories longer than 455 frames to find the potential. The influence of pointing accuracy is also dreadful, and so is the accurate determination of the center mass (Jin et al., 2007). A perfectly immobile particle with Gaussian localization accuracy will exhibit a spring-like potential and as far as I know, using this method, experimentalists only found spring like potentials.

2.3.4.4 Potential inference

A force derived from a potential would modify the Langevin and Focker –Plank equations as follow:

$$\ddot{r}(t) + \gamma\dot{r}(t) + \nabla V(r(t)) = \sigma\zeta(t) \qquad (72)$$

$$\frac{\partial p}{\partial t} = D\Delta p + \nabla\left[\left(V(X)\right)\ p\right] \qquad (73)$$

However, the analytical dependence between the propagator or trajectory and potential is hard to find and methods to solve are not popular in the single molecule community (Risken, 1996). Numerical methods have been developed for the Focker Planck equation by numerical simulation such as Monte Carlo Markov Chain or matrix continued fraction expansion (Chen, 2002). Exact calculation of the propagator have been made in the case of spring potentials, or two wells located far apart with a transition probability (Chen and Huang, 2001), but most of the time random trajectories are computed by simulation with a given time shift and then compared to real (Biess et al., 2011). For simplification, authors restrict the study to the drifted random walk.

2.3.4.4.1 Drift

With a constant force, the Focker Planck diffusion equation can be re-written as follow in an arbitrary $\vec{x}$ direction:

$$\frac{\partial p_x}{\partial t} = D\Delta p_x + F_{ext}.\vec{x} \qquad (74)$$

If particles were in the void, such potential would result in a constant acceleration. In a crowed environment, however, in a regime where friction prevail and causes energy loss, a weak force would only result in a constant drift (Cuche et al., 2012). In such a regime, at the first order the propagator has a simple form: the non-square displacement Δr has still variance 2Dt but the expectancy is the non-zero drift rate:

$$\mu = \frac{F_{ext}\Delta t}{\gamma} \qquad (75)$$

The orientation of the force drift is obtained by the angle of the shift: $\theta_{out} = \arctan(\overline{\Delta x}/\overline{\Delta y})$. In such cases, to estimate the force, the drift rate μ must be significantly higher than the step displacement standard displacement that is given: $\sqrt{4Dn\Delta t\left[n/(N-n)\right]^{1/2}}$ where n is lag time and N is the length of the trajectory(Qian et al., 1991). Particles undergoing drifted motion will therefore exhibit facilated diffusion. Haggie et al found an heuristic to determine the potential (Haggie et al., 2006).

- Subtract offset on the 3 first points of the MSD

$$\left\langle r^2(t)\right\rangle = 4D_{1-3}t + offset \qquad (76)$$

- Fit the MSD to the it to the corresponding form obtained by the conservation of the energy from ballistic mode of motion trap in a potential.

$$\left\langle r^2(t)\right\rangle_{fit} = \mu t^2 + a_2\left[1-\exp(a_3 t)\right] \qquad (77)$$

Such heuristic was also applied by Crane et al. (Crane et al., 2008) and similarly, Bouzigues and Dahan computed the drift of GABA receptors in the membrane by fitting the mean square displacement to the following formula (Bouzigues and Dahan, 2007):

$$\left\langle r^2(t)\right\rangle = 4Dt + \mu \times t^2 \qquad (78)$$

Studying the motion of nano-particles that was trapped into lipid rafts Masson et al. linearize the potential in small ij sub-area of the raft so that the (Masson et al., 2009)

$$\frac{\partial \vec{p}}{\partial t} = D\Delta\vec{p} + \vec{F}_{ij} \qquad (79)$$

Using the crowed regime approximation and assuming that the propagator had still a Gaussian form, Masson at al computed the likelihood of the force of the one step displacement F_{ij} and diffusion coefficient observing the one step displacement $T = (r_{\mu+1} | r_\mu)$.

$$P(T | F_{ij}, D|) = \prod_{\mu: r_\mu \in S_{ij}} P((r_{\mu+1} | r_\mu) | F_{ij}, D\ ) = \prod_{\mu: r_\mu \in S_{ij}} \exp\left(\frac{-(r_{\mu+1} - r_\mu - F_{ij}\Delta t / \gamma)^2}{4\pi D\Delta t} \right) \qquad (80)$$

Masson and colleagues later refined equation (80) to take into account all kinds of displacement $(r_2, t_2 | r_1, t_1)|$ for different time lags and local diffusion coefficient D_{ij} (Türkcan et al., 2012)

$$P((r_2, t_2 | r_1, t_1) | F_{ij}, D_{ij}) = \exp\left(\frac{-(r_2 - r_1 - F_{ij}(t_2 - t_1)/\gamma)^2}{4\pi\left(D_{ij} + \sigma^2/(t_2 - t_1)\right)(t_2 - t_1)'} \right) \qquad (81)$$

The method was applied by Voisinne et al. for assessing the potential that maintained Lipid rafts on the membrane (Voisinne et al., 2010), and also on pore-forming toxins (CPeT) and display a polynomial potential (Türkcan et al., 2012) . Of course the method is highly dependent to the distribution of the propagator p_x which can be far more complex than Gaussian in the case of a FBM with a drift (Karine Bertin). Masson and colleagues also misleadingly referred to the method as “Bayesian”. With a high number of points, Bayesian schemes and maximum likelihood method are equivalent. Mason et al also chose all a-priori distributions to be constant. Finally, with a Gaussian form of the density, the method is exactly equivalent to a simple ordinary weighted least square regression (Gouriéroux and Monfort, 1996).

2.3.4.5 Combining statistics

I’ve introduced some of the statistics that authors have computed on SPT data, but this is not an exhaustive inventory and authors’ imagination is limitless. As we have seen in detailed with the MSD, inferring models from a single statistic is not an easy task. Below are twoexamples

computed on the different statistics introduced and of the rules of thumbs method to classify them.

- Studying secretory vesicle dynamics on the plasma membrane region of human carcinoid BON cells, Huet et al. used together the rolling diffusion coefficient, the "MSD curvature" and the skewness to put trajectories in the following categories: constrained, facilated and free and then settin threshold (Huet et al., 2006).
- Studying Adenovirus-2 trajectories, Helmuth and al. used the "additional straightness" (mean cosinus value for all detections, between successive detections), net displacement, bending (mean sinus value for all points), efficiency (deviation from normal diffusion), skewness and kurtosis (Helmuth et al., 2007). They found 4 types of regimes: directed, fast drift, slow drift, confined.

Indeed, SP motions in cell are most of the time composite. This heterogeneity can arise from the population itself, such different protein conformations but can also be time heterogeneity, with proteins that switch from a regime to another. The analysis of heterogeneous data is far harder than single model inference e have presented here and even the heterogeneity can be hard to prove.

2.3.5 Analysis of an heterogeneous set of trajectories

We have seen in the case of continuous time random walk (CTRW) the time averaged MSD is different from the ensemble average. On this particular model, even with an infinitely long trajectory, it is impossible to recover all the possible behaviors. We have seen with CTRW that such a motion is called *non-ergodic*.. The same protein can have different folding so that, even if we could observe indefinitely a single molecule, it will never display all its possible configurations. So the question that biologists ask is "Do I see multiple populations of moving particles or is it random variation of one single type of movement?".

2.3.5.1 Distribution of the measured diffusion coefficients

In most cases, such as the case of the movement individual integrins nanoclusters (cell membrane adhesion receptors) authors average MSD coming from different trajectories in an time-ensemble MSD (Bakker et al., 2012)

$$MSD_{all}(n\Delta t) = \frac{1}{N_n}\sum_k \frac{1}{N_n^k}\sum_{i-j=n}\left(x_{i,k}-x_{j,k}\right)^2+\left(y_{i,k}-y_{j,k}\right)^2 \qquad (82)$$

Where $x_{i,k}$ and $y_{i,k}$ are the coordinates of the trajectory k, N_n is the number of trajectories that are at least of size n and N_n^k is the number of segments of size n of the trajectory k. This definition, however is not the only one used. In some cases, authors prefer the following (Saxton, 1997).

$$MSD_{all}(n\Delta t) = \frac{1}{N_n^{k'}}\sum_k\sum_{i-j=n}\left(x_{i,k}-x_{j,k}\right)^2+\left(y_{i,k}-y_{j,k}\right)^2 \qquad (83)$$

Where $N_n^{k'}$ is the number of segments of size n of the whole set of trajectories. The difference between the two formulas is the weight of the trajectories in the MSD. The first definition gives an equal weight to all the trajectories, whereas the second definitions favor long trajectories. If all the particles are observations of the same model or if all the trajectories have the same length, both should give similar results (Brameshuber and Schütz, 2008)**.**

Let's consider a Brownian motion with true diffusion coefficient D_0 but finite trajectories of duration $N\Delta t$. What would be the distribution of measured diffusion coefficients D_e obtained from individual linear regressions? Studying the motion of NHC membrane protein, Vrljic and colleagues answer the question simply by looking at the distribution of the Nth mean square displacement (Vrljic et al., 2002). They substitute $\left\langle r^2\right\rangle = 4D_e\Delta t$ the distribution of $p(\left\langle r^2\right\rangle)d\left\langle r^2\right\rangle$ obtained by Saxton and found (Saxton, 1997):

$$p(D_e)dD_e = \frac{1}{(N-1)!}\left(\frac{N}{D_0}\right)^N (D_e)^{N-1}\exp\left(\frac{-ND_e}{D_0}\right)dD_e \qquad (84)$$

So that D_e follows **a gamma distribution** ($\theta = \frac{D_0}{N}$ and K=N) that was indeed observed for lipid molecules in membrane(Sonnleitner et al., 1999). The result was later refined to include of localization error (Michalet, 2010).

A gamma distribution is a left skewed distribution. A **log normal distribution** is also left skewed and, in most cases the two distributions can be equivalently used to model a broad range

of phenomenon. Indeed, only few tests exist to discriminate one from the other (Jackson, 1969). Without, to my knowledge, any model justification for it, authors have switched to the log-normal distribution to estimate relative proportions of populations with different diffusion coefficients.. Studying the SPT trajectories of integrin receptors (cell membrane adhesion receptors) on T cells membrane that change according to activation state of the cell and trying separated diffusive from immobile receptors, Cairo et al. indeed found that both populations were log-normaly distributed (Cairo et al., 2006). Using the kernel density function

$$d_L = Ae^{-\frac{(\ln(x)-\ln(x_0))^2}{2c^2}} \qquad (85)$$

Cairo and colleagues fitted the distribution histogram of diffusion coefficients and found, with the fitted parameter A, the relative proportion of bound vs free receptors[4]. The method was later refined with a variable bandwidth to quantify the proportion of up to 3 populations of freely diffusing proteins on the membrane (Pinaud et al., 2009).

Sometimes, different populations are mixed and the computation and the distribution coefficient is not as straightforward. After micro injection of R-phycoerythrin (RPE) protein inside the cytoplasm, Goulian and Simon found that the diffusion coefficient distribution was broader than the Gamma distribution that was recovered after injection in glycerol (Goulian and Simon, 2000). Studying the motion of beads inside the cyto-skeleton, Raupach and colleagues found that the distribution was too wide to be fitted with only one population but failed in counting them Raupach et al., 2007). On such wide distributions, the computation the relative population proportion is impossible and only qualitative measurement can be performed. To show that the mobility of the integrin nano-clusters that was studied by Cairo and colleagues was increased in T cells after treatment with extra Ca2+, Bakker and colleagues compared the Diffusion

[4] In a kernel-fitting scheme, the most important parameter is the bandwidth "c". Cairo et al obtained the band with from a combination of log normal and normal fitting with corresponding variance $\sigma_L = x_0\sigma_N = x_0 c$. This is true only for small σ_N , the exact formula being $\sigma_L = \left(e^{\sigma_N^2} - 1\right)^{\frac{1}{2}} x_0$

coefficient cumulative probability distribution before and after activation (Bakker et al., 2012). When the distribution of diffusion coefficient is not smooth enough to be fit, one solution is to set an arbitrary threshold. Dahan and colleagues computed the relative proportions of quantum dots in the membrane with diffusion coefficients higher and lower than 0.01µm²/s (Dahan et al., 2003). Some authors have also computed by the correlation of the diffusion coefficient with an additional criterion. For example, Mimoura and colleagues showed that the diffusion coefficient of f hydrophilic nanoparticles that interacts with micro-tubules decreased with the charge (measured as a volume) (Minoura et al., 2010).

When studying changes in the diffusion coefficients with or without treatment, one can argue that the observed difference is due to experimental bias. It is therefore of high importance to image the particle in exact same conditions. For instance, studying the binding of molecular complexes to T cell receptors one important is to have a constant density of image (Axmann et al., 2012). Finally, measured heterogeneity of the movement should always be related to a biological property of the process and biological processes are most of the time transient. If particles remain is segregated state, then heterogeneity only means that no model will ever explain the motion. If transitions are observed, then relative proportions can be interpreted as observation of a composite movement. For example, Oh and colleagues showed that the percentage of bound and unbound molecules determines a dwell time(Oh et al., 2012). To justify ergodicity, it is important to show transitions between regimes.

2.3.5.2 Transition between regimes

In most inner cell single particle studies, the finding of different regimes is common but transitions between regimes are not often shown with statistical significance. From ensemble of trajectories of the motion of lambda phages on E coli, Rothenberg and colleagues found three different populations of diffusing phages according to the diffusion coefficient histogram but did not find transitions between those regimes (Rothenberg et al., 2011). Rothenberg and colleagues argued that the square exponent of the MSD would smooth transitions. The only justification was a trajectory that was supposed to be transiently changing from fast to slow exploration according to the successive absolute displacement in X and Y. From the histogram of diffusion coefficients Axman et al. also showed that there were two populations of fast and slow exploration but transition between regimes was only empirically justified (Axmann et al., 2012).

To understand regime switching, let's imagine that there the motion can be described by 2 free diffusing regimes 1 and 2 with diffusion coefficient $D_1 << D_2$ and that stochastic transition between those regimes with occur with constants k_{off} and k_{on}

$$D_1 \underset{k_{on}}{\overset{k_{off}}{\rightleftarrows}} D_2 \qquad (86)$$

Then $\tau_{off} = 1/k_{off}$ and $\tau_{on} = 1/k_{on}$ are the average time to respectively be in regime 1 or 2. In the case of $\tau_{off} << \tau_{on}$ Jin and colleagues proposed a simulation grounded method to find τ_{off} on a set of individual trajectories. The idea is not to compute a linear regression of the whole MSD curves but to measure it only with one step regression on a particular t_{lag} value $\left\langle (r^2(t_{lag}))/4t_{lag} \right\rangle$. If at the $t_{lag} < \tau_{off}$ then the diffusion coefficient histogram should display two population, and if $t_{lag} > \tau_{off}$ the diffusion coefficient histogram should display only one (**Figure 16**).

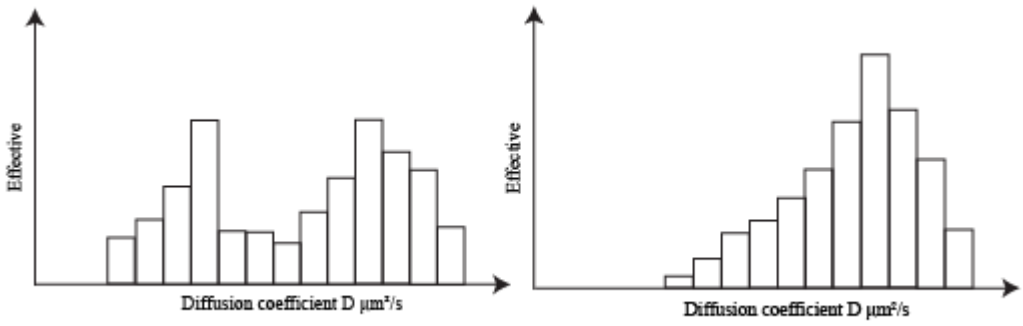

Figure 16: Diffusion coefficient histograms displaying one (left panel, unimodal) or two (right panel, bimodal) populations*. If the motion is switching from fast diffusion to slow diffusion, the diffusion coefficient histogram estimated at different time lag t_{lag} will be bimodal for $t_{lag} < \tau_{off}$ and unimodal $t_{lag} > \tau_{off}$, τ_{off} being residency time in slow diffusing regime adapted from (Jin and Verkman, 2007)*

Another method that can be applied is to find transitions is to compute the diffusion coefficient on a sliding window on the trajectory. For Michalet and colleagues, using less than 10 points for this window is a "useless enterprise" (Michalet, 2010). If one still want to proceed, with a large error accuracy large the best is to use all the 9 points of the MSD for the fit and the uncertainty

of the fit remains large $\sigma_D / D > 1$. For small value of localization accuracy the best fit is obtained with only the first points of the MSD curve and the uncertainty.

When $D_1 = 0$ then the particle would switch between a bound state and an unbound state. Binding of molecules inside the nucleus has been studied for decades and we refer to Mueller and colleagues for a complete study of the different techniques that had been used to measure binding time. From a single molecule tracking point of view, binding time measurement is mostly restricted localization accuracy, and approaching binding time is often achieved by comparing motion to a benchmark of bound references. For instance, Speil and colleagues observed the binding of Stat1 transcription factor inside the nucleus after micro-injection compared with a sliding window the local variance of the detections on a trajectory to the variance Stat1 proteins that were long lasting bound (Speil et al., 2011b). Mazza measured τ_{off} for TMR labeled p53 protein with sliding window MSD compared to a bound reference, H2B protein (Mazza et al., 2012b)

We have seen that most trajectory statistics such as the MSD converges slowly with the trajectory length N. Computing the MSD on a ΔN sliding window drastically reduces its accuracy. Speil et al computed the local variance for $3 \leq \Delta N \leq 7$ and Mazza et al for $\Delta N = 16$. This method is also blind to residency time τ_{off} shorter that the sliding window time $\Delta N \, \Delta t$. found an alternative method to find τ_{off} by varying the time inter-frame Δt and quantifying co-localization of successive detections (Gebhardt et al., 2013)_but this method, and so far to my knowledge no other method, could ever recover an *on rate* $k_{on} = 1 / \tau_{on}$.

Transition between regimes will only be accurately found with not only the MSD but a bunch of alternative statistics such as correlations (Nandi et al., 2012). For example Arcizet and colleagues showed transport of ferromagnetic beads inside amoebas vytoplasm with a sliding window MSD and angles between successive step translocations close to zero active (Arcizet et al., 2008). To quantifying transitions, the most promising methods are, to my opinion, hidden Markov model of regime switching (Das et al., 2009). With such a model, transition probabilities k_{off} and k_{on} are directly inferred with likely likelihood based algorithm.

2.3.5.3 Cumulative distribution of square displacement (cumulative radial analysis)

Most studied single molecule motions are either 2D motion on a surface such as the membrane or the projection in the 2D focal plane of the camera of a 3D motion. This is a restriction, but can be turned into an advantage. In 2D the *cumulative distribution of square displacement* $P(r^2,t)$ as a function of time has simple exponential form (Schütz et al., 1997)

$$P(r^2,t) = \frac{1}{r_0^{\,2}} \exp\left(-\frac{r^2}{r_0^2}\right) \text{ With } r_0^2(t) = 4Dt \qquad (87)$$

Schütz and colleagues used this formula to find out on the mobility of phosphor lipids in membrane was indeed composite, $P(r^2,t)$ being accurately fit by a two exponential variation of the previous formula:

$$p(r^2,t) = 1 - \left[\alpha \exp\left(-\frac{r^2}{r_1^2}\right) + (1-\alpha)\exp\left(-\frac{r^2}{r_2^2}\right)\right] \qquad (88)$$

With α being the relative proportions between the two component of the movement. Axmann et al. found this way the relative proportion between slowly diffusing and fast diffusing MHC proteins in the membrane and the method has been extended to the binding-diffusion mode of motion or two-corral diffusion. (Appelhans et al., 2012) (Vrljic et al., 2002). Wieser et al. highlight the limitations of the method. To faithfully show that the motion is composite, it is mandatory to perform a Kolomogorov Smirnov test to asses non Gaussiannity and to carefully exclude localization accuracy biases (Wieser et al., 2008). To my opinion, the method is limited since we do not clearly see what is averaged. The number of square displacement for different time lags depends on the trajectory length and the relative proportions α will be biased toward long trajectories for increasing time lag. The cumulative distribution of square displacement is therefore non robust for a heterogeneous set of trajectories of various length or transition between regimes that do not have the same characteristic time.

2.3.5.4 Spatial heterogeneity- mapping

A possible explanation for the composite nature of a particle movement can be the heterogeneity of the medium where it diffuses. As a function of its position, a particle will diffuse with different speed. The problem is to define its position, which is not straightforward since the

particle moves. One solution is to diplay the traces as a function of their diffusion coefficient with a color code(Manley et al., 2008) (Benke et al., 2012). Because of a finite observation time imposed by photo-toxicity and to the necessity to be on diluted regimes to accurately track particles, inner cell SPT mapping is mostly sparse. Even if with a high concentration of trajectory, interpretation of diffusion maps can be done only after heavy image processing such as surface rendering (English et al., 2011). On dendrites however, from diffusion maps Hoze et al. found that AMPA receptors can either be pushed in or out dendritic spines (Hoze et al., 2012).

2.3.6 Conclusion on statistics

Single live cell microscopy has recently exploded and so did the possible applications of the technique. Scientists have produced terabytes of trajectories of diffusing molecules in search of their partners in the nucleus of the cell. The statistical interpretation of those trajectories, however, is still an emerging field. Even the most popular statistic that can be computed, the Mean Square Displacement (MSD) is not fully characterized under the most simple model assumption. The main reason is that experimental bias that is specific to single cell microscopy, such localization or tracking error, has still not been properly characterized. Once this achieved, the field could be open to the advances of time-statistics such as stochastic calculus and time series analysis. Pioneer studies have already been published using Markov process and message passing model (Chertkov et al., 2010) or hidden markov model of regime switching (Das et al., 2009). Biologists would argue that more complex models would reduce the reliability of the interpretation of the data. This is true, but sticking to one simple model and doing an impossible fit on it is also a way to misinterpret results. Considering free diffusion for instance, heteroscedastic models such as GARCH and ARCH (Gourieroux, 1992) could be faithfully reproduce the heterogeneity of the medium even if not related to a physical quantity. The next move would be an improvement in particles counting. Dyes can or bleach and the particle putting a final stop to its detection. But dyes can blink. In such conditions multiple trajectories will be recorded and counting is biased. Even with long lasting emitting dyes, trajectories do not have the same time lengths and we have seen that single particle statistics are highly sensitive to the time length. Implication of blinking on statistic robustness is not fully understood.

This censorship bias is all the more limiting in 3D. As we have seen on the first section, 3D live cell imaging has only been achieved a couple of years ago. Most of nuclear motions that was recorded with SPT is the projection on the focal plane of the camera but particle would move in and out of focus. Holzer and colleagues used bright dyes such as quantum dot to limit de-focusing (Holtzer et al., 2007). Bright dyes such as Q dots or organic dyes cannot be expressed by the cell and needs to either micro injected (Grünwald et al., 2008) (Speil et al., 2011b) (Bancaud et al., 2009) or in vivo cross linked to the protein of interest (Mazza et al., 2012a). But even with bright dyes, the particles that move in or out of focus biases the counting scheme based upon 2D statistic. On my thesis I proposed an empirical method to compensate this bias but numerous efforts need to be done to overcome the limitation.

3 Results

3.1 I-SPT PALM

Distinct target search modes of c-Myc and P-TEFb revealed by single molecule tracking in live cells

With Ignacio Izeddin, Lana Bosanac, Ibrahim I. Cissé, Lydia Boudarene, Florence Proux, Claire Dugast-Darzacq, Olivier Bénichou, Raphaël Voituriez, Olivier Bensaude, Maxime Dahan, and Xavier Darzacq

3.1.1 Summary

In the following, we investigated the motion of four proteins with a new technique called I-SPT PALM (Intra-nuclear Single Particle Tracking Photo-Activation Light Microscopy) that enables the recording of protein motion inside the nucleus. The proteins investigated are:

- **Dendra 2** is a free fluorophore that is not supposed to have known partners inside the nucleus.
- **H2b** is an histone protein. It strongly binds to DNA to form the fundamental unit of chromatin, the nucleosome.
- **C-Myc** is a proto- oncogene specific transcription factor. It is implicated in the regulation of 15% of the gene ((Lüscher, 2001)) and is supposed to have many chemical partners inside the cell
- **P-TEFb** is a general transcription factor that phoshorilates the serin 2 of polymerase II CTD to trigger elongation. P-TEFb is an hetero-dimer that consists of two proteins, Cyclin T1 (CycT1) that was tagged with dendra 2 and CdK9. It co-exists in two forms inside the nucleus: the plain hetero-dimer and a bigger complex together with protein Hexim and a small RNA, the snRNP 7SK

We investigated the motion of those four proteins in the nucleus of U2OS osteo sarchoma cell line.

Method

Microscopy

I-SPT PALM is a versatile technique based on stochastic photo-activation of the tag with very low power of activation UV lASER. It extended the SPT-PALM technique to intra nuclear studies (Introduction 2.2.2). We set the activation LASER power low enough so that only a few, maybe only one protein emits light in the red domain where we image the cell. Tuning the LASER power to a suitable regime where the number of emitter is low enough so that we can accurately detect their position but still get robust statistics is the challenge of this technique.

Statistics

For I-SPT PALM, we computed the time and ensemble averaged MSD (82) and the cumulative squared displacement histogram (87). We showed that indeed, even for the free fluorophore dendra 2 the motion was heterogeneous (paragraph 2.3.5), different copies of the same protein undergoing diffusion with a broad range of different diffusion coefficients. This interesting result creates a challenge for exact quantification of the movement. For I-SPT is a selection bias of the recorded trajectories towards slow moving proteins. The slower proteins move, the longer they stay in the focal plane of the camera. We solved the problem by quantifying this selection bias via simulation and by looking at statistics that are less dependent on the averaged displacement size such as correlations and angles (61)(63).

Results

Below is a summary of the results for each of the proteins. One of the main result is that the type of exploration of the nucleus is protein dependent.

- **Dendra 2 :** The motion is heterogeneous but free in the time and length range of I-SPT PALM
- **H2b:** H2b is, for a large part bound to chromatin. However a fraction of H2B is not integrated inside the nucleosome and diffuses freely.

- **C-Myc** movement is characterized by a big heterogeneity that reflect its numerous possible chemical partners. Each of the component of the movement diffuses freely but with different diffusion of motions
- **P-TEFb** movement is also heterogeneous but with state changes in the time range of I-SPT PALM. From the shape of the MSD, of the cumulative square displacements and of the histogram of angles, we got evidence of an anomalous motion of P-TEFb (Introduction 2.1.1.3) .

Discussion

With the anomalous coefficient of P-TEFb MSD (Introduction 2.3.3.1), we found that the exploration of P-TEFb is compact (Introduction 2.1.2.3.1) compared to the Brownian but heterogeneous nature of C-Myc (Introduction 2.1.1.2). We then fully discuss the implication in terms of mean first passage time (Introduction 2.1.2.3.2).

3.1.2 Abstract

Gene regulation relies on transcription factors (TFs) exploring the nucleus in search of their targets. So far, most studies have focused on how fast TFs diffuse and underestimated the role of nuclear architecture. Here, we implemented a single-molecule tracking assay to determine the TFs dynamics using photoactivatable tags in human cells. We found that c-Myc is a global explorer diffusing in the nucleus without spatial constraints. In contrast, the positive transcription elongation factor P-TEFb is a local explorer that oversamples its environment, constrained by a fractal nuclear architecture. Consequently, each c-Myc molecule is equally available for all nuclear sites while P-TEFb reaches its targets in a position-dependent manner. Our observations are consistent with a model in which the exploration geometry of TFs is constrained by their interactions with nuclear structures and not by exclusion properties. The geometry-controlled kinetics of TFs target search link nuclear architecture and gene regulation, which might have major roles in transcription.

3.1.3 Introduction

The nucleus is a complex environment where biochemical reactions are spatially organized in an interaction network devoted to transcription, replication or repair of the genome (Misteli, 2001). Molecular interactions relevant to gene regulation involve transcription factors (TFs) that bind to specific DNA regulatory sequences or other components of the transcriptional machinery. In order to find their targets, TFs diffuse within the seemingly non-compartmentalized yet highly organized nuclear volume. Since the kinetics of a reaction can be largely determined by the mobility characteristics of the reactants (Rice, 1985; Shlesinger and Zaslavsky, 1993; Misteli, 2001), the target search strategy of TFs is a key element to understanding the dynamics of transcriptional activity and regulation.

Over the past decade, the nuclear dynamics of TFs has become an important topic of research and has been investigated with a variety of imaging and biochemical approaches. Overall, these studies have emphasized the high mobility of nuclear factors, which results from a combination of diffusive motion and transient specific and non-specific interactions with chromatin (Misteli, 2001; Darzacq et al., 2009; Mueller et al., 2010; Normanno et al., 2012). These transient interactions are essential to ensure a fine regulation of binding site occupancy—by competition or by altering the TF concentration—but must also be persistent enough to enable the assembly of multicomponent complexes (Dundr, 2002; Darzacq and Singer, 2008; Gorski et al., 2008). In parallel to the experimental evidence of the fast diffusive motion of nuclear factors, our understanding of the intranuclear space has evolved from a homogeneous environment to an organelle where spatial arrangement among genes and regulatory sequences play an important role in transcriptional control (Heard and Bickmore, 2007).

Here, we aim to investigate the principles governing nuclear exploration of different factors involved in transcriptional control. To this end, we used single-molecule (SM) imaging to address the relationship between the nuclear geometry and the search dynamics of two nuclear factors having distinct functional roles: the proto-oncogene c-Myc and the positive transcription elongation factor P-TEFb. c-Myc is a basic helix-loop-helix DNA-binding transcription factor that binds to E-Boxes; 18 000 E-boxes are found in the genome and c-Myc affects the transcription of numerous genes (Gallant and Steiger, 2009; Nie et al., 2012). P-TEFb is composed of the CDK9 kinase and a Cyclin T. It phosphorylates the elongation control factors

SPT5 and NELF to allow productive elongation of class II gene transcription (Wada et al., 1998). The C-terminal domain (CTD) of the catalytic subunit RPB1 of Polymerase II is also a major target (Zhou et al., 2012) of P-TEFb. c-Myc and P-TEFb are therefore two good examples of transcriptional regulators binding numerous sites in the nucleus; the latter binds to the transcription machinery itself and the former directly to DNA.

Single particle tracking constitutes a powerful method to probe the mobility of molecules in living cells (Lord et al., 2010). In the nucleus, SPT has been first employed to investigate the dynamics of mRNAs (Fusco et al., 2003; Shav-Tal et al., 2004) or for rheological measurements of the nucleoplasm using inert probes (Bancaud et al., 2009). Studies of individual nuclear proteins were initially based on the microinjection of dye-labeled molecules (Grünwald et al., 2008; Speil et al., 2011) but this approach cannot be generalized to multi-component complexes that are not amenable to in vitro manipulation. Recently, the tracking of single nuclear factors has been facilitated by the advent of efficient in situ tagging methods such as Halo tags (Mazza et al., 2012). Nonetheless, these experiments relied on the labeling and detection of a small sub-fraction of the molecules that decayed upon photobleaching. An alternative approach for the tracking of proteins in cells takes advantage of photoconvertible tags (Lippincott-Schwartz and Patterson, 2009) and photoactivated localization microscopy (PALM) (Betzig et al., 2006; Hess et al., 2006). In live cells, PALM has been used to achieve high-density diffusion maps of membrane proteins (Manley et al., 2008). An advantage of using PALM is that the number of SM trajectories is not limited by photobleaching and is tuned by photoactivation. However, single particle tracking PALM (sptPALM) experiments have so far remained limited to proteins with slow mobility (Misteli, 2001; Manley et al., 2008; Darzacq et al., 2009; Mueller et al., 2010; Normanno et al., 2012) or those that undergo restricted motions (Dundr, 2002; Darzacq and Singer, 2008; Gorski et al., 2008; English et al., 2010; Frost et al., 2010; English et al., 2011).

In this study, we developed a new sptPALM procedure adapted for the recording of individual proteins rapidly diffusing in the nucleus of mammalian cells. We used the photoconvertible fluorophore Dendra2 (Gurskaya et al., 2006; Heard and Bickmore, 2007) and took advantage of tilted illumination (Tokunaga et al., 2008; Gallant and Steiger, 2009; Nie et al., 2012). A careful control of the photoconversion rate minimized the background signal due to out-of-focus activated molecules and we could thus follow the motion of individual proteins freely diffusing

within the nuclear volume. With this sptPALM technique, we recorded large datasets (on the order of 104 single translocations in a single imaging session), which was essential for a proper statistical analysis of the search dynamics.

We applied our technique to several nuclear proteins and found that diffusing factors do not sense a unique nucleoplasmic architecture: c-Myc and P-TEFb adopt different nuclear space exploration strategies which drastically change the way they reach their specific targets. The differences observed between the two factors were not due to their diffusive kinetic parameters but to the geometry of their exploration path. c-Myc and our control protein, “free” Dendra2, showed unrestricted diffusion in a 3-dimensional nuclear space. In contrast, P-TEFb explored the nuclear volume by sampling a space of reduced dimensionality, i.e. smaller than 3, displaying characteristics of exploration constrained in fractal structures. The role of the space-sampling mode in the search strategy has long been discussed from a theoretical point of view (de Gennes, 1982; Wada et al., 1998). Our experimental results support the notion that it could indeed be a key parameter for diffusion-limited chemical reactions in the closed environment of the nucleus (Bénichou et al., 2010; Zhou et al., 2012). We discuss the implications of our observations in terms of gene expression control and its relation to the spatial organization of genes within the nucleus.

3.1.4 Results

3.1.4.1 Intracellular single-molecule tracking with photoconvertible fluorescent proteins

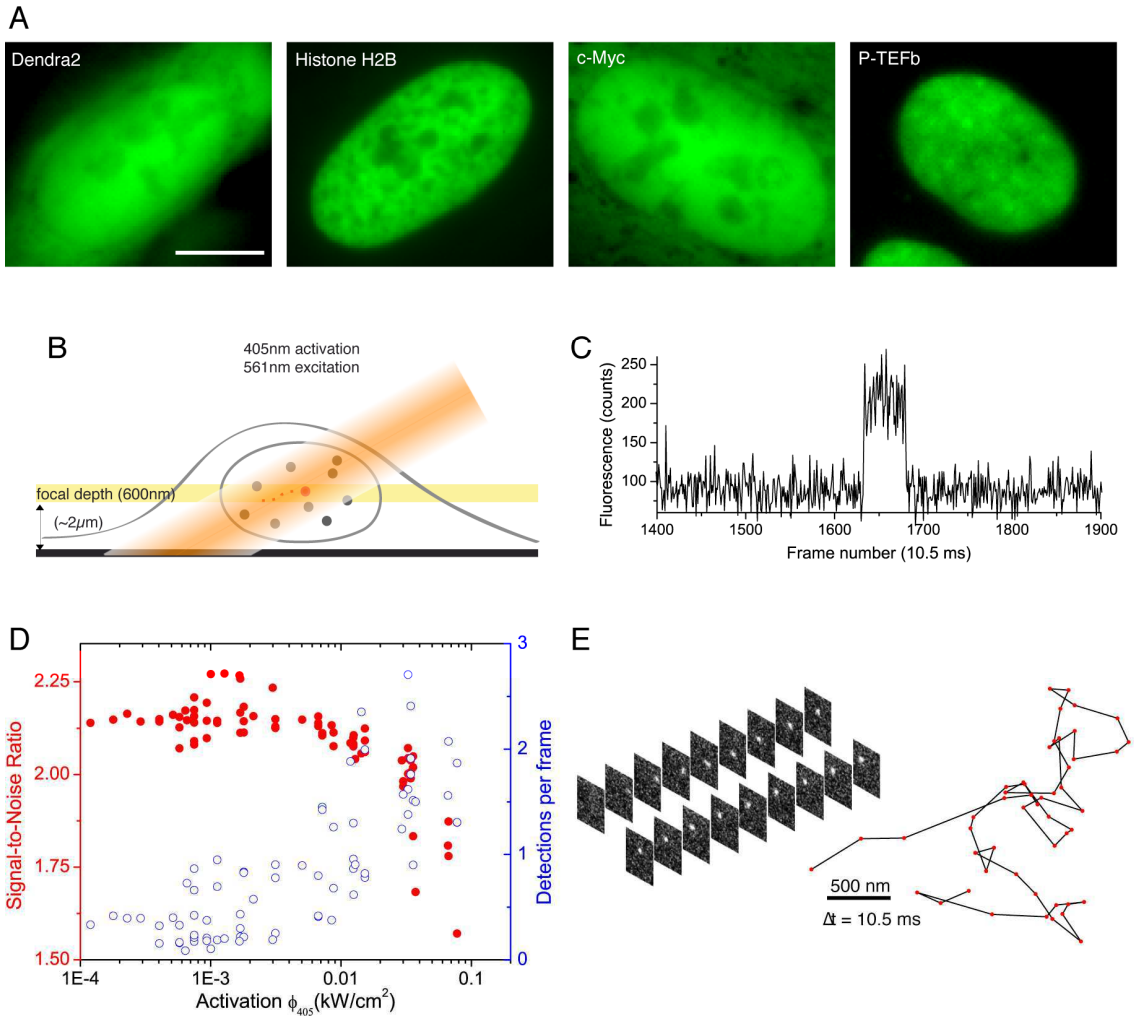

Figure 17: From bulk to single molecule fluorescence imaging *(A) Images of the 525 nm bulk emission of the pre-converted form of Dendra2 in the cellular nucleus for the "free" fluorophore Dendra2 and Dendra2 fused to H2B, c-Myc, and P-TEFb. (B) Schematics of the intracellular sptPALM; wide-field illumination is necessary in order to reach the nucleus of mammalian cells. A signature of single molecule detection is the on/off single-step fluorescence shown in panel (C). To achieve single molecule detection, 405 nm laser photoactivation needs to be reduced to a level where no background noise is produced by out-of-focus fluorophores. Graphic in panel (D) shows the number of detected single molecules (blue data, right axis) and the mean SNR of the single molecule signal (red data, left axis) as a function of 405 nm photoactivation photon flux per pulse (10 ms pulses every 1 s). The signal-to-noise ratio (SNR) of the molecules within the image depth of focus indeed increases as the total number of detected particles decreases. In*

panel (E), the trace of a single Dendra2 molecule freely diffusing in the nucleus of a living cell is depicted, imaged at a rate of 95 Hz (10 ms acquisition time and 0.5 ms interval between frames).

We developed a simple and versatile approach based on photoconvertible protein tags that extends the use of sptPALM to any protein expressed in mammalian cells. To probe the dynamics of transcription factors within the nucleoplasm, proteins of interest were fused to the photoconvertible protein Dendra2(Gurskaya et al., 2006; Lord et al., 2010) (Figure 17 A). As in standard PALM, the imaging set-up used a wide-field activation and excitation scheme, allowing fast and sensitive acquisition with an EMCCD camera (see Supplementary Informationand). The light emitted by activated molecules outside the focal depth contributed to background noise (Figure 17 B). At standard PALM activation intensity (~ 0.1-1 kW/cm^2 at 405 nm), this background prevented the detection of individual molecules. However, by lowering the activation intensity, one could reach the regime of SM detection, characterized by single-step activation and photobleaching (Figure 17 C). The decreasing density of detected particles was correlated with an increasing average signal-to-noise ratio (SNR) (Figure 17 D). We found that an activation intensity around 0.01 kW/cm^2 offered the best trade-off between the number of detected particles (~1) and SNR. When further lowering the intensity, the number of detected particles reached a plateau due to spontaneous activation of photoconvertible Dendra2.

Compared to membrane proteins or other proteins with constrained mobility, diffusion dynamics of intracellular molecules is much higher and can exceed 10 μm^2/s. Images recorded for such fast moving objects depart from the well-defined point spread function (PSF) of the microscope and exhibit a motion blur that cannot be characterized with standard Gaussian localization algorithms (Thompson et al., 2002; Fusco et al., 2003; Shav-Tal et al., 2004). Therefore, we developed new localization and tracking algorithms (see Supplemental Procedures and Figure S 2 Figure S 1) and validated them with simulations (Supplementary Information). We could thus obtain single trajectories formed by individual translocations recorded every 10 ms. 50 % of the traces were reconstructed with more than 4 time points, and some of them were as long as 60 consecutive translocations. The step size of single translocations ranged between tens of nanometers (limited by our localization accuracy of ~ 70 nm) and ~ 2 μm (Figure 17). Hence, it became possible to track molecules with diffusion coefficients exceeding 10 μm^2/s.

3.1.4.2 System validation using "free" Dendra2 and histone H2B fused to Dendra2

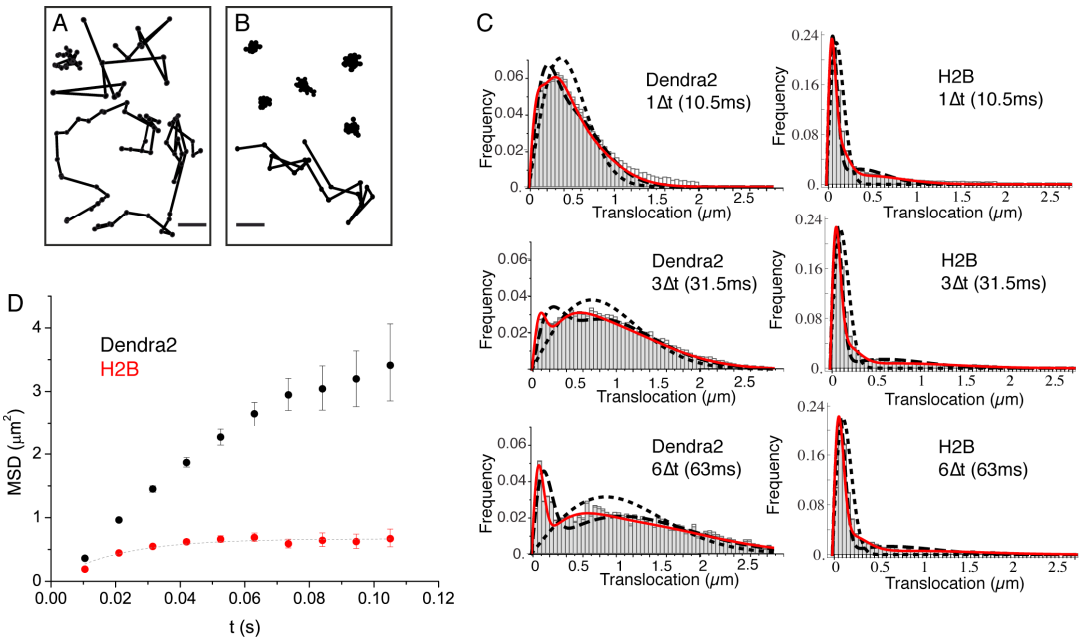

Figure 18: Diffusion properties of "free" Dendra2 and H2B *Examples of single molecule traces of the free fluorophore Dendra2 (A) and DNA-associated histone H2B (B). Recorded traces gave us access to the translocation histograms, plotted for 1Δt (10 ms), 3Δt, and 6Δt for both proteins in panel (C). Fits of the step size distribution with one Brownian diffusive population (dotted line), two populations (dashed lines), and three diffusive populations (red solid line) are represented in the graphs. Also, the averaged mean square displacement (MSD) as a function of time is represented in (D) for both proteins with interval of confidence of 95%.*

We first investigated two limit cases relevant to protein dynamics in the nucleoplasm: Dendra2 and DNA-associated histone H2B. Dendra2 is the fluorescent label that we fused to all other proteins used in our analysis. Intrinsic blinking of Dendra2 is seven times smaller than that of other photoconvertible fluorescent proteins like mEos2 (Bancaud et al., 2009; Lee et al., 2012), which makes it a suitable tag for SPT. Green fluorescent protein (GFP) has no detectable interacting partners in mammalian cells (Grünwald et al., 2008; Trinkle-Mulcahy et al., 2008; Speil et al., 2011) and we therefore considered "free" Dendra2 as a model for freely diffusing particles due to its structural similarity with GFP. In contrast, Dendra2 fused to histone H2B (Dendra2-H2B) was expected to insert into chromatin and thus to display restricted motion.

Indeed, from a visual inspection, “free” Dendra2 and Dendra2-H2B trajectories (Figure 18 A and Figure 18 B respectively) exhibited obvious differences. As expected for free versus chromatin-bound particles, the translocation length of most “free” Dendra2 particles exceeded 0.5 μm within 60 ms whereas most of Dendra2-H2B molecules traveled less than 0.2 μm in 60 ms (Figure 18).

Notably, translocation histograms for “free” Dendra2 and, to a lesser extent, for Dendra2-H2B were not consistent with a single diffusing species (Figure 18, Supplementary Information), thus suggesting that displacements of these molecules were more complex than anticipated. Three distinct populations were needed to fit the translocation histograms corresponding to different time intervals. For “free” Dendra2, one population (~ 4% of all the molecules) corresponded to proteins with translocations within the experimental localization accuracy (~ 70 nm) and were therefore considered as immobile particles (Figure S 1). The other two populations could be distinguished by their diffusion coefficients: 24% moved with a slow diffusion coefficient (D2 = 2.6 μm2/s) and 72% moved faster (D3 = 13 μm2/s). For Dendra2-H2B, 35% of molecules appeared immobile and might correspond to molecules engaged in chromatin-bound nucleosomes. Two populations of mobile Dendra2-H2B molecules (D2 = 0.5 μm2/s, 25%, and D3 = 13 μm2/s, 40%) were also observed, probably corresponding to Dendra2-H2B inserted into “free” nucleosomes and “free” Dendra2-H2B. Histone H2B binding kinetics to chromatin have recently been investigated by SPT (Mazza et al., 2012; 2012), however, fast diffusing histones have not been detected in that assay. This is likely due to the fact that the authors used a Gaussian fit detection algorithm, which mainly account for molecules remaining localized within a region of the size of the PSF during the acquisition window (immobile and slow diffusing populations).

To complement our analysis of the translocation histograms, we plotted the mean square displacement (MSD) of the molecules as a function of time. We computed the time-averaged MSD of every SM trace, and averaged it over the ensemble of traces (see Supplementary Information II). The MSD of “free” Dendra2 increased regularly with time. However, it slightly deviated from the linear behavior expected for molecules undergoing normal diffusion. This was attributed to a ‘population exclusion effect’ due to the different defocusing rates of the various diffusive subpopulations of Dendra2. Indeed, because of their three-dimensional motion in the

nucleus, slow moving particles remained within the focal depth of observation (~ 0.5 □m) for a longer time than fast moving ones. As a result, fast diffusing molecules contributed comparatively less than the slow ones to the MSD at longer time lags. Note that this effect is inevitable for any single-molecule experiment involving more than one diffusive population and in which the three-dimensional movement of particles is recorded in two dimensions (see Supplementary Information and *Figure S* 3). For Dendra-H2B, the MSD reached a plateau after ~ 20 ms at ~ 0.5 µm2 (Fig. 2D), consistent with a confined motion of individual histone molecules inserted into chromatin.

Numerical simulations were used to carefully define the range of application of our method (Supplementary Information). On the one hand, the particle localization precision sets the lower bound to a reliable estimation of the diffusion parameters, i.e. ~ 0.01 µm2/s for a pointing accuracy of ~ 70 nm. On the other hand, fast moving particles can be tracked with a mobility up to ~ 20 µm2/s, beyond the experimental values determined for "free" Dendra2. Altogether, our experimental and numerical results provide a benchmark for studying nuclear factors with a mobility ranging between that of chromatin-bound H2B molecules and of "free" proteins such as Dendra2.

3.1.4.3 c-Myc and P-TEFb differ in the nature of their diffusion

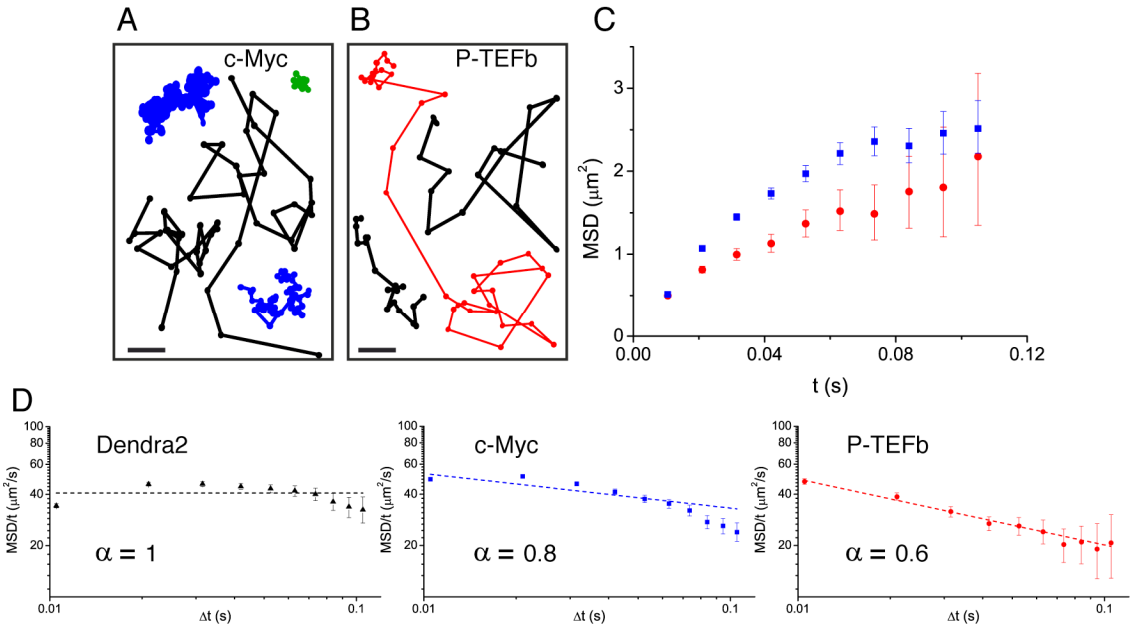

Figure 19: Diffusion properties of c-Myc and P-TEFb *For c-Myc (A) and P-TEFb (B), examples of single molecule traces. From these, we plotted the averaged mean square displacement (MSD) as a function of the lag time with intervals of confidence of 95% (panel C). In panel D, the MSD over time was represented as a function of time in logarithmic scale for "free" Dendra2, c-Myc and P-TEFb. The fit in the inset follows the time rescaling law MSD(t)= D tα, where α = 1 for normal diffusion, and 0 < α < 1 for subdiffusive behavior.*

We next probed the mobility of transcription factors. Dendra2 was fused to the proto-oncogene c-Myc or to the Cyclin T1 subunit of P-TEFb. Translocation histograms for c-Myc were well-fit with 3 diffusive populations (Figure S *4*). The most abundant corresponded to rapidly diffusing particles (13.5 μm2/s, 70% of the molecules) (Figure 19, black trajectories). In addition, a significant fraction of c-Myc was immobile (9.5 %) (, green trajectory) or displayed slow Brownian diffusion (D2 = 0.5 μm2/s, 20.5%) (Figure 19A, blue trajectories). For P-TEFb, the typical translocation length and the translocation histograms were comparable to those obtained for c-Myc (Figure S *6*). Yet, we noted that individual trajectories of P-TEFb molecules often showed abrupt transitions from slow to fast displacement modes within the same trajectory (see example in red in Figure 19B). Such transitions were never observed for "free" Dendra2 or c-Myc and suggested a transport process more complex than heterogenous Brownian diffusion.

When plotting the MSD as a function of time for c-Myc and P-TEFb, we observed a deviation from linearity for both factors (Figure S *5*). Such deviation could be due to the 'population exclusion effect' described above (Figure 18 and Supplementary Information *Figure S 8*), but, alternatively, it could also be the signature of an anomalous diffusion process. Indeed, when a particle undergoes anomalous diffusion, the MSD versus time scales as a power-law t^{α} , where $\alpha < 1$ is characteristic of a subdiffusion process (Saxton, 2007; Lippincott-Schwartz and Patterson, 2009). However, neither the "free" Dendra2 nor the c-Myc MSD data could be properly fit by such a law (Figure 19D). Similarly to "free" Dendra2, c-Myc molecules were distributed between populations of very distinct diffusion coefficients. In contrast, for P-TEFb, the MSD variations were remarkably fit by a t^{α} power law with the anomalous coefficient $\alpha = 0.6$ (Fig. 3D). The subdiffusion of P-TEFb was also apparent when we plotted the cumulative histograms of the square displacement for multiples of the time interval (Δt) between two frames and rescaled them by the factor t^{α}, with α determined from the fit in Fig. 3C. All the rescaled

histograms curves collapsed for P-TEFb but not for c-Myc or "free" Dendra2 (Figure S *6*). We therefore concluded that the characteristics of single P-TEFb trajectories are consistent with an anomalous diffusive behavior whereas the deviation from linearity of the c-Myc MSD curve reflects the heterogeneity of its diffusion dynamics.

3.1.4.4 Asymmetric distribution of angles between consecutive translocations

Subdiffusion in cells is commonly attributed to one of the following two microscopic processes: a broad distribution of trapping times or an obstructed movement resulting from a reduction of the accessible space (Betzig et al., 2006; Hess et al., 2006; Condamin et al., 2008) (for a discussion about subdiffusion causes, see Supplementary Information). In other words, the subdiffusive behavior, evidenced by the sublinear MSD, is due to either temporal or spatial restrictions. In order to probe the spatial characteristics of the exploration independently of temporal considerations, we analyzed the distribution of angles Θ between two consecutive translocations, an observable that is predominantly sensitive to the geometry of the exploration space (Liao et al., 2012).

For "free" Dendra2 and c-Myc, the angular distribution was uniform (Figure 20 A), as expected for Brownian diffusion. In a three-dimensional space, there is no privileged direction and all angles Θ are equiprobable. In contrast, the angular distribution for P-TEFb was significantly biased toward 180°, reflecting an increased probability of the molecule to return backwards. Such anisotropic angular distribution is consistent with diffusion in a space of reduced dimensionality such as a fractal network (ben-Avraham and Havlin, 2005). A particle that diffuses in such a structure encounters dead ends, in which case it cannot but return back to previously visited locations (Θ = 180º). Noteworthy, the diffusing subpopulation of H2B molecules also showed a non-uniform angular distribution, indicating that they also move in a space with reduced dimensionality, as opposed to "free" Dendra2 or c-Myc.

3.1.4.5 Evolution of angular distribution with time sampling

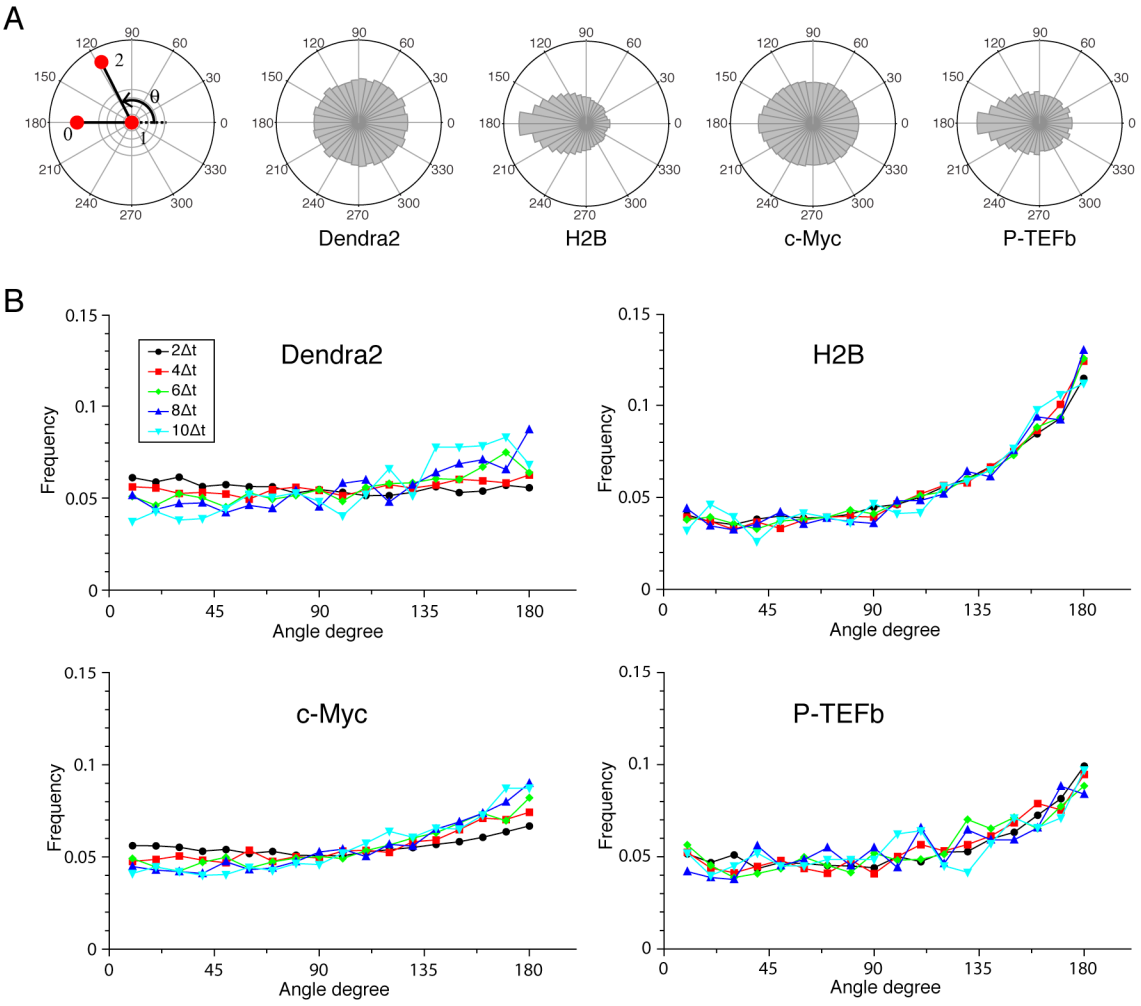

Figure 20: Angle distribution between consecutive steps *(A) Distribution histogram, in polar coordinates, of the angle θ formed between the vectors of two consecutive translocation steps (vectors formed by positions at time 0 and 10 ms, and between 10 ms and 20 ms), for Dendra2, H2B, c-Myc, and P-TEFb. In (B), temporal evolution of the angle distribution at increasing lag times: angle between the vectors formed by the positions at 0 to 10 ms and 10 ms to 20 ms, 2Δt in black; angle between the vectors formed at positions 0 to 20 ms and 20 ms to 40 ms, 4Δt in red; between 0 to 30 ms and 30 ms to 60 ms, 6Δt in green; 8Δt (blue); and 10Δt (cyan).*

A defining property of fractal structures is their scale invariance, namely the repetition of structural motifs at different length scales. For a particle diffusing in such a fractal structure, we expected the scale invariance to be apparent in the characteristics of the movement of the particle. We therefore examined the temporal evolution of the angular distribution in order to further investigate the underlying geometry of the space available for exploration (Figure 20B).

The angle distribution for “free” Dendra2 remained isotropic up to 60 ms (the angle between the two vectors formed by the particle positions at times 0 and 30 ms, and between 30 ms and 60 ms, i.e., total time of 60 ms). Beyond this time point, asymmetric features appeared in the histogram, with slightly higher distribution frequency between 90° and 270°. This is consistent with a significant probability to encounter the nuclear boundary after 60 ms of exploration. Similarly, the angular distributions for c-Myc varied over time and the frequency of angles between 90° and 180° increased for longer temporal increments in a slightly more pronounced manner, potentially reflecting its confinement to domains significantly smaller than the nucleus.

The temporal evolution of the angular distributions for H2B and P-TEFb differed qualitatively from those of “free” Dendra2 and c-Myc. The angle distribution asymmetry for H2B and P-TEFb, already pronounced at the minimum time interval ($2\Delta t$, 20 ms), remained remarkably stable with larger time increments (Figure 20B). Furthermore, for all proteins, the angular distributions and their evolution in time were unaltered upon removal of the translocation steps within our localization accuracy (Figure S *7*). This rules out a potential implication of the pointing accuracy on the asymmetry of the angular distribution.

3.1.4.6 Numerical simulations of particle diffusion in networks with different dimensionalities

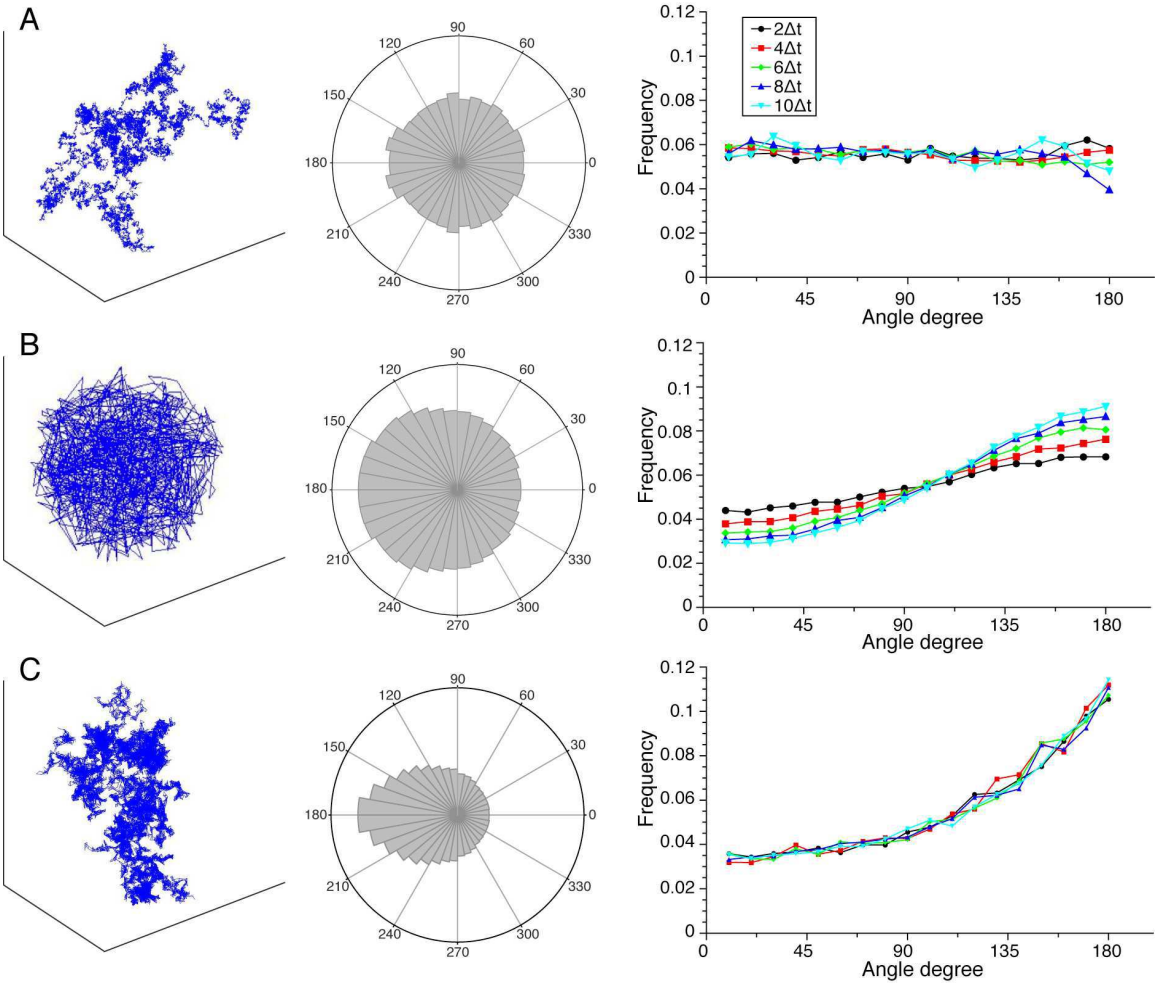

Figure 21: Simulated trajectories and angle distribution *Simulated trajectories of random walks in: (A) infinite Euclidean cubic lattice, (B) 3D fractal critical percolation cluster, and (C) confined Euclidean cubic lattice. From each simulation, we analyzed the angle distribution of consecutive steps (A2, B2, and C2, in polar coordinates) and the time evolution of the angle distribution, with increasing lag time (A3, B3, and C3).*

In order to gain insight about the different scenarios giving rise to the observed angular distributions, we performed numerical simulations of random walks in media with varying dimensionalities (see Supplementary Information III for details about the numerical simulations). First, we simulated molecules undergoing Brownian motion in an infinite cubic lattice (Figure 21A). Predictably, the distribution of angles θ was isotropic at all time scales. Next, we

investigated the movement of molecules with 3D Brownian diffusion in a closed volume Figure 21B), a more realistic scenario than that of an infinite lattice. In this case, the angular distribution revealed a larger occurrence of angles comprised between 90° and 180°, and the anisotropy of the distribution increased over time. The increasing anisotropy of the angle distribution at larger time scales results from the reflecting boundary conditions imposed on the limits of the sphere. Finally, we considered the diffusion of molecules in a fractal structure such as the 3D critical percolation cluster (ben-Avraham and Havlin, 2005) (Figure 21 C). Here, the angular distribution revealed a distinct tendency toward 180° degrees, with the same shape as that observed for P-TEFb and H2B. Importantly, the anisotropy found in the simulations on the percolation cluster was invariant with time, illustrating the scale-invariant features of fractal structures.

3.1.4.7 Compact vs. non-compact space exploration

The choice of a fractal network as an underlying structure on which to simulate the diffusion of nuclear factors was motivated by recent works on the geometry of the nuclear space (Bancaud et al., 2012). Evidence coming from neutron scattering, optical imaging, chromatin capture and rheology suggest that the organization of chromatin and of the nucleoplasm is compatible with a fractal architecture (at least on a length scale comprised between ~10 nm and a few microns) (SACHS et al., 1995; Yokota et al., 1995; Lebedev et al., 2005; Bancaud et al., 2009; Lieberman-Aiden et al., 2009). The fractal architecture is characterized by its dimension Df, a number between 0 and 3, which expresses the reduction of the dimensionality or equivalently, the lacunarity of the accessible space compared to an ordinary 3D medium (for which Df = 3).

The fractal geometry of the nucleoplasm has particularly important implications for the search kinetics of TFs and thereby, their interactions with molecular partners. This can be easily understood by means of scaling arguments. If one considers a region of dimension R, the number Na of sites accessible to the explorer scales as R^{D_f}. To evaluate the efficiency of the search process, Na needs to be compared to the number Nv of sites, not necessarily distinct, visited by the diffusing factor before it escapes the region R. Nv depends on the dynamic properties of the random walker, parameterized by the dimension of the walk Dw. The dimension of the walk can be defined by the scaling law t^{2/D_w} of the mean square displacement as a function of time (Dw =

2 for a regular Brownian motion, and > 2 for subdiffusion processes). As a result, the escape time and consequently, the number Nv of visited sites, scales as R^{D_w}.

With these expressions of Na and Nv in mind, one perceives why the search strategy is entirely determined by the relative values of the parameters Df and Dw (see references (de Gennes, 1982; ben-Avraham and Havlin, 2005; Condamin et al., 2007) for infinite space and for more detailed discussions). In the case Df > Dw, originally referred to as non-compact exploration by de Gennes (de Gennes, 1982), Na increases more rapidly than Nv, meaning that the searcher explores only a fraction of all the accessible sites and leaves many of them unvisited. The search time does not depend on the relative distance between the initial position and the target (or only at very short distances) but rather on the available diffusion volume. In the opposite case Df < Dw, defined as compact exploration (de Gennes, 1982), the number Nv dominates Na. In this case the search is redundant and individual sites are visited several times. A benefit of this spatial oversampling strategy is that no sites are left unexplored. Yet, it also means that the search time now critically depends on the initial distance to the target (Bénichou et al., 2010). At a microscopic level, the notion of compactness is well established in chemistry to describe dimensional effects on reaction rates (ben-Avraham and Havlin, 2005). However, it has not yet been much considered for biological systems, even though it is presumably of great importance for the description of molecular interactions and the geometrical control of their reaction kinetics (Bénichou et al., 2010).

3.1.4.8 c-Myc and P-TEFb adopt opposed search strategies

We have determined that while c-Myc undergoes normal Brownian diffusion, the dynamics of P-TEFb is well described by a subdiffusive behavior. In the case of P-TEFb, our simulations support the notion that anomalous diffusion is compatible with an obstructed mobility of the proteins, as obtained on a fractal structure (we have ruled out other models of subdiffusion *Figure S 10* and Supplementary Information for a more detailed discussion). As previously described, the exponent $\alpha = 0.6$ of anomalous diffusion obtained for P-TEFb (Figure 19) is a direct measure of the dimension of the walk $Dw = 2/\alpha = 3.3$. Since the fractal dimension Df has an upper limit at Df = 3, we can therefore conclude that Dw > Df, and thus that P-TEFb is engaged in a compact exploration of the nucleoplasm. In contrast, the isotropic sampling of space of c-Myc excludes a compact mode of exploration; it undergoes normal 3D diffusion and

therefore the dimension of the walk is Dw = 2, sampling the nucleoplasm in a non-compact manner. These results imply that different factors sense a protein-dependent nuclear environment, which can be determinant for their exploration strategy.

3.1.4.9 The distance-dependence of the mean first passage time differs between c-Myc and P-TEFb

The distinctive properties of compact and non-compact trajectories have potentially important functional consequences on the ability of searchers to find and react with molecular partners. As noted above, a striking difference is the distance-dependence of the mean first passage time (MFPT) of the searcher to the target site. The MFPT of non-compact explorers is essentially constant, depending solely on the total volume and not on the distance r to the target. Conversely, in the compact case, the MFPT still scales with the volume but also increases with the distance as $r^{(D_w - D_f)}$.

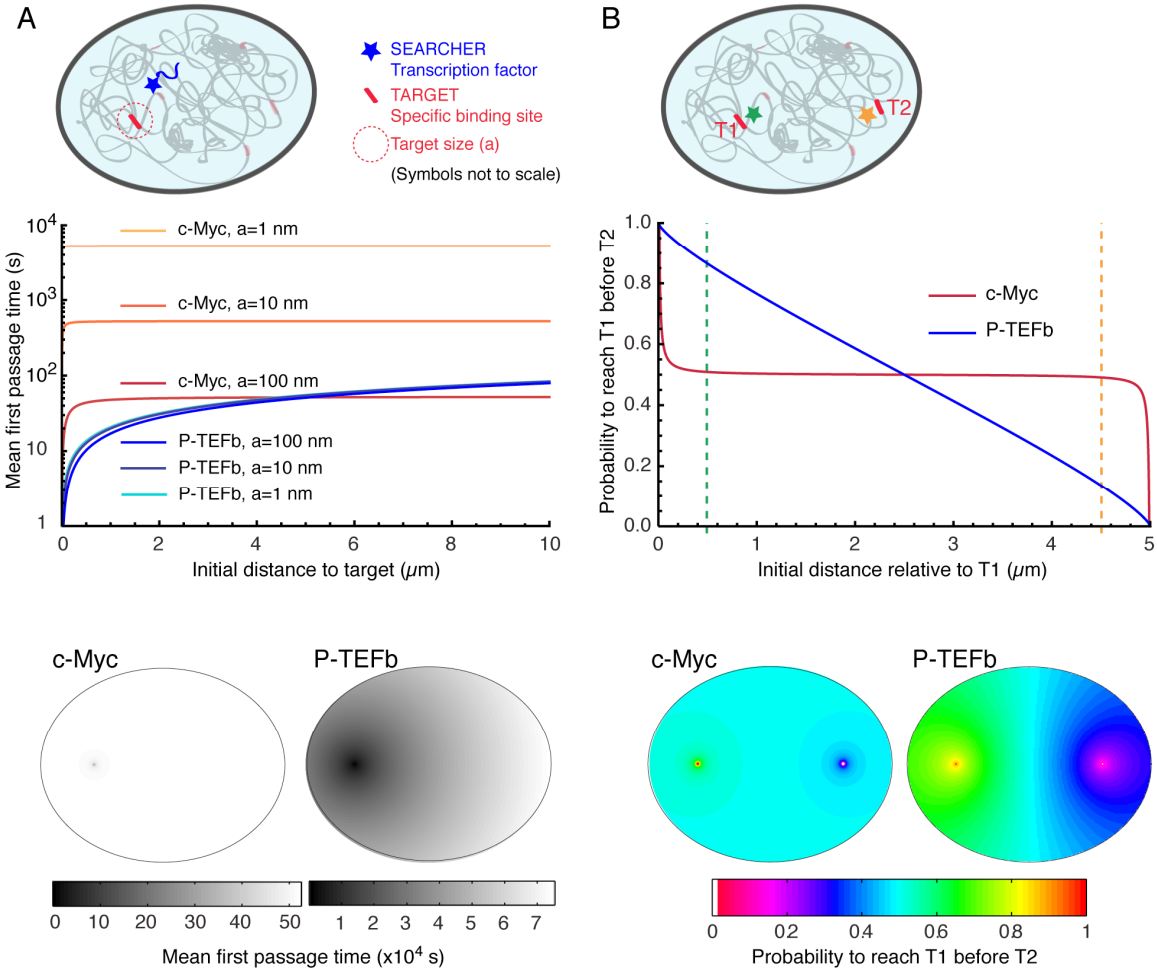

Figure 22: Compact vs. non-compact exploration Entangled polymer interpretation of the anomalous exponent. *(A) Mean first passage time (MFPT) as a function of the initial distance to the target for both c-Myc (non-compact exploration; Df = 3, Dw = 2, and diffusion coefficient D = 9.8 μm2/s) and P-TEFb (compact exploration; Df = 2.6, Dw = 3.3, and scale factor of the MSD fit D = 7.8). The MFPT was calculated for three different target sizes: 1 nm, 10 nm, and 100 nm. Also, two-dimensional representation of the plots for a = 100 nm are depicted in the lower part of the panel. (B) Probability of interaction with target 1 before interacting with target 2, placed at a distance of 20 μm from each other, as a function to the relative distance between the searcher and the targets; two-dimensional plots in the lower side of the panel.*

As an illustration, we computed the MFPT as a function of the distance (see analytical expressions of MFPT in (Condamin et al., 2005; Bénichou et al., 2010)), using the experimental data for c-Myc and P-TEFb, two examples of non-compact and compact explorers. For c-Myc, which behaves as an ordinary Brownian walker, the fractal dimension is D_f = 3, and the dimension of the walk is D_w = 2. We used a diffusion coefficient D = 9.8 $\mu m^2/s$, the value obtained by a weighted average of the diffusion coefficients of the three subpopulations. (It is important to note that the value used for the diffusion coefficient does not affect the dependence of the MFPT on the initial distance to the target.) To calculate the MFPT, we used a nuclear volume of 600 μm^3 and considered a target in its center. For P-TEFb, we did not have direct access to the value of D_f and used several values previously reported (Bancaud et al., 2012). In Figure 22 we used D_f = 2.6 and the results were qualitatively similar for values of D_f = 2.2, and D_f = 3 (see Figure S *9*). For both proteins, we also varied the size *a* of the target between 1 nm (i.e. corresponding to a couple of base pairs), 10 nm (the size of a protein complex) and 100 nm (the size of a large multimolecular complex).

For c-Myc, the MFPT was constant, irrespective of the distance r (Figure 22A). However, it was inversely proportional to the size of the target, similar to what is predicted from the diffusion-limited rate of bimolecular reactions (Nelson et al., 2008). In contrast, the MFPT of P-TEFb increased with the distance *r* but did not depend on the target size. The lack of size dependence can be simply viewed as a consequence of the redundant exploration of compact explorers, and reflects the fact that the limiting step to find a target is the time taken to reach its vicinity. We stress that the differences of MFPT can be very significant. For instance, the time needed to find a 10 nm target located at a distance of 250 nm is 68 times longer for c-Myc compared to P-TEFb

(506.1 s for c-Myc and 7.4 s for P-TEFb). If the target is located at 5 μm of the TFs, the difference in the search time is reduced to a factor of 8 (525.3 s for c-Myc and 64.6 for P-TEFb).

Here we considered that c-Myc has a full access to the nuclear volume. It is interesting to note that if, as suggested by the temporal variance of the angular distribution, c-Myc is confined to a smaller domain, the MFPT would scale linearly with this volume.

We also considered the case of a factor susceptible to bind to two different targets T1 and T2 (Figure 22B). To do so, we computed the splitting probability *P*, that is the probability to reach T1 before T2, as a function of the initial distance to T1. For c-Myc, the probability was equal to 0.5 as soon as the initial distance was larger than a few tens of nanometers, in stark contrast with the case of P-TEFb for which *P* varied almost linearly with the distance.

Overall, our analysis of SM experiments of c-Myc and P-TEFb reveals two characteristics of TFs diffusion relevant to the understanding of transcription regulation kinetics. First, the exploration geometry of the nucleus by TFs is determined by the function and interactions of the nuclear factor. Rather than being subjected to a universal sampling geometry imposed by the nuclear architecture, c-Myc and P-TEFb adopt different modes of exploration leading to normal and anomalous diffusion, respectively. Second, despite apparently similar diffusion coefficients, the different exploration strategies of c-Myc and P-TEFb (non-compact and compact, respectively) can lead to opposite dependence of the search kinetics on the distance to the target and on the target size. The distance-dependence of the MFPT has direct implications on the probability of interaction of c-Myc and the P-TEFb with their respective partners, which in turn may affect transcriptional kinetics and regulation.

3.1.5 Discussion

3.1.5.1 Protein-specific sensing of nuclear organization

With the PALM imaging assay adapted for SM detection of intracellular proteins in eukaryotic cells, we probed the spatial dynamics of different proteins in the nucleus of live human cells: the “free” Dendra2, the histone H2B, the proto-oncogene c-Myc and the elongation factor P-TEFb. The analysis of individual trajectories, supported by numerical simulations of diffusive tracers on free, confined, and fractal structures show that these nuclear proteins fundamentally differ in

their exploration of the nucleoplasm. Our results on “free” Dendra2 are along the lines of those obtained with microinjected fluorescent streptavidin, which explores all nuclear compartments with 3 subpopulations having different diffusion characteristics (0.15, 0.8 and 5 $\mu m^2/s$) (Grünwald et al., 2008). In contrast, FCS experiments using “free” GFP-repeats or SPT tracking of QD aggregates suggested anomalous diffusion (Bancaud et al., 2009).

We determined that “free” Dendra2 and the proto-oncogene c-Myc undergo normal Brownian diffusion in 3D, whereas displacements of P-TEFb and of the mobile subset of histone H2B were accounted for by a subdiffusive movement. This finding was further supported by measurements of the distribution of angles between consecutive translocations. Importantly, this distribution was isotropic for Dendra2 and c-Myc, as expected for a Brownian motion, but showed a pronounced and time- invariant anisotropy for P-TEFb and H2B, consistent with the motion on a fractal structure. Thus, the nuclear geometry, or equivalently, the architecture of the space sampled by diffusing factors, is not unique but constitutes a protein-specific parameter. Furthermore, taking into consideration the diffusion parameters derived from the analysis of the MSD, together with the geometrical aspects of the exploration of c-Myc and P-TEFb, we determined the mode of exploration of these factors to be non-compact and compact, respectively.

We stress that the distinction between compact and non-compact exploration, rather than the one between anomalous and normal diffusion (Saxton, 2007), is the proper criterion to analyze the search dynamics of transcription factors. The notion of compactness is intimately linked to the geometry and the dimensionality of the sampled space. In this regard, there is a specificity of random motions in a three-dimensional medium with respect to the one- and bi-dimensional cases, for which the exploration is always compact since the fractal dimension D_f (less or equal to 1 and 2, respectively) is necessarily smaller than D_w. Only in the case of 3D search, can both compact and non-compact behaviors be observed. Our data demonstrate the relevance of the notion of compactness for the description of nuclear factor dynamics.

3.1.5.2 Possible mechanisms controlling the geometry of nuclear explorations

One microscopic mechanism leading to a compact exploration of the nucleus could be a compartmentalization of the nucleoplasm into interconnected domains forming a fractal labyrinth in which molecules diffuse. In our view, such a model assuming that molecules encounter

physical barriers is poorly compatible with the dynamic nature of nuclear organization and with the lack of correlation between protein size and mobility in the nucleus (Sprague et al., 2004; Mueller et al., 2008; Speil et al., 2011). Moreover, our results showing that Dendra2 and c-Myc are free and unrestricted explorers are not consistent with fixed impermeable frontiers.

Another interpretation is that of a fractal structure restricting the mobility of proteins at its surface. Chromatin has been described as a fractal globule (Grosberg et al., 2007; Lieberman-Aiden et al., 2009) and transient, non-specific interactions to a continuum of binding sites would account for the diffusing factors not escaping from their interaction with chromatin. In this scenario, the number of binding sites with which c-Myc interacts is not sufficient to restrict its motion to chromatin (36 000 E-boxes in a diploid genome, representing less than 50 sites per μm^3). In the same scenario, unassembled histone H2B, with a stronger general affinity to the available DNA, would bind to chromatin in a quasi-continuum manner jumping from site to site.

P-TEFb interacts with the CTD domain of the catalytic subunit of RNA Polymerase II that contains 52 repetitions of a hepta-peptide motif (Taube et al., 2002). RNA Polymerase CTD domain is not folded and can occupy the space very efficiently, potentially forming a mesh offering a nuclear continuum of binding sites for P-TEFb. Such CTD matrix could have an intrinsic existence or be linked to the chromatin globular organization. The existence of a nuclear protein scaffold or matrix has been speculated for more than half a century (Pederson, 2000) and our work offers an indirect observation of a functional role for such a structure. Several studies support this hypothesis, showing that nuclear proteins are in constant interaction with their environment and their motion is governed by specific and non-specific bindings (Misteli, 2001; Phair et al., 2004; Sprague et al., 2004; Hager et al., 2009; Mueller et al., 2010; Speil et al., 2011), therefore opening the door for mechanisms where factors are guided on networks of binding sites (Bénichou et al., 2011).

3.1.5.3 The effect of the exploration strategy on gene regulation by transcription factors

From a general standpoint, the distance-dependence of the search kinetics could have strong implications for gene regulation. Let us consider the case of TFs co-regulating multiple loci; the relative localization of these loci is an important parameter which will play different roles depending on the compact or non-compact exploration of the TFs. Non-compact TFs have a very

similar probability to bind to all loci. In other words, all loci will have the same probability to be occupied, regardless of their spatial position. In contrast, compact factors will be preferentially shared between proximal loci and therefore the probability of a locus to be occupied by a compact explorer is a function of the occupation history of its neighboring sites: it is distance and time dependent. The compactness of the exploration, which is a protein specific parameter, will modulate the amount of material shared between different sites. Importantly, this indicates that two loci, such as two regulatory sites located a few tens of kbp away from one another, can transfer information and influence one another without direct physical contact. This spatial relation could underlie the process of sequestration of factors away from their targets (Yao et al., 2011), which would occur only with compact explorers. Such geometrically controlled long-distance interactions are not detectable using conventional chromatin capture assays, which predominantly rely on the chemical crosslinking between contacting sites.

3.1.5.4 Compact transcription factors and the stability of molecular complexes

A remarkable feature of compact searchers is their propensity to visit their neighboring sites multiple times. As a result, they have a probability equal to one to return to a site that they previously occupied, a property designated as the recurrence of compact trajectories. From a biochemical viewpoint, this property might affect our understanding of the kinetic stability of molecular complexes. Indeed, molecular machines controlling the nuclear functions such as transcription, splicing, and replication are composed of large numbers of molecules. Some of these molecules are stable constituents while others can be rapidly exchanged in order to control the specificity and modulate the activity of a particular complex (Fong et al., 2012). It is therefore important to understand how these molecular machines can assemble from their principal components. For instance, we cannot yet reconcile the need for strong and stable interactions, believed to be required for the viability of such complexes, and the requisite of weak and transient interactions required for molecules to compete for the same target regulating their composition. The observation of compact modes suggests that strong binding, associated to small dissociation rates, is not required to ensure high occupancy.

3.1.5.5 Compact transcription factors favor transcriptional bursting

Recently, the role and importance of transcriptional fluctuations within a single cell have been extensively studied (Raj et al., 2008; Zenklusen et al., 2008; Larson et al., 2009; Itzkovitz and

van Oudenaarden, 2011; Li and Xie, 2011). Using a simple model in which the activation of a gene is controlled by the binding of a single TF to a locus, Meyer et al. have modeled how the search dynamics of these TFs affects the transcriptional response (Meyer et al., 2012). For compact TFs, the recurrence of the trajectories and the facilitated re-association to the locus result in transcriptional bursting. In contrast, for the non-compact case, the gene activation rate is determined by the total TF concentration in the nucleus and the transcriptional activity is uncorrelated in time. This further illustrates how the translocation properties of nuclear factors might underlie the kinetics of functional cellular events.

3.1.6 Experimental Procedures

3.1.6.1 Cell culture and Transfection

U2OS (Human Osteosarcoma) cells were grown in DMEM (Life Technologies, CA92008 USA) with 1g/l glucose and glutamax supplemented with 10% FBS (Fetal Bovine Serum, Life Technologies, CA92008 USA) and 1% Penicillin/Streptomycin (Life Technologies, CA92008 USA) at 37°C with 5% CO2. 48 hours prior to the imaging, cells were seeded at 30-40% confluence on a plasma-cleaned (2mn with air with Femto model, Diener Electronic, MI48073 USA) and collagen-coated (Collagen I from Rat tail, Life Technologies, CA92008 USA) coverslips (N°1 25mm, Marienfeld 97922 Germany).

For experiments with c-Myc (fused to Dendra2 on C terminal), and H2B (fused to Dendra2 on C terminal), cells were transfected 24 hours before imaging with the plasmid of interest (10ng/25mm coverslip) using Fugene 6 (Roche Applied Science, IN46250-0414 USA) according to manufacturer instructions. Clones with very low expression of fluorescent protein, as judged by low fluorescence intensity of pre-converted Dendra2, were used.

Experiments with P-TEFb (Cyclin T1 fused to Dendra2 on N terminal) and Dendra2 (alone) were performed on U2OS cell line stably transfected and selected with geneticin (Life Technologies, CA92008 USA). Clones with very low expression of fluorescent protein (CyclinT1-Dedra or Dendra), as judged by low fluorescence intensity of pre-converted Dendra2, were used.

3.1.6.2 Single-molecule imaging

Single-molecule imaging was performed on an inverted microscope Nikon Ti Eclipse, with a high numerical aperture objective (1.49 NA) and 100X magnification; extra magnification of 1.5X was used in the tube lens of the microscope, resulting in a total magnification of 150X. We also used perfect focus system® (Nikon) designed to avoid drift on the Z-axis (focus) of the objective, relative to the coverslip. The excitation (561 nm) and activation (405 nm) laser beams were injected into a fiber and focused in the back focal plane of the objective, using an appropriate dichroic (Di01-R561-25x36) Figure S 1, panel a). A motorized mirror allowed us to choose between wide-field or inclined excitation configurations; a small angle, between 0 and 30

degrees, was typically used to avoid stray-light reflections and reduce background from cell auto-fluorescence. Experiments were acquired under continuous excitation (561 nm laser, 5 kW/cm2 on the sample) and pulsed activation (405 nm laser, 1 pulse of 10 ms per second, 0.01 kW/cm2 during the pulse on the sample). Fluorescence emission from individual Dendra2 molecules was filtered with a single band emission filter centered at 617 nm and a bandpass of 73 nm, and recorded on an EMCCD camera (iXon 897). The pixel size of the EMCCD was 16 μm, and we imaged a small region of interest (ROI) of about 100pixelsx100pixels. This ROI was sufficient for imaging a large cross-section within the nucleus of single cells, and allowed acquisition rates as fast as 100 Hz (10 ms per frame). Images of the pre-converted (green) form of the ensemble fluorescence of Dendra2 were taken using a mercury lamp for illumination (excitation: 485 nm, emission FF01-525/30).

Cells were imaged in Leibovitz's L15 medium (Life Technologies, CA92008 USA) containing 10% FBS (Fetal Bovine Serum, Life Technologies, CA92008 USA). The sample was placed on the microscope, on a stage heated at 37°C on the microscope. Once an ROI was selected from the pre-converted (Dendra2 green-form) fluorescence imaging of the live cells, activation pulses were fired every 100 frames, and movies of several thousands of frames were acquired under continuous 561 nm illumination (typically 2000 to 10000 frames per cell). Each coverslip was used for a maximum of 45 minutes after placing them on the scope.

3.1.6.3 Pre-converted Dendra2 imaging

Same conditions as for SM imaging using an Intensilight (Nikon) as a light source and in order to compensate the very weak expression levels, images were reconstituted averaging 100 images of a temporal sequence therefore minimizing the noise observed in single images.

3.2 P-TEFb Dynamics

With: **Lana Bosanac** Ignacio Izeddin, Claire Dugast-Darzacq, Florence Proux, Olivier Bensaude and Xavier Darzacq

3.2.1 Summary

In the following session we investigated in details the motion of P-TEFb by perturbing its functional properties. We investigated together the influence of the complex Hexim 7SK and the interaction with Polymerase II CTD on the way P-TEFb explores the cell nucleus. We indeed found that the type of exploration of P-TEFb driven by its ability to chemically interact

Method

Drug treatment

We dissociated the complex containing protein Hexim and snRNP 7SK using:

- **Transcription inhibitor DRB** (5,6-Dichloro-1-β-D-ribofuranosylbenzimidazole) specifically targets Cdk9 kinase leaving no detectable traces of the large 7SK containing complex .
- **RNAi** that specifically target snRNP 7SK

We investigated P-TEFb motion in the absence of interaction with the CTD using **α-amanitine** that triggers the complete degradation of the RNAPolII catalytic subunit Rpb1 within hours **.**

Microscopy

We used I-SPT PALM to investigate the motion of P-TEFb for the different conditions. We also used FRAP (Introduction 2.2) and FLIP (Introduction 2.2.3) to quantify the global exploration of the molecule.

Results

We found that P-TEFb exploration is compact (Introduction 2.1.2.3.1 and results 0) and that its exploration is driven by its chemical interactions. The CTD matrix constrained its motion so that P-TEFb wandering in the nucleus is highly recurrent. snRNP 7SK and Hexim chaperon P-TEFb interaction with the CTD, enabling a more global and efficient exploration of the nucleus in search of a distant target.

3.2.2 Abstract

Proteins move throughout the nucleus by diffusion, transiently and repetitively contacting their target sites. While DNA has been reported as a guide facilitating target search in the cell by restricting 3 dimensional explorations to a 1 dimensional search, such exploration modes were not envisioned for proteins. In an accompanying report, we showed using single particle tracking that the Positive Transcription Elongation Factor b (P-TEFb) explores the nucleoplasm in a compact mode consistent with a guided mechanism. In this report, using a combination of photobleaching techniques and single particle tracking, we demonstrate that P-TEFb nuclear mobility is controled by the interaction of its component Cycline T1 to the CTD of the polymerase subunit RPB1. Constant oversampling of adjacent binding sites on the CTD repeats guides its exploration to the transcriptional machinery. Finally we show that the 7SK snRNP acts as a chaperone to this guiding transient interaction modulating the local oversampling and therefore facilitating longer-range explorations. This work highlights the role of the CTD as a major platform for transient interactions acting as a net, guiding factors to polymerases in a spatially and temporally controlled and regulated manner.

3.2.3 Introduction

Gene regulation is a highly organized and controlled process at the core of all cellular functions. Gene expression occurs within the nucleoplasm, where genes are not compartmentalized nor separated from each other by impermeable barriers. Transcription factors regulating gene expression have thus potentially equal opportunity to access all existing genes in the nuclear

compartment. Since several nuclear factors are enriched in nucleoplasmic domains; it has been proposed that chromatin and its associated proteins could offer a primary spatial segregation barrier to contain the active transcription factors and facilitate their accumulation to ensure efficient transcription of a particular gene depending on its chromatin condensation state. Other nucleoplasmic compartments are formed and maintained by proteins and poorly rely on their DNA content. Transcription is controlled at several different steps: (Saunders et al., 2006)(Sims et al., 2004), in eukaryotic transcription, the process of elongation is considered the critical control mechanism of gene transcription. In order to maintain efficient transcription of a gene, transcription factors necessary for initiation and processivity of RNA elongation need to be available in sufficient local concentration. The Positive Elongation Factor b (P-TEFb) is a heterodimer consisting of Cycline T1 and the serine protein kinase Cdk9 ,which phosphorylates Ser2 residues on the Pol II CTD along with negative transcription elongation factors NELF and DSIIF. This defines P-TEFb as the major factor controlling elongation of Pol II transcription. P-TEFb exists in two forms, the heterodimer alone and a catalytically inactive complex sequestered by 7SKsnRNP. The 7SKsnRNP complex consists of the snRNA 7SK, Hexim1 and Larp7 (PIP7S). The two forms associate in a specific and reversible manner. P-TEFb exists in a dynamic equilibrium with its inactive form at 50% ratio in HeLa cells. The ability to shift this ratio reversibly by intracellular signalling, stress or pathological conditions indicates a highly regulated mechanism of this equilibrium. While the P-TEFb engaged in the 7SKsnRNP complex is catalyticaly inactive, this complex never inhibits all the cellular P-TEFb (20 to 50% depending on cell lines or conditions). It is therefore believed that this control is necessary for a fine tuning of the P-TEFb activity or alternatively serves as a “reservoir” to balance general transcription fitness

Transcription factors that interact with macromolecular complexes on chromatin exhibit high mobilities within the nucleus, transiently and repetitively contacting their target sites (Gebhardt et al., 2013). Diffusive properties of molecules are modified by their binding to immobile substrates or interactions with largem macromolecular complexes. Diffusion is a stochastic process that does not orient molecules movements but spatial constraints like impermeable organelles or numerous weak binding sites can constrain the geometry of the exploration effectively leading to guiding mechanisms. In an accompanying report, P-TEFb was shown to

explore the nucleoplasm adopting a mode of motion consistent with random motion guided on an underlying structure. Such guiding mechanisms demonstrate that proteins can be sequestered and committed to explore subregions of the space without being trapped in a particular location but rather being restricted to a network on which they will locate their binding sites.

In this work we investigate the exploration mechanism of P-TEFb in relation to its co-existence in the 7SKsnRNP complex and identified the molecular interactions responsible for this guiding mechanism. Using live cell imaging techniques such as photobleaching and single particle tracking, we found that the P-TEFb nuclear exploration guiding is mediated by the transcriptional machinery itself in a process that requires an intact cyclin T1 binding domain to the RNA pol II CTD. In addition we found that this exploration is tightly controlled by the 7SK snRNP that acts as a chaperone facilitating the nuclear exploration. Altogether our findings point toward a cellular mechanism controlling P-TEFb target search efficiently controlling its sampling properties.

3.2.4 Results

3.2.4.1 P-TEFb mobility is governed by its binding kinetics to the transcriptional machinery

The P-TEFb subunit Cyclin T1 was fused to GFP and stably expressed in a U2OS human cell line named U2OS-TG1b. A western blot showed an overexpression level equivalent to the endogenous protein. The overexpressed fusion protein is homogeneously nuclear, with an exclusion of nucleoli as its endogenous counterpart.

To quantify the diffusion and binding of P-TEFb in the nuclear environment, we perform fluorescent recovery after photobleaching (FRAP) on the TG1b cell line (data not schown) FRAP experiments lead to the conclusion that CycT1 dynamics in the nucleoplasm is limited by its specific and non-specific binding properties and that the major binding sites responsible for the observed kinetics are linked to the transcriptional machinery. This result implies that the pool of free diffusing P-TEFb is neglectable compared to the pool of bound complexes. Since P-TEFb catalytic activity is regulated by its interaction with the 7SK snRNP, we next addressed the influence of this regulation on P-TEFb dynamics.

3.2.4.2 R-FLIP, a measure for P-TEFb exploration at the nuclear scale

Binding dominant dynamics of P-TEFb as observed by FRAP indicating an excess of CycT1 binding sites across the nucleus. These observations are consistent with the ones made in the accompanying paper showing that P-TEFb nuclear explorations are guided by an underlying structure. Single particle tracking experiments however, could only account for short trajectories. Next, we addressed whether the nucleoplasmic exploration of P-TEFb is consistent with a guided exploration at the scale of the entire nucleoplasm. To reveal the nuclear search process at the scale of the entire nuclear compartment, we implemented the method of fluorescent loss in photobleaching (FLIP). FLIP was previously performed in the nucleus by (Kimura et al., 2002) to reveal differences in mobility of RNA Pol II upon treatment with different transcriptional inhibitors, mainly focusing on fixed fractions of PolII. (Miermont et al., 2013) used FLIP to measure turnover rates between nuclear and cytoplasmic pools of fluorescent molecules. Quantitative analysis of FLIP extended to analysis of dissociation kinetics of SF/A2 and fibrillarin from nuclear compartments(Phair and Misteli, 2000), while (Wüstner et al., 2012) describes a quantitative measure of FLIP to diagnose dynamics of the fluorophore in the bleached region in direct comparison to the unbleached regions by a stretched exponential function, giving a relative measure of mobility with the parameters fitted.

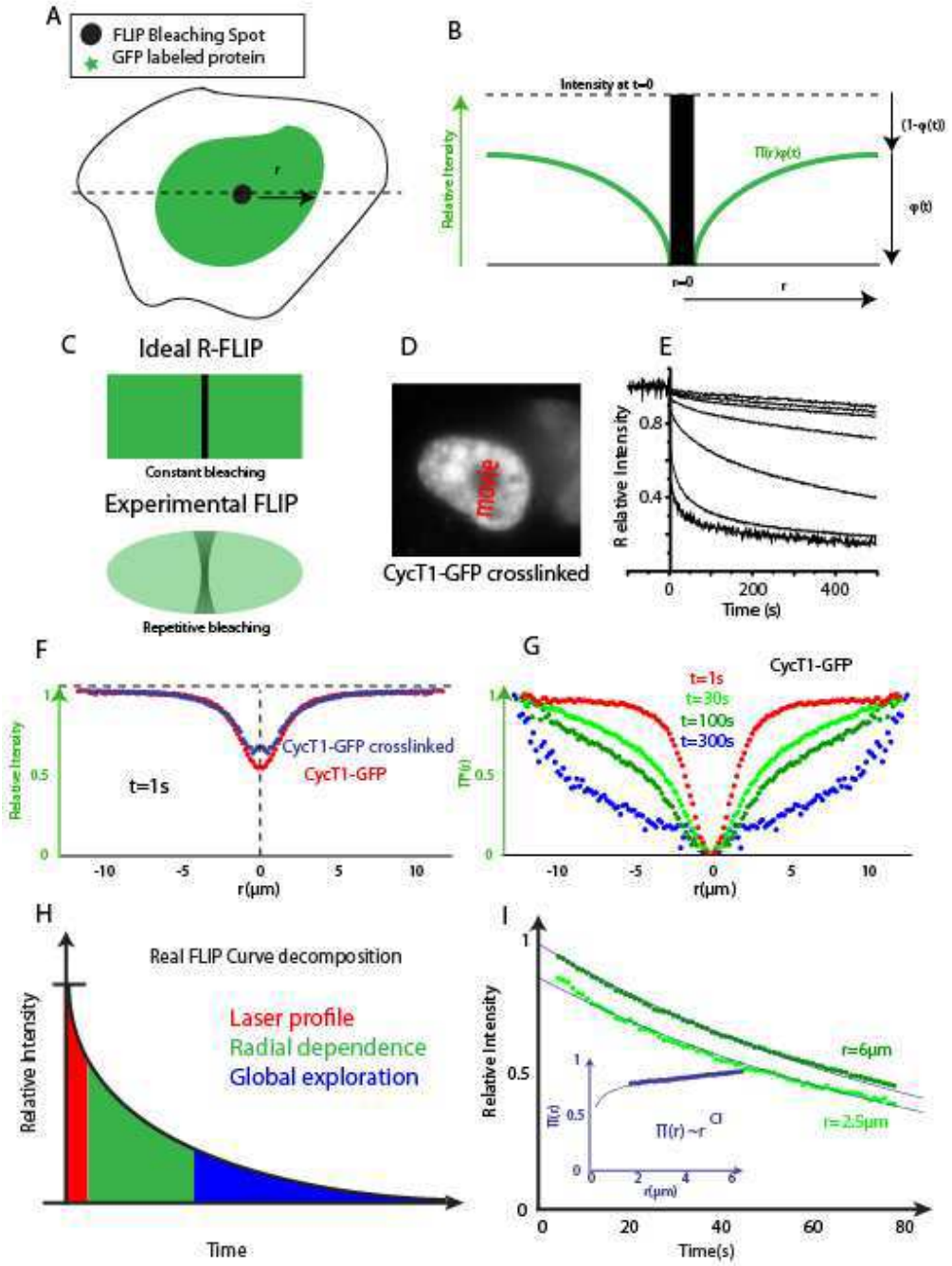

Figure 23: R-FLIP, a method for the measure of the inverse first passage time of the P-TEFb

Panel A **:** *Representation of ideal R-FLIP experiment. A small focus in the nucleus is constantly bleached in the nucleus which expresses PTEFb-GFP. R-FLIP curves are the decays as a function of distance to the bleaching spot. Panel B* **:** *Representation of the theoretical R-FLIP intensity profile* $I(r,t)$ *as a function of the distance to the bleaching spot. The radial factor* $\Pi(r)$ *is independent of the time and the decay rate* $\varphi(t)$ *is the same for every radius. Panel C* **:** *Comparison between ideal and experimental R-FLIP. For ideal R-FLIP, the volume is large*

compared to the bleaching spot and there is no side effect of the nuclear boundaries. For experimental R-FLIP, the bleaching efficiency is spread in the laser beam profile and the bleaching is sequential. Panel D : Exemplary movie of a FLIP experiment conducted on a fixed cell of the stable cell line transfected with CycT1-GFP. Panel E : The R-FLIP graph of the decay in (D); We used that experiment to investigate the effect of the LASER beam. Panel F : The intensity profile $I(r,1s)$ *shortly after laser lighting for the crosslinked and free CycT1-GFP. For short times, the main effect on the intensity profile is the LASER beam profile. Panel G : Evolution of the radial factor* $\Pi^*(r,t)$ *as a function of time for CycT1-GFP. The rescaling was done using the minimum and maximum intensity* $I(r,t)$ *for different time t. For short times* $\Pi^*(r)$ *is the LASER beam profile is the main effect then* $\Pi^*(r)$ *reaches a long lasting form that is the convolution beween the LASER beam and diffusion. For long time ranges, the profile vanishes. Panel H : Decomposition of the R-FLIP curves according to time. The radial dependence is only expected to be measured at medium times. Panel I : Computation of the Compactness Indicator (CI). We used the rescaled R-FLIP curves and fitted to a function of the form* $\Pi(r)e^{-\frac{t}{T}}$ *for r between 2.5µm and 6µm. Fitting of a power law dependency on* $\Pi(r)$ *gives the compactness indicator CI.*

Here we introduce a spatial quantification method of FLIP for homogeneusly distributed fluorophores in the nuclear environment FLIP decays were quantified as a function of the radial distance to the bleached spot and abbreviated R-FLIP. In an R-FLIP experiment, the local loss of fluorescence corresponds to the probability that molecules present at time T_0 to be replaced by molecules that have already at least once travelled through the bleached region at a particular time T. Thus, R-FLIP can be considered as a spatial measure of the inverse mean first passage time (ie. the survival time of the fluorophore) Figure 10 and Figure 23. By measuring the spatial inhomogeneity of the fluorescent decay, we are able to quantify the level of compactness of the fluorophore bleached Figure 23 I.

For quantification, we implemented a continuous radial analysis and quantitative measure that we named a Compact Indicator (CI) Figure 23 H. R-FLIP datasets consist of a matrix of fluorescent intensities resolved in time and as a distance to the bleached spot. To extract information on the dynamics of fluorophores at different distances from the bleach spot, the direct contribution of the laser is calibrated and corrected using fixed cells (see Supplementary Information). For each radial annulus emerging from the bleach center, the fluorescent decay was fitted to an exponential of fixed temporal decay, and the radial kinetic parameter was

extracted Figure 23 kE I. The radial dependence of this kinetic parameter, named compactness indicator CI, is a direct indicator of the exploration mode of the protein.

The CI for a YFP tagged with a nuclear localization signal nls was measured and gave the reference for a non-specifically binding explorer while Cyclin T1 GFP served as a reference for a compact explorer. The observed difference is in agreement with single particle experiments reported on the previous result session. This result shows that indeed P-TEFb compact exploration is homogeneous and general over the whole nucleoplasm.

To test the R-FLIP quantitative analysis, we performed R-FLIP in the nucleoplasm of cells transfected with YFP tagged with a nuclear localization signal *nls*, as well as on the TG1b CycT1-GFP cell line. We find two distinct radial dispersions of FLIP dynamics Accordingly, the resulting CI value is three times higher for CycT-GFP in comparison to YFPnls, indicating a fluorophore of higher compactness. This result shows that indeed P-TEFb compact exploration is homogeneous and general over the entire nucleoplasm.

3.2.4.3 7SK snRNP facilitates long-range exploration of P-TEFb

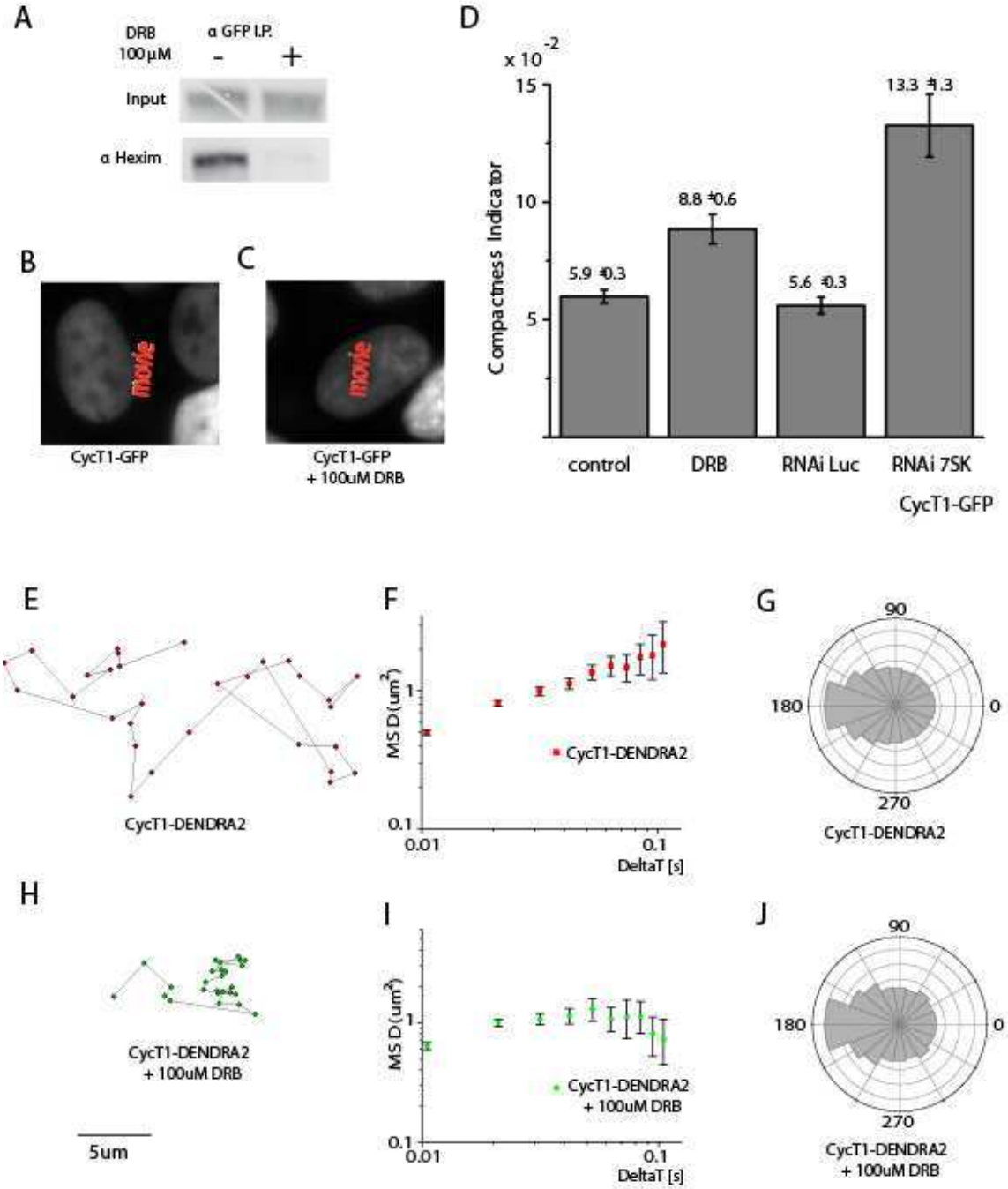

Figure 24: FLIP reveals chaperon-regulated dynamics of P-TEFb *Panel A* ***:*** *Western blot showing co-immunopercipitation of Hexim, a part of the 7SKsnRNP complex. In the second lane, upon addition of DRB showing breakdown of the 7SKsnRNP complex by absence of Hexim in the pull-down Panel B* ***:*** *Exemplary movie of the CycT1-GFP FLIP shows homogeneous decay of*

*fluorescence throughout the cytoplasm Panel C **:** Movie of the CycT1-GFP stable cell line treated with DRB shows a sink forming towards the laser bleach spot, i.e. an inhomogeneus decay of fluorescence. Panel D **:** The compactness indicator reveals higher values obtained by the FLIP curves of cells lacking the 7SKsnRNP complex due to DRB treatment. RNA interference against 7SK likewise breaks down 7SKsnRNP and reveals higher values of the CI compared to its Luciferase control. Panel E **:** SPT single molecule trajectory of CycT1-DENDRA2 shows a single molecule capable of diffusing over long distances Panel F **:** MSD graph of CycT1-DENDRA2 shows linear trend in log scale, fitable by a power law of exponent 0.6, indicative of anomalous diffusion Panel G **:** The angle distribution of CycT1 has a preference for the return angles, indicative of compact movement Panel H **:**The typical SPT trajectory of CycT1 obtained from nuclei treated with DRB shows a decrease in step size and confinement of movement: Panel I **:**MSD graph consistently plateaus at early time scales: Panel J **:**The angle distribution upon breakdown of 7SKsnRNP shows an even larger preference for the back-direction, indicative of an amplified compactness*

The binding nature of the P-TEFb remains unaltered upon loss of the 7SKsnRNP complex, as shown by FRAP and accumulation experiments.. This implies a global increase in interaction of the two molecules in absence of 7SKsnRNP. To investigate this phenomenon in terms of nuclear dynamics, we conducted R-FLIP experiments on T1GB cells under conditions known to affect the equilibrium between the 7SK-P-TEFb complexes. Treating cells with 100uM DRB resulted in dissociation of the 7SKsnRNP complex **Figure 24** A. FLIP recordings show a quasi-homogeneous decay of fluorescence throughout the nucleoplasm in presence of the 7SKsnRNP complex, while in absence of the complex there is an inhomogeneity at the nucleoplasm forming a sink at the bleach spot .R-FLIP analysis consistently yields an increase of the CI value indicating more compact dynamics of P-TEFb in absence of the 7SKsnRNP complex. Likewise, RNA interference mediates knockdown of 7SKsnRNA. CI-values of 7SK RNAi showed an even sharper increase in compactness level, possibly due to a contribution of the kinase activity **Figure 24** D

In order to investigate the differences of compactness at the single molecule level, we used the method of sptPALM as described in the previous session to capture single molecule dynamics of P-TEFb in the nucleus. Single molecule measurements require sparse signal and thus allowed us to work at overexpression levels closer to the endogenous situation

Trajectories of single molecules recorded by sptPALM showed significantly different signatures of the case with P-TEFb alone and the one treated with DRB. In the case where both complexes co-exist in the cell, it is possible to identify two different interchanging behaviors of the

molecule: one with a low displacement per time unit, and another one able to cover larger distances Figure 19. The case where 7SKsnRNP is dissociated from P-TEFb exhibits traces only with low displacements, consistent with a higher compactness as observed in FLIP results **Figure 24** H.

The mean square displacement obtained from these trajectories both show a subdiffusive behavior, as they are not directly proportional to the time. Fitting to the power law gives a anomalous coefficient of alpha = 0.6 for P-TEFb in presence of both complexes Figure 19. In the case of treatment with DRB, the MSD graph forms a plateau **Figure 24** I and is not fittable by a power law.

Consistently, the angle distribution of P-TEFb movement, calculated from the angle presented between two consecutive translocations shows preference for the reverse direction **Figure 24** G indicating dependence on the geometry of exploration space, and thus compact modes of movement. This preference for the reverse direction is amplified **Figure 24** J upon breakdown of 7SKsnRNP, indicating higher compactness.

3.2.4.4 P-TEFb nuclear distribution is limited by its binding to the transcriptional machinery

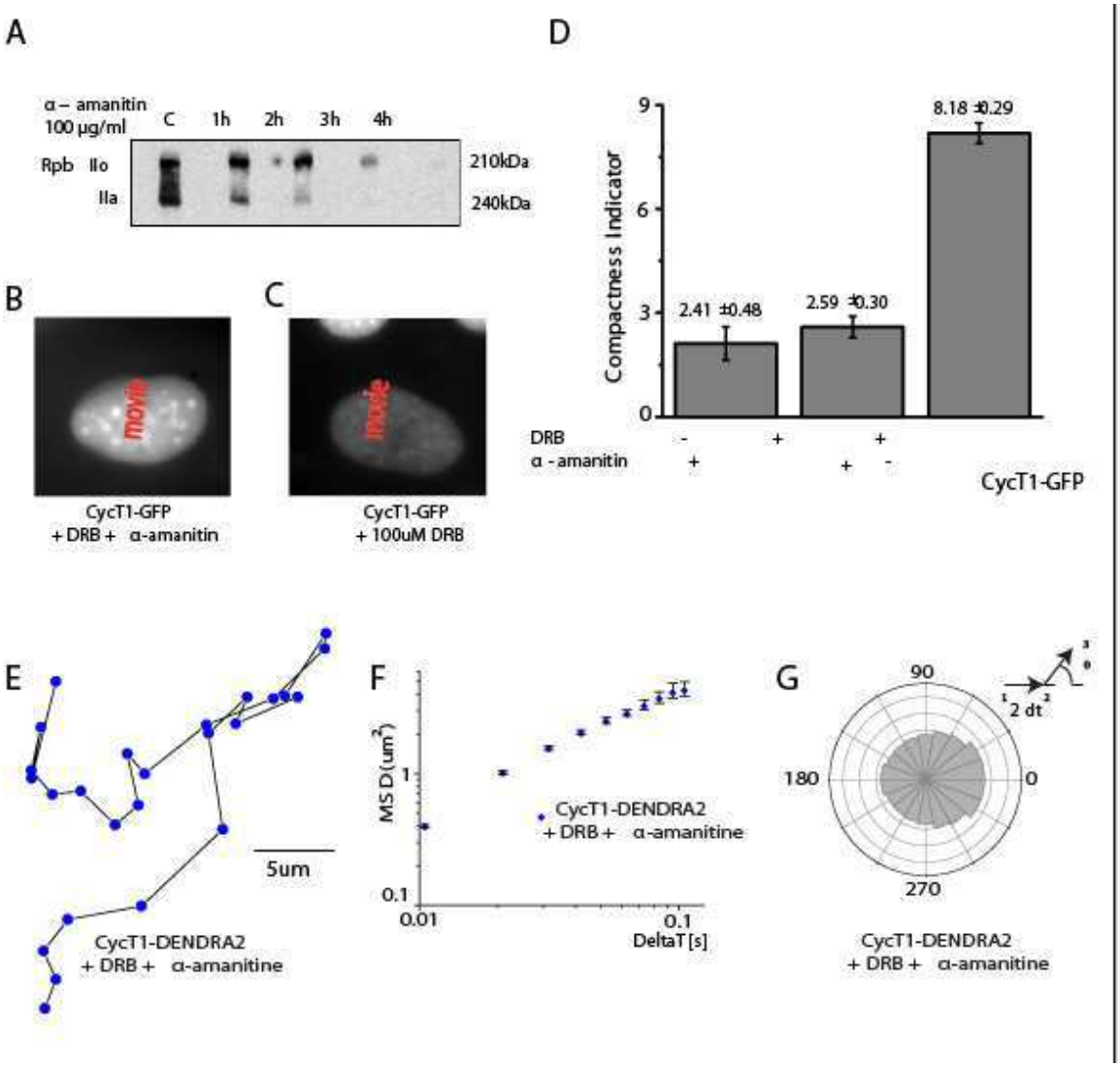

Figure 25: FLIP and SPT reveal RNA PolII as the binding substrate via the histidine-rich domain. *Panel A **:** CycT1-YFPnls truncation was constructed removing the histidine rich domain known to interact with the CTD of the Rpb1 subuinit _Panel B **:**An exemplary movie of the FLIP conducted on a cell transiently transfected with CycT1(1-490)-YFPnls shows homogeneus decay throughout the nucleoplasm_Panel C **:** As a control to (B), a movie of the transiently transfected CycT1-YFP shows attenuated diffusion as observed by the inhomogeneus decay of fluorescence Panel D **:** The CI value for (A) shows to be similar to the one upon degradation of binding substrate (alpha-amanitine treatment). The CI value for (B) is higher due to addition of the nls tag. Panel E **:** A CycT1 mutant was constructing to test the CTD binding by making a point mutation at the within the histidine rich region Panel F **:** The trajectory obtained resembles the one of treatment by alpha-amanitine, resembling large step size and area covered by exploration Panel G **:** The MSD likewise fits a pure diffusion model, yielding a straight line of slope 1 in the log scale against deltaT_Panel H **:**The angle distribution is isotropic, indicating absolute freedoœm of diffusion within the nucleoplasm*

Next, we explored the relation between the presence of a functional RNAPolII complex in the nucleoplasm and the compactness of P-TEFb dynamics. We treat the cells with a massive dose of α-amanitine sufficient to trigger the complete degradation of the RNAPolII catalytic subunit Rpb1 within four hours Figure 25A. Upon treatment, P-TEFb dynamics exhibits a homogeneus decay of fluorescence in FLIP Figure 25B as compared to its control without alpha-amanitin Figure 25B and C. The CI obtained upon treatment with alpha-amanitine is comparable of that of the free nuclear fluorophore yfp-NLS. The CI is not sensitive to DRB Figure 25D

Next, we pursued single molecule measurements of CycT1-DENDRA2 stable cell line under alpha-amanitin treatment. Consistently with our FLIP measurements, the fluorophore's trajectories exhibit a fast-moving molecule, as the MSD graph shows a linear correlation with time Figure 25F, indicating free diffusion throughout the nuclear environment. The angle distribution of P-TEFb after alpha-amanitin treatment shows equal distribution at all angles Figure 25G, similar to the angular profile of free Dendra2 Figure 20. This indicates that P-TEFb, without the presence of its substrate Rpb1, is free to diffuse until it eventually hits the nuclear boundary.

P-TEFb phosphorylates the Pol II CTD of the catalytic subunit of Rpb1 on 54 potential sites. While P-TEFb function in elongation control relates most likely to NELF and DSIF phosphorylation, the Pol II CTD is by far the most abundant target. It was shown that binding of P-TEFb to RNAPolII CTD is not mediated by the Cdk9 kinase but rather the C-terminal domain of Cyclin T1

3.2.5 Discussion

In the present work, we have addressed the nuclear dynamics of P-TEFb with several different imaging techniques in order to provide insight into the spatial and temporal factor of its regulation in vivo.

,We address the spatial dynamics of P-TEFb by conducting fluorescence loss in photobleaching (FLIP). The results obtained from FLIP experiments clearly demonstrate attenuation in the mobility of P-TEFb in the case where only the small complex is present. Considering the sizes of the small and large complexes and the high density of the nucleus, this result might look

paradoxical at first. However, we have to remember that the small complex is the catalytically active one that is shown to bind to the RNA PolII, while the large is unable to bind.

Consistent results were obtained in single molecule measurements: upon recording traces of single P-TEFb molecules and plotting the translocations into a histogram, one obtains a clear decrease in the long-range traveling population in the case where the large complex has been broken down. The population of the short-range traveling molecules rises at its expense.

We conclude that the 7SKsnRNP acts as a nuclear transporter of the small catalytically active complex, and uses 3D diffusion to transport it throughout the nuclear environment. This indicates indeed that diffusion within the nucleus is a process that can tightly be regulated by the cell with means of sequestering the active into inert complexes that freely diffuse around the nucleus. The small complex sequestered within the big does not change its conformation, enabling fast release and recruitment to genes. The distribution of free P-TEFb in the form of the large complex thus presents the population efficient in recruiting factors to newly activated sites at longer distances from its initial positions, while the small complex is efficient in maintaining its pool of active complexes and reactivating genes at shorter distances to its initial starting position.

3.2.6 Material and methods

3.2.6.1 Cell Culture and Reagents

Human U2OS osteosarcoma cells were cultured in phenol-red low D-glucose (1g/L) DMEM (Invitrogen) with 10% fetal calf serum (FCS). Cells were transfected by FuGene 6 transfection reagent for both transient and stable transfections.

Stable cell line clones were selected by media containing 1.5mg/ml geneticin (GIBCO) which was changed every 3 days. Selection of clones was conducted after visual judgement – approximately 10days. CycT1-GFP cell lines were subcloned and selected according to their expression levels for the overexpression experiment.

RNA interference was conducted with OPTIMEM and oligofectamine transfection reagent. The treatment lasted 3days involving 4hours/day of starvation and transfection.

3.2.6.2 Plasmids:

CycT1-GFP at N1 (by Gaelle Diribarne)

LacI-CFP

MS2-Cherry

YFPnls (Clontech)

CycT1-YFPnls, CycT1 (1-490)- YFPnls, CycT1 (1-503)- YFPnls, CycT1 (1-533)- YFPnls, CycT1 (1-551)- YFPnls (by Nina Verstraete)

Rpb1-YFP (by Vera Ruda)

CycT1-DENDRA2 at N1 (by Florence Proux)

siRNA:

7SK siRNA (from OB lab Gaelle)

Luciferase siRNA (from OB lab Gaelle)

3.2.6.3 Drug Treatments

DRB (5,6 Di-chloro-1-beta-D-Ribofuranosylbenzimidazole) (Sigma) was used to inhibit transcription at a concentration of 100□M, keeping the DMSO concentration at a 1000x dilution. DRB was added to the media maximally avoiding contact of solution with plastics to ensure the DRB concentration at cell level to be the one put into the solution.

Alpha-amanitin (…) was incubated into the cells at a concentration of 100µg/ml over the course of 4h. 1hour before imaging/3h into alpha-amanitin treatement, DRB was added to the cells.

For experiments involving the activation of the gene array, transcription was induced by addition of 1µg/ml doxycycline for 6 hours minimum to maximize the probability of steady state transcription during experiment.

3.2.6.4 Antibodies

Polyclonal goat anti-CycT1 (from Giuliana Napoletano, OB lab); rabbit anti-Rpb1, and rabbit anti-Hexim1 (OB lab).

Secondary antibodies for Western/coIP Western: anti-rabbit HRP; anti-goat, anti-mouse HRP.

Secondary antibodies for Immunofluorescence: anti-goat Cy3, anti-rabbit Cy3.

3.2.6.5 Western Blot

Cells were lysed, boiled, sonicated and loaded on gel; then the denatured protein was transferred to a nitrocellulose membrane. The membrane was treated with goat antibody against CycT1 500x dilution, then secondary antibody (anti-goat HRP and anti-mouse-HRP at 7500x dilution and transferred to film.

3.2.6.6 Co - Immunoprecipitation

Cell lysates with/without DRB treatment were ran on a glycine gel, transferred on a nitrocellulose membrane, blocked and treated with the primary antibody Hexim1 C4 at 1:5000 dilution and anti-CycT1 at 1:500 dilution; then washed, and treated with secondary antibody anti-rabbit HRP at a dilution of 1:5000, and anti CycT1 anti-mouse and anti-goat at 1:5000 dilution each.

3.2.6.7 Immunofluorescence

Cells expressing LacI-CFP on coverslips were crosslinked with 4% formaldehyde; permeabilized with Triton x100; blocked with BSA 3%; then incubated with the primary (anti-goat CycT1 1000x, anti-rabbit Rpb1 1000x dilution) and secondary antibodies (anti-goat-Cy3, anti-rabbit-Cy3 1000x dilution) for the duration of 1hour each; then transferred with mounting media on microscope slides for imaging.

3.2.6.8 Fluorescence Microscopy

Images of fixed cells were obtained on a wide-field Olympus equipped with illumination box. All cells were imaged in z-stacks of 30 frames 200nm apart. Metamorph interface was used for acquisition.

Live cell imaging was conducted on cells plated on 25mm coverslips in phenol-red-free DMEM. DRB was induced 1hour before imaging. Experiments were performed at 37^{o}C using temperature control of stage, lid and objective by heat calibrator and 5% CO2. Occasionally L15 was used as imaging medium in case of absence of CO2.

FRAP and FLIP experiments were conducted on an inverted wide-field Nikon microscope With an oil-immersion 60x objective. The μscope is equipped with a DG4 illumination box and

Quantem camera as well as a laser box with 488nm Argon laser. Metamorph was used as the controlling interface.

FRAP images were acquired at a fast-imaging protocol by cropping the area of imaging to include the entire nucleus only as a control area, and thus allowing an exposure time of 15ms/frame. FRAP diffusion-coupling was tested bleaching increasing areas of bleach (FRAP recovery curve comparison at diameters of 0.8, 1.2, 1.6 and 2 μm; the Gaussian profile of bleach measured from a 2μm diameter bleach). The bleach duration was kept below $1/10^{th}$ of the recovery time.

FLIP was conducted by time-lapse of 100s pre-bleach and 500s of 1bleach/s with an exposure time of 50ms/frame.

Single molecule measurements were conducted on a Nikon Ti. microscope and Andor camera equipped with a Mercury illumination lamp and lasers of 405nm, 561nm wavelength.

GFP channel was visualized by the mercury lamp; while the red channel used laser illumination at 561nm visualization. Stochastic conversion of single DENDRA2 molecules was obtained by low power 405nm laser of pulse duration 10ms, interval 2s, calibrated to minimize possibility of new conversion before decay. The exposure time was 10ms with a writing delay of 2.5ms.

Interface of image acquisition used is micromanager by ImageJ.

3.3 Single cell correlation fractal dimension of chromatin.

A framework to interpret 3D single molecule super-resolution

With: Ignacio Izeddin, Lana Bosanac and Xavier Darzacq

3.3.1 Summary

In the following paper we investigated the 3D position of H2B histones molecules inside the nucleus with superresolution microscopy. We showed that the relative position of H2B has the characteristics of a fractal structure.

Method

Microscopy

We used PALM microscopy (Introduction 2.2.1.1) on U2OS osteo-sarchoma cell line that was preliminary transfected with H2B-Dendra2. The cells were fixed using para-formaldeide (PFA). With a deformable we induced astigmatism in the optical pathway to recover the z position of H2B-Dendra 2 with respect to the focal plane of the camera (Introduction 2.2.1.3). We obtained the 3D position of 500 000 H2B molecules in a 600 nm thickness slice of the nucleus

Statistics

We considered the measured PALM distribution of H2B as the monte carlo estimation of a density (Introduction 2.2.1.2.2). We computed the pair distance distribution of H2B, namely the K Ripley (Introduction 2.2.1.4). We found that it indeed have fractal scaling properties.

Results and discussion

We computed the correlation fractal dimension of chromatin and found a 2.6 value. We fully discussed the implication of this number in terms of chromatin conformation. Indeed, Chromatin is non-uniformly packed. This heterogeneity impacts the distance between loci and is supposed to have a high impact on gene regulation.

3.3.2 Abstract:

Chromatin is a major nuclear component and it is an active matter of debate to understand how it is folded and its implication in gene regulation. Several models coexist and are supported by Conformation capture experiments (Hi-C) and Fluorescent in situ hybridization. In a possible scenario, the fractal globule, chromatin folding generates strong relations linking nucleoplasmic proximity to genomic distances. An alternative hypothesis, the equilibrium globule, would be that links between genomic and spatial distances are weak and rapidly vanish for distant loci. High-resolution imaging opens new possibilities to measure chromatin organization in situ. Here, we performed a direct measure of chromatin compaction at the single cell level. We used histone H2B, one of the 4 core proteins forming the nucleosome, as a chromatin density marker. Using photoactivated localization microscopy (PALM) and adaptive optics, we measured the three-dimensional distribution of H2B with nanometric resolution. We computed the distribution of distances between every two points of the chromatin structure, namely the Ripley $K(r)$ distribution. We found that the $K(r)$ distribution of H2B followed a power law, leading to a precise measurement of the chromatin correlation fractal dimension of 2.6. Using photoactivable Histone H2B, we measured the dynamics of different chromatin domains in time over several hours and observed massive compaction and decompaction events As a result, the correlation fractal dimension of chromatin reported here can be interpreted as a measure of the distribution of sizes of topologically segregated domains that constantly evolve in time. This highly dynamic view of chromatin provides with a solid frame to interpret the different levels of chromatin organization known to regulate nuclear functions.

3.3.3 Introduction

Chromosomes are meter-long polymers that fold into a micrometric nucleus. Recent studies have shown that chromatin folding is not random with potential consequences in gene regulation (Fraser and Bickmore, 2007). One aspect of chromatin organization that has been intensively studied recently is the relation between the linear genetic distance s along a chromosome and its

physical distance $R(s)$ in the nucleus. During the interphase, chromosomes decondense and loci that are close on the linear DNA sequence could be segregated from each other. However, it has long been shown that a certain degree of proximity is maintained along the cell cycle (van Dekken and Hulspas, 1993). Recent evidences for this nonrandom folding of the de-condensed chromatin were drawn from fluorescent in situ hybridization (FISH) (Mateos-Langerak et al., 2009) that addresses the physical distance $R(s)$ as a function of the linear distance on the chromosome s. Chromosome conformation capture assays such as Hi-C also highlighted a relation in between the probability of contact $P_c(s)$ and the physical 3D distance (XXX) averaged on a whole population of cells (Lieberman-Aiden et al., 2009) . Taking all the inter-loci distances lower than 10Mb and averaging them , FISH showed that $R(s) \propto s^{\frac{1}{3}}$ (Rosa and Everaers, 2008) and Hi-C that $P_c(s) \propto s^{-1}$ (Lieberman-Aiden et al., 2009) (Mirny, 2011), and that the corresponding scaling exponents $\frac{1}{3}$ and -1 significantly deviate from the value $R(s) \propto s^{\frac{1}{2}}$ and $P_c(s) \propto s^{-\frac{3}{2}}$ that was expected upon random organization of the genomic material. One possible explanation is that chromatin folds into a knot-less structure, a fractal globule that homogeneously fills the nuclear space (Grosberg et al., 1993). However such a description relies on nuclear DNA representation as a uniform space filling polymer. This assumption of uniformity can be questioned by any DNA stained image of nucleus such as DAPI that shows regions of lower and higher density. An alternative hypothesis is a particular distribution of sizes of segregated DNA domains, from chromatin domains to super-domains and chromosome territories (Meaburn and Misteli, 2007). Recently an in-silico model "strings and binders" showed that it was possible to recover the scaling of $R(s)$ and $P_c(s)$ found with Hi-C and FISH with DNA modeled as a self-avoiding polymer and a given surrounding concentration of binding proteins (Barbieri et al., 2012). In a "strings and binders" model the apparent fractal exponents could be explained either by the equilibrium between two segregate states of DNA compaction or an equilibrium concentration of binders that would lead to a fractal organization. However such a model is purely stochastic with a random distribution of binding sites. It does not take into account the sequence specific nature of the DNA domains such as binding regions

(Bickmore and van Steensel, 2013) nor the known dynamics of chromatin(Dion and Gasser, 2013). Chromosome conformation captures assays are also blind to deviation from equilibrium since measurements are retrieved from an average of millions of cells and it is impossible to distinguish a strong but transient interaction between loci from a weaker relation that is constitutive. To our knowledge, no studies so far have confronted the fractal exponent found in Hi-C and FISH to the non-uniform density of chromatin observed at the single cell level, although numerous efforts have been developed to reveal the fractal nature of single cell chromatin organization in eukaryotes nuclei (see reference (Bancaud et al., 2012) for a review and citations therein).

The first set of evidence of the fractal nature of the nucleoplasm came from the diffraction pattern of neutron scattering data (Lebedev et al., 2005) and by direct visualization of the nucleus with light microscopy. By imaging a May-Grünwald-Giemsa stained nucleus (Adam et al., 2006) or studying the movement of an inert tracer inside different nuclear compartments (Bancaud et al., 2009), regions of lower and higher density were observed evaluating a so-called mass fractal dimension of the nucleus. Unfortunately, a consensus has not been reached for this dimension, with reported values ranging from 2 to 2.8. The greatest shortcoming of these microscopic assays has been their limitation to two-dimensional imaging. In 2D microscopy, images are formed by projecting on a plane the 3D object captured within the focal depth of observation (typically ~ 500-1000 nm). With a probability equal to 1, it is impossible to recover a fractal dimension ranging between 2 and 3 from a 2D projection (theorem 6.2 of reference (Falconer, 2003)). Therefore, the impact of imaging in 2D is largely under-evaluated in those studies, even though some rescaling methods were proposed. To overcome this limitation in the most straightforward manner, there is a need to acquire the experimental data in 3D.

Photo-activated localization microscopy (PALM) (Betzig et al., 2006) is a technique that enables to retrieve the organization of proteins with a resolution lower than the fundamental diffraction limit of light. Initially developed for 2D imaging it has been extended to 3D by the induction of astigmatism in the optical path(Huang et al., 2008). The output of a PALM experiment are the x,y, and z coordinate positions of a tagged protein of interest. Lists of points coordinates or “point pattern” have been studied for decades addressing the question of homogeneity (Diggle, 2003). The Ripley $K(r)$ distribution of a point process is the inter-point distance distribution

(Ripley, 2004). This statistics has been recently used for analyzing PALM experiments in the case of specific enriched regions of proteins. When proteins gather in clusters, the $K(r)$ distribution of PALM experiments can quantify the ratio of clusterization (Owen et al., 2010), as well as the cluster size (Williamson et al., 2011). Although Localization microscopy has already been applied to chromatin it has indeed been restricted to 2D projection along the focal depth of the set-up (Bohn et al., 2010).

Here, we performed a direct visualization with 3D PALM microscopy of the chromatin structure using advanced adaptive optics (Izeddin et al., 2012). We detail a method to quantify chromatin enrichment at the nanometric scale, in the cellular nucleus of an osteosarcoma cell line (U2OS) in the inter-phase. We specifically address histone H2B, one of the 4 core proteins forming the nucleosomes which strongly bind to DNA (Mazza et al., 2012b). H2B covers nearly all the cellular DNA fiber and can be used as a density reference for chromatin with super-resolution imaging techniques (Matsuda et al., 2010). We computed the 3d $K(r)$ distribution of H2B and found that this protein does exhibit clusterization. Notably, the H2B clusters do not have any specific size within the range of the experimental limits (between 30nm to 1µm). Such an observation is coherent with a fractal nature of chromatin organization. We also found a power law dependency between the $K(r)$ distribution and that of a random distribution, with an exponent of 2.6 that is stable among the cell population. To assess the stability of such a structure, we performed H2B Photo-Activation assays on live cells labeling chromatin domains and found that this organization is very transient. This number, 2.6, corresponds the so-called "correlation fractal dimension of the chromatin" (Cheng and Agterberg, 1995a) m. As the correlation fractal dimension characterizes the fractal nature of the distance between two randomly chosen point of the chromatin structure, it can be confronted to the exponent found with Hi-C assays. It helps understand how inter-loci distances can be lower than expected upon a random organization of chromatin regardless their relative position on the DNA strand.

3.3.4 Results

3.3.4.1 PALM images of H2B heterogeneity

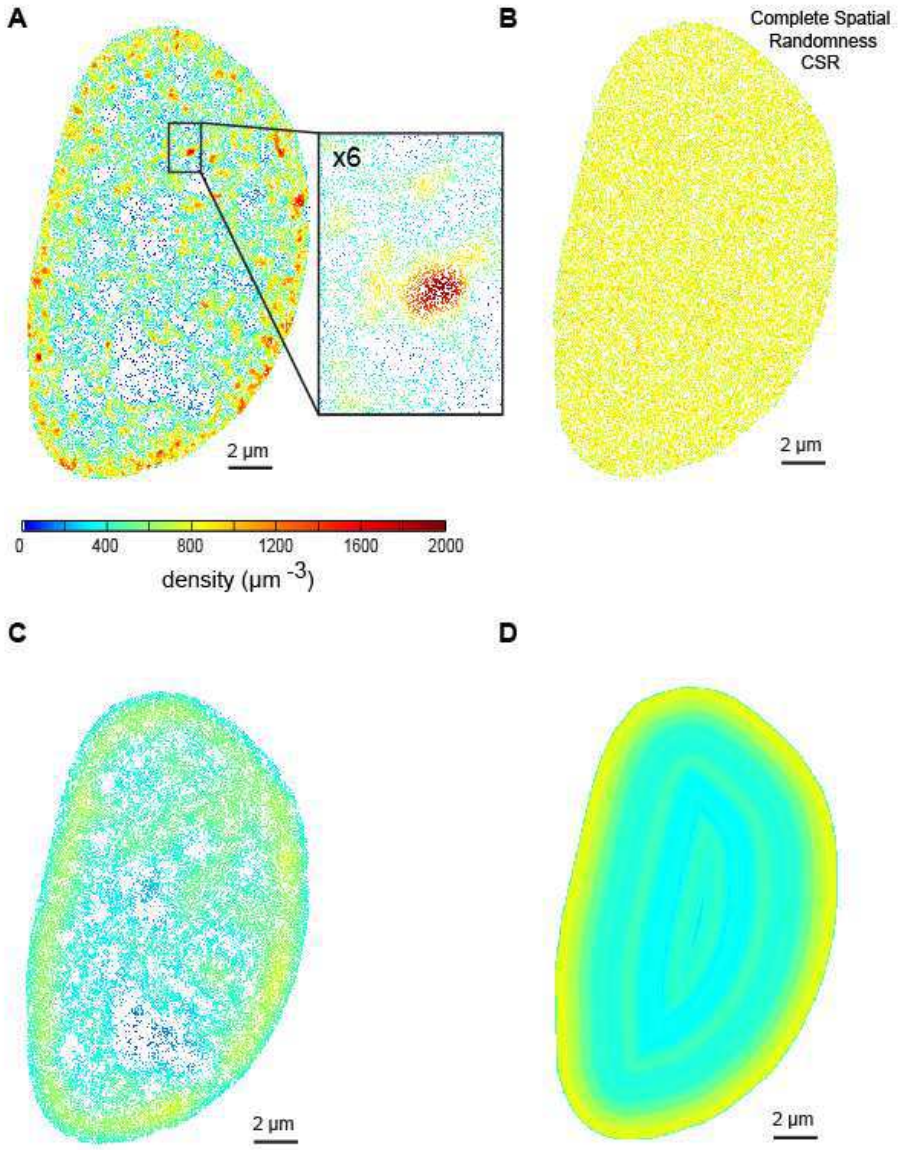

Figure 26:. H2B PALM localization inside the cellular nucleus. *Panel A: Projection of a 3D PALM image of tagged histone H2B in the xy focal plane of the camera. The color code is local the density, estimated on a 100 nm circular sliding window showing heterogeneous regions that could be labeled as clusters. Inset: Image zoomed with a 10 nm binning, displaying an intra-nuclear cluster. Panel B: H2B PALM detections spatially re- distributed over complete spatial randomness (CSR) in the nuclear envelope, with 100 nm circular sliding window density, showing no clusters. Panel C: PALM image of tagged histone H2B with local density estimated over a 1µm circular sliding window, showing an enrichment of H2B on the edges of the nucleus. Panel D: Density map estimated over the 50 nm annular regions defined by their distance to nuclear membrane.*

In order to directly determine the spatial distribution of chromatin, we performed 3D PALM experiments of H2B tagged with the photoactivatable fluorescent protein Dendra2 (Baker et al., 2010). We used an adaptive optics system, placed in the emission optical path between the microscope and the recording EMCCD, in order to induce an astigmatism deformation to the point-spread function (PSF) of the detected single molecules (SM). With such controlled deformation, we were able to determine the z position of the individual fluorophores within the focal depth of observation (Izeddin et al., 2012). We thus obtained the planar as well as axial position of H2B molecules with a pointing accuracy of ~ 15nm and ~ 30 nm, respectively. The observation was limited in the axial direction to a region of ~ 1 μm, with a Normal distribution of detections along the optical axis (FWHM ~ 600 nm) determined by the fundamental limit of the diffraction of light (*Figure S 11*) (Betzig et al., 2006) . Typically, we obtained ~ 500 000 detections of H2B-Dendra2 molecules in one nucleus, within the aforementioned optical depth. For visualization purposes, we then represented the planar projection of the H2B distribution density, calculated for all the SM detections as the number of neighbors within a radius of 100 nm (Figure 26A). Such image representation of the chromatin distribution revealed clusterization patterns, notably, but not only, within an annular region of 3 μm from the nuclear envelope. The clusterization and heterogeneity of H2B distribution is blatant when compared to an image where the experimental data points have been randomized within the nuclear volume, followed by the same image processing method (Figure 26Fig. 1B)

The outcome of single-molecule based super-resolution microscopy experiments are lists of coordinates with a given localization accuracy. Points are dimensionless objects and therefore the outcome of the representation of point patterns is highly dependent on the chosen image rendering method. When the radius used to calculate the number of neighbors was increased to 1 μm, the H2B clusters were not any longer visible in the image (Figure 26). Conversely, the H2B enrichment in the proximity of the nuclear membrane became all the more evident as it is when representing the density as a function of the distance to the membrane (Figure 26D). We can say that there is local enrichment of H2B in the nucleus and that the corresponding enriched regions can be selectively enlightened by different image rendering method. We therefore have an indication that H2B distribution cannot be accounted for simply by a random distribution of clusters of similar size and shape. The heterogeneous density of H2B in the nucleoplasm exists at

different sizes and for a more detailed description of H2B clusterization in 2D we refer to reference (Bohn et al., 2010).

The alternation of enriched and depleted regions raise the question of the average density of chromatin compared to random organization of the genome. Let's note that pure spatial averaging would only smooth H2B density so that it would be undistinguishable from uniform distribution (Fig. S1 and Supplementary text 1). For that reason, only chromatin to chromatin distance can quantify the heterogeneity. The inter-distance distribution $K(r)$ of single molecule detections of H2B is a suitable tool to further quantify the implication of the non-uniform chromatin on the expected distance between loci.

3.3.4.2 Test against Complete Spatial Randomness (CSR)

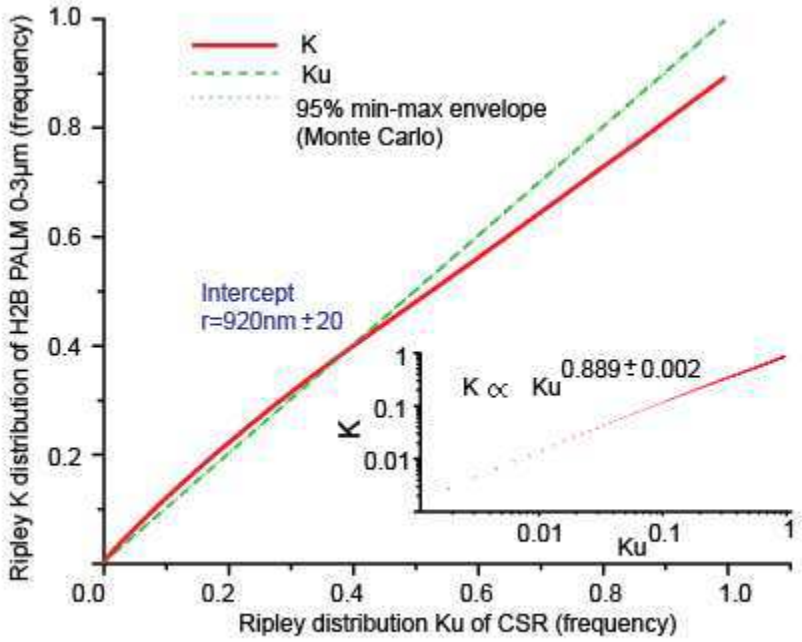

Figure 27:. Test of H2B distribution against complete spatial randomness.. *Re-sampling test of the distribution of H2B detections inside the nucleus against Complete Spatial Randomness (CSR) based on the inter-point Palm distribution. The Palm distribution is the number of points that lie within a circular vicinity of a reference point, averaged on all possible reference.* $K(r)$ *is the Palm distribution of H2B detections and* $K_u(r)$ *the Palm distribution obtained under complete spatial randomness, averaged over 100 Monte Carlo repeats. For distance "r"*

between 0 and 3um with a 10nm step, we computed $K(r)$ *and* $K_u(r)$. *We then plot* $K(r)$ *against* $K_u(r)$ *f. We also plot the 5% and 95% minimum and maximum quantile of the distribution that are hardly distinct due to the fast convergence of the statistic As the K statistic never lie in the quantile envelope, the test that the actual distribution of H2B detection could be observed with CSR is rejected at almost every scale the 10% confidence level. The two distributions cross at radius r=1µm that gives the distance at which H2B distribution is on average denser than CSR. Inset is a log-log representation that displays a power law dependence between* $K(r)$ *and* $K_u(r)$.

The Ripley $K(r)$ distribution, is the reference function to assess the heterogeneity of lists of spatial coordinates or point patterns (Diggle, 2003). It is obtained by choosing a reference point coordinate, counting all the points that lie within a distance r of this reference, and finally averaging $K(r)$ for all the possible references. If one divides the $K(r)$ distribution by the average density of points of the region of interest, one gets a rescaled function that is invariant upon any stochastic diminution of the number of points also called thinning (2007). This a crucial characteristic of the $K(r)$ distribution function that allows us to analyze PALM data which, by the nature of the technique, gives us access to a stochastic subset of the total number of H2B molecules. Moreover, it makes the $K(r)$ statistically independent from the level of H2B-Dendra2 expression and we are therefore able to compare cells upon this criterion. DNA-FISH assays also statistically address $K(r)$ such the distance between loci but with the additional information of their position in the genome sequence and only for one or two sites, the averaging being done at the inter-cell level.

It has recently been shown that experimental data resulting in point patterns in biology can be misinterpreted as clustered due to a low pointing accuracy or a poor number of observations (Weston et al., 2012). We therefore had to test whether the H2B PALM distribution significantly deviates from uniformity. We compared the $K(r)$ distribution of the experimental data to that of randomized data named complete spatial randomness (CSR) (Diggle, 2003) (Figure 27). We took exactly the same number of detections and disposed them randomly in the volume defined by the nuclear envelope and the focal depth. Here the distribution probability of SM detections along the optical axis was limiting but the shape and amplitude of this distribution μ_D is highly conserved in all the nuclear regions (*Figure S 12*). We could therefore use this distribution to

randomly distribute point along the z axis (see Supplementary Information). We then computed the Ripley distribution of the CSR data for 100 different independent realizations. We obtained from this resampling approach the reference $K_u(r)$ and the corresponding 5% and 95% quantiles that define the upper and lower limits of acceptance of uniformity at a particular radius. For every distance from 0 to 3 μm estimated within a 10nm interval, we obtained an envelope for $K(r)$ in which we could accept the complete spatial randomness of H2B-PALM. Due to a fast convergence of the statistics $K(r)$, this envelope is hardly distinguishable from the reference $K_u(r)$. By plotting the points $(K(r), K_u(r))$ for all the distance "r", that is K against K_u together with upper and lower limit envelope, we obtain a curve whose deviation from the line enables to compare the dataset spatial organization to that of the CSR generated dataset.

The first observation is that the $K(r)$ distribution never lies in the min-max envelope around the line $y = x$ except when crossing. The value at which the cross is approximately r=1µm. This means that before r=1µm H2B PALM is on average enriched, so that clusters of size lower than 1µm exist. After that limit, H2B PALM is depleted, thus r=1µm also corresponds to the average distance to a region of lower density. We have therefore a locally enriched distribution of H2B inside the nucleus. Provided the fact that H2B distributes homogeneously along the chromatin fiber, we have therefore chromatin clusters.

It has been shown that quantifying detections from a Palm image can lead to an over estimation of the numbers of particles as the fluorophore blinks (Owen et al., 2012) that could be responsible for local enrichment. Some methods have been proposed to reduce this bias with computational efforts (Sengupta and Lippincott-Schwartz, 2012). We chose to reduce the number of detection incorporated into our analysis according to increasingly strong blinking schemes and to compute the $K(r)$ statistic on the resulted data *Figure S 13*). Blinking is shown to have a minimal contribution to our measurements and the conclusions are still valid even with a drastic rejection of the all possible blinking events. We also ruled out a possible effect of the labeling by repeating the same measurement on the fluorescent free protein Dendra2 without finding the same shape of the CSR test and no enrichment at the cell membrane (*Figure S 14*). Interestingly, the nucleoli of the cell were enriched in Dendra2 and the CSR test was able to

recover this specific enrichment. We investigated several models of cluster distribution to show that the CSR test was indeed able to assess model specificities (*Figure S 15*).

The $K(r)$ distribution has been used in previous studies to compute cluster sizes and distributions on PALM data (Hsu and Baumgart, 2011)(Williamson et al., 2011) or electron microscopy data(Prior et al., 2003). We investigated the H2B cluster dimension and recovered the specific enrichment to the distance r=1µm (Supplementary text 2 and Figure S6). We also showed that after this limit, the deviation of $K(r)$ from $K_u(r)$ is mainly due to the depletion of H2B-PALM segregated in enriched areas which sets an upper limit for our study. Let's note that this threshold is approximately our focal depth so that there is no evidence that our assumptions are not valid at longer length scale.

3.3.4.3 Interpretation of the CSR test

The cluster interpretation of the $K(r)$ function rely on the assumption that there is a typical size for enriched and depleted regions, which is not true if the distribution of sizes is scale-less such as in the case of a fractal structure. The deviation of $K(r)$ from $K_u(r)$ after the 1µm limit shows that effects of the depletion could be seen on larger scale, and the shape of the $K(r)$ and $K_u(r)$ is compatible with a power law. A mean least square log log fit (**Figure 27** inset) gives the dependence $K(r) \propto K_u(r)^{0.9}$. To summarize this result, we can say that the local concentration at a given scale is lower than the same concentration measured on a larger scale. This is compatible with a reduction of dimension. Indeed the portion of space occupied by a fractal is also a power law whose exponent is the fractal dimension (Falconer, 2003).

Theoretical fractals are mathematical objects built upon the repetition of simple rules that also exhibit subunits of various sizes (Mandelbrot, 1975). A fractal can be defined by the following properties: i) a certain degree of self-similarity, ii) an irregular contour and iii) the existence of a fractal dimension that extends the notion of Euclidean dimension (1D, 2D and 3D) to non-integer figures (Falconer, 2003). Self-organized fractals are common in nature and fractals have the very interesting property of summarizing heterogeneity into one single number: the fractal dimension. Typically, a 3D embedded object with a fractal dimension between 2 and 3 will exhibit

lacunarities at every length scale, thus never completely filling its environment. The most common mathematical definition of fractal dimension is the Haussdorff dimension f but its exact formulation makes it irrelevant to a finite data set (Falconer, 2003). Alternative approaches have been proposed to estimate fractal dimensions that are related to the Hausdorff dimension on real data. Among them, the Ripley distribution $K(r)$ can give access to the so-called correlation fractal dimension df of point patterns (Ogata and Katsura, 1991), if we are able to find a spatial range when it scales as a power law as a function to the distance.

The test against complete spatial randomness is a preliminary way to compute the correlation fractal dimension of H2B PALM. A reasonable assumption would be that the complete spatial randomness has a correlation fractal dimension of 3 so that $K_u(r) \propto r^3$ where r is the distance. Extending the power law dependence that we have found, we get $K_u(r) \propto r^{3\times 0.9}$ so that the correlation fractal dimension the H2B localization is $3 \times 0.9 \approx 2.7$. This calculation may be untrue since we do not know the influence of the confinement nor the spatial range of radius where the fractal dimension would be valid and it does not give any spatial range for validity. To accept or reject the fractal nature of chromatin, we had to use a statistic that is independent from cell shape.

3.3.4.4 Correlation fractal dimension

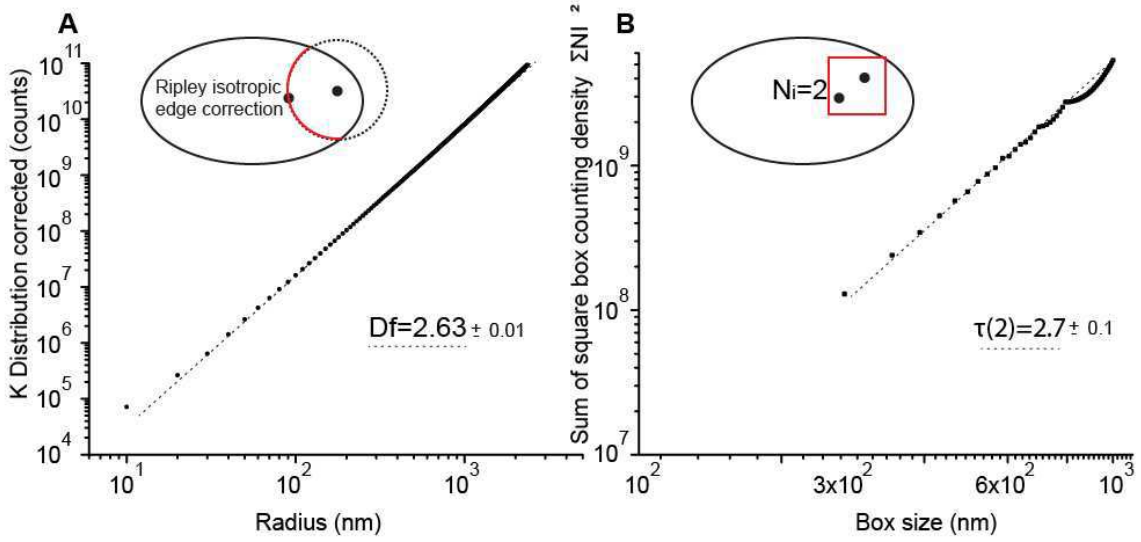

Figure 28: Correlation fractal dimension of H2b distribution. *Panel A: Ripley inter-point distribution for H2B PALM $\hat{K}(r)$, corrected from focal depth and as a function of the distance correction estimated between 0 and 1um displaying a power law dependence. This power law can be interpreted as the correlation fractal dimension H2B. Panel B: Box counting estimation of the correlation fractal dimension. The method is less efficient due to side effects of regions of zero densities, but reveals a scaling factor of the second moment $\tau(2)$, that is close to the value Df that was measured with Ripley $\hat{K}(r)$.*

In order to compare the chromatin structure of different cells, independent of the shape or volume of the nucleus, we treated the nuclear envelope as a restricted region of interest whose effect needed to be corrected. We used the isotropic correction protocols first introduced by Ripley (Ripley, 2004). The basis of this correction is to weight each pair of detections as a function of their relative distance in the $K(r)$ statistic to compensate the bias introduced by the envelope. We also introduced a focal depth correction to obtain to obtain a corrected $\hat{K}(r)$ that only depends on the distance r (see Supplementary Information). The $\hat{K}(r)$ statistic was drastically limiting as the weight smoothed all heterogeneities for distance further than 1µm (*Figure S 16*). Furthermore, the fact that H2B-PALM is enriched close to the cell membrane contradicts the isotropic assumption of the correction. Despite these limitations, the corrected $\hat{K}(r)$ shows a good match with a power law of value 2.63 ± 0.05 (Figure 28). Both the $\hat{K}(r)$ and $K(r)$ scaling are conserved among the cell population (Figure S6 and Figure S7). This number is a reliable estimate of the correlation fractal dimension df of H2B-PALM.

The correlation fractal dimension of a density can also be recovered by ordinary box counting measure. In that case, dividing the space with a cubic mesh, ^{df} should be equivalent to the power law exponent of the sum of square inner density of the meshes as a function of their size, ie the second moment exponent $\tau(2)$. In Figure 3B we show the result of the box counting evaluation of $\tau(2)$. Due to the 1µm focal depth of the experiment, boxes were restricted to the size of 1µm but still do not overlap for big boxes even with density correction. Despite those limitations, for a very small range of boxes, a log log fit of the box counting curve gives the value $\tau(2) = 2.7$ that is the value obtained with the CSR test and K Ripley distribution. $\tau(2)$ is indeed characteristic of multi-fractals that extend the notion of fractals to densities(Falconer,

2003). The multi-fractal framework can also display a fractal spectrum that ranges from 0 to 2.8 (Figure S7) whose implication and formalism is discussed in Supplementary text 3.

FiSH and Hi-C is ensemble averages and any fluctuation in the cell population of the distance between loci is smoothed by those techniques. In order to confront our measure to FISH or Hi-C data, we needed to know its stability between cells and within time. Since super-resolution is not suitable for live cell imaging, we chose a different and more qualitative approach to monitor through time chromatin compaction.

3.3.4.5 Photo-activation of H2B

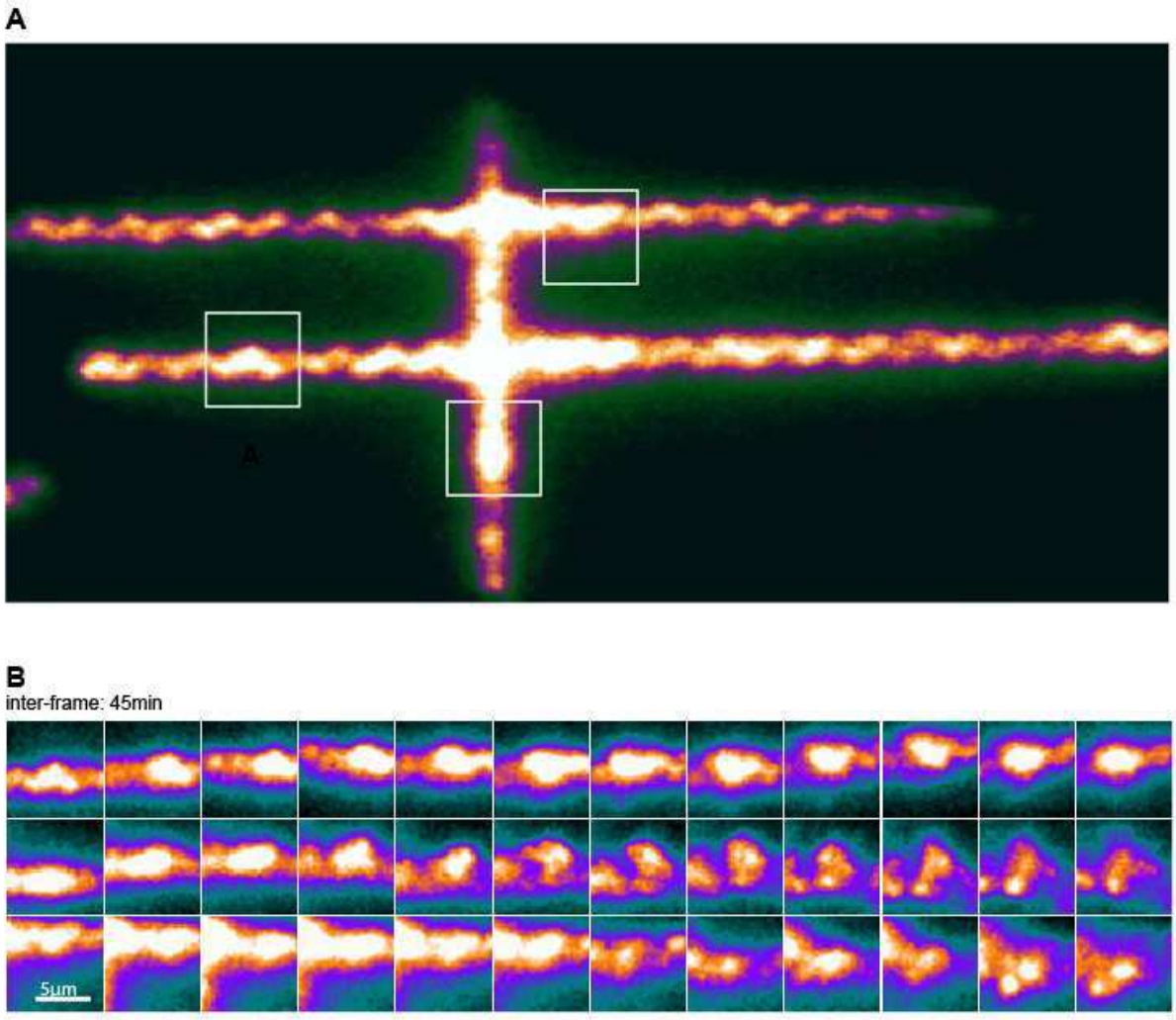

Figure 29:. Time evolution of H2B density *Panel A: U2OS cell nucleus in the inter phase transfected with Photo Activatable –GFP (PA-GFP) tagged H2B. We photo-activated a linear region, and then followed the evolution of the with one frame every 45 minutes. Panel B: 3 photo-activated sub-regions the nucleus followed through time during a 9 hours experiment. We were able to see condensation and de-condensation of the chromatin showing that H2B fractal is not stable.*

The fractal nature of chromatin folding is stable among the population (Figure S6 and Figure S7), but we can ask the following question: "Is this structure stable through the cell fate?", a question that ca not be answered with 3D PALM since the experiment is conducted on fixed cells and live PALM imaging is too transient to recover such a structure. We therefore proceeded to photo-activation assay. We transfected cells with H2B tagged with photo-activatable GFP and draw a pattern with a UV laser on the tagged H2B protein scaffold (Figure 29A). We then followed the condensation and de-condensation of sub-regions of the interphase chromatin fiber for several hours taking an image every 15 mn (Figure 29B). Such events show that the chromatin density is not stable through time and is constantly rearranged.

We therefore have a self-organized yet transient organization of the chromatin. This time dependence makes our result not possible to be fully recovered from ensemble averages such the ones obtained by FISH or Hi-C. Since we do not have information of the position of condensed regions along the DNA chain, we ca not know if such events occur always at the same loci among the cell population. Interestingly we previously observed that chromatin organization in strongly affected by ATP depletion (Shav-Tal et al., 2004) also reflecting this constant remodeling. To summarize this last result, the fractal correlation is a fixed characteristic on a moving chromatin.

3.3.5 Discussion

With this work, we were able to measure the three-dimensional distribution of H2B molecules inside the nucleus of human U2OS cells, using PALM microscopy. We confirmed that H2B distribution is heterogeneous in the nucleoplasm, and we could determine that chromatin is organized in regions of enriched density that can be seen at different length scales, from 10 nm to 1 μm (the technical limit of our measure). The single-molecule nature of PALM microscopy allowed us to address the Ripley distribution of H2B, i.e. the distribution of distances between all

detected H2B molecules. With these tools, we developed an analytical method that revealed that H2B distribution deviates significantly from that of complete spatial randomness. Moreover, this deviation follows a power law which exponent corresponds to a fractal dimension of 2.6, an invariant value among different cells analyzed.

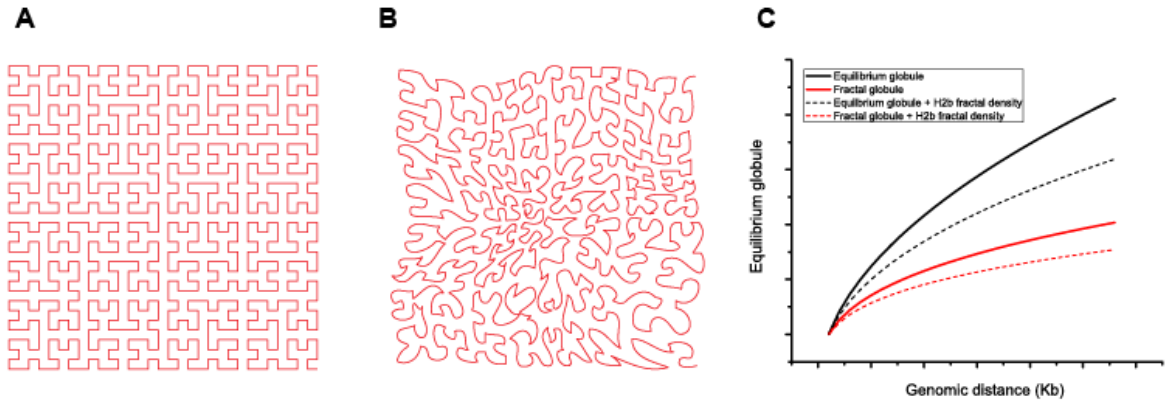

Figure 30: Superposition of H2B fractal density on the fractal and equilibrium globule model. *Panel A: The Hilbert space filling curve that homogeneously fills the 2D space used as an graphic example of the space filling DNA fractal globule. By applying a density over the representation, we gets the heterogeneously space filling curve of Panel B. Panel C: The physical distance as a function of the genomic distance for 4 models: the equilibrium globule, the equilibrium globule with fractal density, the fractal globule and the fractal globule with fractal density, with respective power laws of* $\frac{1}{2}$*, 0.43,* $\frac{1}{3}$ *and 0.29.*

A chromatin fiber with a spatial distribution of correlation fractal dimension of 2.6 will exhibit zones of enriched and zones of depleted density. These enriched and depleted regions will be juxtaposed, and found at all the length scales. Subsequently, close pairs of loci are more numerous than expected upon random organization. The finding that loci are closer than expected by a random distribution taking into account only their genomic distance was the reason for the development of the fractal globule model of chromatin organization as opposed to the equilibrium globule (Mirny, 2011). The fractal globule is also a non-equilibrium state that represents of chromatin as a non-entangled space filling polymer. However, the nature of our result significantly differs from the globule interpretation. Chromatin conformation capture related techniques are averaged over a large population of cells and thus unable to recover the correlation fractal dimension we present here.. While every tested cell showed the same correlation fractal dimension of 2.6, Photo-activation assays also show that chromatin compaction is the result of a highly dynamic system. Since ensemble measurements are blind to cell to cell and dynamic variation, we can hypothesized that the correlation dimension we present

here is an additional layer of organization to the globule model. Although there is no exact representation of the fractal globule, the best mathematical model is a space-filling curve such as the Hilbert curve (Figure 30A). On a fractal globule, the average physical distance $R(s)$ between two loci as a function of their relative genomic distance s scales as a power law: $R(s) \propto s^{\frac{1}{3}}$ that is significantly different from the exponent expected at the equilibrium state, the equilibrium globule, for which $R^{equilibrium}(s) \propto s^{\frac{1}{2}}$. On a chromatin structure with correlation fractal dimension of 2.6, two loci taken at random will have a relative distance "lower than expected" because they have higher chance to have be picked in the same cluster and chromatin density is no longer uniform (Figure 30B). More precisely, if R_e is the distance expected if the space was homogenously filed and R_o is the observed distance we get: $R_o \propto R_e^{\frac{2.6}{3}}$. Taken together with the fractal globule exponent, we obtain: $R_o(s) \propto s^{\frac{2.6}{9}} \approx s^{0.29}$. The same calculus can be extended to the equilibrium globule and in both cases existence of chromatin density clusters adds a higher level of complexity in the understanding of chromatin folding creating a relation between genomic and physical distances lower than expected (Figure 30C).

The previous results only hold if chromatin is indeed a globule. The validity of the globule interpretation of the link between genomic and physical distance is strongly discussed among the scientific community (Bickmore and van Steensel, 2013) and our result may be in line with this controversy. On a fractal or on equilibrium globule the density of chromatin is uniform, which we have proven to be wrong. Rejecting globule interpretation, we believe the cluster organization of chromatin we present here is rather consistent with the existence of DNA domains of higher compaction such as the topological associated domains found with chromosome conformation capture related techniques (Bickmore and van Steensel, 2013). As a result of our direct observation and analysis of the correlation fractal dimension, we can now assert that such domains do not have a characteristic size but rather can be found at all sizes. With all the evidences in hand, the chromatin environment we propose is a non-equilibrium state that favors interactions between distant loci. This organization extends the genomic distance at which distant enhancers can act on specific genes.

Our 3D-PALM assay cannot discriminate between different models of dependence between genomic and physical distance since we only have access to foci and not to sequence loci. However, our live cell experiment rules out the possibility that the observed non-equilibrium chromatin organization is the result of insufficient relaxation time in between mitotic condensations which was proposed as a possible explanation for the fractal globule. Our results are in favor of a model where chromatin organization is actively maintained by enzymes acting on chromatin compaction. In such a dynamic model, particular genomic regions constantly explore their neighboring DNA constantly sampling distant enhancers. Therefore transcription activation involving a distant enhancer would just be the result of the trapping of a chromatin conformation that occurs naturally even for loci separated by large genomic distances.

3.3.6 Material and Methods

3.3.6.1 PALM imaging

Microscopic image has a resolution limited by Abbe's formula $d = \frac{\lambda}{2NA}$, where, λ and NA are respectively the illumination wavelength and the numerical aperture of the objective. It gives the value $d = \frac{551}{2 \times 1.49} \approx 184nm$ for an inverted microscope under green illumination that is far from the precision needed to assess nucleus organization. The PALM principle is to resolve tagged proteins sequentially so that they never overlap. We transfected U2OS cells with a tagged version of H2B. The tag we used is dendra 2, a photo-switchable fluorochrom, that can be turned from a green emitting state to a red emitting state under UV illumination. After fixation with para- formaldeid, we stochastically photo activate the sample to reach single molecule signal (Betzig et al., 2006). The single molecule signal is the so-called point spread function whose center gives the localization of the single protein in the focal plane xy of the camera.

To determine the z position of the molecule, we used deformable mirror to induce astigmatism on the Point Spread Function (Izeddin et al., 2012). Therefore, by fitting the signal with a 2D Gaussian with free sx and sy width, we are able to compute the x and y position with 10-20nm precision accuracy as well as the sx/sy ratio (Sergé et al., 2008). With the computation of calibration curves on beads preliminarily deposed on the coverslip we can estimate the z axis position with a 50nm pointing accuracy

3.3.6.2 Focal depth and Z correction

The distribution of H2B-PALM $\mu_D(z)$ along the z axis is limited by the focal depth of the camera. $\mu_D(z)$ is the convolution between the real distributions of position $\mu(z)$ and a detection bias that favors positions in the focal plane of the camera. This detection bias varies from one experiment to another as a function of the noise level, but is remarkably stable among different regions of the cell (Figure S1).

As we are acquiring H2B positions on a large area, the best assumption is the stationarity of the point pattern In the z direction so that $\mu_D(z)$ is the best estimator of $\mu(z)$ (Baddeley, 2004). We assumed that this distribution $\mu_D(z)$ is independent of the real distribution of H2B position $\mu(x, y, z)$ that we would have obtained without this bias, so that, with Bayes theorem:

$$\mu(x, y, z) = \frac{\mu'(x, y, z)}{\mu_D(z)} \qquad (89)$$

where $\mu'(x, y, z)$ is the measured distribution of H2B detections in the nucleus.

Density measurement of the box counting method where subsequently corrected using a 10 nm binning estimation of this distribution.

Drawing CSR points, one needs to define the boundaries of the distribution. In the z direction, the distribution was drawn according to the selection bias $\mu_D(z)$. In the x y plane the limit of the cell was defined as the convex envelope of the z projected PALM image of H2B with 10nm bining, and a 10 nm opening an closure of the image to exclude isolated detection. $\mu_u(x, y) \vdots \mu_D(z)$ where $\mu_u(x, y)$ is uniform inside the convex envelope.

3.3.6.3 Isotropic correction of the $K(r)$ distribution

The $K(r)$ distribution is an ever-increasing function, sensitive to pointing accuracy (Kagan, 2007) and highly dependent of the embedded volume. The latter can be clearly observed when considering a point pattern randomly distributed in a circular or spherical domain of radius R. In that case, the $K(r)$ function exhibits a saturation behavior at distance $\frac{R}{D+1}$, where D is the D is the embedded dimension 2 or 3, for the circular and the spherical case, respectively (Kagan,

2007). For computational speed and efficiency, we pre-estimated those weights and stored them as an image before computing the corrected $\hat{K}(r)$ statistic. In those weights, we also integrated the limiting focal depth.

We assume that the cell boundaries is independent from the z direction so that the theoretical weights can be expressed in the following way:

$$W_{ij} = \frac{\int_{r=-|i-j|}^{|i-j|} w_{ij} \times 2\pi r \times \mu_D(i+r)dr}{4\pi r^2} \qquad (90)$$

where w_{ij} is the Ripley weight and is estimated on the 2D projection of the nucleus in the focal plane of the camera. However, the correction is very computer time consuming and is to be made on all the pairs of H2B detections. To get around this problem, we estimated the Ripley weight on a 10nm grid and then interpolated the results. The 2D weight w_{ij} was estimated by the convolution of the binary image of the nuclear envelope with a circular mask for successive radius between 10nm and 3um every 10nm All those manipulations make the estimation a lot faster, since most weight estimation are stored in images. However, as the Ripley weights increase quadratically as a a function of the distance to the focal plane, we had to restrict our analysis for reference point i of the $K(r)$ distribution to a region were the z distribution is relatively high, within the 100nm peak of the distribution.

3.4 Yeast locus mobility

with Judith Miné-Hattab, Ignacio Izeddin, Rodney Rothstein and Xavier Darzacq

This is a work in progress. Most of the results shown here are still debated and investigated by authors.

3.4.1 Introduction

Chromosomes are meter long molecules that fold into a micrometric envelope, the nucleus. This folding is not static, but dynamic even in the interphase when chromosome are de-condensed (Miné-Hattab and Rothstein, 2013). Saccharomyces cerevisiae yeast is a model organism that has been intensively used to study chromosome mobility (Fung et al., 1998) (Heun et al., 2001). Recent works in Saccharomyces cerevisiae yeast have shown that the resulting mobility is related with the cellular functions or dysfunctions. For instance transcription (Cabal et al., 2006), cancer (Fudenberg et al., 2011), or double strand break (DSB) significantly modify loci movement. DSB is the accidental breaking of the DNA strand that has the potential to dramatically alter the genetic material. One pathway to repair DSBs is by homologous recombination. The broken loci will pair with its corresponding allele which will be used as a template for DNA repair. In yeast, recent studies reveal that chromosome ability to explore its environment is significantly increased following DSB induction (Miné-Hattab and Rothstein, 2012)(Dion and Gasser, 2013) Surprisingly, the increased mobility was not because DSB would create a loose DNA chain, since, in 80% of the cases both broken double strands stayed glue together (ref).

There are some specific features in the yeast nucleus that has proven or is supposed to have impact on loci mobility. Among those features, some are mechanical constraints that are not sequence specific. Its genome is composed of 16 chromosomes in the haploid form and 16 pairs in the diploid form. The chromosome in anchored in nucleoplasm membrane in the telomeric region and in the centromeric region via the spindle pole body (SPB). Motions of those anchoring exist either for the telomere (Hozé et al., 2013) or the SPB but have proven to be order of magnitudes slower than the intra chromosomal motion. Aside mechanical constrains, several

nuclear factors have also a role to play in chromosome mobility, and most of them have been studied in the specific case of DSB. Among those factors are ATP dependent chromatin remodelers, and proteins of the repair complex composed of protein rad51 among others . The relative importance of mechanical compared to chemical factor is still debated. It has recently been hypothesized that a simple mechanical model could recover most of the characteristic of the motion observer *in-vivo*(Wong et al.) .

To quantify the mobility of the loci, the standard statistic remains the mean square displacement (MSD), but several models have been confronted to measure MSD. A proposed model is *confined diffusion*, free diffusion in a restricted area (Miné-Hattab and Rothstein, 2012). An alternative model that has been proposed to is anomalous diffusion, characterized by a power law form of the $MSD \propto t^{\alpha}$. The confined diffusion model implies an upper limit for the MSD that is not satisfied with anomalous diffusion model. Anomalous diffusion has been theorized to be crucial to understand reaction kinetics at the individual reactant scale, which chromosome pairing is an example (Bénichou et al., 2010). Different anomalous exponent α have been reported in the literature ranging from 0.4 to 0.5(Cabal et al., 2006),(Weber et al., 2010b) which has been related to polymer physics, but so far no consensus no consensus exists.

We have followed the movement of a yeast locus consisted of repeated LacO or TetO repeats that binds to fluorescently tagged protein for different times and recovered that the locus was moving sub-diffusively at least up to our experimental limit. Surprisingly, the anomalous exponent was dependent of the exposure time of the camera that would define regimes of the observed motion. As expected in the case of DSB, either randomly induced by □-irradiation or site specific with the I-*Sce*l system, the mobility was increased. We measured this increase with a higher anomalous coefficient. We did our measurement on diploid cells. On haploid cells, the motion was measured less anomalous and features the 0.5 exponent that was previously reported(Bancaud, 2012). Those results are coherent with a model of chromosome as free polymers with different degree of interminglement that was proposed by PG de Gennes as *the reptation model* (de Gennes, 1971).

3.4.2 Results

We used the construction of Miné-hattab et al. (Miné-Hattab and Rothstein, 2012) in which two homologous loci (*URA3* on each chromosome V) are fluorescently labelled by inserting a LacO/LacI-YFP and a TetO/TetR-RFP array respectively. We also labelled the SPB by fusing SPC110 to YFP. A specific DSB could be induced with galactose via an I-scel site near TetO array (**Figure 31** A and B). We imaged diploid cells in S phase when a bud was forming in the periphery of the membrane and recorded the loci position, provided that they stay in the back focal plane of the camera. We used three different exposure times for recording the position of the locus: 0.005s, 0.05s and 0.5s. For long exposure time (0.05-0.5s), we used the SPB as a reference point to correct the displacements of the locus inside the cell.

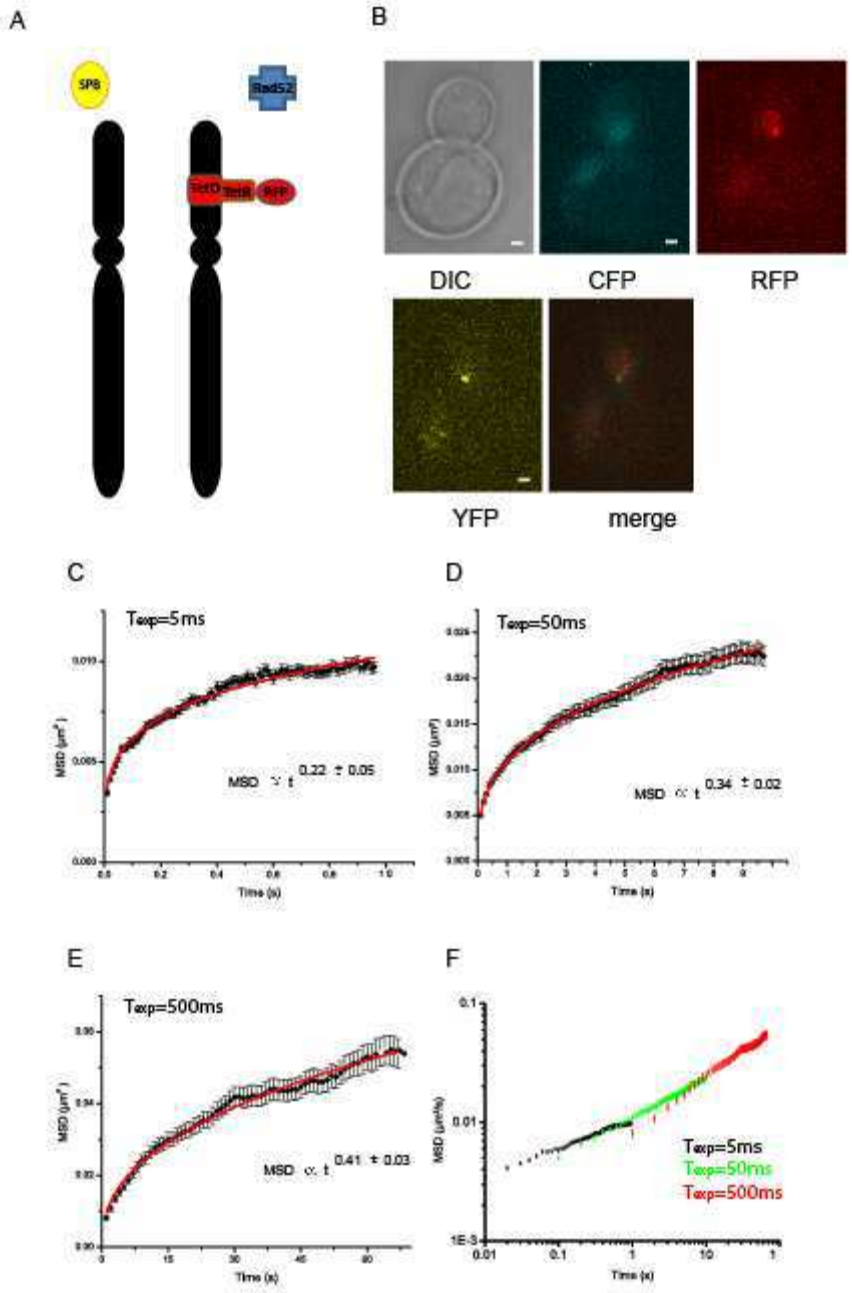

Figure 31:.Different regimes of movement as a function of the exposure time. *Panel A: Description of the strain used to study chromosome dynamics. The tetO array (3x112 copies) is adjacenton chromosome V at URA3 (top). The Rad52, TetR and Spindle Pole Body (SPB) proteins are tagged with CFP, RFP and YFP, respectively. Some strains also contain a galactose-inducible I-SceI insertedat the LYS2 locus. (b) DIC, CFP, RFP and YFP images. Flattened images of all 15 z -stacks are shown inmaximum z -projection. In the absence of a DSB, there is no Rad52 focusand each chromosome V is visualized by an RFP and YFP focus. Scale bar:1 µm. Panel C, D E: Global Mean square displacement, time and ensemble averaged, of the movement of the locus in diploïd yeast for different exposure times in S phase. The time*

upper bound was set as one third of the longest recorded trajectory. 3 trajectories out of 15 and 1 trajectories out of 7 were excluded respectively for exposure time 0.05s and 0.005s, for aberrant displacements one order of magnitude higher than the other trajectories. The error bar is the 95% confidence interval of the mean estimated by bootstrap. We fitted the data with ordinary least square fitting to a function of the form $f(r) = at^{\alpha} + b$ *with constraint* $b > 0$. *Panel F Global mean square displacement in log log scale showing the 3 different regimes.*

After tracking we plot the time and ensemble averaged MSD up to 1/3 of the recorded longest trajectory. Less than 10% of the recorded trajectories were excluded from the analysis due to an average squared displacement one order of magnitude larger (Figure 31 C, D and E). We fitted the resulted MSD to a power law and found very good agreement. In log log scale the power law exponent of each graph is blatant (Figure 31 F). Fitting MSD to a power law has been the subject of discussion in the scientific community (Destainville et al., 2008) (Saxton, 2012b). Authors shown that power law exponents can appear as artifact in the case of confined diffusion (Lill et al., 2012) or due to a bad pointing accuracy in log-log scale (Martin et al., 2002). We fitted the MSD either in lin-lin scale with a positive offset term or in log log and found similar values which discarding artifact from a bad pointing accuracy(*Figure S 20*). We also try to fit the data to an exponential form that would account for confined diffusion(Wieser and Schütz, 2008) without satisfactory results(*Figure S 21*). Since the power law exponent is real, yeast locus motion can be labelled as *sub-diffusive* (Metzler R. and Klafter J., 2000).

The most surprising aspect of the anomalous fit is that we did not find the same anomalous coefficient as a function of the exposure time. The anomalous exponents were respectively 0.22, 0.34 and 0.41 for exposure time 0.005s, 0.05s and 0.5s respectively. Although surprising, those results were coherent with one-another. Reproducing 0.05s exposure time data from 0.005s exposure time position averaging and 0.5s from 0.005s exposure time, we were able to recover the exact same anomalous coefficient as the raw data (*Figure S 22*).

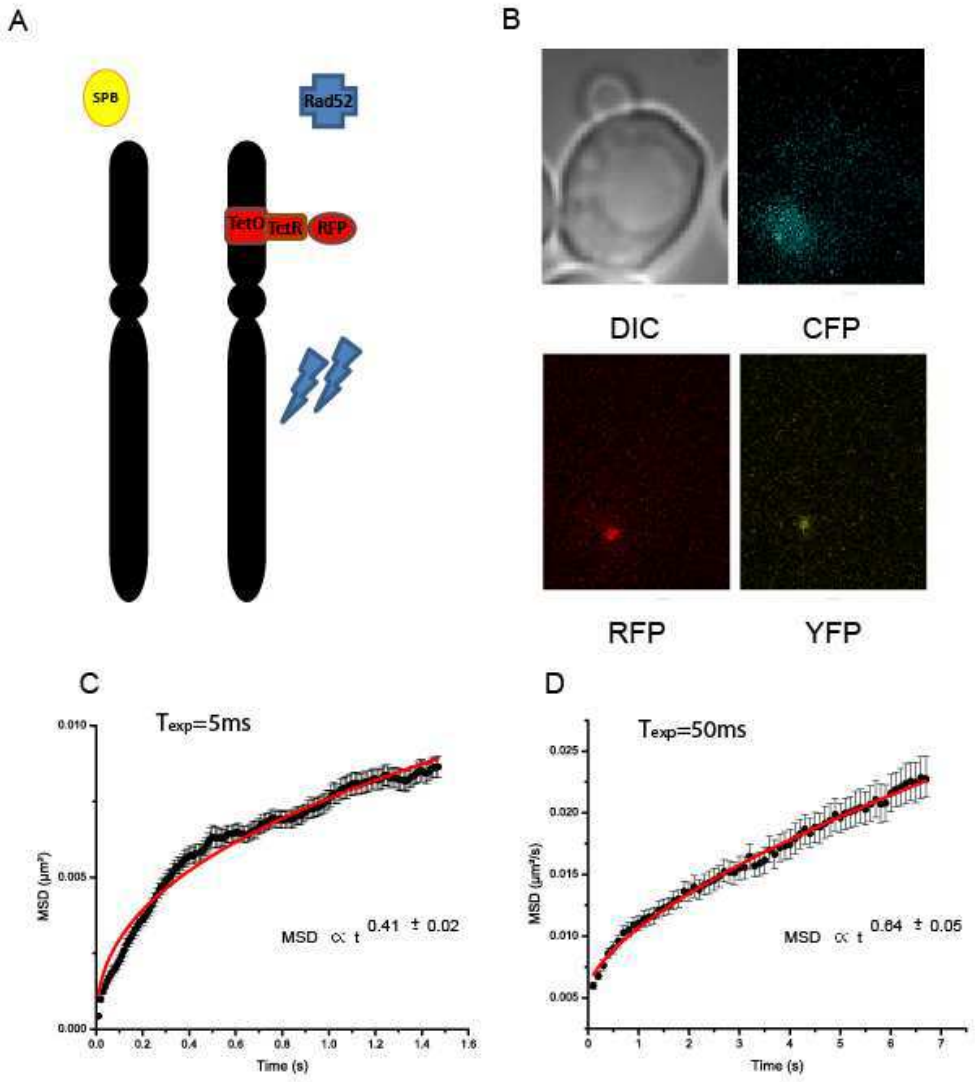

Figure 32:.Evolution of the anomalous coefficient after double stand break (DSB). *Panel A strain with γ- irradiation of 100Gy that would cause an average 10 double strand breaks per nucleus. Panel B Co-localisation of the locus with a rad52 foci Panel C and D Global Mean square displacement for 5ms nd 50ms exposure time*

We investigated the several perturbations of the cell in relation with DNA repair. Inducing random DSBs with γ-irradiation, we observed the increase of mobility that was previously reported. The anomalous exponent shifted from 0.34 for the control to 0.42 (Figure 32)..

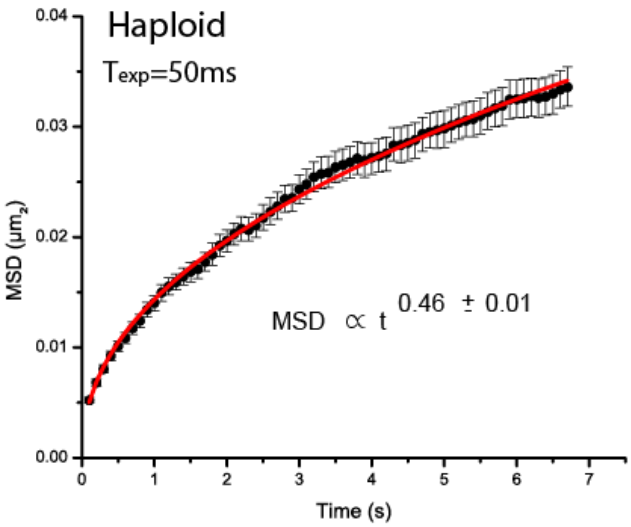

Figure 33: Global mean square displacement for haploïd strain. The anomalous exponent is fit in lin-lin

We also investigated ploidy since authors have reported a 0.5 exponent from anomalous diffusion of loci (Bancaud, 2012) and found the same exponent which is a proof of the reproducibility and the reliability of our approach (Figure 33).

3.4.3 Discussion

3.4.3.1 Comparison of the measured anomalous coefficients to previous studies

Anomalous exponents of the MSD were previously reported in the literature describing the motion of loci in yeast. To our knowledge the first reported exponent was 0.42 by Cabal et al.(Cabal et al., 2006). Weber et al found in bacteria an exponent of 0.39 (Weber et al., 2010b) which was similar to the "comportment" observed in yeast(Weber et al., 2012b). Those two studies were performed using a same exposure time of the camera of 0.2s. The value ~0.4 was consequently considered as the standard value for anomalous loci movement inside the nucleus (Zimmer and Fabre, 2011) and is coherent with the 0.41 value we recovered at 0.5s exposure time. However, this exponent is not the only one measured. Albert and colleagues recently reported an exponent of 0.5 with also a 0.2s exposure time (Albert et al., 2013). Those exponent where confronted to various polymer models

DNA is indeed a polymer although it is unclear if the monomeric unit that should be considered inside the nucleus is the base or the nucleosome. Two models have predicted the anomalous motion of monomers of a polymer in a diluted solution: the Rouse model (Rouse, 1953) and the

Zimm model (Zimm, 1956). The Rouse model predicts a $\frac{1}{2}$ exponent and the Zimm model a $\frac{1}{3}$ exponent. Since 0.5 exponent is the Rouse A Bancaud tried to recover a *persistence length* from his data and the Rouse model. However the nanometric value of the recovered length however does not match the 50nm has been previously measured in-vitro (Garcia et al., 2007). The Rouse model not only theorized a $\frac{1}{2}$ exponent but also a free diffusion regime as time longer than T_R, the time needed for the Rouse chain to relax. The existence of different regimes of sub-diffusion has been previously shown in higher eukaryotes. On U2OS osteosarcoma cell lines, studying the motion of telomeres labelled with GFP-RFP2, Bronstein et al found 3 anomalous exponents 0.32, 0.51 and 1.15 respectively at 100Htz, 5Htz and 0.05 Htz (Bronstein et al., 2009). In mouse embryos, Roukos et al recently exhibited averaged MSD that were apparently free diffusive and therefore with an exponent of ~1 (Figure3A of (Roukos et al., 2013)).

The ~0.4 anomalous exponent cannot be predicted by Rouse and Zimm models and even less the 0.22 and 0.34 that we have measured at fast frame rates. Simulations have shown that high confinement of the polymer would result in monomeric anomalous exponent of at least 0.46 in the Rouse regime (Weber et al., 2010a). To solve that problem Weber et al introduced an additional parameter to explain the low 0.39 coefficient, the *visco-elasticity* of the nucleoplasm so that motion was proposed to undergo a Rouse regime but with fractional dynamics(Weber et al., 2010a).

3.4.3.2 De Gennes's Reptation model

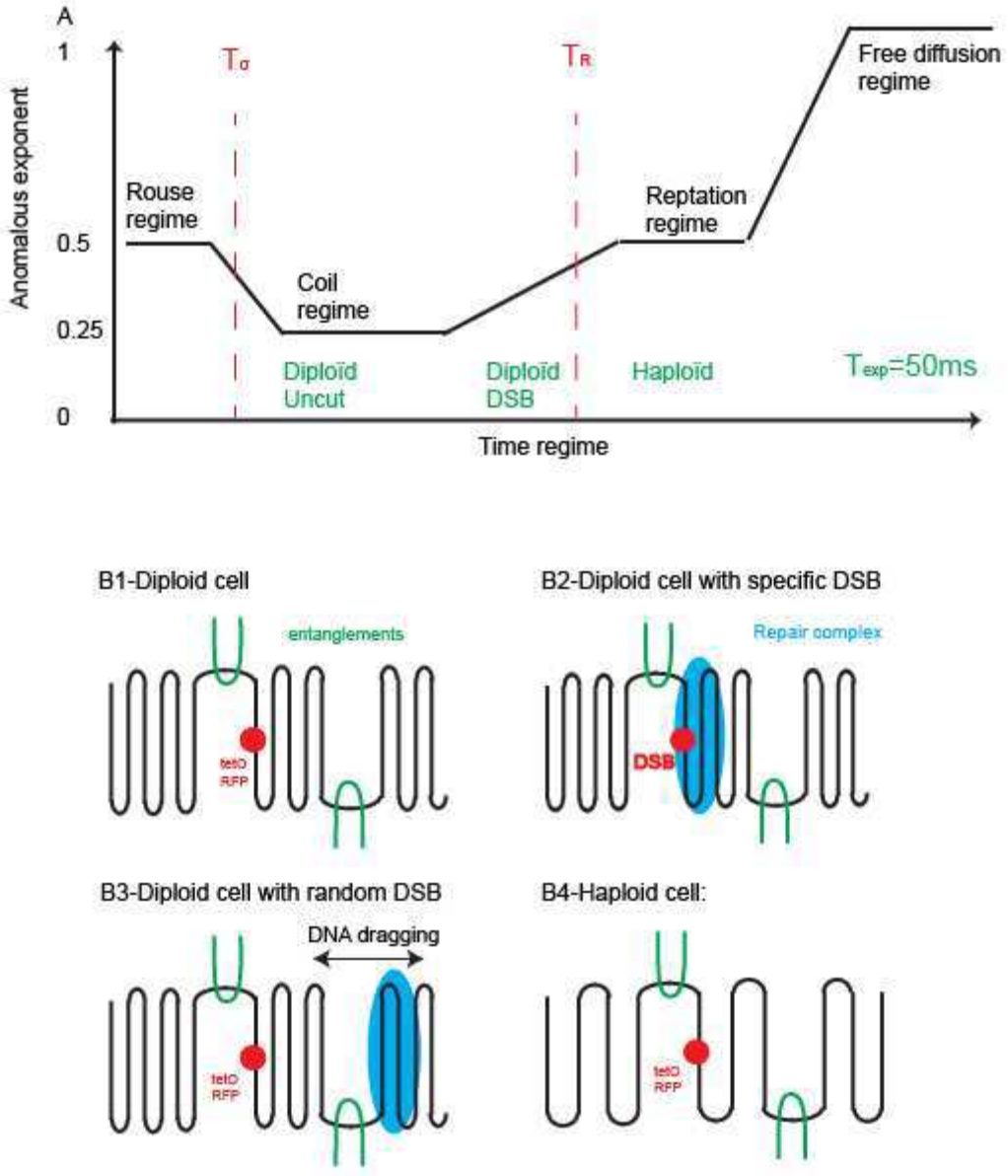

Figure 34: Entangled polymer interpretation of the anomalous exponent. *Panel A: Classification of the time regime for various anomalous exponents for entangled polymer solution.* T_σ *is the time needed for a monomer reach the boundaries imposed by entanglements.* T_R *is the time needed for the chain to relax at entanglement coils. Panel B Different scenarios for exposure time 0.05s. Panel B1 in a diploïd cell, the level of entanglement is high and we are in a coil regime. Panel B2 in the case of a DSB, relaxing time at the coil is reduced at the site by the repair complex that gather the chain together. Panel B3 For random DSB, the chain length reduced either by repair complex gathering or just cut.* T_R*, the time for the whole rouse chain to*

relax is therefor reduced. Panel B4: For haploïd cells, the level of entanglement is lowed than for diploïd cells and the regime is shifted to the reputation mode.

The Rouse model cannot explain anomalous exponent as low as measured, but in the case of high interminglement of polymer chains, another model was developed that could predict anomalous exponent as low as $\frac{1}{4}$. In 1971, PG de Gennes introduced the *reptation model* of individual polymer motion(de Gennes, 1971). In a reptation mode of motion, the polymeric chain is constrained through succesive *coils* that define a *tube* in which the motion of the polymer occurs. In 1982, De Gennes explicited three different regimes of sub-diffusion of individual monomers (de Gennes, 1982a). Those three different regimes are bounded by time T_σ and the Rouse time T_R, which is the time for the whole chain to relax at the coils (Figure 34 Panel A). For regime lower than T_σ, the monomer does not encounter adjacent polymer chains and the motion is Rouse like. For regimes t with $T_\sigma < t < T_R$ the motion is at "coil equilibrium " and its main characteristic is the back and forth movement at the coil. The motion on diploid cell with 0.005s exposure time seems to match this description of frequent re-sampling. When the motion is averaged with higher exposure time (0.05s and 0.5s) , it changes regime so that we get closer to the Rouse time T_R. Let's note that the exponent $\frac{1}{2}$ and $\frac{1}{4}$ proposed for the tube regime came indeed respectively random walks on the diffusion reptation tube and all its possible conformation, ensemble averaged. For that reason, those exponents cannot be recovered from an individual monomeric MSD unless the observed time would be so long that we switch regime.

Another argument in favour of the reptation model is the difference of regimes observed between haploid and diploid cells at $T_{\exp} = 0.05s$. The Rouse time is function of the interminglement degree that itself depends on the concentration of polymers. Haploid cells have half the genetic material of diploid cell and super-resolution imaging of the chromatin are in favour of a lower degree of crowding in haploid yeast nucleus (data not shown). For that reason motion in haploid cell is rather in the *reptation regime* (Figure 34 B4).

3.4.3.3 Double strands break and reptation

With the reptation model in mind, what would be the implication of a DSB on the broken locus motion? At $T_{\exp} = 0.05s$, we have measured a higher anomalous coefficient compared to control for either I-*Sce*I site induced double strand break or random double strand break induced by irradiation. For that reason we switch regimes compared to simple diploid cells and switching can be either towards a lower or higher time regime.

The bigger mobility that was previously reported(Miné-Hattab and Rothstein, 2012) is not in favour of a reduced time regime. Indeed, it is much more in favour of a decreased rouse time T_R. Since the Rouse time depends on the chain length, it is possible that the repair complex gatherers individual monomers, so that the time to pass through a coil will be reduced(Figure 4 Panel B). Such a scenario however poorly accounts for the reduced mobility that was also observed in the case of random induced double strand break **Figure 34** B). The change of conformation of the DNA chain in the case of DSB will need to be further investigated.

3.4.3.4 Scanning efficiency of sub-diffusive motion of Loci

As a conclusion, we have shown that locus motion in yeast was sub-diffusive with different anomalous coefficients representing different regimes. Those regimes are well described by the *reptation model* of movement of entangled polymers. The anomalous exponent accounts for recurrent motion, with frequent resampling of the space. For that reason anomalous diffusion can have drastic implication on cell DNA reaction kinetics such as chromosome pairing (Bénichou et al., 2010)

What the reptation model does not take into account however is the larger scale barriers that confine the motion. Loci position is confined in micrometric domains (Berger et al., 2008) whose boundaries are supposed to be reached at longer scales that our study. In the case of chromosome pairing, it is unclear what is predominant in the search time. If the broken allele and its homologue are physically close then reaction time will obey “non markovian reaction kinetics” (Guérin et al., 2012). If the broken allele are segregated far away from each other then it’s rather the confinement and would be a key parameter of the search time (Agmon et al., 2013). In the case of double strand break, the constraints induced by the interminglement of the

chromosome are reduced. This brings together chemical nuclear factor action and biophysical constraints to explain the increased mobility of broken locus.

4 Conclusion

"An intellect which at a certain moment would know all forces that set nature in motion, and all positions of all items of which nature is composed, if this intellect were also vast enough to submit these data to analysis, it would embrace in a single formula the movements of the greatest bodies of the universe and those of the tiniest atom; for such an intellect nothing would be uncertain and the future just like the past would be present before its eyes."

"Une intelligence qui pour un instant donné connaîtrait toutes les forces dont la nature est animée et la situation respective des êtres qui la composent, si d'ailleurs elle était assez vaste pour soumettre ces données à l'analyse, embrasserait dans la même formule les mouvements des plus grands corps de l'universe et ceux du plus léger atome; rien ne serait incertain pour elle, et l'avenir comme le passé serait présent a ses yeux."

Pierre Simon de Laplace

Laplace's deterministic assertion is the dream of every scientist. In cellular biology, there is no lower scale than the molecule. Aside their chemical properties, the bio-molecules' precise motion inside cells is the ultimate data to understand the clock of cell metabolism. Indeed, cellular functions are time regulated, especially chemical reactions inside the nucleus. Among nuclear reactions, genes transcription is a striking example of a reaction regulated at the single molecule level. There are, for most genes, only a few copies in the genome and therefore a few places to bind for gene regulators.

Fluorescent microscopy has shed light on cellular functions. During half a century, numerous breakthroughs have increased the resolution of the technique so that the tiny details of the cell architecture can now be imaged live. However, until recently, only the bulk motion and position of molecules could be extracted by the technique. Thanks to some genius inventors who found ways to break the fundamental resolution limit of microscopy, we can nowadays detect and follow cellular single molecules with ordinary inverted microscopes. In order to reach such a resolution, there is an experimental trade-off. Single molecule microscopy requires sparse data and is time consuming to get a sufficient sampling of cells. Another limitation is the indirect availability of the molecule position and displacements. Image acquisition needs to be processed

by algorithms, whose numerous steps are also sources of error. Some efforts have been undertaken and superesolution currently provides robust cellular molecule trajectories.

When it comes to precise quantification of the cellular interactions, nuclear single molecule microscopy is, to my opinion, still an emerging field. Bulk fluorescent imaging provides direct spatial and time image correlation and averaging. Finding the mean comportment of a molecule from an ensemble of trajectories is not as straightforward. Once the possible averaging artifacts ruled out, the wide range of possible spatial statistics on single molecule trajectories helps us to understand the way a molecule is going to find its partner in the nucleus.

We have investigated the motion of nuclear elements with single molecule microscopy. We have shown that the chemical properties of the nuclear elements strongly affect their mode of motion. With the example of the transcription factor P-TEFb, we proved that regulators such as chaperons do not only move the chemical equilibrium but also change the type of nuclear exploration of regulated proteins. One key parameter to understand nuclear reaction is the structure of the nucleus itself. With single molecule microscopy, we can now extract the 3D organization of the nucleus. Specifically addressing the de-condensed nuclear DNA, chromatin, we have effectively established that it has fractal properties. Finally we have used single molecule to quantify the fundamental determinants of DNA motion in yeast.

Single molecule microscopy is now pushing its own limits. It was long restricted to surface imaging in 2D and we obtained among the first results of deep samples imaging in 3D. Fluorochrom will soon be accurately followed for minutes before bleaching. The time frontier will be however the harder to cross since it not only depends on the chemistry but also on the ability of the experimentalist to efficiently track the molecules. However, the time range restricts single molecule imaging to chemical reactions rather than cellular physiology. In the end, there is a limit that cellular molecule live cell imaging will probably never cross. To image a single molecule, the experimentalist needs the molecule environment not to emit light. For that reason, live cell single molecule imaging will always be blind to concentration. We can see live nuclear reactions at single molecule level but Laplace’s dream of a single molecule metabolism will never be achieved.

5 Bibliography

Abraham, A.V., Ram, S., Chao, J., Ward, E.S., and Ober, R.J. (2009). Quantitative study of single molecule location estimation techniques. Opt. Express *17*, 23352–23373.

Abrahamsson, S., Chen, J., Hajj, B., Stallinga, S., Katsov, A.Y., Wisniewski, J., Mizuguchi, G., Soule, P., Mueller, F., Dugast Darzacq, C., et al. (2013). Fast multicolor 3D imaging using aberration-corrected multifocus microscopy. Nat. Methods *10*, 60–63.

Adam, R.L., Silva, R.C., Pereira, F.G., Leite, N.J., Lorand-Metze, I., and Metze, K. (2006). The fractal dimension of nuclear chromatin as a prognostic factor in acute precursor B lymphoblastic leukemia. Anal. Cell. Pathol. *28*, 55–59.

Adler, J., Shevchuk, A.I., Novak, P., Korchev, Y.E., and Parmryd, I. (2010). Plasma membrane topography and interpretation of single-particle tracks. Nat. Methods *7*, 170–171.

Agmon, N., Liefshitz, B., Zimmer, C., Fabre, E., and Kupiec, M. (2013). Effect of nuclear architecture on the efficiency of double-strand break repair. Nat. Cell Biol. *15*, 694–699.

Albert, B., Mathon, J., Shukla, A., Saad, H., Normand, C., Léger-Silvestre, I., Villa, D., Kamgoue, A., Mozziconacci, J., Wong, H., et al. (2013). Systematic characterization of the conformation and dynamics of budding yeast chromosome XII. J. Cell Biol. *202*, 201–210.

Alberts, B. (2008). Molecular biology of the cell (New York: Garland Science).

Alcor, D., Gouzer, G., and Triller, A. (2009). Single-particle tracking methods for the study of membrane receptors dynamics. Eur. J. Neurosci. *30*, 987–997.

Alexander, S., Orbach, R., and others (1982). Density of states on fractals:«fractons». J. Phys. Lettres *43*, 625–631.

Appelhans, T., Richter, C.P., Wilkens, V., Hess, S.T., Piehler, J., and Busch, K.B. (2012). Nanoscale organization of mitochondrial microcompartments revealed by combining tracking and localization microscopy. Nano Lett. *12*, 610–616.

Arcizet, D., Meier, B., Sackmann, E., Rädler, J.O., and Heinrich, D. (2008). Temporal analysis of active and passive transport in living cells. Phys. Rev. Lett. *101*, 248103.

Ben-Avraham, D. (2004). Diffusion and reactions in fractals and disordered systems (Cambridge: Cambridge University Press).

Axelrod, D., Koppel, D.E., Schlessinger, J., Elson, E., and Webb, W.W. (1976). Mobility measurement by analysis of fluorescence photobleaching recovery kinetics. Biophys. J. *16*, 1055.

Axmann, M., Huppa, J.B., Davis, M.M., and Schütz, G.J. (2012). Determination of interaction kinetics between the T cell receptor and peptide-loaded MHC class II via single-molecule diffusion measurements. Biophys. J. *103*, L17–19.

Baddeley, A. (2004). Spatial Point Process Modelling and Its Applications (Universitat Jaume I).

Baker, S.M., Buckheit, R.W., and Falk, M.M. (2010). Green-to-red photoconvertible fluorescent proteins: tracking cell and protein dynamics on standard wide-field mercury arc-based microscopes. BMC Cell Biol. *11*, 15.

Bakker, G.J., Eich, C., Torreno-Pina, J.A., Diez-Ahedo, R., Perez-Samper, G., van Zanten, T.S., Figdor, C.G., Cambi, A., and Garcia-Parajo, M.F. (2012). Lateral mobility of individual integrin nanoclusters orchestrates the onset for leukocyte adhesion. Proc. Natl. Acad. Sci. U. S. A. *109*, 4869–4874.

Bakshi, S., Bratton, B.P., and Weisshaar, J.C. (2011). Subdiffraction-limit study of Kaede diffusion and spatial distribution in live Escherichia coli. Biophys. J. *101*, 2535–2544.

Bancaud, A. (2012). Etude des mouvements des chromosomes dans la levure par suivi de particules individuelles: flexibilité des chromosomes et modèles conformationnels. (Institut Pasteur,),.

Bancaud, A., Huet, S., Daigle, N., Mozziconacci, J., Beaudouin, J., and Ellenberg, J. (2009). Molecular crowding affects diffusion and binding of nuclear proteins in heterochromatin and reveals the fractal organization of chromatin. EMBO J. *28*, 3785–3798.

Bancaud, A., Lavelle, C., Huet, S., and Ellenberg, J. (2012). A fractal model for nuclear organization: current evidence and biological implications. Nucleic Acids Res. *40*, 8783–8792.

Barbieri, M., Chotalia, M., Fraser, J., Lavitas, L.-M., Dostie, J., Pombo, A., and Nicodemi, M. (2012). Complexity of chromatin folding is captured by the strings and binders switch model. Proc. Natl. Acad. Sci. U. S. A. *109*, 16173–16178.

Bates, M., Huang, B., Dempsey, G.T., and Zhuang, X. (2007). Multicolor super-resolution imaging with photo-switchable fluorescent probes. Science *317*, 1749–1753.

Bauer, M., and Metzler, R. (2012). Generalized Facilitated Diffusion Model for DNA-Binding Proteins with Search and Recognition States. Biophys. J. *102*, 2321–2330.

Beheiry, M.E., and Dahan, M. (2013). ViSP: representing single-particle localizations in three dimensions. Nat. Methods *10*, 689–690.

Bénichou, O., Chevalier, C., Klafter, J., Meyer, B., and Voituriez, R. (2010). Geometry-controlled kinetics. Nat. Chem. *2*, 472–477.

Bénichou, O., Chevalier, C., Meyer, B., and Voituriez, R. (2011). Facilitated diffusion of proteins on chromatin. Phys. Rev. Lett. *106*, 038102.

Benke, A., Olivier, N., Gunzenhäuser, J., and Manley, S. (2012). Multicolor single molecule tracking of stochastically active synthetic dyes. Nano Lett. *12*, 2619–2624.

Berg, H.C. (1993). Random Walks in Biology (Princeton University Press).

Berger, A.B., Cabal, G.G., Fabre, E., Duong, T., Buc, H., Nehrbass, U., Olivo-Marin, J.-C., Gadal, O., and Zimmer, C. (2008). High-resolution statistical mapping reveals gene territories in live yeast. Nat. Methods *5*, 1031–1037.

Betzig, E., Patterson, G.H., Sougrat, R., Lindwasser, O.W., Olenych, S., Bonifacino, J.S., Davidson, M.W., Lippincott-Schwartz, J., and Hess, H.F. (2006). Imaging Intracellular Fluorescent Proteins at Nanometer Resolution. Science *313*, 1642–1645.

Bickel, T. A note on confined diffusion. Phys. Stat. Mech. Its Appl. 24–32.

Bickmore, W.A., and van Steensel, B. (2013). Genome architecture: domain organization of interphase chromosomes. Cell *152*, 1270–1284.

Biess, A., Korkotian, E., and Holcman, D. (2011). Barriers to diffusion in dendrites and estimation of calcium spread following synaptic inputs. PLoS Comput. Biol. *7*, e1002182.

Biswas, A., P., H., and Si., C. (2012). Application of Multifractal and Joint Multifractal Analysis in Examining Soil Spatial Variation: A Review. In Fractal Analysis and Chaos in Geosciences, S.-A. Ouadfeul, ed. (InTech),.

Bohn, M., Diesinger, P., Kaufmann, R., Weiland, Y., Müller, P., Gunkel, M., von Ketteler, A., Lemmer, P., Hausmann, M., Heermann, D.W., et al. (2010). Localization Microscopy Reveals Expression-Dependent Parameters of Chromatin Nanostructure. Biophys. J. *99*, 1358–1367.

Bouzigues, C., and Dahan, M. (2007). Transient directed motions of GABA(A) receptors in growth cones detected by a speed correlation index. Biophys. J. *92*, 654–660.

Brameshuber, M., and Schütz, G.J. (2008). How the sum of its parts gets greater than the whole. Nat. Methods *5*, 133–134.

Bronstein, I., Israel, Y., Kepten, E., Mai, S., Shav-Tal, Y., Barkai, E., and Garini, Y. (2009). Transient anomalous diffusion of telomeres in the nucleus of mammalian cells. Phys. Rev. Lett. *103*, 018102.

Burov, S., Jeon, J.-H., Metzler, R., and Barkai, E. (2011). Single particle tracking in systems showing anomalous diffusion: the role of weak ergodicity breaking. Phys. Chem. Chem. Phys. PCCP *13*, 1800–1812.

Burschka, M.A. (1997). A diffusion-limited reaction. In Stochastic Dynamics, L. Schimansky-Geier, and T. Pöschel, eds. (Springer Berlin Heidelberg), pp. 88–100.

Cabal, G.G., Genovesio, A., Rodriguez-Navarro, S., Zimmer, C., Gadal, O., Lesne, A., Buc, H., Feuerbach-Fournier, F., Olivo-Marin, J.-C., Hurt, E.C., et al. (2006). SAGA interacting factors confine sub-diffusion of transcribed genes to the nuclear envelope. Nature *441*, 770–773.

Cairo, C.W., Mirchev, R., and Golan, D.E. (2006). Cytoskeletal regulation couples LFA-1 conformational changes to receptor lateral mobility and clustering. Immunity *25*, 297–308.

Chatterjee, A.P. (2011). Tracer diffusion in fibre networks: the impact of spatial fluctuations in the fibre distribution. J. Phys. Condens. Matter Inst. Phys. J. *23*, 375103.

Cheezum, M.K., Walker, W.F., and Guilford, W.H. (2001). Quantitative Comparison of Algorithms for Tracking Single Fluorescent Particles. Biophys. J. *81*, 2378–2388.

Chen, D., and Huang, S. (2001). Nucleolar Components Involved in Ribosome Biogenesis Cycle between the Nucleolus and Nucleoplasm in Interphase Cells. J. Cell Biol. *153*, 169–176.

Cheng, Q., and Agterberg, F.P. (1995a). Multifractal modeling and spatial point processes. Math. Geol. *27*, 831–845.

Cheng, Q., and Agterberg, F.P. (1995b). Multifractal modeling and spatial point processes. Math. Geol. *27*, 831–845.

Chertkov, M., Kroc, L., Krzakala, F., Vergassola, M., and Zdeborová, L. (2010). Inference in particle tracking experiments by passing messages between images. Proc. Natl. Acad. Sci. *107*, 7663–7668.

Cole, N.B., Smith, C.L., Sciaky, N., Terasaki, M., Edidin, M., and Lippincott-Schwartz, J. (1996). Diffusional mobility of Golgi proteins in membranes of living cells. Science *273*, 797–801.

Condamin, S., B|[eacute]|nichou, O., Tejedor, V., Voituriez, R., and Klafter, J. (2007). First-passage times in complex scale-invariant media. Nature *450*, 77–80.

Condamin, S., Tejedor, V., Voituriez, R., Bénichou, O., and Klafter, J. (2008). Probing microscopic origins of confined subdiffusion by first-passage observables. Proc. Natl. Acad. Sci. U. S. A. *105*, 5675–5680.

Coppey, M., Bénichou, O., Voituriez, R., and Moreau, M. (2004). Kinetics of Target Site Localization of a Protein on DNA: A Stochastic Approach. Biophys. J. *87*, 1640–1649.

Coscoy, S., Huguet, E., and Amblard, F. (2007). Statistical analysis of sets of random walks: how to resolve their generating mechanism. Bull. Math. Biol. *69*, 2467–2492.

Crane, J.M., Van Hoek, A.N., Skach, W.R., and Verkman, A.S. (2008). Aquaporin-4 dynamics in orthogonal arrays in live cells visualized by quantum dot single particle tracking. Mol. Biol. Cell *19*, 3369–3378.

Cuche, A., Stein, B., Canaguier-Durand, A., Devaux, E., Genet, C., and Ebbesen, T.W. (2012). Brownian motion in a designer force field: dynamical effects of negative refraction on nanoparticles. Nano Lett. *12*, 4329–4332.

Dahan, M., Lévi, S., Luccardini, C., Rostaing, P., Riveau, B., and Triller, A. (2003). Diffusion dynamics of glycine receptors revealed by single-quantum dot tracking. Science *302*, 442–445.

Damien Hall, M.H. (2010). Effects of macromolecular crowding on intracellular diffusion from a single particle perspective. Biophys. Rev. *2*, 39–53.

Das, R., Cairo, C.W., and Coombs, D. (2009). A hidden Markov model for single particle tracks quantifies dynamic interactions between LFA-1 and the actin cytoskeleton. PLoS Comput. Biol. *5*, e1000556.

Van Dekken, H., and Hulspas, R. (1993). Spatial analysis of intranuclear human repetitive DNA regions by in situ hybridization and digital fluorescence microscopy. Histochem. J. *25*, 173–182.

Destainville, N., Saulière, A., and Salomé, L. (2008). Comment to the article by Michael J. Saxton: A biological interpretation of transient anomalous subdiffusion. I. qualitative model. Biophys. J. *95*, 3117–3119; author reply 3120–3122.

Dieker, T. (2004). Simulation of fractional Brownian motion. MSc Theses Univ. Twente Amst. Neth.

Dieteren, C.E.J., Gielen, S.C.A.M., Nijtmans, L.G.J., Smeitink, J.A.M., Swarts, H.G., Brock, R., Willems, P.H.G.M., and Koopman, W.J.H. (2011). Solute diffusion is hindered in the mitochondrial matrix. Proc. Natl. Acad. Sci. U. S. A. *108*, 8657–8662.

Dietrich, C., Yang, B., Fujiwara, T., Kusumi, A., and Jacobson, K. (2002). Relationship of lipid rafts to transient confinement zones detected by single particle tracking. Biophys. J. *82*, 274–284.

Diggle, P.J. (2003). Statistical Analysis of Spatial Point Patterns (Hodder Education Publishers).

Dion, V., and Gasser, S.M. (2013). Chromatin Movement in the Maintenance of Genome Stability. Cell *152*, 1355–1364.

Dix, J.A., and Verkman, A.S. (2008). Crowding effects on diffusion in solutions and cells. Annu. Rev. Biophys. *37*, 247–263.

Domanov, Y.A., Aimon, S., Toombes, G.E.S., Renner, M., Quemeneur, F., Triller, A., Turner, M.S., and Bassereau, P. (2011). Mobility in geometrically confined membranes. Proc. Natl. Acad. Sci. U. S. A. *108*, 12605–12610.

Dundr, M., and Misteli, T. (2001). Functional architecture in the cell nucleus. Biochem. J. *356*, 297–310.

Dybiec, B., and Gudowska-Nowak, E. (2009). Discriminating between normal and anomalous random walks. Phys. Rev. E Stat. Nonlin. Soft Matter Phys. *80*, 061122.

English, B.P., Hauryliuk, V., Sanamrad, A., Tankov, S., Dekker, N.H., and Elf, J. (2011). Single-molecule investigations of the stringent response machinery in living bacterial cells. Proc. Natl. Acad. Sci. U. S. A. *108*, E365–373.

Etoc, F., Lisse, D., Bellaiche, Y., Piehler, J., Coppey, M., and Dahan, M. (2013). Subcellular control of Rac-GTPase signalling by magnetogenetic manipulation inside living cells. Nat. Nanotechnol. *8*, 193–198.

Ewers, H., Smith, A.E., Sbalzarini, I.F., Lilie, H., Koumoutsakos, P., and Helenius, A. (2005). Single-particle tracking of murine polyoma virus-like particles on live cells and artificial membranes. Proc. Natl. Acad. Sci. U. S. A. *102*, 15110–15115.

Falconer, K. (2003). Fractal Geometry: Mathematical Foundations and Applications (Wiley).

Ferrari, R., Manfroi, A.J., and Young, W.R. (2001). Strongly and weakly self-similar diffusion. Phys. Nonlinear Phenom. *154*, 111–137.

Fitzgerald, J.E., Lu, J., and Schnitzer, M.J. (2012). Estimation Theoretic Measure of Resolution for Stochastic Localization Microscopy. Phys. Rev. Lett. *109*, 048102.

Foffano, G., Marenduzzo, D., and Orlandini, E. (2012). Facilitated diffusion on confined DNA. Phys. Rev. E Stat. Nonlin. Soft Matter Phys. *85*, 021919.

Fraser, P., and Bickmore, W. (2007). Nuclear organization of the genome and the potential for gene regulation. Nature *447*, 413–417.

Fudenberg, G., Getz, G., Meyerson, M., and Mirny, L.A. (2011). High order chromatin architecture shapes the landscape of chromosomal alterations in cancer. Nat. Biotechnol. *29*, 1109–1113.

Fung, J.C., Marshall, W.F., Dernburg, A., Agard, D.A., and Sedat, J.W. (1998). Homologous chromosome pairing in Drosophila melanogaster proceeds through multiple independent initiations. J. Cell Biol. *141*, 5–20.

Garcia, H.G., Grayson, P., Han, L., Inamdar, M., Kondev, J., Nelson, P.C., Phillips, R., Widom, J., and Wiggins, P.A. (2007). Biological consequences of tightly bent DNA: The other life of a macromolecular celebrity. Biopolymers *85*, 115–130.

Gardiner, C.W. (1985). Handbook of stochastic methods (Springer Berlin).

Gebhardt, J.C.M., Suter, D.M., Roy, R., Zhao, Z.W., Chapman, A.R., Basu, S., Maniatis, T., and Xie, X.S. (2013). Single-molecule imaging of transcription factor binding to DNA in live mammalian cells. Nat. Methods *10*, 421–426.

Gelles, J., Schnapp, B.J., and Sheetz, M.P. (1988). Tracking kinesin-driven movements with nanometre-scale precision. Nature *331*, 450–453.

De Gennes, P.G. (1971). Reptation of a Polymer Chain in the Presence of Fixed Obstacles. J. Chem. Phys. *55*, 572–579.

De Gennes, P.G. (1982a). Kinetics of diffusion-controlled processes in dense polymer systems. II. Effects of entanglements. J. Chem. Phys. *76*, 3322–3326.

De Gennes, P.G. (1982b). Kinetics of diffusion-controlled processes in dense polymer systems. I. Nonentangled regimes. J. Chem. Phys. *76*, 3316.

Genovesio, A., Liedl, T., Emiliani, V., Parak, W.J., Coppey-Moisan, M., and Olivo-Marin, J.-C. (2006). Multiple particle tracking in 3-D+t microscopy: method and application to the tracking of endocytosed quantum dots. IEEE Trans. Image Process. *15*, 1062–1070.

Ghosh, R.N., and Webb, W.W. (1994). Automated detection and tracking of individual and clustered cell surface low density lipoprotein receptor molecules. Biophys. J. *66*, 1301–1318.

Gitterman, M. (2000). Mean first passage time for anomalous diffusion. Phys. Rev. E *62*, 6065–6070.

Goulian, M., and Simon, S.M. (2000). Tracking single proteins within cells. Biophys. J. *79*, 2188–2198.

Gourieroux, C. (1992). Modèles ARCH et applications financières (Paris: Economica).

Gouriéroux, C., and Monfort, A. (1996). Statistique et modèles économétriques. Vol. 1, Vol. 1, (Paris: Economica).

Graham, J.S., Johnson, R.C., and Marko, J.F. (2011). Counting proteins bound to a single DNA molecule. Biochem. Biophys. Res. Commun. *415*, 131–134.

Grosberg, A., Rabin, Y., Havlin, S., and Neer, A. (1993). Crumpled Globule Model of the Three-Dimensional Structure of DNA. Eur. Lett. EPL *23*, 373–378.

Grünwald, D., Martin, R.M., Buschmann, V., Bazett-Jones, D.P., Leonhardt, H., Kubitscheck, U., and Cardoso, M.C. (2008). Probing Intranuclear Environments at the Single-Molecule Level. Biophys. J. *94*, 2847–2858.

Gu, Y., Sun, W., Wang, G., Jeftinija, K., Jeftinija, S., and Fang, N. (2012). Rotational dynamics of cargos at pauses during axonal transport. Nat. Commun. *3*, 1030.

Guérin, T., Bénichou, O., and Voituriez, R. (2012). Non-Markovian polymer reaction kinetics. Nat. Chem. *4*, 568–573.

Guigas, G., and Weiss, M. (2008). Sampling the Cell with Anomalous Diffusion—The Discovery of Slowness. Biophys. J. *94*, 90–94.

Haggie, P.M., Kim, J.K., Lukacs, G.L., and Verkman, A.S. (2006). Tracking of Quantum Dot-labeled CFTR Shows Near Immobilization by C-Terminal PDZ Interactions. Mol. Biol. Cell *17*, 4937–4945.

Hajjoul, H., Kocanova, S., Lassadi, I., Bystricky, K., and Bancaud, A. (2009). Lab-on-Chip for fast 3D particle tracking in living cells. Lab. Chip *9*, 3054–3058.

Halford, S.E., and Szczelkun, M.D. (2002). How to get from A to B: strategies for analysing protein motion on DNA. Eur. Biophys. J. *31*, 257–267.

Hamilton, R.S., Parton, R.M., Oliveira, R.A., Vendra, G., Ball, G., Nasmyth, K., and Davis, I. (2010). ParticleStats: open source software for the analysis of particle motility and cytoskeletal polarity. Nucleic Acids Res. *38*, W641–646.

Hammar, P., Leroy, P., Mahmutovic, A., Marklund, E.G., Berg, O.G., and Elf, J. (2012). The lac Repressor Displays Facilitated Diffusion in Living Cells. Science *336*, 1595–1598.

Hardy, G.H.; L., J. E. ; & G. Polya (1959). Inequalities. (Cambridge: University Press).

Helmuth, J.A., Burckhardt, C.J., Koumoutsakos, P., Greber, U.F., and Sbalzarini, I.F. (2007). A novel supervised trajectory segmentation algorithm identifies distinct types of human adenovirus motion in host cells. J. Struct. Biol. *159*, 347–358.

Henriques, R., Lelek, M., Fornasiero, E.F., Valtorta, F., Zimmer, C., and Mhlanga, M.M. (2010). QuickPALM: 3D real-time photoactivation nanoscopy image processing in ImageJ. Nat. Methods *7*, 339–340.

Heun, P., Laroche, T., Shimada, K., Furrer, P., and Gasser, S.M. (2001). Chromosome dynamics in the yeast interphase nucleus. Science *294*, 2181–2186.

Hida, T. (1980). Brownian motion (Springer).

Hieda, M., Winstanley, H., Maini, P., Iborra, F.J., and Cook, P.R. (2005). Different populations of RNA polymerase II in living mammalian cells. Chromosome Res. Int. J. Mol. Supramol. Evol. Asp. Chromosome Biol. *13*, 135–144.

Von Hippel, P.H., and Berg, O.G. (1989). Facilitated target location in biological systems. J. Biol. Chem. *264*, 675–678.

Höfling, F., and Franosch, T. (2013). Anomalous transport in the crowded world of biological cells. Reports Prog. Phys. Phys. Soc. Gt. Br. *76*, 046602.

Holcman, D., Hoze, N., and Schuss, Z. (2011). Narrow escape through a funnel and effective diffusion on a crowded membrane. Phys. Rev. E Stat. Nonlin. Soft Matter Phys. *84*, 021906.

Holtzer, L., Meckel, T., and Schmidt, T. (2007). Nanometric three-dimensional tracking of individual quantum dots in cells. Appl. Phys. Lett. *90*, 053902–053902–3.

Hoze, N., Nair, D., Hosy, E., Sieben, C., Manley, S., Herrmann, A., Sibarita, J.-B., Choquet, D., and Holcman, D. (2012). Heterogeneity of AMPA receptor trafficking and molecular interactions revealed by superresolution analysis of live cell imaging. Proc. Natl. Acad. Sci. U. S. A. *109*, 17052–17057.

Hozé, N., Ruault, M., Amoruso, C., Taddei, A., and Holcman, D. (2013). Spatial telomere organization and clustering in yeast Saccharomyces cerevisiae nucleus is generated by a random dynamics of aggregation–dissociation. Mol. Biol. Cell *24*, 1791–1800.

Hsu, C.-J., and Baumgart, T. (2011). Spatial Association of Signaling Proteins and F-Actin Effects on Cluster Assembly Analyzed via Photoactivation Localization Microscopy in T Cells. PLoS ONE *6*, e23586.

Huang, B., Wang, W., Bates, M., and Zhuang, X. (2008). Three-Dimensional Super-Resolution Imaging by Stochastic Optical Reconstruction Microscopy. Science *319*, 810–813.

Huet, S., Karatekin, E., Tran, V.S., Fanget, I., Cribier, S., and Henry, J.-P. (2006). Analysis of transient behavior in complex trajectories: application to secretory vesicle dynamics. Biophys. J. *91*, 3542–3559.

Humphries, N.E., Queiroz, N., Dyer, J.R.M., Pade, N.G., Musyl, M.K., Schaefer, K.M., Fuller, D.W., Brunnschweiler, J.M., Doyle, T.K., Houghton, J.D.R., et al. (2010). Environmental context explains Lévy and Brownian movement patterns of marine predators. Nature *465*, 1066–1069.

Information, N.C. for B., Pike, U.S.N.L. of M. 8600 R., MD, B., and Usa, 20894 (1981). Cell-substrate contacts illuminated by total internal reflection fluorescence. J. Cell Biol. *89*, 141.

Izeddin, I., El Beheiry, M., Andilla, J., Ciepielewski, D., Darzacq, X., and Dahan, M. (2012). PSF shaping using adaptive optics for three-dimensional single-molecule super-resolution imaging and tracking. Opt. Express *20*, 4957.

Jackson, O.A.Y. (1969). Fitting a Gamma or Log-Normal Distribution to Fibre-Diameter Measurements on Wool Tops. J. R. Stat. Soc. Ser. C Appl. Stat. *18*, 70–75.

Jaqaman, K., Loerke, D., Mettlen, M., Kuwata, H., Grinstein, S., Schmid, S.L., and Danuser, G. (2008). Robust single-particle tracking in live-cell time-lapse sequences. Nat. Methods *5*, 695–702.

Jeon, J.-H., Tejedor, V., Burov, S., Barkai, E., Selhuber-Unkel, C., Berg-Sørensen, K., Oddershede, L., and Metzler, R. (2011). In vivo anomalous diffusion and weak ergodicity breaking of lipid granules. Phys. Rev. Lett. *106*, 048103.

Jin, S., and Verkman, A.S. (2007). Single particle tracking of complex diffusion in membranes: simulation and detection of barrier, raft, and interaction phenomena. J. Phys. Chem. B *111*, 3625–3632.

Jin, H., Heller, D.A., and Strano, M.S. (2008). Single-particle tracking of endocytosis and exocytosis of single-walled carbon nanotubes in NIH-3T3 cells. Nano Lett. *8*, 1577–1585.

Jin, S., Haggie, P.M., and Verkman, A.S. (2007). Single-particle tracking of membrane protein diffusion in a potential: simulation, detection, and application to confined diffusion of CFTR Cl-channels. Biophys. J. *93*, 1079–1088.

Kagan, Y.Y. (2007). Earthquake spatial distribution: the correlation dimension. Geophys. J. Int. *168*, 1175–1194.

Karine Bertin, S.T. Drift parameter estimation in fractional diffusions driven by perturbed random walks. Stat. Amp Probab. Lett. 243–249.

Kimura, H., Sugaya, K., and Cook, P.R. (2002). The transcription cycle of RNA polymerase II in living cells. J. Cell Biol. *159*, 777–782.

Kiskowski, M.A., Hancock, J.F., and Kenworthy, A.K. (2009). On the Use of Ripley's K-Function and Its Derivatives to Analyze Domain Size. Biophys. J. *97*, 1095–1103.

Kobelev, V., and Romanov, E. (2000). Fractional Langevin equation to describe anomalous diffusion. Prog. Theor. Phys. Suppl. *139*, 470–476.

Kolesov, G., Wunderlich, Z., Laikova, O.N., Gelfand, M.S., and Mirny, L.A. (2007). How gene order is influenced by the biophysics of transcription regulation. Proc. Natl. Acad. Sci. *104*, 13948–13953.

Kopelman, R. (1986). Rate processes on fractals: theory, simulations, and experiments. J. Stat. Phys. *42*, 185–200.

Köster, M., Frahm, T., and Hauser, H. (2005). Nucleocytoplasmic shuttling revealed by FRAP and FLIP technologies. Curr. Opin. Biotechnol. *16*, 28–34.

Kukura, P., Ewers, H., Müller, C., Renn, A., Helenius, A., and Sandoghdar, V. (2009). High-speed nanoscopic tracking of the position and orientation of a single virus. Nat. Methods *6*, 923–927.

Kusumi, A., Sako, Y., and Yamamoto, M. (1993). Confined lateral diffusion of membrane receptors as studied by single particle tracking (nanovid microscopy). Effects of calcium-induced differentiation in cultured epithelial cells. Biophys. J. *65*, 2021–2040.

Lebedev, D.V., Filatov, M.V., Kuklin, A.I., Islamov, A.K., Kentzinger, E., Pantina, R., Toperverg, B.P., and Isaev-Ivanov, V.V. (2005). Fractal nature of chromatin organization in interphase chicken erythrocyte nuclei: DNA structure exhibits biphasic fractal properties. FEBS Lett. *579*, 1465–1468.

Levi, V., and Gratton, E. (2007). Exploring dynamics in living cells by tracking single particles. Cell Biochem. Biophys. *48*, 1–15.

Li, T., Kheifets, S., Medellin, D., and Raizen, M.G. (2010). Measurement of the instantaneous velocity of a Brownian particle. Science *328*, 1673–1675.

Lieberman-Aiden, E., Berkum, N.L. van, Williams, L., Imakaev, M., Ragoczy, T., Telling, A., Amit, I., Lajoie, B.R., Sabo, P.J., Dorschner, M.O., et al. (2009). Comprehensive Mapping of

Long-Range Interactions Reveals Folding Principles of the Human Genome. Science *326*, 289–293.

Lill, Y., Kaserer, W.A., Newton, S.M., Lill, M., Klebba, P.E., and Ritchie, K. (2012). Single-molecule study of molecular mobility in the cytoplasm of Escherichia coli. Phys. Rev. E Stat. Nonlin. Soft Matter Phys. *86*, 021907.

Lomholt, M.A., van den Broek, B., Kalisch, S.-M.J., Wuite, G.J.L., and Metzler, R. (2009). Facilitated diffusion with DNA coiling. Proc. Natl. Acad. Sci. U. S. A. *106*, 8204–8208.

Long, B.R., and Vu, T.Q. (2010). Spatial structure and diffusive dynamics from single-particle trajectories using spline analysis. Biophys. J. *98*, 1712–1721.

Lowe, A.R., Siegel, J.J., Kalab, P., Siu, M., Weis, K., and Liphardt, J.T. (2010). Selectivity mechanism of the nuclear pore complex characterized by single cargo tracking. Nature *467*, 600–603.

Lubelski, A., Sokolov, I.M., and Klafter, J. (2008). Nonergodicity mimics inhomogeneity in single particle tracking. Phys. Rev. Lett. *100*, 250602.

Lüscher, B. (2001). Function and regulation of the transcription factors of the Myc/Max/Mad network. Gene *277*, 1–14.

Lushnikov, P.M., Sulc, P., and Turitsyn, K.S. (2012). Non-Gaussianity in single-particle tracking: Use of kurtosis to learn the characteristics of a cage-type potential. Phys. Rev. E Stat. Nonlin. Soft Matter Phys. *85*, 051905.

MacKintosh, F.C. (2012). Active diffusion: The erratic dance of chromosomal loci. Proc. Natl. Acad. Sci. *109*, 7138–7139.

Mandelbrot, B.B. (1975). Les objets fractals: forme, hasard et dimension (Flammarion).

Mandelbrot, B.B. (1999). Multifractals and 1/f Noise: Wild Self-affinity in Physics (Springer-Verlag New York Inc.).

Manley, S., Gillette, J.M., Patterson, G.H., Shroff, H., Hess, H.F., Betzig, E., and Lippincott-Schwartz, J. (2008). High-density mapping of single-molecule trajectories with photoactivated localization microscopy. Nat. Methods *5*, 155–157.

Manley, S., Gillette, J.M., and Lippincott-Schwartz, J. (2010). Single-particle tracking photoactivated localization microscopy for mapping single-molecule dynamics. Methods Enzymol. *475*, 109–120.

Marshall, W.F., Straight, A., Marko, J.F., Swedlow, J., Dernburg, A., Belmont, A., Murray, A.W., Agard, D.A., and Sedat, J.W. (1997). Interphase chromosomes undergo constrained diffusional motion in living cells. Curr. Biol. CB *7*, 930–939.

Martin, D.S., Forstner, M.B., and Käs, J.A. (2002). Apparent subdiffusion inherent to single particle tracking. Biophys. J. *83*, 2109–2117.

Mashanov, G.I., and Molloy, J.E. (2007). Automatic Detection of Single Fluorophores in Live Cells. Biophys. J. *92*, 2199–2211.

Masson, J.-B., Casanova, D., Türkcan, S., Voisinne, G., Popoff, M.R., Vergassola, M., and Alexandrou, A. (2009). Inferring maps of forces inside cell membrane microdomains. Phys. Rev. Lett. *102*, 048103.

Mateos-Langerak, J., Bohn, M., Leeuw, W. de, Giromus, O., Manders, E.M.M., Verschure, P.J., Indemans, M.H.G., Gierman, H.J., Heermann, D.W., Driel, R. van, et al. (2009). Spatially confined folding of chromatin in the interphase nucleus. Proc. Natl. Acad. Sci. *106*, 3812–3817.

Matsuda, A., Shao, L., Boulanger, J., Kervrann, C., Carlton, P.M., Kner, P., Agard, D., and Sedat, J.W. (2010). Condensed mitotic chromosome structure at nanometer resolution using PALM and EGFP- histones. PloS One *5*, e12768.

Mazza, D., Abernathy, A., Golob, N., Morisaki, T., and McNally, J.G. (2012a). A benchmark for chromatin binding measurements in live cells. Nucleic Acids Res. *40*, e119.

Mazza, D., Abernathy, A., Golob, N., Morisaki, T., and McNally, J.G. (2012b). A benchmark for chromatin binding measurements in live cells. Nucleic Acids Res. *40*, e119.

Meaburn, K.J., and Misteli, T. (2007). Cell biology: Chromosome territories. Nature *445*, 379–381.

Meakin, P., and Stanley, H.E. (1983). Spectral Dimension for the Diffusion-Limited Aggregation Model of Colloid Growth. Phys. Rev. Lett. *51*, 1457–1460.

Metzler R., and Klafter J. (2000). The random walk's guide to anomalous diffusion: a fractional dynamics approach. Phys. Reports *339*, 1–77.

Meyer, B., Bénichou, O., Kafri, Y., and Voituriez, R. (2012). Geometry-Induced Bursting Dynamics in Gene Expression. Biophys. J. *102*, 2186–2191.

Michalet, X. (2010). Mean square displacement analysis of single-particle trajectories with localization error: Brownian motion in an isotropic medium. Phys. Rev. E Stat. Nonlin. Soft Matter Phys. *82*, 041914.

Michalet, X., and Berglund, A.J. (2012). Optimal diffusion coefficient estimation in single-particle tracking. Phys. Rev. E Stat. Nonlin. Soft Matter Phys. *85*, 061916.

Miermont, A., Waharte, F., Hu, S., McClean, M.N., Bottani, S., Léon, S., and Hersen, P. (2013). Severe osmotic compression triggers a slowdown of intracellular signaling, which can be explained by molecular crowding. Proc. Natl. Acad. Sci. *110*, 5725–5730.

Min, W., Luo, G., Cherayil, B.J., Kou, S.C., and Xie, X.S. (2005). Observation of a power-law memory kernel for fluctuations within a single protein molecule. Phys. Rev. Lett. *94*, 198302.

Miné-Hattab, J., and Rothstein, R. (2012). Increased chromosome mobility facilitates homology search during recombination. Nat. Cell Biol. *14*, 510–517.

Miné-Hattab, J., and Rothstein, R. (2013). DNA in motion during double-strand break repair. Trends Cell Biol.

Minoura, I., Katayama, E., Sekimoto, K., and Muto, E. (2010). One-dimensional Brownian motion of charged nanoparticles along microtubules: a model system for weak binding interactions. Biophys. J. *98*, 1589–1597.

Mirny, L. (2008). Biophysics: Cell commuters avoid delays. Nat. Phys. *4*, 93–95.

Mirny, L.A. (2011). The fractal globule as a model of chromatin architecture in the cell. Chromosome Res. Int. J. Mol. Supramol. Evol. Asp. Chromosome Biol. *19*, 37–51.

Montroll, E.W., and Weiss, G.H. (1965). Random Walks on Lattices. II. J. Math. Phys. *6*, 167.

Mortensen, K.I., Churchman, L.S., Spudich, J.A., and Flyvbjerg, H. (2010). Optimized localization analysis for single-molecule tracking and super-resolution microscopy. Nat. Methods *7*, 377–381.

Mueller, F., Mazza, D., Stasevich, T.J., and McNally, J.G. (2010). FRAP and kinetic modeling in the analysis of nuclear protein dynamics: what do we really know? Curr. Opin. Cell Biol. *22*, 403–411.

Murase, K., Fujiwara, T., Umemura, Y., Suzuki, K., Iino, R., Yamashita, H., Saito, M., Murakoshi, H., Ritchie, K., and Kusumi, A. (2004). Ultrafine membrane compartments for molecular diffusion as revealed by single molecule techniques. Biophys. J. *86*, 4075–4093.

Murphy, D.B., and Davidson, M.W. (2012). Fundamentals of Light Microscopy and Electronic Imaging (Wiley-Blackwell).

Nandi, A., Heinrich, D., and Lindner, B. (2012). Distributions of diffusion measures from a local mean-square displacement analysis. Phys. Rev. E Stat. Nonlin. Soft Matter Phys. *86*, 021926.

Nasse, M.J., and Woehl, J.C. (2010). Realistic modeling of the illumination point spread function in confocal scanning optical microscopy. J. Opt. Soc. Am. *27*, 295–302.

Ng, W., Li, J., Godsill, S., and Vermaak, J. (2005). A review of recent results in multiple target tracking. In Proceedings of the 4th International Symposium on Image and Signal Processing and Analysis, 2005. ISPA 2005, pp. 40–45.

Niehaus, A.M.S., Vlachos, D.G., Edwards, J.S., Plechac, P., and Tribe, R. (2008). Microscopic simulation of membrane molecule diffusion on corralled membrane surfaces. Biophys. J. *94*, 1551–1564.

Normanno, D., Dahan, M., and Darzacq, X. (2012). Intra-nuclear mobility and target search mechanisms of transcription factors: A single-molecule perspective on gene expression. Biochim. Biophys. Acta BBA - Gene Regul. Mech. *1819*, 482–493.

Ogata, Y., and Katsura, K. (1991). Maximum Likelihood Estimates of the Fractal Dimension for Random Spatial Patterns. Biometrika *78*, 463–474.

Oh, D., Ogiue-Ikeda, M., Jadwin, J.A., Machida, K., Mayer, B.J., and Yu, J. (2012). Fast rebinding increases dwell time of Src homology 2 (SH2)-containing proteins near the plasma membrane. Proc. Natl. Acad. Sci. U. S. A. *109*, 14024–14029.

Olivo-Marin, J.-C. (2002). Extraction of spots in biological images using multiscale products. Pattern Recognit. *35*, 1989–1996.

Ott, T., and Bonitz, M. (2009). Is Diffusion Anomalous in Two-Dimensional Yukawa Liquids? Phys. Rev. Lett. *103*, 195001.

Owen, D.M., Rentero, C., Rossy, J., Magenau, A., Williamson, D., Rodriguez, M., and Gaus, K. (2010). PALM imaging and cluster analysis of protein heterogeneity at the cell surface. J. Biophotonics *3*, 446–454.

Owen, D.M., Sauer, M., and Gaus, K. (2012). Fluorescence localization microscopy: The transition from concept to biological research tool. Commun. Integr. Biol. *5*, 345–349.

Parthasarathy, R. (2012). Rapid, accurate particle tracking by calculation of radial symmetry centers. Nat. Methods *9*, 724–726.

Perkins, T.T., Smith, D.E., and Chu, S. (1994). Direct observation of tube-like motion of a single polymer chain. Science *264*, 819–822.

Perry, G.L.W. (2004). SpPack: spatial point pattern analysis in Excel using Visual Basic for Applications (VBA). Environ. Model. Softw. *19*, 559–569.

Pertsinidis, A., Zhang, Y., and Chu, S. (2010). Subnanometre single-molecule localization, registration and distance measurements. Nature *466*, 647–651.

Phair, R.D., and Misteli, T. (2000). High mobility of proteins in the mammalian cell nucleus. Nature *404*, 604–609.

Phillips, R. (2013). Physical biology of the cell (London: Garland Science).

Pinaud, F., Michalet, X., Iyer, G., Margeat, E., Moore, H.-P., and Weiss, S. (2009). Dynamic partitioning of a glycosyl-phosphatidylinositol-anchored protein in glycosphingolipid-rich microdomains imaged by single-quantum dot tracking. Traffic Cph. Den. *10*, 691–712.

Plachta, N., Bollenbach, T., Pease, S., Fraser, S.E., and Pantazis, P. (2011). Oct4 kinetics predict cell lineage patterning in the early mammalian embryo. Nat. Cell Biol. *13*, 117–123.

Platani, M., Goldberg, I., Lamond, A.I., and Swedlow, J.R. (2002). Cajal body dynamics and association with chromatin are ATP-dependent. Nat. Cell Biol. *4*, 502–508.

Pólya, G. (1921). Über eine Aufgabe der Wahrscheinlichkeitsrechnung betreffend die Irrfahrt im Strassennetz. Math. Ann. *84*, 149–160.

Prior, I.A., Muncke, C., Parton, R.G., and Hancock, J.F. (2003). Direct visualization of Ras proteins in spatially distinct cell surface microdomains. J. Cell Biol. *160*, 165–170.

Pusey, P.N. (2011). Brownian Motion Goes Ballistic. Science *332*, 802–803.

Qian, H., Sheetz, M.P., and Elson, E.L. (1991). Single particle tracking. Analysis of diffusion and flow in two-dimensional systems. Biophys. J. *60*, 910–921.

Raupach, C., Zitterbart, D.P., Mierke, C.T., Metzner, C., Müller, F.A., and Fabry, B. (2007). Stress fluctuations and motion of cytoskeletal-bound markers. Phys. Rev. E Stat. Nonlin. Soft Matter Phys. *76*, 011918.

Riggs, A.D., Bourgeois, S., Newby, R.F., and Cohn, M. (1968). DNA binding of the lac repressor. J. Mol. Biol. *34*, 365–368.

Ripley, B.D. (2004). Spatial Statistics (Wiley-Interscience).

Risken, H. (1996). The Fokker-Planck equation: methods of solution and applications (Berlin [u.a.: Springer).

Ritchie, K., Shan, X.-Y., Kondo, J., Iwasawa, K., Fujiwara, T., and Kusumi, A. (2005). Detection of non-Brownian diffusion in the cell membrane in single molecule tracking. Biophys. J. *88*, 2266–2277.

Rosa, A., and Everaers, R. (2008). Structure and Dynamics of Interphase Chromosomes. PLoS Comput Biol *4*, e1000153.

Rothenberg, E., Sepúlveda, L.A., Skinner, S.O., Zeng, L., Selvin, P.R., and Golding, I. (2011). Single-virus tracking reveals a spatial receptor-dependent search mechanism. Biophys. J. *100*, 2875–2882.

Roukos, V., Voss, T.C., Schmidt, C.K., Lee, S., Wangsa, D., and Misteli, T. (2013). Spatial Dynamics of Chromosome Translocations in Living Cells. Science *341*, 660–664.

Rouse, P.E. (1953). A Theory of the Linear Viscoelastic Properties of Dilute Solutions of Coiling Polymers. J. Chem. Phys. *21*, 1272–1280.

Rust, M.J., Bates, M., and Zhuang, X. (2006). Sub-diffraction-limit imaging by stochastic optical reconstruction microscopy (STORM). Nat. Methods *3*, 793–795.

Sainis, S.K., Germain, V., and Dufresne, E.R. (2007). Statistics of particle trajectories at short time intervals reveal fN-scale colloidal forces. Phys. Rev. Lett. *99*, 018303.

Sarkar, S.K., Marmer, B., Goldberg, G., and Neuman, K.C. (2012). Single-molecule tracking of collagenase on native type I collagen fibrils reveals degradation mechanism. Curr. Biol. CB *22*, 1047–1056.

Saunders, A., Core, L.J., and Lis, J.T. (2006). Breaking barriers to transcription elongation. Nat. Rev. Mol. Cell Biol. *7*, 557–567.

Saxton, M.J. (1995). Single-particle tracking: effects of corrals. Biophys. J. *69*, 389–398.

Saxton, M.J. (1997). Single-particle tracking: the distribution of diffusion coefficients. Biophys. J. *72*, 1744–1753.

Saxton, M.J. (2007). A biological interpretation of transient anomalous subdiffusion. I. Qualitative model. Biophys. J. *92*, 1178–1191.

Saxton, M.J. (2008a). Single-particle tracking: connecting the dots. Nat. Methods *5*, 671–672.

Saxton, M.J. (2008b). A biological interpretation of transient anomalous subdiffusion. II. Reaction kinetics. Biophys. J. *94*, 760–771.

Saxton, M.J. (2012a). Wanted: a positive control for anomalous subdiffusion. Biophys. J. *103*, 2411–2422.

Saxton, M.J. (2012b). Wanted: A Positive Control for Anomalous Subdiffusion. Biophys. J. *103*, 2411–2422.

Sbalzarini, I.F., and Koumoutsakos, P. (2005). Feature point tracking and trajectory analysis for video imaging in cell biology. J. Struct. Biol. *151*, 182–195.

Schiessel, H., Widom, J., Bruinsma, R.F., and Gelbart, W.M. (2001). Polymer Reptation and Nucleosome Repositioning. Phys. Rev. Lett. *86*, 4414–4417.

Schmidt, T., Schütz, G.J., Baumgartner, W., Gruber, H.J., and Schindler, H. (1996). Imaging of single molecule diffusion. Proc. Natl. Acad. Sci. *93*, 2926–2929.

Schmit, J.D., Kamber, E., and Kondev, J. (2009). Lattice Model of Diffusion-Limited Bimolecular Chemical Reactions in Confined Environments. Phys. Rev. Lett. *102*, 218302.

Schütz, G.J., Schindler, H., and Schmidt, T. (1997). Single-molecule microscopy on model membranes reveals anomalous diffusion. Biophys. J. *73*, 1073–1080.

Sengupta, P., and Lippincott-Schwartz, J. (2012). Quantitative analysis of photoactivated localization microscopy (PALM) datasets using pair-correlation analysis. BioEssays News Rev. Mol. Cell. Dev. Biol. *34*, 396–405.

Sergé, A., Bertaux, N., Rigneault, H., and Marguet, D. (2008). Dynamic multiple-target tracing to probe spatiotemporal cartography of cell membranes. Nat. Methods *5*, 687–694.

Shafique, K., and Shah, M. (2005). A noniterative greedy algorithm for multiframe point correspondence. IEEE Trans. Pattern Anal. Mach. Intell. *27*, 51–65.

Shav-Tal, Y., Darzacq, X., Shenoy, S.M., Fusco, D., Janicki, S.M., Spector, D.L., and Singer, R.H. (2004). Dynamics of Single mRNPs in Nuclei of Living Cells. Science *304*, 1797–1800.

Shimomura, O., Johnson, F.H., and Saiga, Y. (1962). Extraction, Purification and Properties of Aequorin, a Bioluminescent Protein from the Luminous Hydromedusan, Aequorea. J. Cell. Comp. Physiol. *59*, 223–239.

Shusterman, R., Alon, S., Gavrinyov, T., and Krichevsky, O. (2004). Monomer Dynamics in Double- and Single-Stranded DNA Polymers. Phys. Rev. Lett. *92*, 048303.

Sibarita, J.-B. (2005). Deconvolution Microscopy. In Microscopy Techniques, J. Rietdorf, ed. (Springer Berlin Heidelberg), pp. 201–243.

Simo Srkk, T.T. (2004). Probabilistic Methods in Multiple Target Tracking.

Sims, R.J., 3rd, Belotserkovskaya, R., and Reinberg, D. (2004). Elongation by RNA polymerase II: the short and long of it. Genes Dev. *18*, 2437–2468.

Smith, M.B., Karatekin, E., Gohlke, A., Mizuno, H., Watanabe, N., and Vavylonis, D. (2011). Interactive, Computer-Assisted Tracking of Speckle Trajectories in Fluorescence Microscopy: Application to Actin Polymerization and Membrane Fusion. Biophys. J. *101*, 1794–1804.

Sonnleitner, A., Schutz, G., and Schmidt, T. (1999). Free brownian motion of individual lipid molecules in biomembranes. Biophys. J. *77*, 2638–2642.

Speil, J., Baumgart, E., Siebrasse, J.-P., Veith, R., Vinkemeier, U., and Kubitscheck, U. (2011a). Activated STAT1 transcription factors conduct distinct saltatory movements in the cell nucleus. Biophys. J. *101*, 2592–2600.

Speil, J., Baumgart, E., Siebrasse, J.-P., Veith, R., Vinkemeier, U., and Kubitscheck, U. (2011b). Activated STAT1 transcription factors conduct distinct saltatory movements in the cell nucleus. Biophys. J. *101*, 2592–2600.

Sprague, B.L., Pego, R.L., Stavreva, D.A., and McNally, J.G. (2004). Analysis of binding reactions by fluorescence recovery after photobleaching. Biophys. J. *86*, 3473–3495.

Szabo, A., Schulten, K., and Schulten, Z. (1980). First passage time approach to diffusion controlled reactions. J. Chem. Phys. *72*, 4350.

Tejedor, V., Bénichou, O., Voituriez, R., Jungmann, R., Simmel, F., Selhuber-Unkel, C., Oddershede, L.B., and Metzler, R. (2010). Quantitative analysis of single particle trajectories: mean maximal excursion method. Biophys. J. *98*, 1364–1372.

Thompson, N.L. (2002). Fluorescence Correlation Spectroscopy. In Topics in Fluorescence Spectroscopy, J.R. Lakowicz, ed. (Springer US), pp. 337–378.

Thompson, M.A., Lew, M.D., Badieirostami, M., and Moerner, W.E. (2010). Localizing and Tracking Single Nanoscale Emitters in Three Dimensions with High Spatiotemporal Resolution Using a Double-Helix Point Spread Function. Nano Lett. *10*, 211–218.

Thompson, R.E., Larson, D.R., and Webb, W.W. (2002). Precise nanometer localization analysis for individual fluorescent probes. Biophys. J. *82*, 2775–2783.

Tokunaga, M., Imamoto, N., and Sakata-Sogawa, K. (2008). Highly inclined thin illumination enables clear single-molecule imaging in cells. Nat. Methods *5*, 159–161.

Türkcan, S., Alexandrou, A., and Masson, J.-B. (2012). A Bayesian inference scheme to extract diffusivity and potential fields from confined single-molecule trajectories. Biophys. J. *102*, 2288–2298.

Voisinne, G., Alexandrou, A., and Masson, J.-B. (2010). Quantifying biomolecule diffusivity using an optimal Bayesian method. Biophys. J. *98*, 596–605.

Vrljic, M., Nishimura, S.Y., Brasselet, S., Moerner, W.E., and McConnell, H.M. (2002). Translational diffusion of individual class II MHC membrane proteins in cells. Biophys. J. *83*, 2681–2692.

Wachsmuth, M., Weidemann, T., Müller, G., Hoffmann-Rohrer, U.W., Knoch, T.A., Waldeck, W., and Langowski, J. (2003). Analyzing Intracellular Binding and Diffusion with Continuous Fluorescence Photobleaching. Biophys. J. *84*, 3353–3363.

Wang, F., Redding, S., Finkelstein, I.J., Gorman, J., Reichman, D.R., and Greene, E.C. (2012). The promoter-search mechanism of Escherichia coli RNA polymerase is dominated by three-dimensional diffusion. Nat. Struct. Mol. Biol.

Weber, S.C., Theriot, J.A., and Spakowitz, A.J. (2010a). Subdiffusive motion of a polymer composed of subdiffusive monomers. Phys. Rev. E *82*, 011913.

Weber, S.C., Spakowitz, A.J., and Theriot, J.A. (2010b). Bacterial chromosomal loci move subdiffusively through a viscoelastic cytoplasm. Phys. Rev. Lett. *104*, 238102.

Weber, S.C., Thompson, M.A., Moerner, W.E., Spakowitz, A.J., and Theriot, J.A. (2012a). Analytical tools to distinguish the effects of localization error, confinement, and medium elasticity on the velocity autocorrelation function. Biophys. J. *102*, 2443–2450.

Weber, S.C., Spakowitz, A.J., and Theriot, J.A. (2012b). Nonthermal ATP-dependent fluctuations contribute to the in vivo motion of chromosomal loci. Proc. Natl. Acad. Sci. U. S. A. *109*, 7338–7343.

Weigel, A.V., Simon, B., Tamkun, M.M., and Krapf, D. (2011). Ergodic and nonergodic processes coexist in the plasma membrane as observed by single-molecule tracking. Proc. Natl. Acad. Sci. U. S. A. *108*, 6438–6443.

Weihua Deng, E.B. (2009). Ergodic properties of fractional Brownian-Langevin motion. Phys. Rev. E Stat. Nonlin. Soft Matter Phys. *79*, 011112.

Weisstein, E.W. CLEAN Algorithm -- from Eric Weisstein's World of Physics.

Weston, D.J., Adams, N.M., Russell, R.A., Stephens, D.A., and Freemont, P.S. (2012). Analysis of spatial point patterns in nuclear biology. PloS One *7*, e36841.

Wieser, S., and Schütz, G.J. (2008). Tracking single molecules in the live cell plasma membrane-Do's and Don't's. Methods San Diego Calif *46*, 131–140.

Wieser, S., Axmann, M., and Schütz, G.J. (2008). Versatile Analysis of Single-Molecule Tracking Data by Comprehensive Testing against Monte Carlo Simulations. Biophys. J. *95*, 5988–6001.

Williamson, D.J., Owen, D.M., Rossy, J., Magenau, A., Wehrmann, M., Gooding, J.J., and Gaus, K. (2011). Pre-existing clusters of the adaptor Lat do not participate in early T cell signaling events. Nat. Immunol. *12*, 655–662.

Wong, H., Arbona, J.M., and Zimmer, C. How to build a yeast nucleus.

Wong, Y., Lin, Z., and Ober, R.J. (2011). Limit of the Accuracy of Parameter Estimation for Moving Single Molecules Imaged by Fluorescence Microscopy. IEEE Trans. Signal Process. *59*, 895–911.

Wu, P.-H., Agarwal, A., Hess, H., Khargonekar, P.P., and Tseng, Y. (2010). Analysis of Video-Based Microscopic Particle Trajectories Using Kalman Filtering. Biophys. J. *98*, 2822–2830.

Wüstner, D., Solanko, L.M., Lund, F.W., Sage, D., Schroll, H.J., and Lomholt, M.A. (2012). Quantitative fluorescence loss in photobleaching for analysis of protein transport and aggregation. BMC Bioinformatics *13*, 296.

Yuste, S.B., and Lindenberg, K. (2001). Subdiffusion-limited reactions.

Zareh, S.K., DeSantis, M.C., Kessler, J.M., Li, J.-L., and Wang, Y.M. (2012). Single-image diffusion coefficient measurements of proteins in free solution. Biophys. J. *102*, 1685–1691.

Zhang, B., Zerubia, J., and Olivo-Marin, J.-C. (2007). Gaussian approximations of fluorescence microscope point-spread function models. Appl. Opt. *46*, 1819–1829.

Zhao, B., and Brittain, W.. (2000). Polymer brushes: surface-immobilized macromolecules. Prog. Polym. Sci. *25*, 677–710.

Zhu, L., Zhang, W., Elnatan, D., and Huang, B. (2012). Faster STORM using compressed sensing. Nat. Methods *9*, 721–723.

Zimm, B.H. (1956). Dynamics of Polymer Molecules in Dilute Solution: Viscoelasticity, Flow Birefringence and Dielectric Loss. J. Chem. Phys. *24*, 269–278.

Zimmer, C., and Fabre, E. (2011). Principles of chromosomal organization: lessons from yeast. J. Cell Biol. *192*, 723–733.

(2007). Spatial Point Processes and their Applications. In Stochastic Geometry, W. Weil, ed. (Springer Berlin Heidelberg), pp. 1–75.

6 Supplementary information

6.1 I-Spt-PALM

6.1.1 Supplementary Figures

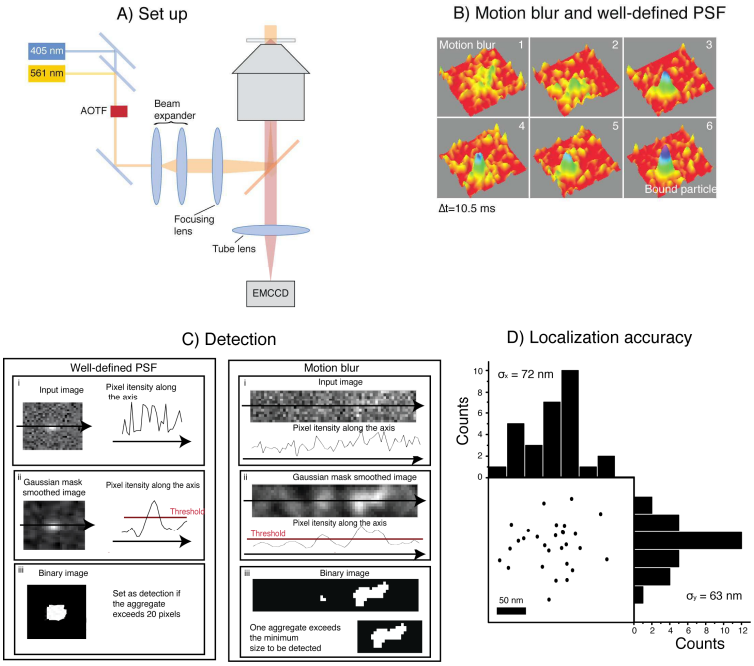

Figure S 1: Motion blur and detection algorithm

In panel A, schematics of the experimental set-up. The activation (405 nm) laser and the excitation (561 nm) laser were aligned on a single beam using a dichroic beamsplitter. Their intensity and on/off switching ratio were independently controlled with an acousto-optic tunable filter (AOTF). The combined laser beam was expanded through a beam expander and focused on the rear plane of the objective in an inverted microscope, with the help of a long-pass dichroic. The emission from the sample was imaged through the tube lens with an EMCCD. Panel B shows the transition of a fast diffusing particle to a bound state. .The image of the moving particle results in a motion blur whereas the image of the bound molecule is a well-defined PSF. In panel C, schematics of the steps followed by the detection algorithm for both a well-defined PSF and a motion blur. The initial image (i) was smoothed by a Gaussian mask and the threshold value set as the 80% percentile of the raw image (ii). Finally, the image was binarized according to the threshold and aggregates of sufficient size set as a positive detection. Panel D shows the estimation of the experimental localization accuracy computed for an immobile-like H2B protein. The position of the centroid of 29 consecutive detections represents the experimental error of the detection. Computation of the standard deviation of the mean along the X and Y axes is a measure of the pointing accuracy.

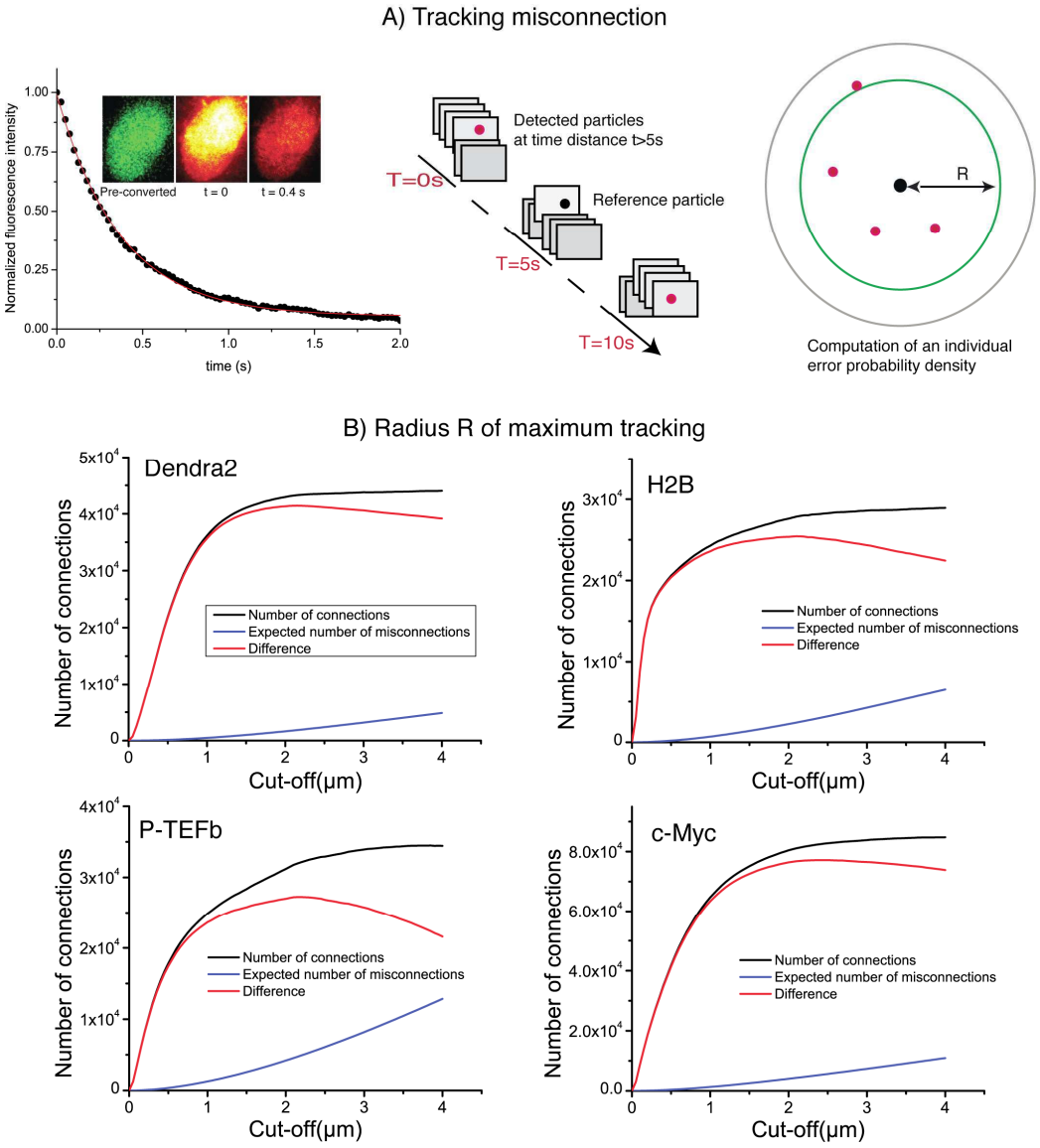

Figure S 2: Tracking algorithm *In A, decay of fluorescence intensity of the ensemble of Dendra2 fluorophores in the nucleus of a cell, after strong pulsed activation. The decay was fitted to a single exponential of lifetime* τ *= 600 ms. After 5 second of illumination, 99.9999% of the particles have bleached, allowing us to compute the misconnection probability. For each detected molecule, detections located at a time distance of at least five seconds were taken into account. Those detections have a negligible probability of 10-6 to arise from the same protein. For a given radius R, we could therefore compute the expected number of misconnections. In panel B, the number of connections, misconnections, and their difference as a function of the cut-off tracking radius R, for each protein under study are shown. Gradual increase of the cut-off distance increases the number of both connections and misconnections. The optimal cut-off radius R is reached when the number of connections reaches a plateau and only the number of misconnections increases. For all the proteins, we found an optimal value of ~ 2 µm.*

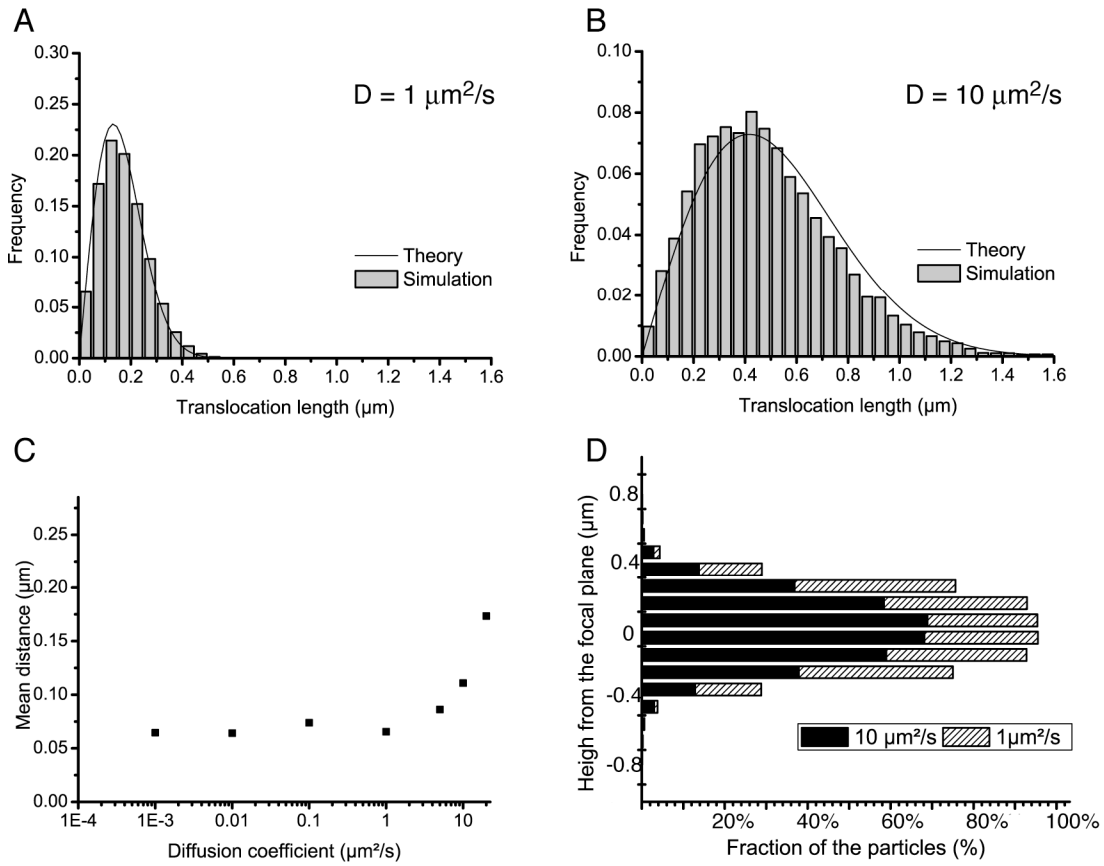

Figure S 3: Localization accuracy and detection efficiency as a function of diffusion coefficient *In panels A and B, step translocation histograms as retrieved by the detection and tracking algorithms on simulated movies of particles following pure Brownian diffusion, with different diffusion coefficients (D = 1 µm2/s and D = 10 µm2/s for A and B, respectively). In panel C, the localization accuracy of the detection is plotted as a function of the diffusion coefficient of the particle, for a series of simulated movies with increasing diffusion coefficient (0.001, 0.01, 0.1, 1, 10, and 20 µm2/s). In panel D, the percentage of detected particles is plotted as a function their distance to the focal plane, averaged over the acquisition time, for two diffusion coefficients: 1 µm2/s and 10 µm2/s.*

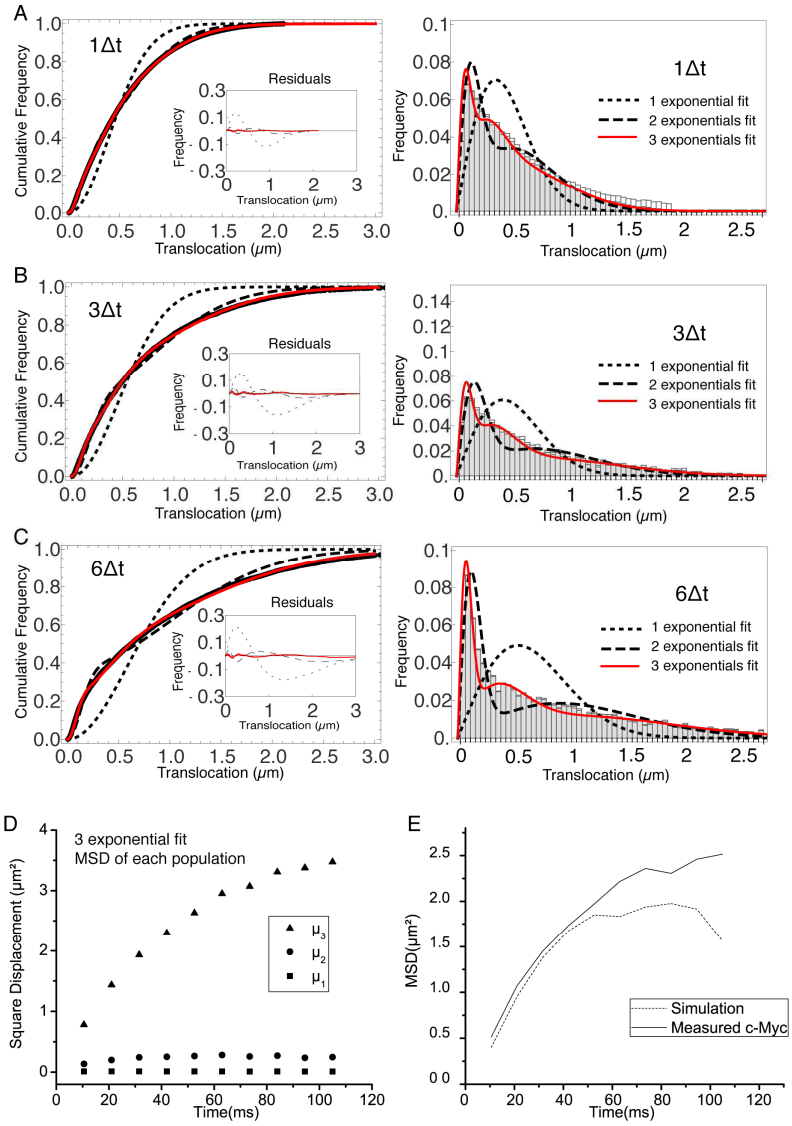

Figure S 4 Analysis of the cumulative distribution function of step translocations for c-Myc *Cumulative distribution function (CDF) of the step translocations is plotted in red for three different time intervals (1Δt, 3Δt and 6Δt in panels A, B, and C, respectively; Δt = 10.5 ms). The fit of the CDF is shown for 1 (dotted line) 2 (dashed line) and 3 (solid line) Brownian diffusive populations. In the inset, the residuals of the fits are shown. On the right hand side, the step translocation histograms from which the CDF were calculated, shown with the results of the CDF fit for 1, 2, and 3 populations. At increasing lag times, 3 diffusive species were needed to retrieve a good fit of the data. In panel D the temporal evolution of the exponential coefficient* μ *for each population is shown. The diffusion coefficient for each population was calculated by a linear regression of the first four points of the MSD. In panel E, a simulation was performed using the results of the measurement of the diffusing coefficients and corresponding rescaled proportions (D1 = 0 μm2/s, 9%; D2 = 1.4 μm2/s, 20%; D3 = 14.4 μm2/s, 70%) and the resulting MSD is shown.*

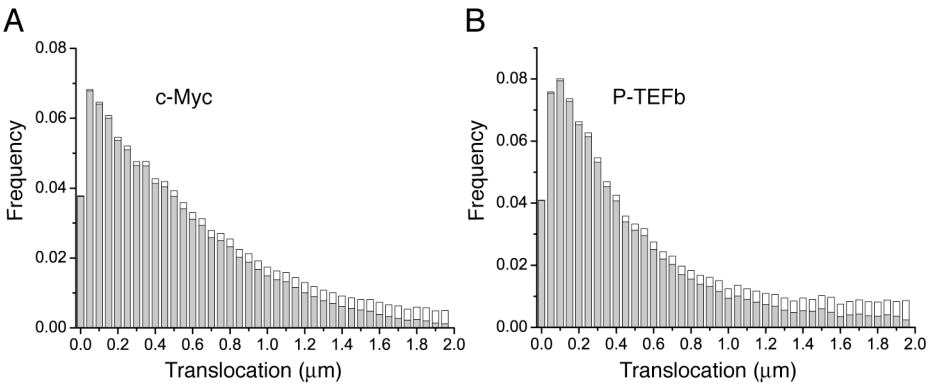

Figure S 5_Histogram of single translocations for c-Myc and P-TEFb *Histograms of single step translocation lengths for c-Myc (A) and P-TEFb (B), for 1Δt = 10.5 ms. Black curves are the result of the fit of the cumulative distribution function with three populations. Note that both histograms span within the same range of lengths.*

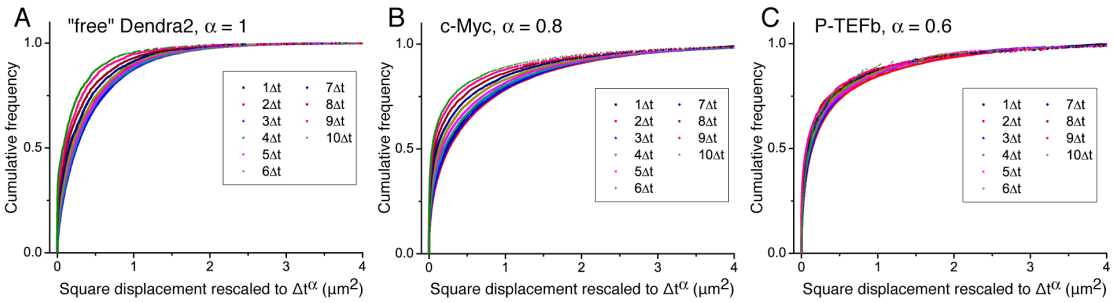

Figure S 6_Cumulative histogram of square displacements rescaled in time *For "free" Dendra2 (A), c-Myc (B) and P-TEFb (C), cumulative histograms of the square displacements rescaled in time to Δtα, for increasing lag times. Only the data obtained from P-TEFb show a collapse of the curves, indicating the goodness of the fit to the anomalous diffusion model.*

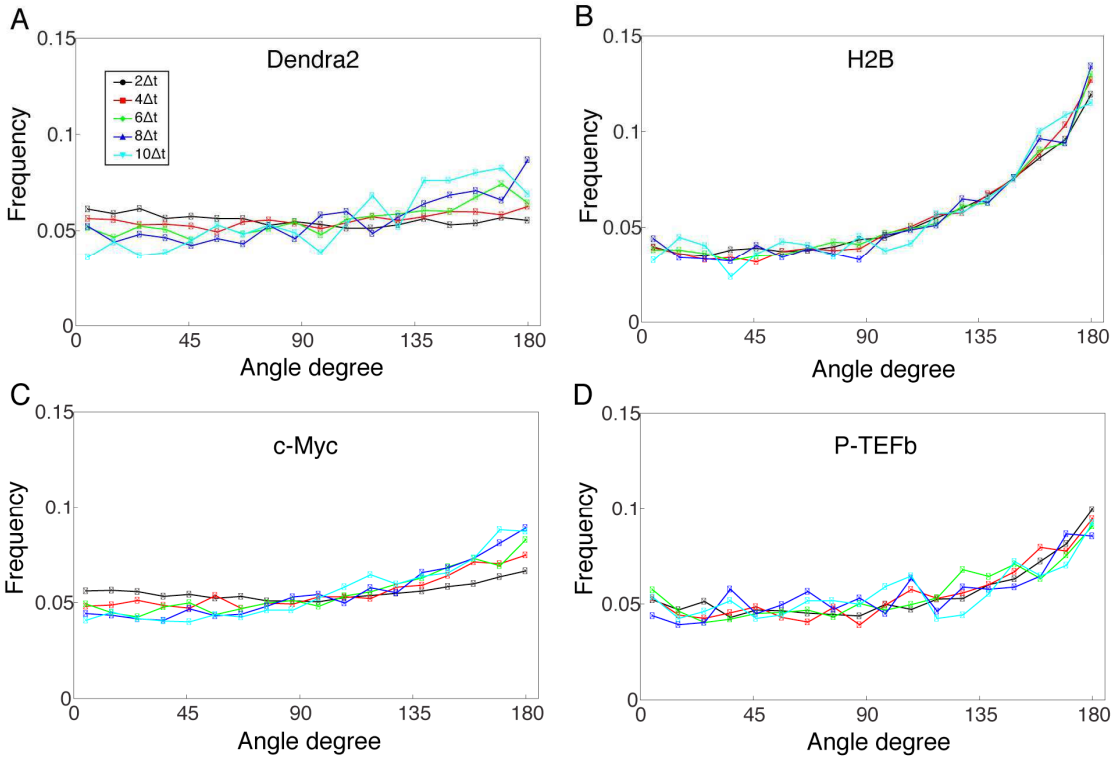

Figure S 7 Angular distribution and its temporal evolution without immobile steps *The angular distribution and its temporal evolution is calculated for consecutive translocations whose summed distance (from position 1 to position 2 plus distance from position 2 to position 3, i.e. 2Δt) is larger than 0.1 µm. For each molecule (Dendra2, A; H2B, B; c-Myc, C; P-TEFb, D) distribution histogram of the angle θ formed between the vectors of two consecutive translocation steps (2Δt, in black) and its temporal evolution (up to 10Δt) is plotted. Δt = 10.5 ms.*

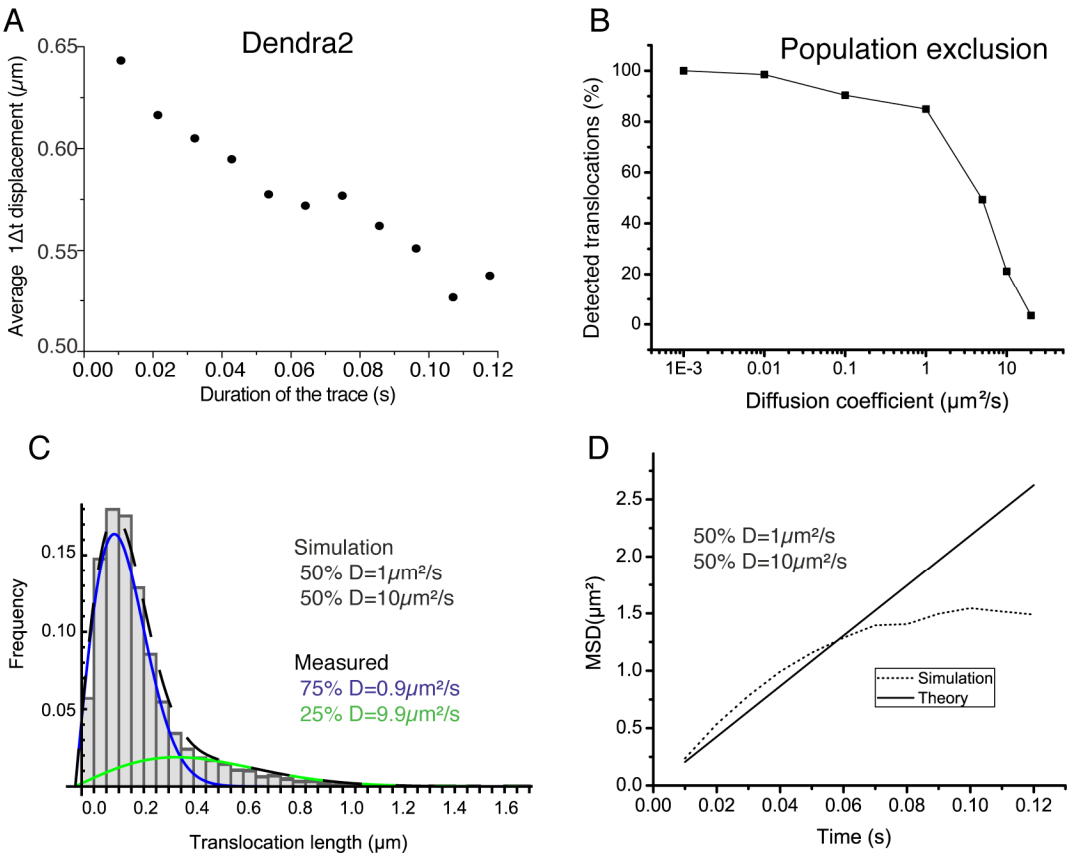

Figure S 8 Supplemental Figure S4: Population exclusion *In panel A, the average single step translocations (Δt = 10.5 ms) plotted as a function of the length of the trace for "free" Dendra2. In panel B, the number of detected translocations is shown for increasing diffusion coefficient (0.001, 0.01, 0.1, 1, 10, and 20 μm2/s) for simulated movies of the same duration, volume and particle concentration (one single diffusing particle). Simulations with a mixture of two diffusive species with different diffusion coefficients of 1 μm2/s and 10 μm2/s were also performed. The translocation histogram in panel C shows the effect of the bias due to the lower percentage of detections of fast particles. The same effect can be observed at larger lag times in the difference for the theoretical and measured averaged MSD shown in panel D.*

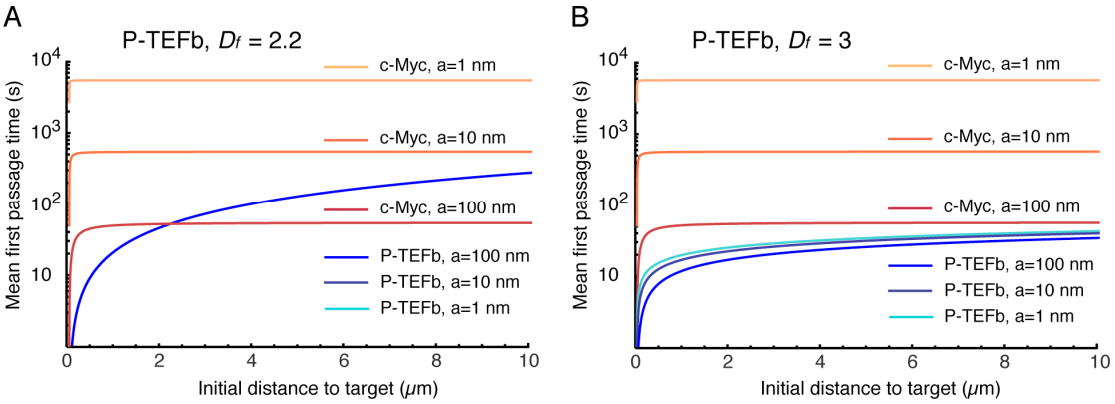

Figure S 9 Mean first passage times with Df = 2.2 and Df = 3 *Mean first passage time (MFPT) as a function of the initial distance to the target for c-Myc (non-compact exploration; Df = 3, Dw = 2, and diffusion coefficient D = 9.8 μm2/s) and P-TEFb calculated with two fractal dimensions: Df = 2.2 in (A), and Df = 3 in (B) (Dw = 3.3, and scale factor of the MSD fit D = 7.8). The MFPT was calculated for three different target sizes: 1 nm, 10 nm, and 100 nm (in A, the three curves overlap in the case of P-TEFb).*

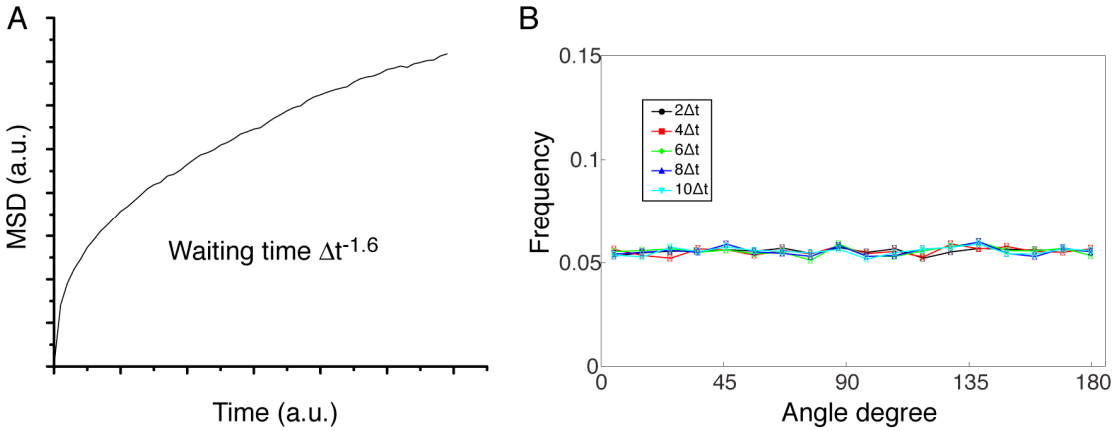

Figure S 10 Supplemental Figure S9: Continuous-time random walk *In A, ensemble averaged mean square displacement (MSD) for a continuous-time random walk (CTRW) on a cubic lattice, with a heavy-tailed probability distribution of power -1.6 and a position recorded every 1000 steps. The MSD exhibits an anomalous curvature. The corresponding angular distribution is shown in panel B. The angular distribution of angles is symmetric and uniform at all time scales.*

6.1.2 Supplementary texts

6.1.2.1 Detection and tracking of single molecules

6.1.2.1.1 Particle detection

The diffusion of the molecules imaged in the nucleus of eukaryotes can be as fast as ~ 10 $\mu m^2/s$. This implies that the detected molecules can travel a distance larger than the diffraction limit of light (~ 250 nm) during the characteristic acquisition time (10 ms). The intensity profile is therefore a convolution between the Airy pattern of the point spread function (PSF) and the trajectory of the particle during the 10 ms acquisition time (**Figure 17**, panel *b*). While such motion blur contains potentially useful information (English et al., 2011), it has some detrimental consequences: a decrease of the SNR and the ineffectiveness of traditional Gaussian fit localization algorithms. An approach, demonstrated in bacteria, to minimize the blurring effect consists in illuminating the sample with brief (1 ms or less) and intense (up to 100 kW/cm^2) laser pulses. In bacteria, this stroboscopic method is all the more necessary since the extension of the motion blur is often comparable to the size of the cell itself (section of 1 μm^2) (English et al., 2011),. However, given the larger dimension (section ~ 200 μm^2) of a mammalian nucleus, this method requires high laser power, not practical with standard microscopes or live cell microscopy due to phototoxicity effects. Hence, we favored an approach using lower intensity (~ 4 kW/cm^2) and longer illumination time (~ 10 ms), limited by the readout rate of our camera. At this time scale, trajectories are not affected by the nuclear confinement.

In this case, the emission of fast diffusing single fluorophores cannot be detected with traditional two-dimensional Gaussian fit algorithms (Cheezum et al., 2001) (Abraham et al., 2009). We developed an alternative, comprehensive algorithm capable of detecting fast diffusing molecules that typically have low signal to noise ratio (SNR) as well as immobile particles with higher SNR.

For each frame, background intensity was estimated at each pixel as the median intensity of the pixel over the entire movie. This background was subsequently subtracted from the raw image. Fluorescence signal from individual molecules may still appear as an aggregate of disconnected pixels, therefore a smoothing step was applied using a Gaussian mask with standard deviation of σ = 121 nm. Those pixels with an intensity corresponding to the highest 20% of the non-

smoothed (but background corrected) image were selected (Fig. S1, panel C). At such threshold level random noise fluctuations were still included in the pixel selection, we therefore disregarded any spot that spanned less than 0.2 μm² (~20 pixels, or about half the theoretical optical response of the system). Individual pixel aggregates were then selected for each frame, with one additional constraint to account for molecules diffusing outside and back inside the focal plane during the acquisition time; we considered detected spots closer than 500 nm as originating from the same molecule. The position of each spot was calculated as the center of mass of the pixel aggregate as a good estimator of the particle position suggested by deconvolution approaches (Michalet, 2010).

We tested our detection algorithm with simulated movies consisting of white noise (without single particles signals) with pixel intensity values and standard deviation comparable to the background noise of our live cell data, resulting on a detection rate of 10^{-6} detections per frames per μm², three orders of magnitude lower than the typical detection rates obtained with the experimental data.

The localization accuracy of the detection algorithm could also be estimated. We calculated the standard deviation of the position coordinates of a H2B molecule, detected in 290 consecutive frames (3 seconds tracking) with no apparent diffusion. As shown in Fig. S1, panel D, we obtained a localization accuracy of ~ 70 nm.

6.1.2.1.2 Tracking

In order to connect consecutive detections of one given molecule, we defined the maximum distance R allowed for the translocation of a single step of the particle. For each single particle detection, the radius R defined an area centered on the particle position at time T on the consecutive frame at T+Δt. When a detection at T+Δt was found within the area defined by R, the two detections were linked in a trajectory. When two or more particles were detected within this area, the trajectory was truncated and the positions considered as the first detection of new trajectories. When the detection of one particle could be included in two different trajectories, both trajectories were also truncated, and the detection disregarded. We defined such a restrictive policy of tracking in order to reduce the number of misconnections, or false-positive tracking connections. A misconnection occurs when two consecutives detections from two different

molecules are included in the same tracking sequence. Therefore, when there is any ambiguity between two spatially closed detections the algorithm truncates the trajectories.

Such restricting tracking policy reduced the number of misconnection but also reduced the total number of traces suitable for analysis. Therefore, in order to set an appropriate maximum radius R, we computed the probability of detecting two different molecules in consecutive frames within a distance lower than R.

6.1.2.1.3 Maximum tracking radius R and misconnection probability

Considering the detection of a given molecule in consecutive frames we could estimate the probability of tracking error by determining the local density of molecules different than the molecule of interest. In order to do so, we determined the local particle density at a time point where the probability of detecting the same particle is close to zero. We estimated the fluorescence photobleaching characteristic time under our experimental conditions by measuring the fluorescence lifetime of an ensemble of proteins in the nucleus, after a high intensity activation pulse, and under usual imaging conditions (Fig. S2, panel A). We measured a fluorescence half-life of ~ 600 ms, suggesting that the probability of a molecule photobleaching between two consecutive frames is 0.02. After 5 seconds (476 frames) of the initial detection, it is highly improbable (0.0001 probability) that a detection originates from the same molecule. For each molecule detected, we could therefore calculate the number of detections around the same spatial coordinates but at a time separation of 5 seconds or more and thus estimate the average local density within a radius R of the molecule.

Considering the set of all the detections (x_i, y_i, t_i), where (x_i, y_i) are the spatial coordinates and t_i the time, for each detection i we defined N_i, the total number of frames recorded more than 5 seconds after each particular detection i. The detections made during this period are estimators of the local density around detection i. We therefore defined $W_i(R)$ as the total number of detections during these time-shifted frames within a distance smaller than R (i.e. the total number of detections within R, after 5 seconds). Being M the total number of detections, we could calculate the total number of expected misconnections within a radius R as follows:

$$W(R) = \sum_{i=1}^{M} \frac{W_i(R)}{2N_i} \qquad (91)$$

By comparing the value obtained from this expression to the number of connections we measured, we could estimate the probability to miss-connect two detections. The total number of connections *C(R)* could be then calculated integrating both, the misconnections and the positive translocations. For every detection *i* we calculated $C_i(R)$, the number of detections at the consecutive frame at a distance smaller than *R*. The sum of all detections was therefore:

$$C(R) = \sum_{i=1}^{M} C_i(R) \qquad (92)$$

In Fig. S2, panel B, we plotted the measured *W(R)* and *C(R)* as well as their difference, for the free fluorophore Dendra2 as well as for all the proteins under study. We observed that for *R* bigger than ~ 2 µm the total number tracking assignments was dominated by misconnections; we therefore set the maximum allowed radius *R* for tracking under our imaging conditions to be 2 µm.

A tracking misconnection could occur at the first or last translocations of a trace, or in the middle of the trajectory. If a false connection occurred in the middle of the trace, its origin was the erroneous link of two traces from different molecules, being the first one detected until frame *i* and the second one frame *i+1*, appearing in the vicinity of the first molecule. The probability of such event to happen is very low because the number of single frame detections outnumbered by two orders of magnitude the number of trajectories with at least two consecutive detections. We could therefore consider that the tracking error misconnections occurred mainly at the beginning or end of the trajectories. Taking into account only the detections that are at the extremities of a trajectory, after tracking with a maximum radius of 2µm, we could therefore estimate the probability of false connection from the fraction of misconnections as:

$$P^W = \begin{cases} 0 & \text{Within trajectories} \\ P^W_{extremity}(d_i) & \text{for the first and last steps} \end{cases} \qquad (93)$$

$$P^{W}_{extremity}(x) = \frac{W'(x)}{C'(x)} \qquad (94)$$

Where W' and C' stand for the first order derivative of W and C, that were estimated for mathematical convenience every 0.05 µm and then linearly extrapolated.

To extend the notion of one-step translocation error probability to several steps displacement, the probability for a trajectory to be false was set to be the mean of all the one-step translocations that composed the trajectory.

6.1.2.2 Cumulative histogram analysis and mean square displacement

The data of proteins diffusing in the nuclear volume is the 2D projection of a 3D motion. Provided the nucleus is isotropic along the three spatial axes X, Y, and Z, the XY projection data fully reflects the 3D behavior of the molecules.

The analysis of the cumulative translocations histogram allows the determination of individual components from a mixed set of translocations, i.e. translocation steps that cannot be governed by a single diffusion coefficient. For the 1Δt time step (10.5 ms), the cumulative distribution function (CDF) is a function $F_1(x)$ that represents the probability that a random translocation may be found at a distance smaller than x.

The cumulative function weighted with the probability of misconnection is:

$$\overline{F_1}(x) = \frac{\sum_i H(x - d_i)(1 - P^W(d_i))}{\sum_i (1 - P^W(d_i))} \qquad (95)$$

where the sum is computed for all the recorded translocations d_i , H represents the heavy side step function, which is 1 for $x - d_i \geq 0$ and 0 for $x - d_i < 0$ and P^W is the misconnection probability that was described in the previous section .

The probability distribution of 2D translocations for a single diffusion coefficient D and an inter-frame lag time T is given by $\frac{1}{\sqrt{4DT}} e^{-\frac{x^2}{4DT}}$. This imposes a CDF of translocations for a set of translocations that can be described by single population of diffusion to be:

$$1 - e^{-\frac{x^2}{4DT}} \qquad (96)$$

When the dynamics pool reflects a range of square-translocations with different diffusion kinetics, this single exponential function fails to describe the empirical CDF. In the case of k diffusing species, the empirical CDF is best described by

$$1 - a_1 e^{-\frac{x^2}{4D_1 T}} - a_2 e^{-\frac{x^2}{4D_2 T}} - \cdots - a_k e^{-\frac{x^2}{4D_k T}} \qquad (97)$$

where a_i represents the fraction of translocations in the probability distribution imposed by a diffusion coefficient D_i. The normalization condition $a_1 + a_2 + \cdots + a_k = 1$ has to be satisfied, and k, the number of different diffusing populations, is as small as possible.

The evaluation of the CDF for different time lags (Δt = 1, 2, … 10) allowed us to estimate the individual diffusion coefficients (Wieser and Schütz, 2008) (Fig. 2C). This analysis of the cumulative distribution function fits the experimental data with a model of Brownian diffusion of different populations. Further analysis of the mean square displacement of translocations and the step correlation was necessary to determine the nature of diffusion and validate or refuse the simple Brownian model independently for each protein.

6.1.2.2.1 Mean Square Displacement (MSD)

We first computed the mean square displacement of translocations for each individual trace *j* (MSD_j) of length *n*, weighted with the probability of misconnection previously described. The MSD_j is therefore:

$$MSD_j(t) = \frac{\sum_{i=1}^{n-t} d_{i,i+t}^2 \left(1 - P^w(d_{i,i+t})\right)}{\sum_{i=1}^{n-t} \left(1 - P^w(d_{i,i+t})\right)} \qquad (98)$$

where $d_{i,i+t}$ is the translocation distance between the frames i and $i+t$. The MSD_j for individual traces was then computed for increasing lag times up to $10\Delta t$ ($t = 1\Delta t, 2\Delta t, \ldots 10\Delta t$) where Δt is the experimental inter-frame time interval of 10.5 ms. We then calculated the average mean square displacement $MSD(t)$ for $t = 1\Delta t, 2\Delta t, \ldots 10\Delta t$ as the mean of all the individual traces $MSD_j(t)$ for all the trajectories that had a length of at least equal to *t*. Finally, error bars for

each data point of the average *MSD(t)* were calculated as the 95% interval of confidence computed by bootstrap resampling of the population.

6.1.2.3 Numerical simulations

In order to validate our detection and tracking algorithms and analysis, we performed a series of numerical simulations. These simulations consisted in movies of particles with the optical response of our optical system, diffusing in 3D Brownian motion with a given diffusion coefficient. The signal was then corrupted with additional noise composed by a mixture of Gaussian and shot noise that mimicked our raw experimental data.

6.1.2.3.1 Parameters of the simulation

The PSF of the single particle signal was obtained with the PSF Lab software (Nasse and Woehl, 2010). The parameters used to retrieve the PSF were: emission wavelength 600 nm, objective NA 1.49, coverslip thickness 150 μm, oil refractive index 1.51, coverslip refractive index 1.52, and sample refractive index 1.3. The PSF was computed for a total height of 4 μm in layers of 100nm and radius of 2 μm, on a pixelated image with pixel size of 107 nm. Intermediate values were estimated by linear interpolation of the 8 surrounding points.

In order to estimate the noise, we analyzed the distribution of the pixel intensity values of experimental movies after removing the values of those pixels included in any detection. We then fitted this distribution to a combination of Gaussian and Poisson distributions, with a result of 95% Poisson distribution ($\lambda = 20$) multiplied by a factor determined by the camera gain, and 5% white noise.

The movement of the particles was simulated to take place in the interior of a closed box with similar dimensions to those of the eukaryotes nucleus: 10 μm x 10 μm x 6 μm. The particle density inside the box was set to be constant (ie the photobleaching rate and the photoactivation rate were the same), and therefore the ratio of disappearance and appearance of a new particle at a random position was set accordingly to the measured photobleaching half-life.

The movie images were finally obtained as a convolution of the PSF with the displacement of the particle in the pixelated matrix during the acquisition time. We computed this by estimating the position (x,y,z) every 1 ms (10 estimations per frame) and by adding the convolved PSF at

(x,y,z) to the final image. To take into account the displacement during the EMCCD transfer time between two consecutives images, an additional unrecorded movement of 0.5 ms was added to the simulation.

6.1.2.3.2 Reconstruction of diffusion

We then run the simulated movies of one single population of 3D Brownian diffusing particles through our detection and tracking algorithms. The histogram of translocations retrieved from the analysis of simulated films was in very good agreement with the theoretical values for diffusion coefficients between 0.1 µm²/s and 20 µm²/s (Fig. S3, panels A and B).

6.1.2.3.3 Diffusion coefficient boundaries

In our experiments, the minimum inter-frame displacement was limited by the experimental single molecule localization accuracy. The pointing error can be defined as the distance between the real centroid of the particle and the coordinates of the detection (Fig. S3, panel C). Using our simulations, we could determine the localization accuracy as the mean value of the pointing error, as a function of the diffusion coefficient. It was estimated to be ~ 70 nm with a dramatic increase for particles with diffusion coefficient higher than 10 $\mu m^2/s$. This is in agreement with the experimental estimation of the localization accuracy retrieved from the consecutive detections of an immobile H2B molecule (Fig. S1, panel D). The lower bound of a detectable diffusion coefficient was thus ~ 0.01 $\mu m^2/s$.

The analysis of simulated movies also allowed us to determine the percentage of detected particles. We could determine that the percentage of detections followed a Gaussian-like distribution along the optical axis, centered at the focal plane (Fig. S3, panel D). The width of such distribution determined the focal depth and it is in good agreement with the axial width of the PSF in our experimental conditions (~ 600 nm). Moreover, the amplitude of the detection distribution was dependent on the diffusion coefficient of the particles. There is a higher rate of detection for slow particles than for those with higher diffusion coefficient. This effect could also be observed in the in vivo data by plotting the averaged $1/\Delta t$ displacement as a function of the duration of the trajectory (Fig. S4, panel A, for Dendra2). Particles which were less mobile were detected for longer periods of time.

6.1.2.3.4 Population exclusion

The dependency of the percentage of detected particles with the diffusion coefficient of the particles needs to be taken into account when analyzing the mobility of a heterogeneous mixture of molecules with different diffusion coefficients. We performed simulations of an extreme case with 50% of the molecules following Brownian diffusion at 1 µm²/s and 50% at 10 µm²/s. As expected, fast particles had a higher probability of escaping the focal depth of observation between two consecutive frames, and therefore slow particles were over-represented in the measurement (Fig. S3, panel C). Such exclusion of the fast diffusing particles population significantly affects population analysis as well as the average Mean Square Displacement. The population analysis of the one step translocation histogram gave a proportion rate of 80% of particles with D = 1 µm²/s and 20% D = 10 µm²/s. Despite the bias on the population, the values of diffusion coefficients were not affected by the population exclusion (Fig. S4, panel *C*). Similarly, the resulting MSD analysis of the simulated data showed a deviation from linearity, suggesting an apparent subdiffusive behavior of the ensemble of molecules (Fig. S4, panel D).

In order to take this bias into account in our analysis, we measured the number of translocations detected on single particle simulation movies with diffusion coefficients ranging from 0.001 µm²/s to 20 µm²/s (Fig. S4, panel B). We then used this graphic as the reference curve to correct the proportions of populations retrieved from the analysis of our experimental data.

In order to perform such correction, we considered an arbitrary fit of the one step translocation histogram with three populations: (a_1, D_1), (a_2, D_2) and (a_3, D_3), with a_1, a_2 and a_3 representing the fractions of populations and D_1, D_2 and D_3 their diffusion coefficients. We found, interpolating the reference curve for each diffusion coefficient, the proportion of the population that was integrated in our study $p(D_1)$, $p(D_2)$ and $p(D_3)$. For instance, when D = 1µm²/s, we detected p(D) = 97% of the translocations. We then computed the corrected values for a_1, a_2 and a_3 as $\frac{a_1}{p(D_1)}$, $\frac{a_2}{p(D_2)}$ and $\frac{a_3}{p(D_3)}$ to obtain the relative rate of diffusive populations.

It is important to note that this correction assumes Brownian diffusion of the molecules, and therefore has to be understood as a first order correction of the population rates in all our experimental data. However, due to this selection bias, fast diffusing molecules, for which the

MSD slope is the highest, contribute less to the average MSD at longer time lags. As a result, the average MSD observed for Dendra2 is consistent with a normal diffusive behavior for 3 species.

6.1.2.4 Numerical simulations of anomalous diffusion models

6.1.2.4.1 Models for subdiffusion

Subdiffusion motion has been frequently reported in SPT experiments {Saxton:2007fm}. In cells, it is commonly attributed to one of the following two processes: a broad distribution of trapping times or an obstructed movement due to crowding effects. In our experiments on P-TEFb, we could rule out the former, often referred to as the continuous time random walk model (CTRW) {Metzler:2000tt}). Indeed, we noted that the power-law scaling of the MSD for the P-TEFb was unchanged upon removal of immobile steps in the trajectories, which excludes that the observed sub-diffusion is induced by long trapping times (see Fig. S8). We also address this model by simulation to compute its angle distribution. In Fig. S9, we show the result of a Monte Carlo simulation of a continuous time random walks performed on an infinite cubic lattice. The position was recorded every 1000 steps and the waiting times were uncorrelated following a discretized heavy tailed probability distribution

$$\begin{cases} P(T < 1) = 0 \\ P(1 < T < t) = 1 - t^{-\alpha} \end{cases} \qquad (99)$$

with α set as 0.6. The MSD shown in Fig. S9A is an ensemble MSD, averaged on 10000 trajectories and rescales as a power law $\langle r^2(t)\rangle \sim t^{\alpha}$. It is noteworthy to point out that the time-average MSD of a CTRW realization does not result in a sublinear relationship with time (Ben-Avraham, 2004). The experimental MSD curves shown in Fig. 2 and Fig. 3 were averaged over time and also over the ensemble of all the trajectories, which was an additional indication against the CTRW model for our data.

For an obstructed diffusion model giving rise to the observed subdiffusion behavior, we considered a modification of the accessible space for the diffusing particle. Bancaud and colleagues have for instance shown by fluorescence correlation spectroscopy (FCS) on GFP-multi repeats and tracking of microinjected quantum dots aggregates that the accessible nucleoplasm is not a standard 3D environment but, rather, has a fractal dimension $D_f \sim 2.6$ and

2.2 for euchromatin and heterochromatin, respectively (Bancaud et al., 2012). We addressed this model by simulations and computed the angular distribution of consecutive steps. We computed a fractal network as the maximum cluster of a cubic lattice at critical site percolation probability (Ben-Avraham, 2004). The initial cubic lattice dimensions were 2000 x 2000 x 500 sites. We then removed sites from the lattice according to the critical probability P_c =0,311604 probability (Ben-Avraham, 2004). The size of the maximum cluster, was 5 967 870 sites. We then performed random walks on such fractal structure by recording a position every 2000 steps on the lattice.

6.1.2.4.2 Angular distribution evaluation by Monte Carlo simulations

Simulations of trajectories on cubic and fractal lattices were performed in order to obtain the angular distribution of consecutive steps, and their temporal evolution. The angular distribution was obtained by Monte Carlo simulations of 10000 realizations of trajectories of 500 steps with a randomly distributed start. The cubic lattice and the maximum percolation cluster are isotropic only at a very large scale. Since the initial mesh was a cube, there were privileged directions with higher number of sites and thus a higher number of possible successive positions. In computations of the angular distributions on such simulated trajectories, this results in an over representation of the 90°angle that vanished with an increasing time lag. This bias would be negligible if the percolation cluster had a large number of sites, such that allowed us to record the position of the trajectory for at time lag significantly larger than 2000 steps. The limitation to perform such a simulation was the random access memory of the computer. We therefore applied a simple correction to the angular distribution of the simulated trajectories. We recorded all the possible translocations from our simulations for time lags 1Δt to 10Δt. These translocations were then shuffled to compute the distribution of the angles that was inherent to the network itself and not to the successive displacement correlation. Such “structural distribution” reflected therefore the anisotropy of the structure due to the finite scale of the computations and we used it as a normalization distribution. We verified that this “structural” angular distribution flattened at increasing time lag. The angular distributions shown in Fig. 5 were therefore rescaled by dividing each bin proportion by the corresponding one in the structural distribution.

In Fig. S9 panel b we show the angular distribution of a CTRW, computed as explained on the previous section, after removal of the steps where no displacements were performed. Since the geometry of the space available for diffusion of the regular Brownian motion and of the CTRW is the same, the angle distribution does not show anisotropy.

6.2 P-TEFb dynamics

6.2.1 Supplementary texts

6.2.1.1 R-FLIP

The P-TEFb experiments were conducted with a Gaussian profile LASER and a bleach duration of more than 10ms and an image exposure of 50ms each second.

Correction of bleach was estimated by the first hundred images before the bleach start. Additional bleach correction was necessary since different intensity areas within the nucleus, with intensities decreasing from the center to the outerskirts of the nucleus resulting from the nuclear egg-shape on the coverslip had a different bleach-rate. Thus after the initial estimated bleach correction we fitted the first hundred images to exponentials and thereby multiplied the curve by the correction. This consistently gave horizontal lines for all different radii emerging from the nucleus.

Nucleus geometry was treated by ignoring the first 10 and measuring up to the 70th ring which is consistently avoiding nuclear borders. Nucleoli were diminished in significance by multiplication of a significance – factor that linearly corresponds to the initial intensity of the pixel set by a certain threshold estimated by the average intensity of the nucleus.

Number of cells averaged ranges from 6 – 12. Same size nuclei were picked for averaging since the FLIP behaviour largely depends on the size of container in which the measurements were conducted.

To be completed by Lana: Correction of the bleach, inter-frame interval, number of cells averaged, nucleus geometry treatment

Complete depletion of fluorescence was achieved at approximately 400 bleaches, while bleaching was resumed until 500s of duration. We represent the FLIP by radial analysis in which

the LASER spot is taken as the reference point. Originating from the LASER bleach position, circular strips of 160nm width are defined at multiples of 160nm distances all the way to the outskirts of the nucleus. The final result is the rescale intensity level $I(r,t)$ as a function of time t and radius r. Here, we present an interpretation of the R-FLIP curves in terms of the geometry of exploration. We first present ideal R-FLIP experiment in the case of a perfect nuclear geometry and LASER beam. We then present the approximation made with real curves.

6.2.1.1.1 Theoretical Modeling of Ideal R-FLIP decays

An ideal R-FLIP experiment done on a given tagged protein of interest can be described as follow

- The LASER beam is a restricted and infinitely small area (point).
- Every molecule that pass through the LASER beam is bleached.
- The nucleus is isotropic around the bleaching point, meaning that $I(r,t)$ is the same at every point of annular region of radius r.
- There is no side effect of the shape of the nucleus and, at every radius there is a fixed amount of pooled fluorescent and bleached molecules. In such a case, $I(r,t)$ corresponds to the fraction of unbleached proteins at radius r at a time t and therefore $1-I(r,t)$ corresponds to the fraction of bleached proteins.

The un-bleached proteins have passed at least once through the bleaching site. Here we assume the reversibility of the exploration process so that any protein trajectory inside the nucleus has the same probability to occur whatever the direction. If we mentally reverse time the fraction $I(r,t)$ of light that remains at a particular place corresponds to the fraction of particles that was there at time t and that have not passed through the bleaching point. It is therefore a survival probability that depends only on the position inside the nucleus. The time at which the particle is bleached is first passage time through the bleaching point. In the case of pure diffusion with 3d spherical nucleus and bleaching point, this first passage time interpretation can resolved the Smolukowski master equation of reaction diffusion and we have global rate of bleaching that set as an exponential [ref A. Szabo 1980].

In the case of a more complex geometry in the so called large volume limit , Benichou et al. [ref geometry controlled kinetics nature chemistry] showed that $I(r,t)$ can be decomposed in two terms:

$$I(r,t) = (1-\Pi(r))\sigma\left(\frac{t}{T}\right) + \Pi(r)\varphi\left(\frac{t}{T}\right) \qquad (100)$$

where σ is the Dirac function that is zero except for $t = 0$ and T is the first passage time integrated on all possible starting points inside the nucleus, the mean first passage time. The instantaneous bleaching profile $\Pi(r)$ corresponds to the proteins that reach the bleaching site prior bouncing to the cell membrane. For time t>0, we therefore have a variable separation $I(r,t) = \Pi(r)\varphi\left(\frac{t}{T}\right)$ meaning that the decay rate is the same on every point of the nucleus far from the bleaching point and the bleaching profile $\Pi(r)$ is permanent (sup fig B).

The form of $\Pi(r)$ and $\varphi\left(\frac{t}{T}\right)$ varises from the characteristic of the underlying random walk as a function of being compact or non-compact. In the case of a compact random walk we get $\Pi(r) \propto r^{ds}$ and $\varphi\left(\frac{t}{T}\right) = \sum_{i=1}^{+\infty} \exp\left(-k_i \frac{t}{T}\right)$ and in the case of a non compact random walk such as free diffusion, we get $\Pi(r) = 1-\alpha\left(\frac{1}{r}\right)^{-ds}$ and $\varphi\left(\frac{t}{T}\right) = \exp\left(\frac{t}{T}\right)$. The parameters α is proportional to the size of the bleaching point and ds is the spectral dimension that characterize the recurrence of the random walk. At any given starting point, the expected number of time you pass again through your starting point is $\propto t^{\frac{ds}{2}}$. For a compact mode of motion we have $ds > 0$ and for a non-compact mode of motion, we get $ds < 0$ so that a non-compact search is highly non-recurrent.

Theoretical results were obtained in the case of spherical symmetry. Provided that the motion is isotropic, the cylindrical symmetry and projection of the FLIP measurement do not change the results

6.2.1.1.2 Real FLIP data

There are limitations to the application of the exact theoretical model to experimental R-FLIP data. With experimental setup, we do not image the movement of the endogenous protein. The LASER beam is not a point and every particle that goes through bleaching area is stochastically bleached according to the LASER power. The nucleus is not isotropic. Finally, the bleaching is sequential and not continuous (sup fig C). A continuous bleaching would have bleached the nucleus in only a few seconds. In the following, we assume that the impact of repetitive bleach can be integrated to the bleaching efficiency

The experimental bleaching of the nucleus $I(r,t)$ therefore could be expressed as:

$$I_e(r,t) = I_e(r,t) \otimes KL(r) \qquad (101)$$

Where K the bleaching efficiency as a function of the LASER power and $L(r)$ is the radial profile of the LASER.

To investigate the influence of the LASER profile on our measurement, we performed R-FIP experiment on CycT1-GFP transfected cells that we crosslinked with paraformaldeid (PFA). We observed a small decay rate and fixed bleaching profile. Comparing the rescaled profile with our CycT1 FLIP data, we showed that at time short (1-5s), the main effect was the LASER, with both profile being superimposed (sup fig F). The radial profile $\Pi(r)$ is therefore the LASER profile at short time scale. At medium time scale $\Pi(r)$ is stable and is the convolution between LASER profile and mobility. Finally $\Pi(r)$ when the level of protein is low, side effects of the LASER beam appear and the overall decay is representative to the global search time T of the protein.

In the end, we could decompose FLIP curves in three different regimes. At short time scale, the decay is due to the LASER profile, then the stability of decay profile shows the influence of the of the geometry. In the end of the bleaching, the profile vanishes, leaving only an overall decay rate.

6.2.1.1.3 Analyzing FLIP curve

To capture the radial dependency, we focused on the central part of the FLIP curve. We restricted our analysis to a radial distance between 1.5 to 6.5µm as for long distances, the effect

of the LASER was restrictive. We also restricted our time interval from 5 to 80 seconds. We then shifted all the curves up so they start at value 1 as a raw de-convolution the Laser effect.

FLIP decays have recently been successfully fitted to a skewed exponential showing that there were not one single decay [ref FLIP skewed]. However, we found that their only one decay rate on this particular restricted domain as predicted by the non-compact mode of motion. We believe that the larger time scale (>5s) makes most of the modes of the compact mode exploration vanish. The inverse decay rate T is the global mean first passage time through the bleach area.

To find T the curve at central radius of 4µmwas fit to an exponential the form $Ae^{\frac{t}{T}}$. Then we fitted all the radiuses from 1.5 to 6.5µm to a function $\Pi(r)e^{\frac{t}{T}}$ (figure I). The output is a list of values that are estimators of the radial factors $\Pi(r)$.

We then fitted $\Pi(r)$ to a compact $\Pi(r) \propto r^{ds}$ or a non-compact form $\Pi(r) = 1 - \alpha\left(\frac{1}{r}\right)^{-ds}$. Surprisingly, the compact form gave always the best fit, maybe because of its scale free form. We used the estimated value of compact ds as our compactness indicator CI. The larger ds is, the larger the dependence of the bleach decay on the radius.

6.2.1.1.4 A note on the interpretation of CI

Our compactness indicator CI is an estimation of the spectral dimension ds. The exact expression of ds is $dw - df$ where dw is the dimension of the walk and df is the dimension of the space. Due to raw de-convolution of the laser beam profile, projection of the data and sequential bleaching, we didn'nt have an exact estimation of $dw - df$. The fact that the non-compact form of $\Pi(r)$ was always weaker to describe the mode of motion is an additional argument in favor of the bad specification of the model. However experimental estimatison show that our compact indicator CI sort protein movement according to intuition. We believe that CI can be interpreted the same way than ds but with different scaling.

6.3 Single cell correlation fractal dimension of chromatin

6.3.1 Supplementary figures

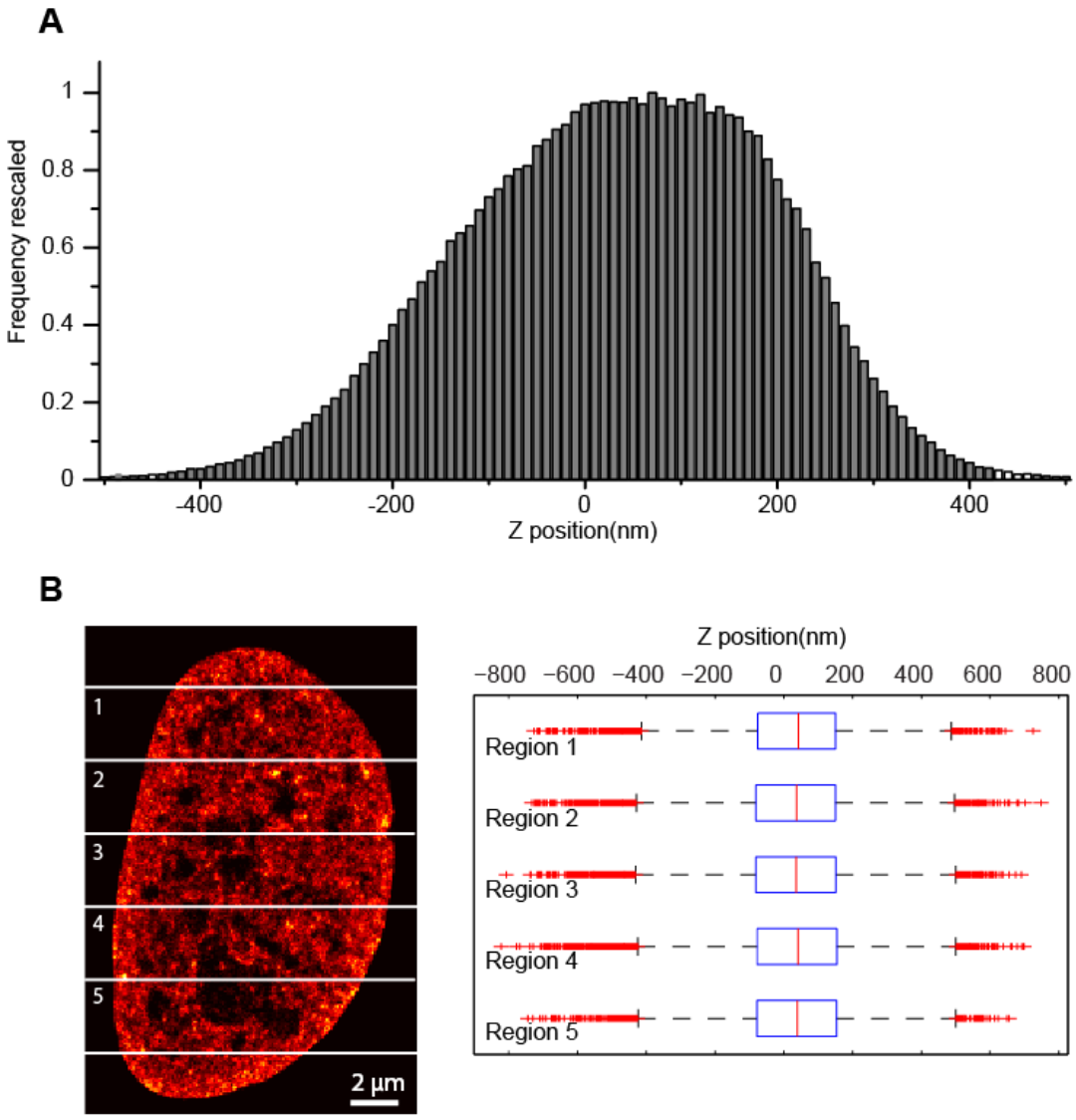

Figure S 11 . PALM H2B distribution along the z axis *Panel A: Distribution of Z position* $\mu_D(z)$ *over the whole nucleus with a 10nm binning, obtained with the deformation of the Point Spread Function (PSF) induced by deformable mirror. The resulting focal depth is about 1µm but is not uniform, the detection being further away from the focal plane having a lower probability to be detected. Panel B:* $\mu_D(z)$ *distribution for different sub-areas of the PALM image of the nucleoplasm. The stability of this distribution inside the nucleus for several regions,*

provided that they are large enough allow us to use it as a rescaling factor. It was estimated with a 10 nm bins and nanometric values were interpolated.

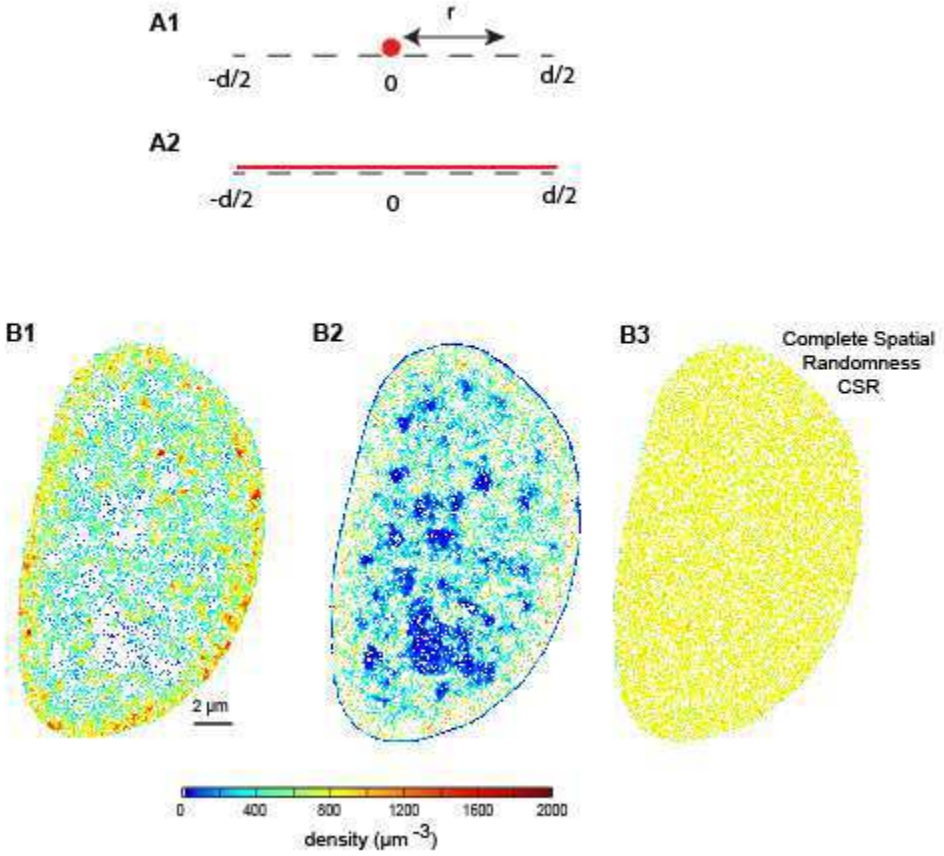

Figure S 12 . Average density estimation for a finite point pattern*. Panel A1: schematic representation of a simple point pattern in one dimension consisting of one point in the middle of segment of length* d *. The local density as a function of the distance* $\overline{d}_s(r)$ *, if averaged over all the points of the segment, will scale as* $\overline{d}_s(r) \propto r$ *like the local density measured on a uniform distribution pictured on panel A2. Similarly, The PALM H2B local the density, estimated on a 100 nm circular sliding window with a 10nm binning (Panel B1), if averaged with the same density, but on bins that are detections empty (Panel B2), will have the same average scaling that complete spatial randomness (Panel B3)*

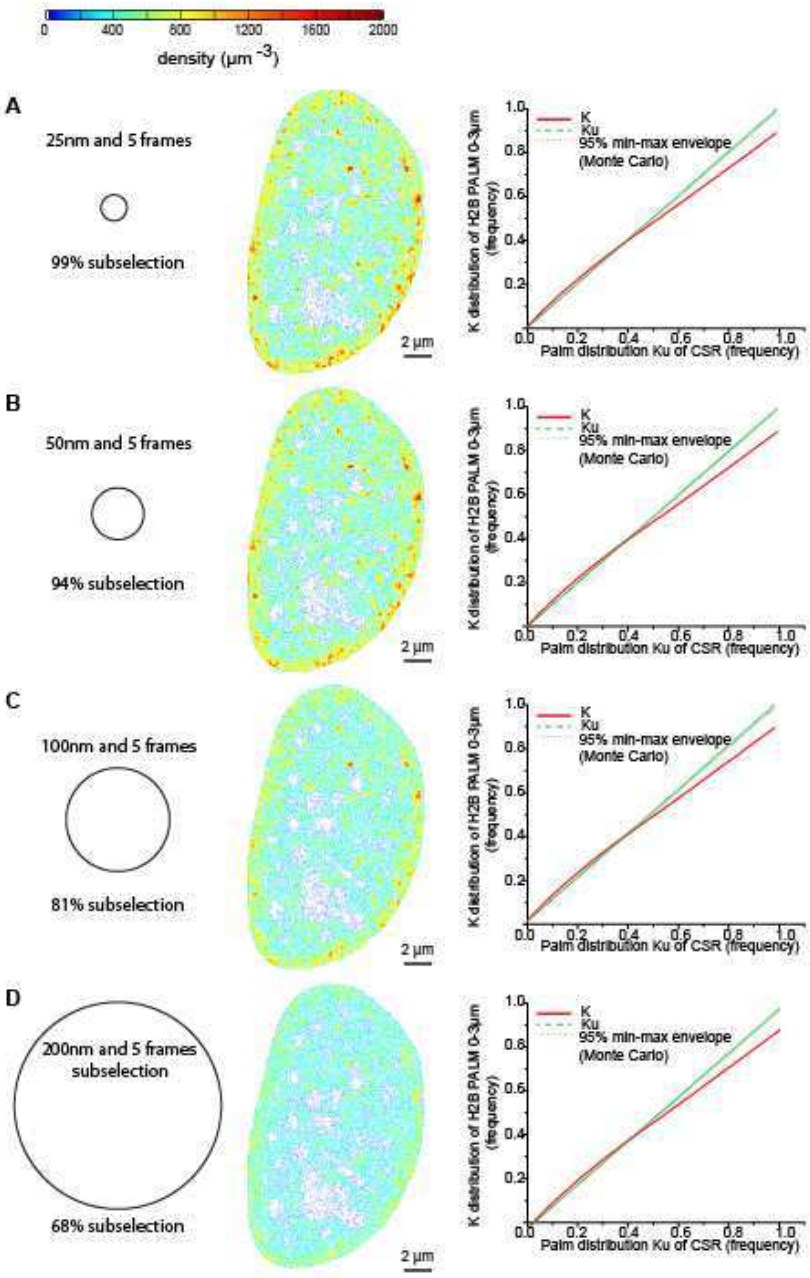

Figure S 13 Blinking *A protein can be detected up to five times sequentially before bleaching, but all with the same stochasticity, which could lead to an over estimation of the local density. We tried several filters to discard this bias. Every step, the H2B dendra2 proteins signals that are detected in the radial vicinity of another detection in the next 5 frames are discarded from the analysis. It reduces the consistency of the test against Complete Spatial Randomness but do not change its conclusions.*

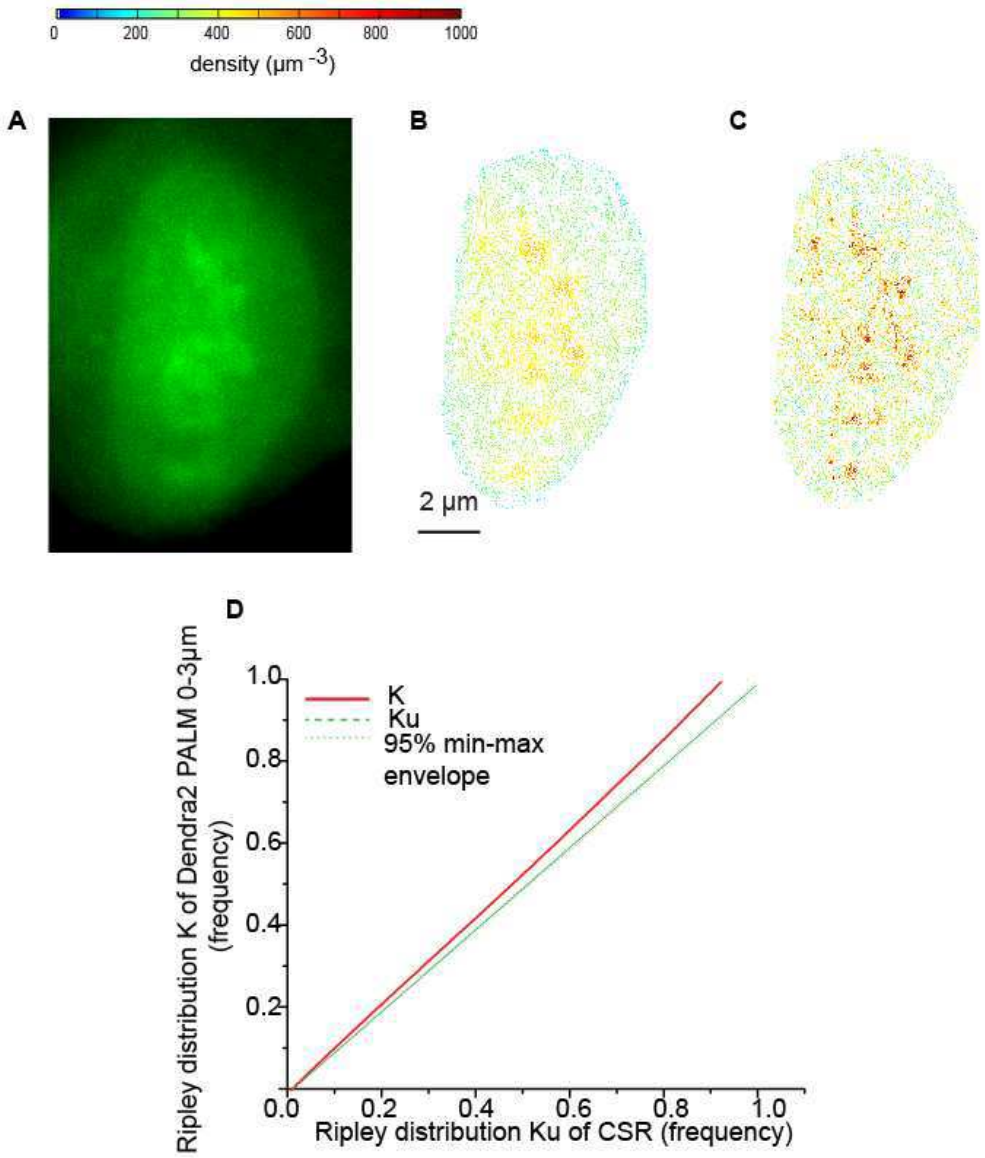

Figure S 14 .*3D PALM analysis done on U2OS cells transfected with the tag Dendra2.Panel A: Image in the green GFP channel. It shows enrichment in the nucleoli, but homogeneity elsewhere. Panel B and C: Projections of a 3D PALM image of tagged histone H2B in the xy focal plane of the camera. The color code are local densities, estimated on a 100 nm and 1 µm circular sliding mask respectively. It shows in refine details the enrichment in the nucleoli but not the enrichment in the vicinity of the membrane that we have with H2B-PALM. Panel D: CSR test showing a deviations from complete spatial randomness that is similar to the cluster model (see Supplementary Figure 5 A2 and B2)*

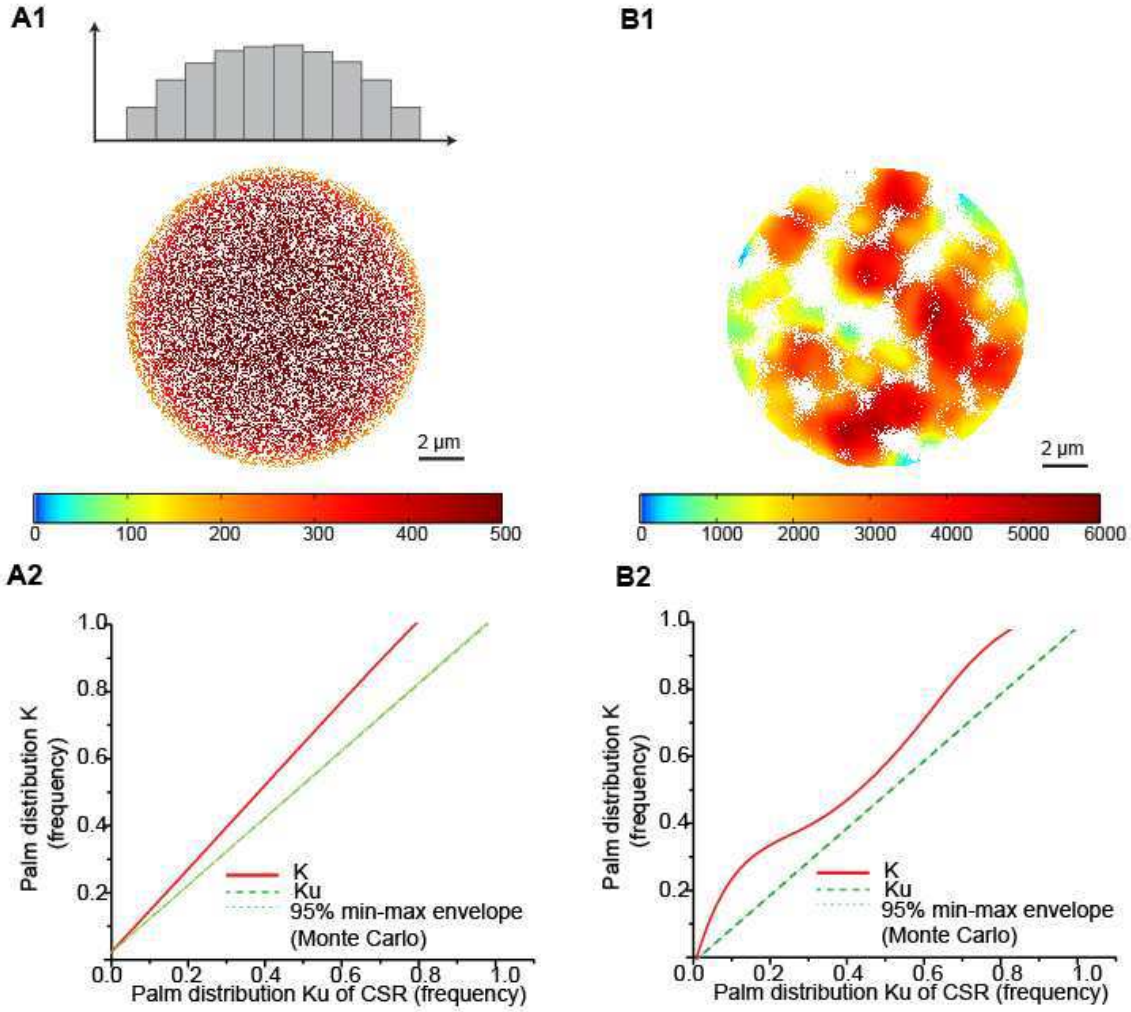

Figure S 15 *. Performance of the CSR test on two cluster models of distribution.*
Panel A1 and B1: On an infinite cluster centered, the test never saturates and always over-perform the uniform Ripley distribution K_u *. Panel A2 and B2: uniformly distributed Gaussian clusters of 300 nm radius (standard deviation). The test shows two bumps corresponding to the clusters and the averaged inter-cluster distance.*

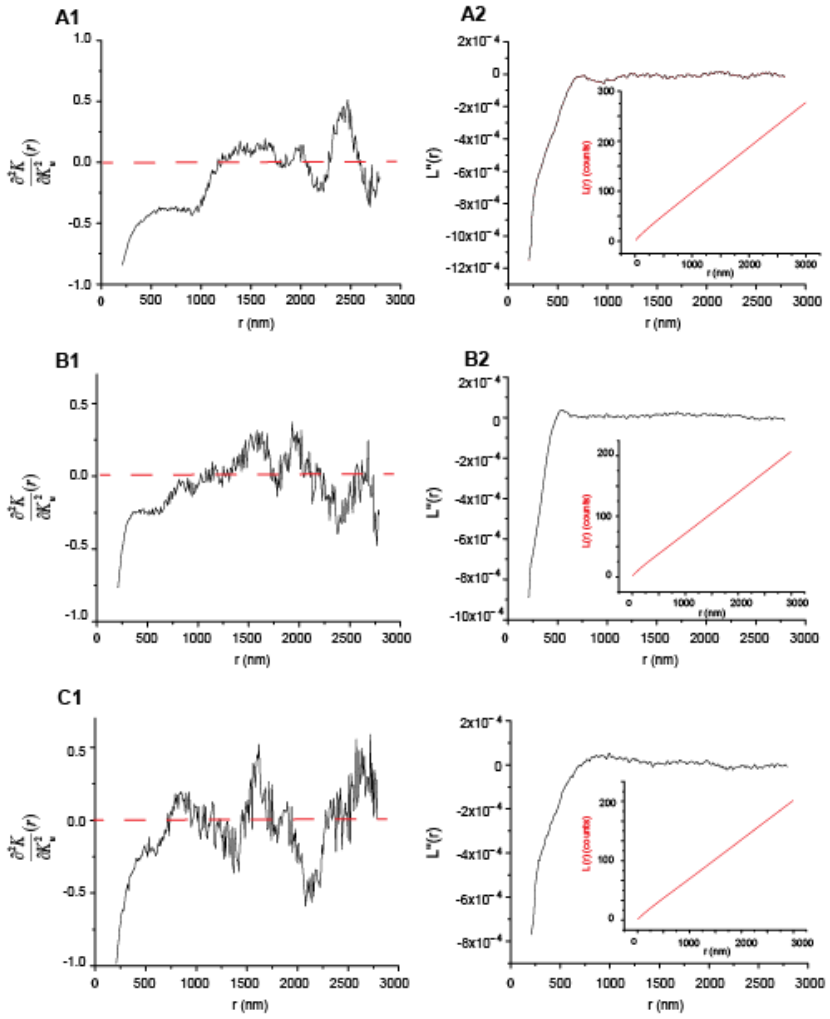

Figure S 16 *Computation of the cluster size. A1-B1-C1: Cluster size as a function of the distance estimated with the second derivative of the Ripley K function* $\frac{\partial^2 K}{\partial K_u^2}(r)$ *for 3 different cells. The function was estimated with the formula :* $\frac{K(r+h)-K(r)}{K_u(r+h)-K_u(r)} - \frac{K(r-h)-K(r)}{K_u(r-h)-K_u(r)}$ $\frac{}{K_u(r+h)+K_u(r-h)-2K_u(r)}$ *for a value* $h = 100nm$*. When reaching zero, the function shows a saturation effect that could define cluster size. A2-B2-C2:The same calculation but for the rescaled* $L = \left(\frac{\hat{K}}{\frac{4}{3}\pi\lambda}\right)^{\frac{1}{3}}$*, for the formula*

$\frac{L(r+h)-2L(r)+L(r-h)}{h^2}$. *The saturation is visible before 1 µm, but, after that limit, the distribution is heavily corrected with isotropy.*

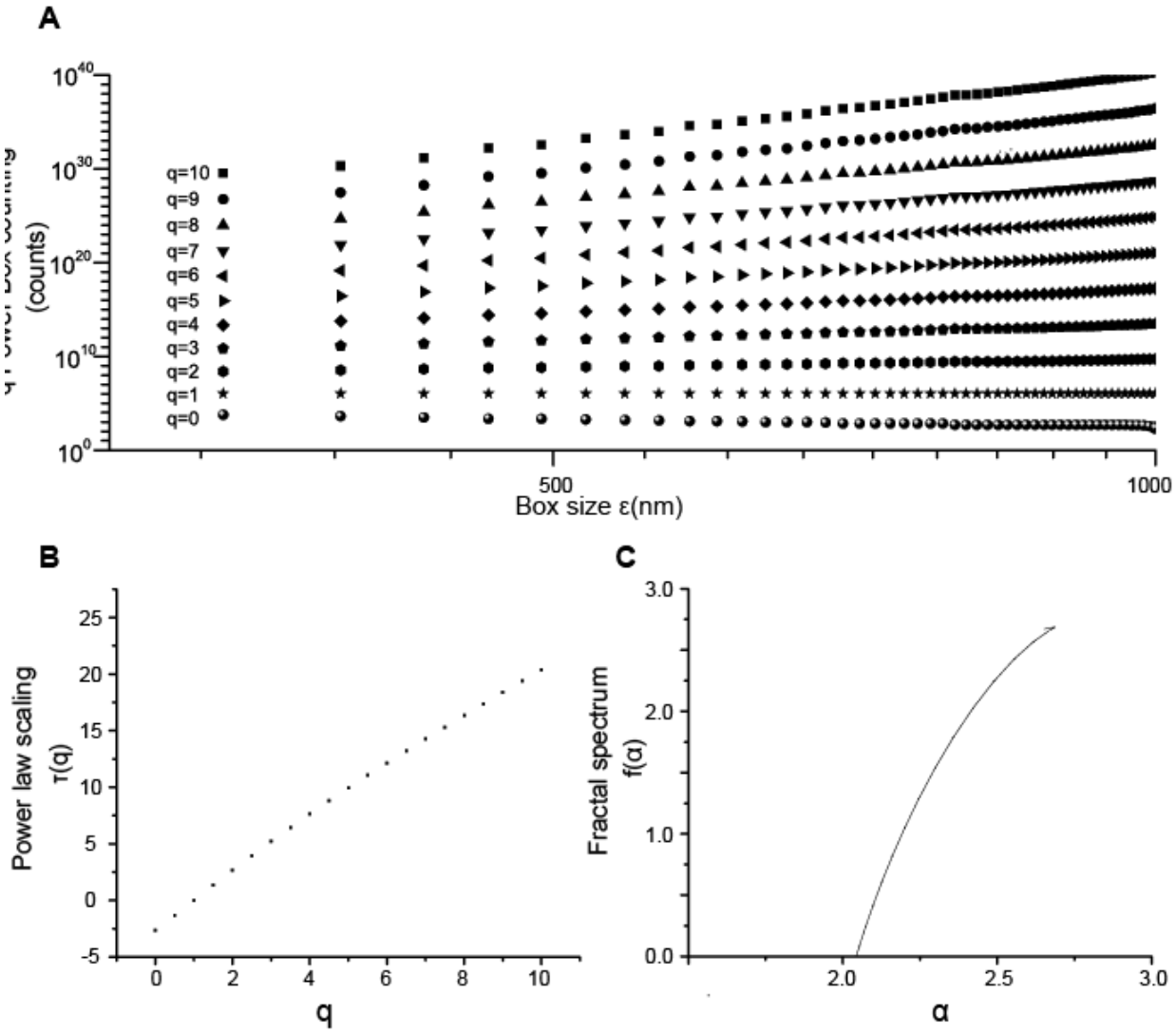

Figure S 17 Box counting computation of the multi-fractal spectrum. *Panel A: Cubic box counting of the H2B point pattern for exponent q applied on the density of each box from 10nm to 1 µm wich is the thickness of the point pattern. The curve for q=0 is the regular box counting. Each of them shows a good power law dependency that is a characteristic of multi fractal scaling. Panel B is the result of the linear regression the log log dependence for each value of q. Deviation from the line is a proof that the space is not fractal but indeed multi fractal. Panel C is resulting truncated fractal spectrum that is the deviation from the line in the previous graph. The spectrum recovers power laws ranging from 0 to 2.8.*

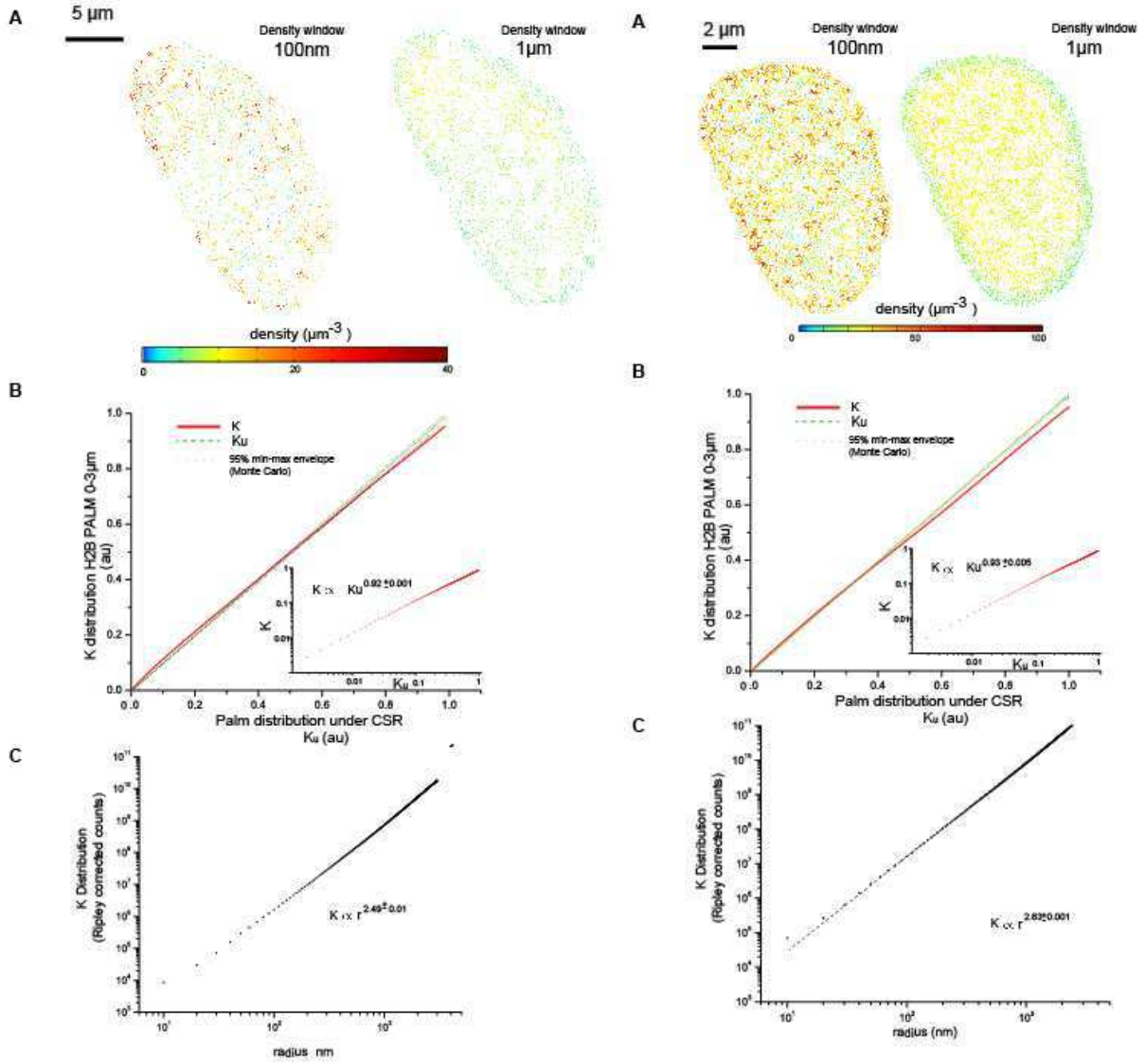

Figure S 18 and Figure S 19 Repetition of the experiment for different cells showing the consistency of the results.

6.3.2 Supplementary texts

6.3.2.1 Density averaging

The radial density $d_i(r)$ that is the number of points of a given point pattern that lie within the distance r of a point i, will have a totally different form if averaged on all the points of the point pattern or summed on all the point of the space. To clearly see the difference let's simplify the problem by estimating the average in 1D on the simplest point pattern consisting on one point

on a segment of size d at position 0 (Figure S2 panel A1). Since there is only one point the density average over this point:

$$\bar{d}(r) = 1_{\{r>0\}} \qquad (102)$$

Where $1_{\{r>0\}}$ is the in indicative function that r is positive . Average $d_i(r)$ on all the point of the space, we have a different form $\bar{d}_s(r)$:

$$\bar{d}_s(r) = \frac{1}{d}\int_{-d/2}^{d/2} 1_{\{|x|<r\}}\,dx \qquad (103)$$

By symmetry and for $r < \frac{d}{2}$, we have

$$\bar{d}_s(r) = \frac{2}{d}\int_{0}^{d/2} 1_{\{x<r\}}\,dx = \frac{2}{d}\int_{0}^{r} 1\,dx = \frac{2r}{d} \qquad (104)$$

And in the end, $\bar{d}_s(r)$ is the same $d_i(r)$ would be measured on any inner point i of the segment if we did not have a point pattern but a uniform density of value $\frac{1}{d}$ (Figure S2 panel A2). By superposition, this result is also valid in 2D or 3D and with multiple points.

For PALM-H2B, this means that if we measure the density on regions where we have detections (Figure S2 panel B1) and we average it with regions that do not have detections (Figure S2 panel B2), we will get the same average density $\bar{d}_s(r)$ that Complete Spatial randomness (Figure S2 panel B3).

6.3.2.2 Finite cluster size analysis

Several models of clustered point pattern exists such as cluster processes or double Poisson cluster processes but the $K(r)$ statistic is not powerful to discard one model from another and estimate their parameter, at least for small datasets (Ripley, 2004) but rather give qualitative information about the point pattern. We simulated different kinds of cluster processes and superimposed our experimental limitation and try to understand what would be the resulting $K(r)$ statistic (Supplementary Fig 4). A cluster of infinite size such as enrichment in the center of the cell would produce a statistic K always deviating from the uniform K_u and so does a randomly distributed cluster family of a given size provided that they sometimes overlap. However, it was impossible to rule out all the possible existing models of local enrichment, but we investigated the maximum distance at which the effect could be seen.

Properties such as cluster sizes and numbers are highly dependent on the underlying model. In the case of distant circular clusters of uniform inner concentration a methodology was studied (Kiskowski et al., 2009). The idea is to use the rescaled statistic $L(r) = \left(\frac{\hat{K}(r)}{\frac{4}{3}\pi\lambda} \right)^{1/3}$ where λ is the intensity or number of detection per unit of space and to compare it to the radius r. *Kislowski et al* found a correspondence between the cluster size and the maximum of the function $H(r) = L(r) - r$ and the minimum of its derivative $H'(r)$, the latter being more efficient in the case of overlapping clusters. On PALM-H2B, we chose the $H'(r)$ approach that is independent from the intensity λ as we could criticize the stationarity of the point pattern due to enrichment at the edges. Let's note that this method is equivalent to finding the minimum of the function $L'(r)$. We plotted both the second derivatives $L''(r)$ and the uncorrected $\frac{\partial^2 K}{\partial K_u^2}(r)$ to see where the enrichment stops and to define a typical size of our domain. We found a maximum cluster size of $1 \pm 0.1\,\mu m$ (Supplementary Fig 5). After that limit, $L(r)$ is a linear function of the intensity

6.3.2.3 Multi-fractal and fractal densities

The Haussdorff dimension f quantifies the minimum number N_ε of sets of radius ε needed to cover the fractal structure. The Haussdorff dimension can subsequently be calculated for epsilon tending to 0, as the exponential of the power law that exactly compensates N_ε such that $N_\varepsilon \ \varepsilon^f$ is bound (Falconer, 2003). Because in a PALM experiment, we detect single molecules coordinates, the notion of space filling is difficult to address. Indeed, **the theoretical Haussdorff fractal dimension of every finite point pattern is strictly zero**, due to the fact that the minimum distance between two points of the pattern is a non-zero value, and below that limit, the minimum number of sets needed to cover the pattern is fixed. In the case of H2B only a small fraction of molecules were labeled and detected. We can postulate that there is H2B everywhere but with different concentration with PALM-H2B being only a sparse subset of a non-zero density. However, since it fills the space, **the Haussdorff dimension of a non-zero density should be 3,** the dimension of the embedding 3D space itself .

The paradox, either 0 or 3 for the fractal dimension of any 3D finite point pattern, illustrates our apparent inability to address the potential lacunarity of H2B distribution and its possible fractal scaling. The paradox however does not hold if the density is multi-fractal (Falconer, 2003). Multi-fractals extend the notion of fractals to continuous density (Biswas et al., 2012). In a multi fractal formalism the correlation fractal dimension we measured does not necessarily converge to the Hausdorff dimension (Cheng and Agterberg, 1995b). Using the multi fractal formalism, different levels or organization can be retrieved addressing spatial distributions of points but also providing a measure of higher order relations in between groups of points (clusters)(Mandelbrot, 1999).

We address multi fractals by box counting, covering the 3D nucleus with cubic boxes A_i, then counting the number of detection $N(A_i)$ that lie within those boxes so that $\sum_i N(A_i) = N$ with

N being the total number of detections (Falconer, 2003). The box counting exponents $\tau(q)$ are the power law dependence between the sum $\chi_q(\varepsilon) = \sum_i N(A_i(\varepsilon))^q$ and the box size (Falconer, 2003). For q=0, one gets the ordinary box counting method. Here we compute N as $N(A_i) = \sum_k \frac{1}{\mu_D(z_{ik})}$ where z_{ik} are the z positions of tagged H2B detections inside the A_i mesh so that take into account the anisotropy of the distribution in the z direction and limited the maximum mesh size to 1µm.

Pigure S7 A shows that for every q we get a good power law dependency. The value of the log log slope $\tau(q)$ is shown on the Figure S7 B. A fractal model would result in a straight line and we get a deviation from it. To compute its deviation from it we compute the first order derivative $\frac{\tau(q+1)-\tau(q-1)}{2}$ and, by comparing by comparing $q\alpha(q)$ to $\tau(q)$, one gets:

$$f(\alpha) = q\alpha(q) - \tau(q) \qquad (105)$$

$f(\alpha)$ is the fractal, spectrum of H2B PALM that is displayed on Figure S7 C. We only get half of the spectrum because the spectrum computation needs a very high density of points (Cheng and Agterberg, 1995b). Especially, we get apparently absurd estimation for negative values of q, since empty meshes of the network ca not be raised at the power of q. The value of the spectrum at q =0 : 2.65 is the box counting fractal dimension of the support. It is theoretically addressed as the maximum of the spectrum, which does not seem to be the case. We believe that the low density far away from the focal plane of the camera creates a lack of measurement of small densities that shifts the spectrum toward the right. Despite those limitations, the box counting curve gives the value $\tau(2) = 2.7$ which is close to the value obtained for the K Ripley estimation of the correlation fractal dimension.

6.1 Yeast locus mobility

6.1.1 Supplementary figures

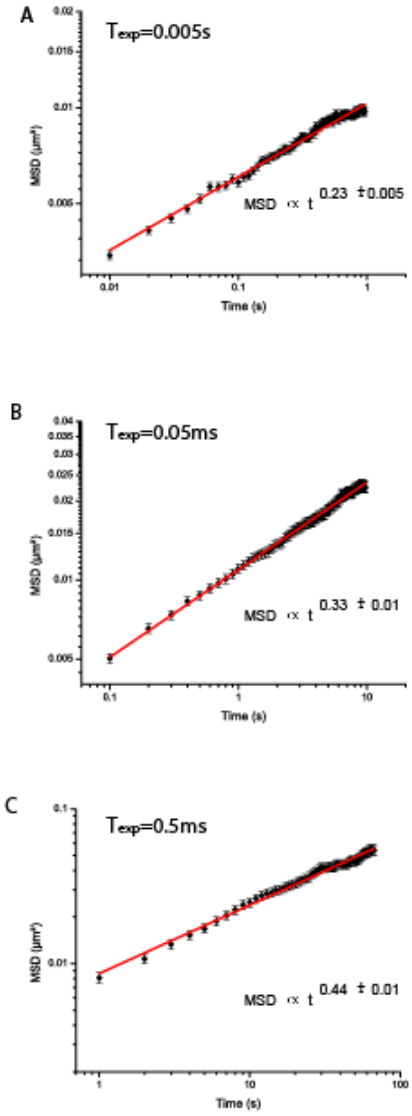

Figure S 20 Mean square displacement of figure 1 in log log scales. *The alpha anomalous exponents were those obtained by linear least square fitting of the data* $\log\left(\frac{MSD}{t}\right)$ *to a function of the form* $y=(\alpha-1)t+b$.

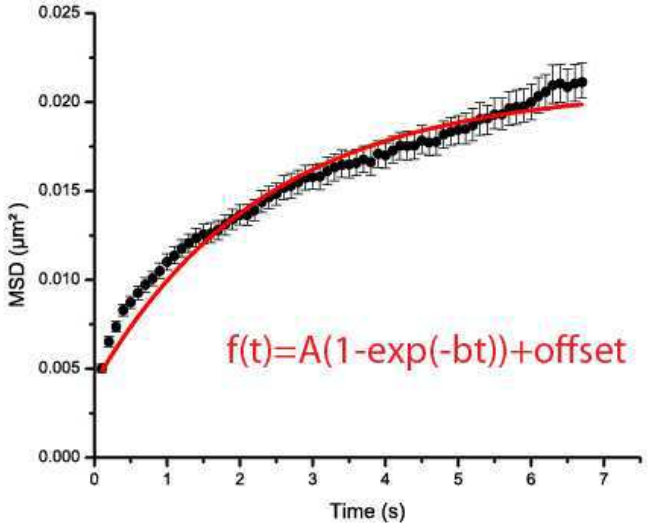

Figure S 21 Fitting the data with 0.5s to an exponential function. *The offset was found with linear regression of the first four points and intercept with the vertical axis.*

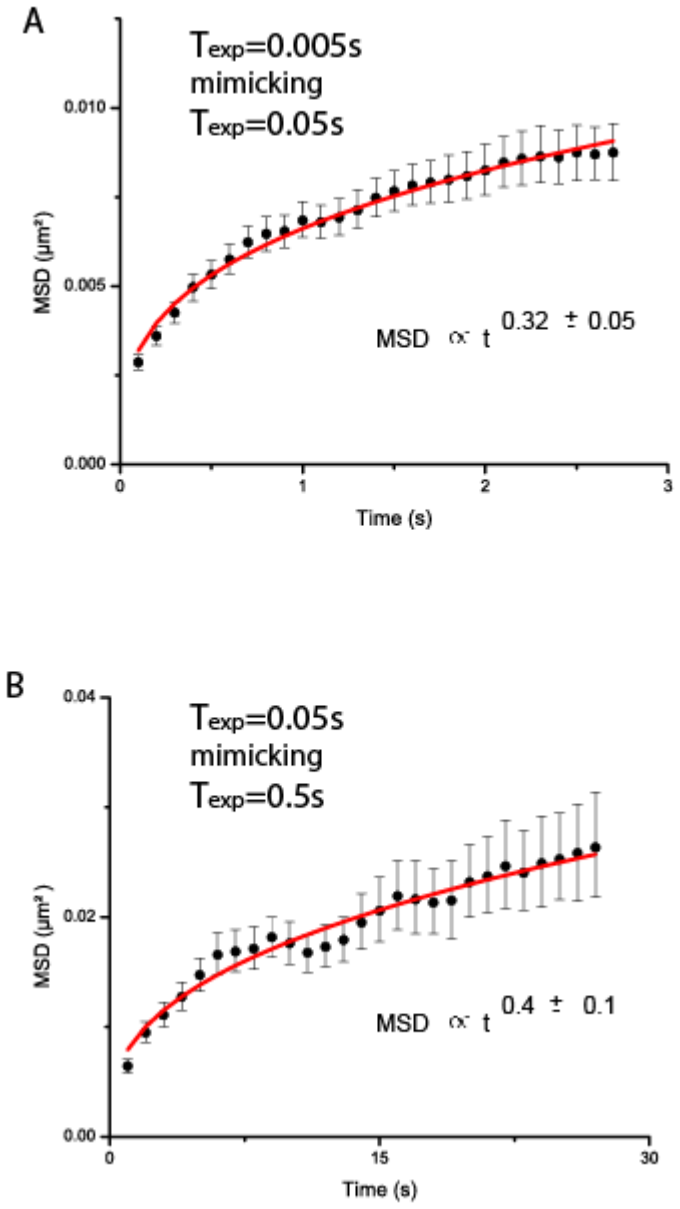

Figure S 22 Mimicking higher exposure time with lower exposure time*. Position recovered with lower exposure time was time averaged with a ten fold window. The exponent, were the same, although less consistent then the one measured on Figure 1..*